USE OF SATELLITE DATA FOR IMPROVED WETLAND MODELING AND MANAGEMENT: APPLICATION TO THE SUDD WETLAND, NILE RIVER BASIN

A Dissertation
Presented to
The Academic Faculty

by

Courtney Di Vittorio

In Partial Fulfillment
of the Requirements for the Degree
Doctorate of Philosophy in the
School of Civil and Environmental Engineering

Georgia Institute of Technology
May 2020

USE OF SATELLITE DATA FOR IMPROVED WETLAND MODELING AND MANAGEMENT: APPLICATION TO THE SUDD WETLAND, NILE RIVER BASIN

Approved by:

Dr. Aris Georgakakos, Advisor
School of Civil and Environmental Engineering
Georgia Institute of Technology

Dr. Yao Xie
School of Industrial and Systems Engineering
Georgia Institute of Technology

Dr. Jingfeng Wang
School of Civil and Environmental Engineering
Georgia Institute of Technology

Dr. Augusto Getirana
Earth System Science Interdisciplinary Center
University of Maryland

Dr. Rafael Bras
School of Civil and Environmental Engineering and School of Earth and Atmospheric Sciences
Georgia Institute of Technology

Date Approved: [Dec 02, 2019]

ACKNOWLEDGEMENTS

Earning my doctorate degree at the Georgia Institute of Technology has certainly been a privilege, and I have many people to thank for their support along the way. I would first like to thank my advisor, Dr. Aris Georgakakos, who has inspired me with his commitment to integrity in research, and with his passion and dedication to pursing meaningful projects. I am also very grateful for my committee members, Dr. Jingfeng Wang, Dr. Rafael Bras, Dr. Yao Xie, and Dr. Augusto Getirana for offering their support and dedicating their time to improving my dissertation. I am thankful to the students and staff within the GWRI lab: Martin, Xiaofeng, Husayn, Saubhagya, Bilal, Lida, and Xie. I appreciate their positive attitudes and have truly enjoyed getting to know them. I would also like to express gratitude toward many of my peers at Georgia Tech who have been both friends and mentors, including Brittany, Alison, Eric, Emma, Brian, Xenia, Fikret, Caroline, and Camille. I appreciate our many insightful conversations, your feedback and support, and look forward to following your successful careers. I am also thankful to many mentors at Georgia Tech that have guided me over the past six years, including Dr. Wendy Newstetter, Dr. Lisa Rosenstein, the CTL team, and Dr. Marta Hatzell. I am extremely grateful to my new co-workers at Wake Forest University, for their patience, support, and understanding as I was still completing this dissertation as an Assistant Professor in the newly established Engineering Department.

Most importantly, I would like to thank my family. I appreciate my parents, who allowed my husband, daughter, and I to live in their basement (my childhood home) while I was finishing my degree. I hope my daughter Gabriella forgives me for reading academic journals to her when she was a newborn, and I am grateful to Annalee for being such an easy-going infant and allowing me to get some sleep while I was finishing this research. Finally, I am especially grateful to my husband, Damien, who has been by my side through the ups-and-downs, never doubted me, and has been a never-ending supply of much-needed support and energy.

This research made use of extensive hydrologic data (river flows and lake levels) that were made available by my advisor, Professor Aris P. Georgakakos, through his past and continuing involvement with the Ministries of Water Resources and Irrigation in Uganda, Sudan, and Egypt. In-situ hydrologic observations provided by Dr. Georg Petersen were also valuable for assessing satellite-derived estimates. Additionally, this material is based upon work partially supported by the National Aeronautics and Space Administration (NASA) under Award No. 80NSSC17K0325 issued through the Mission Directorate, and in part by the National Science Foundation Graduate Research Fellowship Program (NSF-GRFP) under Grant No. DGE-1650044. Any opinions, findings, and conclusions or recommendations expressed in this article are those of the authors and do not necessarily reflect the views of the NSF, NASA, or other organizations.

TABLE OF CONTENTS

LIST OF TABLES

LIST OF FIGURES

SUMMARY

Decision support tools used in water resources management allow stakeholders to make informed decisions and assess the trade-offs of alternative management options. However, these tools are typically driven by the regulation of lakes and reservoirs and often do not fully incorporate the dynamics of wetlands. Wetlands provide important socio-economic and environmental services that should be protected and sustained. However, the cost associated with collecting enough in-situ data to accurately characterize the hydrology of many wetlands impedes their integration into hydrologic models. This study investigates how remotely sensed information (from satellites) can be leveraged to develop and calibrate hydrologic models of wetlands in data scarce areas. The value of this research is demonstrated for the Sudd Wetland, a vast seasonal wetland located in South Sudan that is a critical component of the Nile River hydrology.

CHAPTER 1: INTRODUCTION

Wetlands are valued by society for the many socioeconomic and environmental services they provide, including the provision of fish, bird and other wildlife habitats, natural water filtration, flood mitigation, groundwater and aquifer recharge, climate regulation through Nitrogen and Carbon cycling, and spaces for recreational activities [*Mitsch and Gosselink*, 2007]. The Millennium Ecosystem Assessment [2005] warned that these services are at risk and estimated that more than 50% of wetlands in parts of North America, Europe, Australia, and New Zealand were destroyed in the twentieth century. This wetland degradation has continued since the 2005 Assessment and will be exacerbated by climate change. The National Climate Assessment [*A. P. Georgakakos et al.*, 2014; *Groffman et al.*, 2014] emphasized that coastal wetlands are vulnerable to sea level rise, which will lead to storm surges having more drastic impacts on coastal communities. Inland floodplain wetlands are vulnerable to excessive flooding from the increased magnitude and frequency of heavy storms and to more prolonged and severe droughts caused by climate change. The degradation of these wetlands will increase the amount of infrastructure damaged during heavy floods, and will cause surface water quality to further deteriorate as these natural buffers will no longer modulate sediment, nitrogen, and other pollutant loads. Therefore, there is an urgent need to improve our understanding of wetlands and implement policies and procedures towards the long-term sustainability of these vital resources.

The amount of water wetlands receive is dependent on the regulation of connected rivers, lakes, reservoirs and aquifers; inversely, the hydrologic processes within wetlands impact the water balance of entire river basins. This impact is substantial considering the global wetland surface area is approximately double that of lakes and reservoirs [*Lehner and Döll*, 2004], and their extents are estimated to have a significant seasonal fluctuation [*Papa et al.*, 2010]. However, water management assessments all too often focus on impacts and benefits associated with rivers, lakes, reservoirs, aquifers, and estuaries [*Cai*, 2008; *A. P. Georgakakos et al.*, 2012; *Hassanzadeh et al.*, 2014; *Kotir et al.*, 2016; *Tidwell et al.*, 2004] and do not consider wetland responses in detail. Therefore, wetland responses and their roles in regional water balances and ecosystem preservation need to be better quantified and understood.

Many wetland models have been developed to estimate water quality and quantity variables [*Hattermann et al.*, 2006; *Hudak*, 2014; *Yongbo Liu et al.*, 2008; *Su et al.*, 2000; *X. Wang et al.*, 2008; *X Wang et al.*, 2010]. However, these models are often highly parameterized, dependent on an extensive amount of in-situ data, and difficult to integrate into basin-wide water management models. Due to the remoteness and vast extent of many wetlands, collecting adequate in-situ data required for hydrologic model calibration is often cost prohibitive and infeasible [*Finlayson*, 2003]. Fortunately, satellites provide opportunities to observe wetlands remotely and derive key hydrologic variables with sufficient spatial and temporal resolution.

This proposed study explores how remote sensing information can be used to estimate wetland hydrologic variables and subsequently develop wetland hydrologic

models that can be integrated into decision support tools for basin-wide water resources assessments and management. The potential impact of this research is demonstrated for the Sudd Wetland, located in South Sudan.

The Sudd is part of the Nile River Basin, which is shared by 11 African countries (Burundi, Democratic Republic of Congo, Egypt, Eritrea, Ethiopia, Kenya, Rwanda, South Sudan, The Sudan, Tanzania, and Uganda) and supplies water to nearly 500 million people [*Nile Basin Initiative NBI*, 2016]. Water demand within the Nile Basin is expected to increase five-fold primarily due to projected population growth [*United Nations Environment Programme*, 2018], and a key question the Nile countries are grappling with is: How can the Nile water be shared to meet the needs and aspirations of human communities and to sustain the environment? The answer to this question may partially lie within the Sudd Wetland. Decision support tools that estimate the amount of water flowing *through* the Sudd are available (e.g., the Nile Decision Support Tool (Nile DST), [*A P Georgakakos et al.*, 2003]), but they do not represent other wetland processes that sustain the ecosystem diversity and the wetland influences on the pastoral way of life for over a million people who live in the area [*United Nations Environment Programme*, 2018]. At the same time, rising water scarcity pressures in the Northern Nile have motivated various water conservation project proposals, including a canal to divert some of the Sudd water downstream of its exit. Such proposals need to be carefully assessed as part of a shared-vision basin-wide sustainable plan through tools that explicitly incorporate wetland sustainability as an assessment criterion or metric.

To address the aforementioned challenges, this research focused on developing a hydrologic model of the Sudd using satellite-based information. This hydrologic model can be used to assess how water management scenarios within the Nile River Basin might affect the social, environmental, and economic services that the wetland provides. While this research was applied to the Sudd, novel methods in wetland land cover classification, inundation mapping, and wetland hydrologic modeling were developed that can be applied to wetlands in data scarce areas worldwide.

1.1 Thesis Objective, Scope, and General Approach

1.1.1 Objective

Based on the abovementioned challenges and opportunities related to remote sensing information and wetland hydrologic modeling and management, the objective of this research is motivated by the following overarching question:

> *How can satellite data be leveraged to develop process-based hydrologic models of wetlands with limited in-situ data, enabling the integration of wetland socio-economic and environmental services into basin-wide water resource assessments and management?*

1.1.2 Scope

In addressing the overarching question, several more specific research questions were addressed, defining the scope of research:

1. Can multi-temporal satellite imagery be leveraged to improve existing wetland land cover classification procedures?
2. Can wetland inundation maps be derived from satellite imagery with sufficient accuracy and spatial and temporal resolution to inform hydrologic wetland models?
3. Can reliable estimates of precipitation and evapotranspiration (ET) rates be obtained from satellite-based data products in areas with limited in-situ data?
4. Can the Sudd inflows and outflows be estimated from a limited amount of in-situ data available upstream and downstream of the Sudd entrance and exit, with sufficient accuracy to calibrate a hydrologic model of the Sudd?
5. How does the uncertainty of the estimated hydrologic fluxes and flows propagate through a hydrologic model of the Sudd?
6. Are the satellite-based estimates of the Sudd flooded area extents, precipitation rates, and ET rates, and estimates of the Sudd inflows and outflows consistent with one-another in terms of the overall Sudd water balance? Can data correction procedures be developed from a holistic comparison of these independently-derived estimates?
7. What are the dominant wetland hydrologic processes that must be represented in a model for the Sudd? Are there existing models that can accurately simulate these processes and the wetland response?
8. What are the advantages and disadvantages of statistical, physically-based hydrologic (lumped or semi-distributed), and hydrodynamic wetland models, and what model type would be most appropriate for the Sudd, given its dominant processes and data availability?

9. What is a suitable approach for developing a model and assessing its performance in a way that considers the uncertainty from the satellite-derived data, the model structure, and the calibration parameters jointly, to make recommendations on how to incrementally improve the model without overfitting uncertain "observations" of the Sudd flooded areas and outflows?

1.1.3 General Approach

The nine questions that define the scope of this research were addressed in the following primary research tasks that are discussed in detail in Chapters 3 through 6:

1) Develop a method to derive reliable multi-temporal inundation maps of the Sudd Wetland from satellite imagery.
2) Acquire and compare various satellite-based data sources for precipitation and ET rates in the Sudd, concurrent with the satellite-derived inundation maps.
3) Estimate the Sudd inflows and outflows concurrent with the satellite-derived inundation maps using available in-situ flow data in the Nile River Basin combined with supplementary data sources and physically and statistically based river routing models.
4) Evaluate the consistency of the Sudd inundation extents, hydrologic fluxes, and river flows in terms of the Sudd water balance to select from alternative precipitation and ET estimates, and determine whether correction procedures can be developed and applied to improve this consistency.

5) Combine the available satellite and in-situ estimates of river flows, precipitation and ET rates, and inundated area extents to develop a process-based hydrologic model of the Sudd that adequately simulates wetland dynamics and considers data and model uncertainties jointly.

The flow chart shown in Figure 1 provides an overview of the research workflow and illustrates how different data sources and research tasks are related in the hydrologic model development process. The modeling process is initiated by the model performance criteria. Many of the social, environmental, and economic services that the Sudd provides are linked to the flooded area extents. Therefore, a model of the Sudd should be able to simulate the wetland's multi-temporal flood extents. Additionally, this model should simulate outflows from the Sudd's exit to enable its integration into basin-wide models that are used for water resources planning, such as the Nile DST. These performance criteria were used to help identify appropriate model processes and scales (task #1).

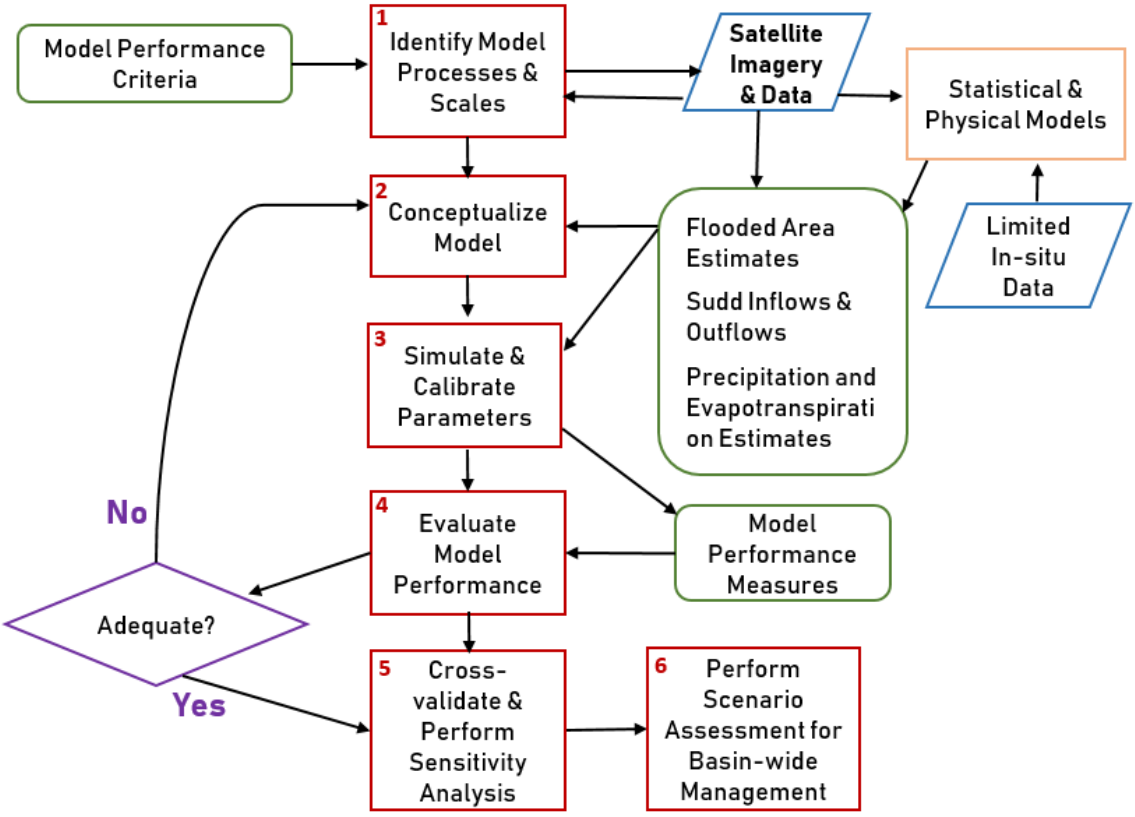

Figure 1: Flow chart describing research workflow. Red boxes represent primary tasks, orange boxes represent intermediate tasks, green boxes represent task inputs and outputs, blue boxes represent data sources, and purple box indicates a decision.

A large component of this research was the derivation of multi-temporal wetland flood extent maps from satellite imagery. The ideal model processes and scales identified by the performance criteria influenced the selection of an appropriate source of satellite imagery. The availability of satellite images and their corresponding spatial and temporal resolutions in-turn influenced the temporal horizon of the model and the time step that could be simulated and calibrated. Subsequently, the data sources and models used to estimate inflows, outflows, precipitation, and ET were chosen to align with the modeling horizon and time step of the satellite images.

The second research task, the model conceptualization, was a substantial portion of this research and was an iterative process that was adapted according to insights from the satellite-derived data sets and initial modeling results. The satellite-based estimates of flooded area, precipitation, ET, and the estimated inflows and outflows were evaluated individually for seasonal variations and intra-annual trends, and compared to each other to understand the overall wetland water balance, relative magnitudes of hydrologic processes, and the wetland storage-attenuation characteristics. Insights from these analyses were considered when developing conceptual hydrologic model structures. Initial model conceptualizations were intentionally simple, and more complex representations of hydrologic processes and interactions were added only if deemed necessary according to the model performance.

Each potential model was calibrated (task #3) by minimizing an objective function that accounts for differences between simulated and observed flooded areas and outflows, in terms of both magnitude and timing. Each model was then evaluated (task #4) using time series and scatter plots of the simulated hydrologic fluxes and states, and the causes of discrepancies between the simulated and observed flooded areas and outflows were explored to determine how the model structure could be improved in subsequent iterations.

The best performing the model was then cross-validated and its sensitivity to uncertainties in the calibration parameters, satellite-based data sources, and estimated river flows was assessed (task #5). This exercise provided insights on where future modeling efforts should be focused to improve the model performance while reducing uncertainty.

Although beyond the scope of this research, the final model can be simulated from the early 1900's using historical flow records from the Nile Basin Volumes [*Hurst and Phillips*, 1932], and precipitation and evapotranspiration estimates provided by the Climate Research Unit [*University of East Anglia Climatic Research Unit*, 2017].This historical simulation will allow the Nile Basin stakeholders to understand how the wetland responds to variations in flows, hydrologic fluxes, and water infrastructure development processes. The insights gained from this simulation could inform the water-sharing dialog in the Nile Basin. Additionally, water managers can examine how future water development projects might impact the Sudd and the services it provides by simulating the model under potential future management and climatic scenarios (task #6).

1.2 Thesis Organization

This dissertation contains seven chapters. The second chapter provides an extensive literature review of the Sudd Wetland, remote sensing of wetland areas, and hydrologic models of wetlands. Chapter 3 presents a new method that was developed to derive wetland land cover maps from optical satellite imagery and subsequently obtain multi-temporal wetland inundation maps. This research has been published in Remote Sensing of Environment [*Di Vittorio and Georgakakos*, 2018]. The published paper has been included here and modified slightly to incorporate updates and improvements that were identified during the hydrologic modeling process. Chapter 4 presents multiple estimates for precipitation and ET rates, obtained from satellite-based data products and in-situ databases. This chapter also contains a detailed description of how the Sudd inflows and outflows were estimated. Chapter 5 combines the inundation maps from Chapter 3 with the

hydrologic data from Chapter 4 to assess the consistency between the flux estimates in terms of the Sudd water balance. This analysis led to a closer examination of the inundation maps and the connectivity of the wetland areas as it expands and contracts, and a procedure for adjusting the inundation maps to align more closely with the hydrologic fluxes was developed and applied. Chapter 6 presents alternative hydrologic models of the Sudd that were formulated, calibrated, and evaluated using the iterative modeling process described in Figure 1. Chapter 7 summarizes this research and the progress made toward answering the questions listed in Section 1.1, and makes recommendations for future research efforts to improve the Sudd model for applications in water resources management within the Nile Basin.

CHAPTER 2: LITERATURE REVIEW

2.1 The Sudd Wetland

2.1.1 Overview

An overview of the Sudd Wetland and its hydrology is illustrated in Figure 2. The Sudd inflow originates from the Great Equatorial Lakes (Lakes Victoria, Kyoga, and Albert) in Uganda. The large storage of these cascading lakes makes for gradually varying river flow. After exiting Lake Albert, the river receives surface run-off contributions from seasonal tributaries (known as the Torrents) and enters the Sudd wetland in South Sudan. The Sudd region is characterized by mild river slopes and impermeable clay soils, and at moderate to high flows, the water spills over the top of the riverbank and spreads into the surrounding floodplains. Evaporation exceeds precipitation in most months of the year in this region, and much of the water inundating the floodplains becomes evapotranspiration and does not return to the river, known as the Bahr el Jebel in this region. Thus, only about half of the water entering the Sudd emerges at its exit (Sutcliffe and Parks 1999).

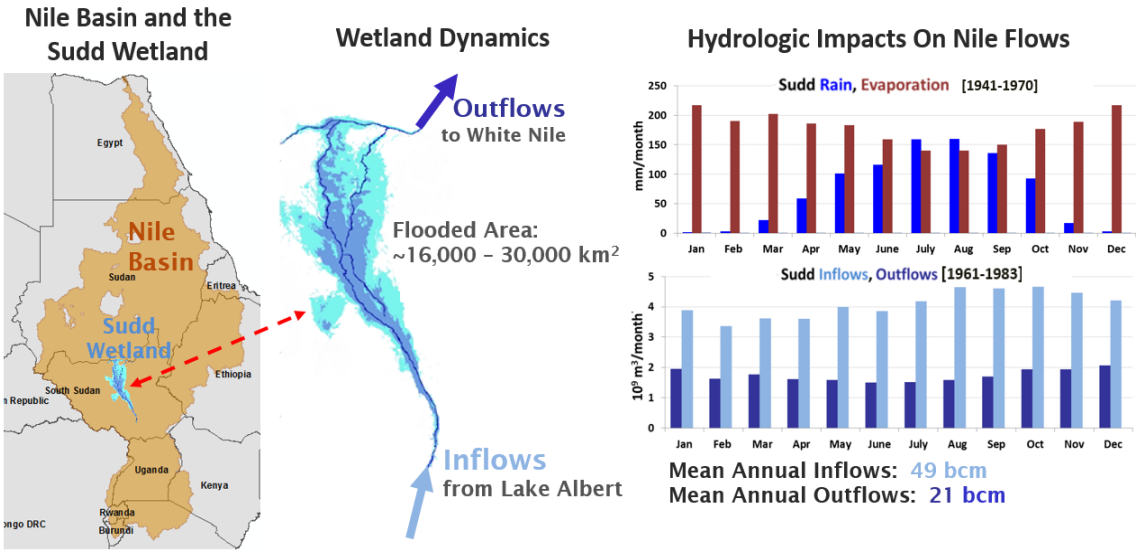

Figure 2: Left: Location of Sudd Wetland within the Nile Basin. Middle: Typical permanently (blue) and seasonally (cyan) flooded areas estimated in previous work. Right: Historical observations within the Sudd measuring rainfall, evaporation, inflows, and outflows obtained from Sutcliffe and Parks (1999).

The Sudd flooding regime sustains a diversity of plants and animals as well as the local economy. This vast seasonal floodplain is believed to be the lifeline of biota within the Nile, because the seasonal flood pulse allows plant and animal life to travel between aquatic and terrestrial environments [*Junk*, 1989]. Additionally, the nomadic communities in the Sudd rely on its seasonal flooding to sustain their livelihoods, with grasslands flourishing while flooded and providing grazing pastures for cattle when the water recedes. A large extent of seasonal flooding is required to regenerate enough grasslands to sustain cattle throughout the dry season [*Howell et al.*, 1988].

2.1.2 Mapping the Sudd Extents

The Ramsar convention recognized the Sudd as a wetland of international importance and designated 57,000 km^2 –an area nearly equal to that of Netherlands and

Belgium combined—for preservation [2006]. The actual inundated area of the Sudd varies both seasonally and annually. The most recent ground survey of the full extent of the wetland was performed in 1979–1980 and used field observations combined with aerial and satellite imagery. The report estimated that the permanently inundated area was 16,200 km^2 and the seasonally inundated area was 13,600 km^2 (Sutcliffe and Parks 1999). Due to the wetland size and limited accessibility, in-situ data required to delineate the flooding extent of the Sudd could not be collected.

More recent studies have explored the utility of remote sensing data. Mohammed et al. [2004] estimated flooded areas indirectly using evaporation maps, derived based on the Surface Energy Balance Algorithm for Land (SEBAL). This model requires many input parameters that must be estimated directly from ground measurements or indirectly from remote sensing products to partition energy between soil, sensible, and latent heat flux. This analysis led Mohammed to conclude that the average Sudd area is 74% larger than the area reported by Sutcliffe.

In a study completed by Rebelo et al. [2012], a single image differentiating permanently and seasonally flooded areas within the Sudd was obtained using four ALOS-PALSAR images. The area considered for flooding was taken as the full area delineated between the Sudd entrance and exit using the 90 meter hydrologically corrected digital elevation model (DEM) from the Shuttle Radar Topography Mission (SRTM) distributed by HydroSHEDS (http://www.hydrosheds.org). Any pixels within this area that were flagged as flooded according to a threshold value were considered part of the wetland system, despite the fact that many of these pixels are only temporally flooded from rainfall

and likely never contribute to the river flow [*Howell et al.*, 1988; *Petersen and Fohrer*, 2010].

Remondi et al. [2013] derived a wetness index from a multi-year time series of MODIS (MOderate Resolution Imaging Spectrometer) land surface reflectance data and applied a threshold value to a wetness index to identify areas that were flooded. The optimal threshold value was required to be consistent with existing global MODIS land cover data, and temporal trends of the indices were used to distinguish between pixels that were permanently flooded, seasonally flooded, or non-wetland. The resulting wetland extents were then related to hydrological indices that accounted for estimates of river flow, precipitation, and evapotranspiration.

(Sosnowski et al. [2016] used MODIS land surface temperature differences between day and night to identify the Sudd flood extent. However, they only evaluated images during the dry season where it was possible to distinguish between wet and inundated areas. Their study along with Mohammed's [2004] suggest that there is a connection between the Sudd and the western Bahr El Ghazal basin.

Most recently, Wilusz et al. [2017] extracted monthly flood maps from 2007-2011 using Envisat Advanced SAR (Synthetic Aperture Radar) C-band imagery. In this study, a similar technique to that of Rebelo et al. was used to delineate the area considered for flooding. The resulting flood maps show a maximum flooded area in September, a time that coincides more closely to the peak of the rainy season than the max flood extents of the Sudd. This result supports the idea that some of the flooded area delineated in this study

is not connected to the Nile system, and is therefore not appropriate for incorporation into a hydrologic model of the Sudd Wetland.

The abovementioned estimates of the Sudd flooded area extents have limitations with regards to spatial and temporal resolutions, the delineation of the outer wetland extents, and the classification approach employed. New land cover and inundation mapping methods should therefore be explored as part of this research. These methods should be developed through an iterative process that considers how appropriate the resulting flood maps are for the calibration of a hydrologic model.

2.1.3 Hydrologic Modeling of the Sudd

The most well-known and referenced hydrologic model of the Sudd was developed by Sutcliffe and Parks [*J V Sutcliffe and Parks*, 1987; 1999]. A simple mass balance model that represents the Sudd as a lumped system was formulated and is described as follows:

$$\delta V = [Q - q + A(R - E)]\delta t - r\delta A \quad [1]$$

where:

V = volume of flooding
Q = inflow into the Sudd
q = outflow from the Sudd
R = average rainfall over the flooded area
E = average evaporation over the flooded area
A = total flooded area
r = soil moisture recharge depth

The soil moisture recharge rate represents infiltration, which is positive only for the change in flooded area as the wetland expands in size. Deep groundwater interactions were considered insignificant because the soil is considered an impermeable clay.

If this differential equation is discretized for increments of i = 1 month it can be re-formulated as follows:

$$V_{i+1} - V_i = Q_i - q_i + A_i(R_i - E_i) - r_i(A_{i+1} - A_i) \quad [2]$$

Sutcliffe and Parks had estimates of the flooded area obtained from areal satellite images for four dates. These images were used to calibrate the model, but a relationship between the flooded area and volume of flooding had to be assumed a priori to solve the system over a continuous period. They chose to use a simple linear relationship, A=kV, where k is the inverse of a spatially representative depth of flooding and is assumed invariant with time. Substituting this relationship into Equation 2:

$$V_{i+1} - V_i = Q_i - q_i + kV_i(R_i - E_i) - kr_i(V_{i+1} - V_i) \quad [3]$$

To account for the precipitation and evaporation that occurs over the newly flooded area during a monthly interval, Sutcliffe and Parks interpolated the area over two time steps:

$$V_{i+1} - V_i = Q_i - q_i + \frac{1}{2}kV_i(R_i - E_i) + \frac{1}{2}kV_{i+1}(R_i - E_i) - kr_i(V_{i+1} - V_i) \quad [4]$$

Then after combining terms and solving Equation 4 for V_{i+1} the final equation is:

$$V_{i+1} = \frac{V_i\left[1+k\left\{r_i-\frac{1}{2}(E_i-R_i)\right\}\right]+Q_i-q_i}{1+k\left\{r_i+\frac{1}{2}(E_i-R_i)\right\}} \quad [5]$$

Available data that were used as inputs into this model were: measured 10-day inflows and outflows, rainfall records averaged over eight stations within the area, and

average monthly evaporation estimated from both ground observations and Penman equation calculations. The soil moisture recharge was assumed to be 200 mm at the beginning of the rainy season and was reduced by the net precipitation as the rainy season progressed. The model was simulated from 1905 – 1983 using an estimate of the initial volume of water. The depth variable (k) was treated as a parameter that was calibrated to the flooded area images. A value of k = 1m was reported to achieve reasonable results.

Sutcliffe and Brown [2018] recently used this same hydrologic model and historic flow data obtained between the Sudd entrance and exit to assess flooding characteristics for different regions of the Sudd. They extracted flow records from the Nile Basin Volumes that were collected by boats operated by the Egyptian Ministry of Irrigation. Sutcliffe and Brown calculated the flooded area for Sudd sub-basins separated by the transects where they had flow data for the 1927 – 1964 period. They could not extend this analysis to 1983 because the flow records were incomplete following the sharp rise in Lake Victoria and subsequent alterations to the Sudd hydraulics and flooding extents. Instead they utilized vegetation maps of the Sudd estimated from an aerial survey in 1982 as a proxy for flooded area. They observed that the flooded area in the downstream section of the Sudd had increased substantially and deduced that the increased water levels after 1961 augmented backwater effects near the Sudd exit and caused widespread flooding in the lower portion of the Sudd.

Petersen [2005] attempted to develop a process-based, distributed model of an upstream portion of the Sudd to assess the impact of a road and levee construction project. As part of this effort, a significant amount of ground data was collected and integrated into

the model: bathymetric profiles along with current velocities at cross sections along the Bahr el Jebel, hydrometeorlogical station data containing measured rainfall, wind speed, solar radiation, humidity, and temperature, experimental measurements on evapotranspiration and soil water recharge, soil samples and their hydraulic conductivity, and water levels in permanent swamps and along a newly constructed dike that is seasonally flooded. This data was collected from April – November 2005, which does not cover a full hydrologic cycle. Petersen used the DHI (Danish Hydraulic Institute) Mike 11 GIS (Geographic Information System) modelling system, a one-dimensional model that relies on cross section data derived from a DEM to route flows through the wetland. The inaccuracy of the DEM combined with the fact that field measurements were collected over a relatively short period of time lead Petersen to conclude that the model outputs of flooded areas and water depths should be given a low confidence level.

Mohammed et al. [2005] modeled the hydroclimatology of the entire Nile Basin using a regional atmospheric climate model to evaluate the potential impact of channelizing the Sudd. The model simulated vertical hydrologic fluxes over 50-km square grids and tracked the volume of water within 4 layers of soil to a 5-m depth. To simulate the wetland, Mohammed forced the model to spread upstream river discharges over 15 grids covering the Sudd. This discharge was assumed to enter into the soil layers and model parameters were calibrated to match Sudd hydrologic fluxes and flooded areas estimated in his previous research [2004]. Because the accuracy of the Sudd hydrologic model itself was not a primary goal of this research, this study did not advance present knowledge and understanding of the Sudd hydrology

2.1.4 Management of Sudd in the Context of the Nile River Basin System

As part of the efforts to develop a shared vision management plan for the river, the Nile Basin countries have been considering various management options including the full regulation of the Great Equatorial Lakes and the construction of the Jonglei Canal [*Garstin*, 1904]. This canal was a channel located to the East of the wetland designed to by-pass the Sudd region and increase the amount of water exiting the wetland. Construction of the canal was initiated in the late 1970's but was abandoned due to the Second Sudanese Civil War. Sutcliffe and Parks [1999] simulated the altered Sudd flooded area that would result from the operation a canal. They achieved this by using their hydrologic model with a reduction in inflows of 20 and 25 mcm/day (approximately 15% of average annual flow) and a regression relationship between historical inflows and outflows to estimate the resulting altered outflows. Their results showed that the seasonally flooded area would be reduced by 17% and 21%, respectively, for hydrologic conditions similar to those of 1961-1980 (following the rise of Lake Victoria). They found that the loss of seasonally flooded land could be reduced to 10% if the canal flows were varied between 15 and 25 mcm/day to align with the natural seasonal inflow variation.

The Georgia Water Resources Institute (GWRI) has been supporting the Nile Basin planning processes through the development of information and decision support tools (DST) such as the Nile DST [*A P Georgakakos et al.*, 2003], the Decision Support System for the Management of the High Aswan Dam , the Lake Victoria DST [*A. P. Georgakakos and Yao*, 2007], and the assessment of basin-wide water management scenarios [*A. P. Georgakakos and Yao*, 1999]. In these tools and assessments, the Sudd region is

represented through statistical models calibrated based on historical inflow-outflow data. While these models represent well the historical inflow-outflow behavior, they cannot represent the underlying physical processes, nor can they assess the Sudd response under conditions dissimilar to those of the historical climate and regulation practices.

The Nile Basin Initiative (NBI) was established in 1999 aiming "to achieve sustainable socio-economic development through equitable utilization of, and benefit from the shared Nile Basin water resources" (http://nilebasin.org/). One of their key projects was the development of the Nile Decision Support System (DSS), completed in 2012 (http://nbdss.nilebasin.org). This software allows the 11 Member States to share knowledge and information and evaluate alternative management strategies. The Nile DSS relies on MIKE commercial modelling products (https://www.mikepoweredbydhi.com/); but, no information on whether and how the Sudd Wetland is modeled nor any related published assessments are available to date. The NBI recently launched the Nile Basin Trans-boundary Wetlands Project in 2016, aiming to enable the Member States to manage their wetlands more sustainably [*Nile Basin Initiative*, 2016; 2017]. The overarching goals of this project do not explicitly mention the integration of wetland sustainability metrics into the Nile DSS or an alternative hydrologic model for the Nile Basin.

2.1.5 Research Opportunities

Stakeholders have been interested in modeling and understanding the Sudd and its impact on the Nile River system for decades. However, they lack a comprehensive study centered on the Sudd that integrates in-situ and satellite observations, hydrological

modelling, and basin-wide water resource assessments. Section 2.1.2 summarized studies that have estimated the Sudd flood extents using remotely-sensed data, but these estimates are not helpful for the development and calibration of an accurate hydrologic model. The hydrologic model from Sutcliffe and Parks presented in Section 2.1.3 was not rigorously validated and potentially neglects important hydrologic processes. Petersen and Mohammed attempted to develop more complex models, but relied on rigid model structures that might not be representative of the Sudd hydrology and are difficult to calibrate considering the availability and accuracy of data. Finally, management initiatives within the Nile River Basin discussed in Section 2.1.4 do not consider the Sudd in sufficient detail to quantitatively link alternative management options to impacts on the socio-economic and environmental services that the Sudd provides.

2.2 Satellite-derived Wetland Land Cover and Inundation Maps

2.2.1 Existing Satellite Products

In contrast to land classes that are commonly mapped with satellite data, the complex and dynamic interplay between soil, water, and vegetation in wetland ecosystems results in unique land class features with various flooding regimes [*Gallant*, 2015]. Consequently, many existing global satellite-derived land cover and flood mapping products do not accurately portray the land classes and flooding dynamics of wetlands. For instance, The MODIS land cover product shown in Figure 3, has a single wetland class that does not capture the full extent of the Sudd. These global products are typically calibrated

using a set of ground truth points which do not represent the true variety of wetland classes and are thus inaccurate over wetland areas [*Mark A. Friedl et al.*, 2010].

Alternatively, satellite-based data products specific to wetlands are available. The Global Lakes and Wetlands Database provides the estimated outer extents of wetlands [*Lehner and Döll*, 2004] but does not capture the expansion and contraction of seasonal wetlands. Global near-real-time flood detection maps, such as those of the Dartmouth Flood Observatory (http://floodobservatory.colorado.edu/), have a very coarse spatial resolution and use thresholds that detect open water but fail to detect flooded vegetation [*Brakenridge and Anderson*, 2006]. A global surface water extents map was derived at a monthly temporal resolution using multiple satellites and successfully represented wetlands, but the spatial resolution is very coarse (0.25^o x 0.25^o) [*Papa et al.*, 2010; *Prigent et al.*, 2001]. This product was later downscaled to a 500-m spatial resolution using topographic metrics, but there was considerable variation in the measured accuracy [*Fluet-Chouinard et al.*, 2015] limiting its hydrologic applications.

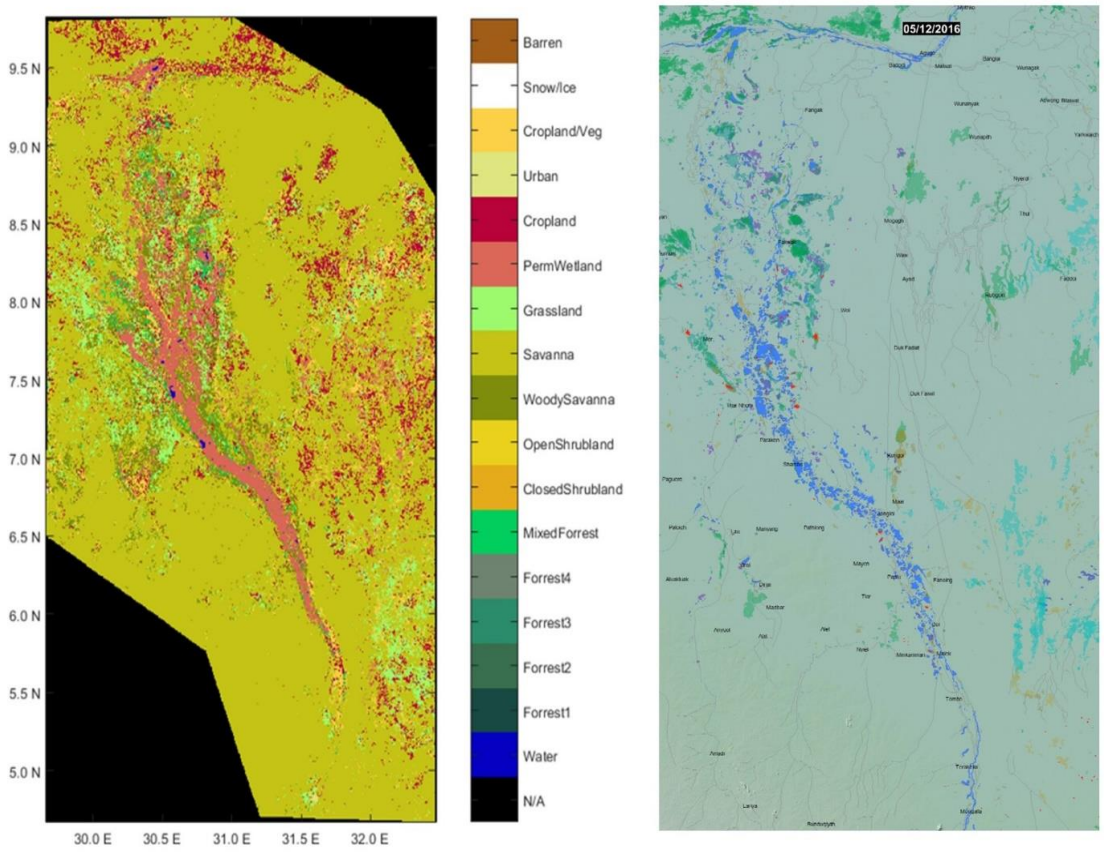

Figure 3: Left: MODIS Land cover classification map for 2010 over Sudd area. Right: Snapshot from Dartmouth Flood Observatory over Sudd area, where each color corresponds to flooding events from different years.

2.2.2 Identification of Flooded Vegetation

A significant challenge in remote sensing of wetlands is the detection of surface water beneath vegetation. A variety of satellite systems have been evaluated for their ability to map flooded vegetation. Two common data sources used are optical and SAR land surface imagery, each having distinct strengths and weaknesses. In optical imagery, the vegetation cover tends to dominate the spectral signal, and subsequently many inundation classification procedures detect open water bodies but neglect flooded vegetation

[*Guerschman et al.*, 2011; *Soti et al.*, 2009]. Flooded vegetation has been mapped using optical imagery; however, the algorithms are highly dependent on in-situ data and are often calibrated using single instances in time [*Gumma et al.*, 2014; *C Huang et al.*, 2014; *Ordoyne and Friedl*, 2008].

SAR images are favored for their ability to penetrate cloud cover. However, radar systems typically measure reflectance in a single wavelength, and each wavelength has a different success rate for detecting flooding beneath various types of vegetation [*Whitcomb et al.*, 2009]. Longer wavelengths can penetrate deeper into canopies and have been used to detect flooded forests using the double-bounce effect [*Hess et al.*, 2003]. However, for flooded herbaceous wetland species, the reflectance of longer wavelengths varies depending on the height of the underlying water, and shorter wavelengths might be more appropriate [*Bourgeau-Chavez et al.*, 2005; *Pulvirenti et al.*, 2011]. Obtaining temporally and spatially consistent radar imagery at multiple frequencies over a significant period is not yet possible, which limits the utility of radar imagery for multi-temporal wetland inundation mapping in hydrologic studies.

Many studies have used optical and radar imagery jointly to detect flooded areas [*Dronova et al.*, 2015; *Torbick and Salas*, 2015; *Ward et al.*, 2014]. However, these data often cannot be obtained contemporaneously, which leads to inconsistent temporal classification of land areas. The recent launch of the Sentinel-1 satellites are expected to provide new opportunities in this research area [*Drusch et al.*, 2012]. Studies have also combined radar and optical imagery with auxiliary data sources such as topographic indices from digital elevation models [*Landmann et al.*, 2010; *Margono et al.*, 2014], or remotely

sensed hydrologic variables such as precipitation [*Bergé-Nguyen and Crétaux*, 2015]. While inclusion of these variables has been shown to improve classification performance, this information can no longer be used to independently assess the accuracy of satellite-derived inundation maps. Additionally, if the same variables are used to develop hydrologic models, the uncertainties ingrained in the satellite data need to be considered explicitly in model calibration and use.

Remotely-sensed land surface temperature, which is an indicator of soil moisture, has also been used to detect flooded areas. For example, Zhang et al. [2015] used the maximum or minimum daily temperature and Ordoyne and Friedl [2008] used the temperature difference between day and night, which exploits the concept that water has a higher thermal inertia than land and will consequently have a lower diurnal temperature variation. While these indices may show a sharp contrast between flooded and dry areas during dry periods, this contrast weakens during wet periods when upland areas are moist but not flooded [*Leblanc et al.*, 2011]. Therefore, obtaining a continuous time series of flooded area using this index alone is tentative; additionally, temperature data products are typically coarser in spatial resolution when compared to available optical and radar products.

2.2.3 Common Classification Methods Applied to Remote Sensing Data

Numerous classification methodologies have been applied to convert remote sensing data into maps that discriminate land classes and flooded areas. A common, relatively simple method is to apply thresholds to remote sensing indices [*Brakenridge*

and Anderson, 2006; *Kuenzer et al.*, 2015; *Leauthaud et al.*, 2013; *Ogilvie et al.*, 2015; *Wu and Liu*, 2014]. While this method has shown promise for detecting deep, open water bodies, thresholds for areas with shallow water and vegetation typically vary spatially and temporally, and a significant amount of in-situ data is required for accurately determining these thresholds [*Ji et al.*, 2009; *Xiao et al.*, 2005; *Zhou et al.*, 2016]. A variety of more complex statistical and computational classification techniques have been used for land classification and flood detection, which should be modified based on the goal of the study and the properties of the input data. These techniques are broadly categorized into unsupervised or supervised classification methods. In unsupervised classification, classes are chosen by an algorithm that maximizes the separation between classes, often using a statistical distance measure [*Bartholomé and Belward*, 2005; *Papa et al.*, 2010]. When a specific set of classes is desired, supervised classification is more appropriate—a sample set of each class is provided a priori, the algorithm is calibrated, and the remaining pixels are classified. Some common supervised classification algorithms rely on parametric statistical measures, such as the maximum likelihood method [*Glanz et al.*, 2014; *Jenny et al.*, 2003], considered to be the most commonly used classification method for remote sensing applications [*Waske*, 2009]. This method assumes that the data is normally distributed and is difficult to implement for general, multi-temporal data sets. Another common approach to supervised classification uses the sample sets to develop decision trees [*Carroll et al.*, 2009; *Feng et al.*, 2016; *Fluet-Chouinard et al.*, 2015; *M. A. Friedl et al.*, 2002; *Hansen et al.*, 2000]. While this method does not require any assumptions about the underlying distributions of the classes, the success of these algorithms depends on the

quality and quantity of the sample data sets, and classification logic typically lacks physical interpretation.

An additional distinction can be made between classification procedures that evaluate images individually and procedures that incorporate multi-temporal sets of imagery. Often, classification is performed image-by-image, and the resulting classified images are compared to detect change [*Kuenzer et al.*, 2015; *Ogilvie et al.*, 2015; *Soti et al.*, 2009]. This approach is easy to implement with automated algorithms that do not require customization. Another common approach is to evaluate multiple images and derive statistics for each pixel such as the mean, standard deviation, and extreme values over the time series. Subsequently these statistics are processed to obtain a single land cover map that accounts for seasonal variations of land classes [*Arnesen et al.*, 2013; *Hansen et al.*, 2000; *Kontgis et al.*, 2015; *Sexton et al.*, 2013]. Alternatively, a set of images can be compressed temporally by performing a principal component analysis and deriving a few images that account for most of the variance within the full set. This reduced set is then used in the classification procedure [*Dronova et al.*, 2015; *Glanz et al.*, 2014]. Reducing the dimensionality of data decreases computation time and may eliminate the influence of noise on classification results. However, if temporal behavior of land classes is considered an important feature, then important information is lost by reducing time histories into singular statistics or applying linear transformations.

2.2.4 Research Opportunities

Although much research exists in wetland classification and inundation mapping, these algorithms can be improved by developing them for a specific application. Relatively few wetland land cover and inundation maps were developed specifically for hydrologic model development and validation. Consequently, the derived maps lack sufficient spatial and temporal resolution and are often dependent on ancillary hydrologic variables, introducing statistical dependencies when applied to hydrologic models. In addition, wetland classification algorithms could be further improved by considering site-specific land cover types and flooding regimes *jointly* to capture the dynamic nature of wetland land classes. Finally, while many studies have utilized multi-temporal data sets in classification algorithms, they often reduce time series to statistical measures instead of using all the data, including extreme values that may prove most important for detecting wetland flooding and drying processes.

2.3 Wetland Modeling

2.3.1 Wetland Types and Their Hydrologic Processes

Defining wetlands and differentiating between the various types has historically been a challenging endeavor. Many attempts have been made to define what constitutes a wetland and these definitions can be vague and even contradictory [*Mitsch and Gosselink*, 2007]. A popular wetland definition that has been adopted by the U.S. Fish and Wildlife Service and chosen for this study is:

> "Wetlands are lands transitional between terrestrial and aquatic systems where the water table is usually at or near the surface or the land is covered by shallow water.… Wetlands must have one or more of the following three attributes: (1) at least periodically, the land supports predominantly hydrophytes; (2) the substrate is predominantly undrained hydric soil; and (3) the substrate is nonsoil and is saturated with water or covered by shallow water at some time during the growing season of each year [*Cowardin et al.*, 1979]."

The above definition requires the presence of water as well as vegetation and soils that are endemic to wetlands. However, wetlands have more characteristics that need to be specified to conceptualize and model their hydrology. Hence the adoption of terminology such as swamps, marshes, bogs, fens, mangroves, peatlands, and deltas to further characterize wetlands. Wetland naming conventions tend to vary by country, and enforcing an international standard can be difficult. Fortunately, the Ramsar Convention, which engages 163 countries and monitors over 2,000 wetlands, has agreed to a standardized

wetland classification scheme [*Ramsar Convention Secretariate*, 2013]. The general categories are marine/coastal wetlands, inland wetlands, and man-made wetlands, consisting of multiple wetland types described by their size, vegetation, and whether the presence of water is permanent, seasonal, or intermittent.

Mitsch and Gosselink [2007] listed general hydrologic fluxes that occur in most wetlands, including surface inflows and outflows, groundwater inflows and outflows, evapotranspiration, precipitation, and tidal inflows and outflows. The most accurate mathematical representation of these fluxes and their influence on the hydrologic balance will vary substantially for different types of wetlands. For instance, the importance of groundwater fluxes will be greater for wetlands that rest on highly permeable soils, riparian wetlands will be strongly influenced by the magnitude of adjacent river flows, and tundra wetland models will need to account for snowmelt and sublimation. These variations were illustrated by Mitsch and Gosselink in Figure 4, where they evaluated hydrologic fluxes and their relative magnitudes for several wetlands using a simple water balance model. Even when wetlands have similar characteristics, their dominant hydrologic processes can vary depending on whether they are on a slope or in a depression [*Golet et al.*, 1993]. These

processes can also change seasonally. Pyzoha et al. [2008] demonstrated that the presence of groundwater flows in a wetland depended on fluctuations in the water table.

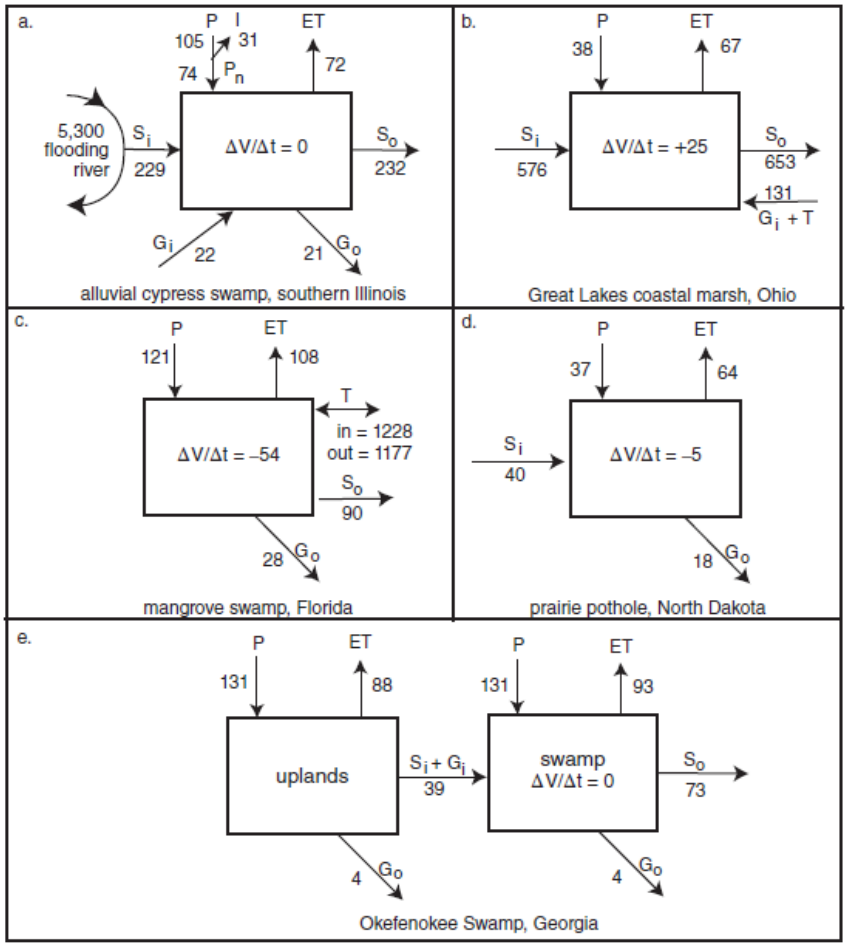

Figure 4: Hydrologic fluxes and their relative magnitudes (cm/yr) for various wetlands, from Mitsch and Gosselink [2007]. Notation: V: volume, t: time, P: precipitation, ET: evapotranspiration, Si: surface inflow, So: surface outflow, Gi: groundwater inflow, Go: groundwater outflow, T: tidal flow.

Figure 5 shows the potential hydrologic fluxes occurring in a riparian wetland, identified by Dall'O et al. [2001], who emphasizes that not all of these fluxes will be present in a single wetland. This detailed diagram can serve as a tool for hypothesizing the important hydrologic processes within the Sudd Wetland. However, modeling each of these fluxes in detail is not practical, considering the spatial and temporal resolution of available data and the intended application of the model.

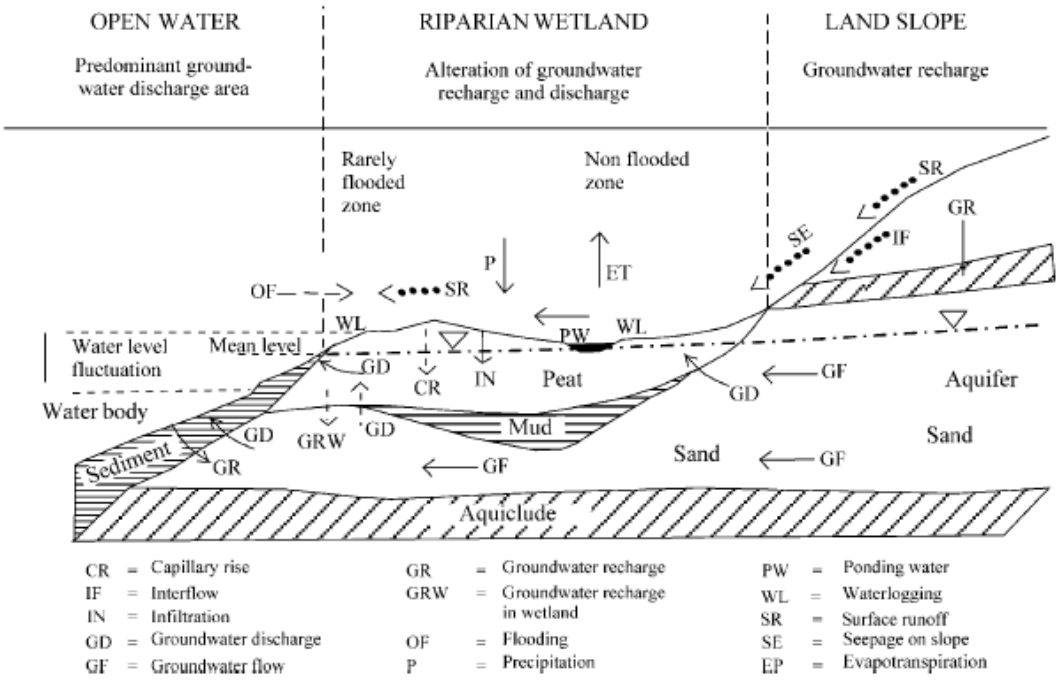

Figure 5: Schematic of potential hydrologic fluxes occuring in riparian wetlands, from Dall'O [2001].

2.3.2 Statistical Wetland Models

As briefly mentioned in Section 2.1.4, The Nile DST currently uses a statistical model to estimate the total volume of water that is lost in the Sudd Wetland, where losses

are defined as the difference between inflows and outflows at the Sudd's entrance and exit. During the development of the Nile DST, Georgakakos et al. [2003] evaluated both linear autoregressive models and an artificial neural network (ANN) model. A relatively simple autoregressive model (Equation 6) was able to achieve a very high correlation coefficient (0.9974) and low standard error (about 2% of the total outflow) and was thus chosen to be integrated into the Nile DST. While this model successfully routes flow through the wetland, it does not provide estimates of additional hydrologic variables that are of key interest to stakeholders, such as the time-varying flood extents.

$$Q_{LSS}(k) = 0.9923Q_{MON}(k) - 0.9522Q_{MON}(k-1) + 0.9435Q_{LSS}(k-1) - 1.0379 + \varepsilon(k) \quad [6]$$

where:

$Q_{LSS}(k)$ = *Sudd losses at time k*
$Q_{MON}(k)$ = *Sudd inflows at time k*
$\varepsilon(k)$ = *error at time k*

Statistical models such as those shown in Equation 6 are frequently applied in hydrology to model flows; however, relatively few studies utilize statistical methods to model other wetland hydrologic variables. ANNs have been used to estimate environmental variables, such as methane emissions, dissolved oxygen, and phosphorous removal and can outperform process-based models [*Akratos et al.*, 2009; *Naz et al.*, 2009; *Schmid and Koskiaho*, 2006; *Zhu et al.*, 2013]. However the application of ANNs to estimate wetland water quantities is less common, although Ali [2009] successfully calibrated an ANN that provides near-real-time predictions of water levels in the Florida Everglades from precipitation and evapotranspiration (ET) measurements. While ANNs may be advantageous for specific applications, they have several limitations. The models

can only be applied when conditions are similar to those of the calibration data, they are often not suitable for long-term simulations and scenario assessments, and most importantly, they do not provide valuable insights on physical hydrologic processes.

2.3.3 Process-based Wetland Models

In most water resources management applications, models must be able to predict hydrologic processes for potential future scenarios that deviate from historic conditions. Under this criterion, process-based models that contain mathematical representations of the physics of hydrologic processes are preferable to statistical models. Process-based wetland models can generally be categorized as lumped, semi-distributed hydrologic models and spatially-distributed hydrodynamic models. In lumped models, critical hydrologic fluxes are estimated, but the model does not account for the spatial heterogeneity of these processes. Semi-distributed models separate an area into multiple connected units with similar characteristics and treat each unit as a lumped system. Spatially distributed hydrodynamic models simulate the transfer of water from cell-to-cell within a grid and rely on topographic information and equations derived from the conservation of mass and momentum. The choice between these model structures should be governed by the intended application. For instance, a distributed hydraulic model with short time scales would be needed to derive a map showing areas that are temporarily flooded following a heavy rainfall event. Examples of lumped, semi-distributed, and distributed hydrologic and hydraulic wetland models found in the literature are described next.

Lumped Hydrologic Models:

Mitsch [2007] presents a general form of a lumped wetland mass balance water budget model, based on Equation 7. This formulation captures the dominant water fluxes of most wetland systems, although derivations of the individual terms should be customized to the wetland being modeled and the availability and accuracy of relevant data. For example, groundwater flows may need to be split into several terms that represent different layers and temporal scales.

$$\frac{\Delta V}{\Delta t} = P_n + S_i + G_i - ET - S_0 - G_0 \pm T \quad [7]$$

where:

V = volume of water storage in wetland
$\frac{\Delta V}{\Delta t}$ *= change in volume of water storage per unit time, t*
P_n *= net precipitation*
S_i *= surface inflow, including flooding streams*
G_i *= groundwater inflows*
ET = evapotranspiration
S_o *= surface outflows*
G_o *= groundwater outflows*
T = tidal inflow (+) or outflow (-)

An example of a lumped model that follows this general form was presented in Section 2.1.3, the Sutcliffe and Parks [1999] model of the Sudd Wetland. Zhang and Mitsch [2005] used a similar water budget model to simulate the hydrology of four different constructed wetlands. Their model had sufficient predictive efficiency to inform the design of future constructed wetlands.

Most lumped wetland models reported in the literature were developed to be integrated into larger catchment-scale hydrologic models that are designed to simulate river

flows. These catchment-scale models are typically semi-distributed, where the catchment is split into sub-basins that have unique characteristic and parameter sets. Each of these sub-basins are then treated as a lumped system when calculating hydrologic fluxes and river flows. Therefore, a wetland can be modeled as a lumped system within a semi-distributed model. However, wetlands are typically included to improve model performance, measured by agreement between modeled and in-situ flow observations, as opposed to how accurately the actual wetland hydrologic processes are represented. Nevertheless, the conceptualization and mathematical formulation of wetlands in these models are relevant to this study and summarized next.

The Soil Water Assessment Tool (SWAT) is commonly used to evaluate how alternative land management scenarios impact water quality and quantity [*Neitsch et al.*, 2011]. In the standard SWAT model, the amount of water stored within a wetland and the flow released to the river channel can be tracked if the user specifies the fraction of the sub-basin that is considered a wetland area. The volume of water that is stored in a wetland for each time step is estimated using a water budget model that accounts for surface runoff, lateral sub-surface flow, groundwater flow, precipitation, and evaporation. Water is then released from the wetland if the storage volume exceeds an amount that is related to user-specified wetland parameters. Wang et al. [2008] observed that while this model accounts for wetland hydrologic processes, it does not consider the storage and attenuation properties of wetlands, which can strongly impact the timing of outflows. Therefore, they adjusted parameters in the routing component of the SWAT model to improve modeled outflows in their area of interest.

The standard SWAT wetland model with Wang et al.'s calibration modification may be able to represent geographically isolated wetlands that do not directly exchange water with rivers, but alternative model formulations should be considered for riparian wetlands. Liu et al. [2008] modified the SWAT wetland mass balance equation by adding a term for flow between wetlands and river channels. To implement this, they reformulated the standard wetland area-storage relationship to also track the wetland water depth using empirical relationships from their area of interest. The direction and amount of water exchanged was determined from the difference between the wetland water depth and the water depth in the river channel calculated in the river routing module. More recently, Rahman et al. [2016] implemented more extensive modifications to SWAT for modeling riparian wetlands that connect to rivers through small side channels. The general approach was similar to Liu at al.'s; however, the water depth and the river depth were used to calculate the average depth of flow through an idealized rectangular channel connecting the river to the wetland. Subsequently, the volume of water exchanged could be calculated using the channel depth and a modified form of Manning's equation. In both applications, the optimal model parameters were calibrated using in-situ and modeled river flows.

Hatterman et al. [2006] reformulated the groundwater modeling component of Soil and Water Integrated Model (SWIM) [*Krysanova et al.*, 1998] to more accurately model sub-basins containing wetlands. This revision allows for the calculation of the water table height of each sub-basin for each modeled time step, which can subsequently be used to assess the depth and area of wetland flooding. According to Hatterman et al.'s formulation, the water table will increase if the net surface water fluxes, including precipitation, surface

runoff, and evapotranspiration, exceed the groundwater recharge rate. This formulation does not consider the exchange of surface water between wetland areas and adjacent rivers; wetlands can only release water to rivers through groundwater recharge.

Said et al. [2007] and Zhang et al. [2009] modeled wetlands using the Hydrologic Simulation Program – FORTRAN (HSPF), which has modules for simulating hydrologic fluxes over pervious and impervious lands (PERLND and IMPLND) and the movement of water through stream channels and reservoirs (RCHRES). To more accurately model the storage-attenuation characteristics of wetland areas that have ponded surface water, they modeled wetlands in the RCHRES module as opposed to the standard approach of lumping them into the PERLND module. Wetland volume, depth and discharge were estimated with empirical relationships that determine the amount of water the wetlands release. In both formulations, wetlands can store and release water to rivers, but cannot receive water from rivers.

Finally, Zhang et al. [2016] evaluated the ability of TOPMODEL [*Beven and Kirkby*, 1979] to capture the spatiotemporal dynamics of global wetlands. This flexible modelling framework is relatively simple and assumes that areas with similar topography will have similar hydrologic characteristics. Therefore, the model is sensitive to a topographic index that can be derived from a DEM and indicates how likely pixels within a sub-basin area are to be flooded and contribute to surface run-off. Zhang et al. performed a global hydrologic simulation and used this index along with estimated water table depths to delineate wetland areas. Their model was calibrated using the GIEMS (Global

Inundation Extent from Multi-Satellites) monthly time series maps, consisting of 0.25 degree (28 km) grids [*Prigent et al.*, 2001].

Semi-distributed Hydrologic Models

As discussed in Section 2.3.1, most wetlands have unique features and hydrologic processes. Consequently, to partition a wetland into component parts in a semi-distributed model requires a customized design that considers general flow characteristics, river connectivity, and the availability of in-situ and satellite data for calibration. There are relatively few semi-distributed wetland models published in the literature. One example was presented in Section 2.1.3, the recent study by Sutcliffe and Brown [*J Sutcliffe and Brown*, 2018] that used historical flow records within the Sudd's interior to apply the existing hydrologic model [*J V Sutcliffe and Parks*, 1999] between transects.

An additional example was published by Dincer et al. [1987] who modeled the Okavango Swamp in Botswana. The swamp and the transects where the area was split into multiple components are shown in Figure 6. Dincer et al. used the following data in their model development and calibration: inflows at the swamp entrance, outflows at two stations near exit points, water level measurements throughout the swamp, precipitation and evaporation estimates from weather stations, and open water extents estimated from satellite imagery on a few dates. They applied a mass-balance equation that accounted for inflows and outflows across each cell and the net precipitation minus evaporation over the wetland area. The proportion of flow going into each finger of the swamp was estimated using relative surface areas. The model was calibrated using the outflow data ($R^2 = 0.84$),

water level measurements (R^2_{avg} = 0.87), and general agreement with the open water area maps.

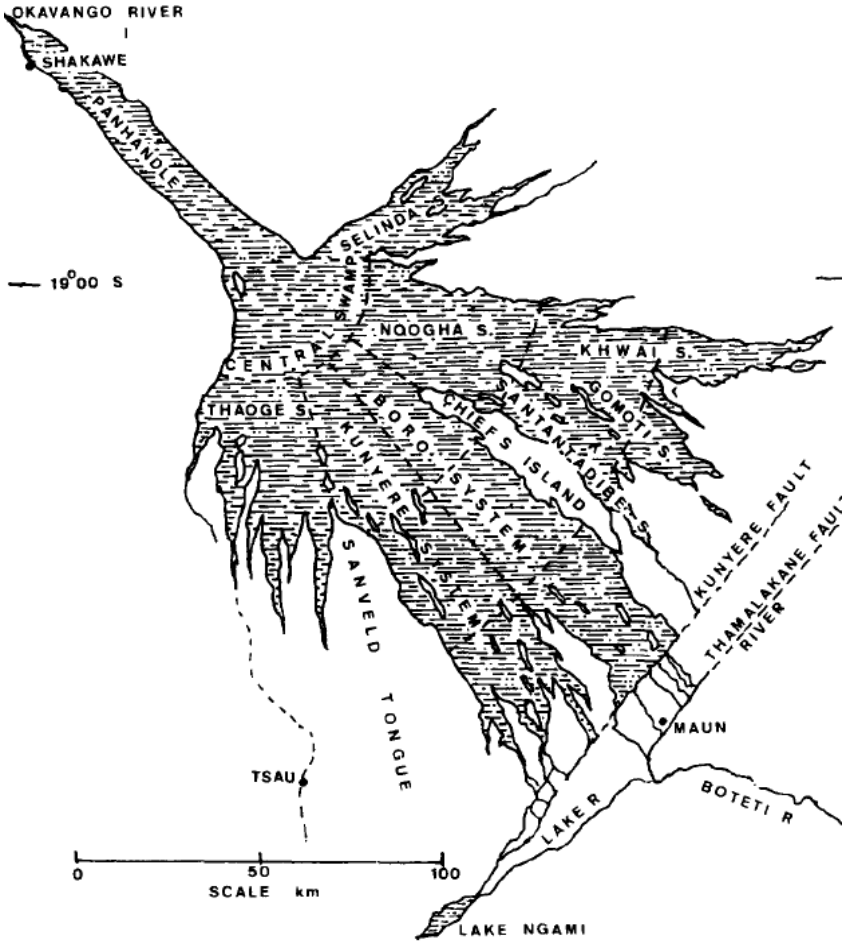

Figure 6: Semi-distributed model of the Okavango Swamp from Dincer et al. [1987].

Spatially-distributed Hydrodynamic Models

The lumped models presented previously capture the volume of water stored within wetlands over time and sometimes track the total wetland area. However, hydrodynamic models might be more appropriate if spatially distributed maps of flooded areas are desired.

Hydrodynamic models are most often applied to assess the extent of flooding along rivers from high flow events to delineate flood-prone areas. These models can also be adapted to riparian wetlands to estimate wetland inundation extents.

A thorough review of hydrodynamic flood inundation models recently presented by Teng et al. [2017] differentiated amongst these models using their dimensionality. 1D models use the simplified one-dimensional shallow water equations to estimate flow and depth for a given cross-section area. Inundation extents can then be extracted from the width of the water surface associated with a flow depth, assuming accurate cross-section geometries are available for many river transects. Currently, the most commonly applied hydrodynamic inundation models are 2D and use the full shallow water equations (derived from the depth-averaged Saint-Venant equations) to model water velocity and depth over a 2D plane. The equations can be discretized using finite element, finite difference, or finite volume methods, and the model domain can be split into regular or irregular grid sizes. Finally, 3D models use the three-dimensional Navier-Stokes equations to capture vertical characteristics of flooding. These models are difficult to calibrate and have high computational costs, making them impractical for many applications.

Section 2.1.3 briefly described the application of a 1D hydrodynamic model to the Sudd Wetland using Mike11 commercial software [*Petersen*, 2005]. However, this study lacked the in-situ data required for rigorous model calibration and validation and concluded that the model outputs could only be used qualitatively based on the accuracy of the DEM used in the model. More recently, Neal et al. [2012] demonstrated how the LISFLOOD-FP hydrodynamic model could be used to map inundation extents and water depths of the

Niger Delta over an 8-year period (2002 – 2009). The LISFLOOD-FP model [*Bates and De Roo*, 2000] couples a 1D river routing model with a 2D floodplain model and was designed to minimize computational costs and run seamlessly with raster data commonly acquired from remote sensing sources. The 2D formulation neglects advection to reduce computational costs and uses a flow limiter and adaptive time steps to minimize numeric instabilities. To enable more realistic simulations for coarse spatial scales, a sub-grid option allows for the representation of both narrow channels and floodplains within a single grid. The channel routing portion of the model requires bed elevations; however, hydraulic geometry relationships were utilized for the Niger Delta, where this information is not available. Inflows to the Niger were downloaded from the Global Runoff Data Center (GRDC), and pan evaporation measurements were obtained from a local station. Precipitation and infiltration were neglected but could have been incorporated into the model. For calibration and validation, model outputs were compared with in-situ discharge records (from the GRDC), water surface elevations from satellite altimetry, and inundation extents derived from 24 Landsat images. Neal et al. found discrepancies between the satellite derived and modeled inundation extents and had difficulty dealing with errors in the DEM, forcing them to manually correct the river network to ensure connectivity across the delta.

The hydrodynamic models discussed thus far focus on surface water dynamics and sometimes account for infiltration rates; however, the hydrodynamics or many wetlands are dominated by groundwater processes. A variety of coupled surface-water and groundwater models have been applied to wetlands [*Amado et al.*, 2016; *Frei et al.*, 2010;

House et al., 2016; *Min et al.*, 2010] where groundwater variables are modeled in detail and included in model calibration and validation. These models required a significant amount of in-situ data, including channel stages, wetland water levels and velocities, and groundwater head levels and would be difficult to apply in large, data scarce areas.

2.3.4 Use of Remote Sensing Data in Wetland Models

A review by Xu et al. [2014] summarized three primary applications of remote sensing data for improved hydrologic modelling. The first is using remote sensing data directly for model inputs (such as precipitation) and for extracting basin information (such as land cover). The second application is calibrating hydrologic model parameters using remote sensing information. For example, soil moisture data products have been used to calibrate soil hydraulic parameters [*Salvucci and Entekhabi*, 2011], and the difference between modeled and satellite-observed ET have been minimized by adjusting parameters in the SWAT model [*Y Zhang et al.*, 2009]. Third, remote sensing data can improve the estimation of state variables in hydrologic models, a technique commonly referred to in the literature as data assimilation. Many studies have assimilated soil moisture into land surface models using variations of Kalman filter techniques which consider both model and observation errors [*W Crow and Ryu*, 2009; *W T Crow et al.*, 2017; *Draper et al.*, 2012; *Reichle et al.*, 2002; *Y Zhang et al.*, 2009]. Estimates of groundwater and surface water storage have also been improved by assimilating data from GRACE (Gravity Recovery and Climate Experiment) into hydrologic models [*Getirana et al.*, 2019; *Kumar et al.*, 2016; *Li et al.*, 2019; *Nie et al.*, 2019]. Despite advances in data assimilation, there is no agreed-upon, systematic approach to understanding, quantifying, and reducing the

uncertainty of hydrologic models that are informed by remotely sensed data [*Yuqiong Liu and Gupta*, 2007]. As more uncertain satellite observations are introduced, estimating and propagating this uncertainty through a hydrologic model becomes more complex and attributing errors amongst data sources and models is challenging.

Research on assimilating remote sensing data in hydrology is generally focused on meeting the objectives of catchment scale hydrologic models as opposed to wetland hydrologic models. Consequently, much of the abovementioned research has not been applied to wetland modeling. The wetland hydrologic models discussed in Section 2.3.3 most often used remote sensing data to delineate and characterize sub-basins and to estimate precipitation and evapotranspiration when in-situ data was not available. As discussed in Section 2.2, much work has been done to derived wetland inundation extents from satellite data; however, the results are rarely used to develop improved wetland hydrologic models. A few studies have used a limited number flooded area estimates in model evaluation [*Dincer et al.*, 1987; *J V Sutcliffe and Parks*, 1999; *Z Zhang et al.*, 2016], but the data was not integrated into the model development process and did not significantly impact model selection.

The application of remote sensing data in developing hydraulic inundation models differs substantially from that of hydrologic models. Inundation models can produce distributed maps of flood extents, water levels and velocities that are sometimes used operationally to evaluate flood risks. Therefore, the ability to validate these models with accurate remotely sensed data is critical in areas where in-situ measurements are not available. Hydraulic models rely on differences in elevation to characterize flow; therefore,

improving the quality of terrain data and the DEM can be more important than improving a model's physical process representations [*Bates,* 2012; *Fernández et al.* 2016]. DEM errors can be reduced through spatial averaging, but the resulting modeled flood patterns may no longer represent the true wetland hydrodynamics [*Jung and Jasinski,* 2015].

Modeled flood extents are often validated using satellite-derived flood maps, reviewed in Section 2.3.3. These flood maps can be combined with DEM's to derive water elevations along shorelines that can be compared with modeled water elevations [*Mason et al.,* 2009]. Water elevations can also be evaluated against variations in water height estimated from satellite altimetry [*Alsdorf et al.*, 2007]. Alternatively, altimetry-based water level elevations can be applied to 2D hydrodynamic floodplain models to calibrate model parameters, such as Manning's n [*Jung et al.*, 2012]. In larger scale studies, the total change in water stored in a wetland or floodplain can be compared with that estimated from GRACE [*Alsdorf et al.*, 2010]. The upcoming SWOT (Surface Water Ocean Topography) mission should provide more frequent and accurate measurements of water elevations, changes in surface water height, and will produce estimates of river flow, enabling the advancement of inundation modeling in data scarce areas.

2.3.5 Research Opportunities

A modelling approach for the Sudd should consider its unique hydrologic characteristics and the intended model application. From literature on the Sudd (Section 2.1), we know that the wetland experiences drastic seasonal and interannual changes, is strongly influenced by river flow, is less dependent on groundwater flows, and has a flat

topography that causes flooding and drying to occur over relatively long time scales. Therefore, the wetland model should allow for bi-directional water fluxes, be dominated by surface water processes, and be evaluated on its ability to capture overall flooding behavior as opposed to small-scale physical processes that are not representative on more aggregated scales. The final model will be used to evaluate long-term water management strategies and potential future scenarios, so a process-based model is preferred to a statistical model.

The lumped hydrologic models that are integrated into catchment-scale models did not emphasize wetlands processes and focused more on quantifying the amount of water that is exchanged between the river and wetland area. There is no need to separate water fluxes amongst the river and wetland within the Sudd; however, the catchment-scale models included fluxes from upland areas that may be important. A drawback of the lumped models is their inability to capture the spatial heterogeneity of hydrologic processes, limiting their ability to represent multiple time scales of flooding and the attenuation of river flows. The semi-distributed modeling approach could offer value in this regard, assuming the individual modeling components can be calibrated and validated.

From the distributed hydrodynamic model class, LISFLOOD-FP would be the most appropriate model for the Sudd considering remote sensing data can be easily integrated and simulations can be run efficiently at relatively coarse spatial and temporal scales. However, the performance of hydrodynamic inundation models is dependent on accurate DEM's. Considering the mild river slopes in the Sudd of approximately 10 cm/km [*Jonglei Investigation Team*, 1954] and the vertical accuracy of global DEM's, about +/-2 m for the

MERIT (Multi-Error-Removed Improved-Terrain) DEM [*Yamazaki et al.*, 2017], a hydrodynamic model of the Sudd will likely be unable to reproduce true flooding patterns.

The lumped and semi-distributed wetland models reviewed here have not fully exploited the potential for integration of satellite information. In contrast, hydrodynamic models can be overly dependent on satellite-derived flood extents, water elevations, and flows, leading to overfitting and misrepresentation of a model's predictive ability. This research will explore how both satellite and in-situ data can be used to calibrate, validate, and inform the structure of wetland models, starting with a simple model and incrementally increasing its complexity. As each alternative model representation is introduced, the model performance will be evaluated to determine whether the proposed alteration adds value to the model predictive ability.

CHAPTER 3: WETLAND LAND COVER CLASSIFICAITON AND INUNDAITON MAPPING USING MODIS

3.1 Overview

The literature review in Chapter 2 summarized research efforts toward improved wetland classification and inundation mapping. The primary goal of many of these studies was to derive the actual wetland land cover and inundation maps, and relatively little research has focused on ensuring that these inundation maps are useful for wetland hydrologic studies. Additionally, past studies have often condensed large data sets and have not fully utilized the multi-variate information provided by long-term time series of satellite images. Therefore, this research proposes a novel wetland land cover classification and inundation mapping method that maximizes the information content of satellite imagery and was designed to produce multi-temporal wetland area estimates that are optimized for applications in hydrologic model development and calibration. While this method is applied to the Sudd Wetland in this research, it could be applied to wetlands worldwide.

This new method consisted of two main components: the classification of wetland land classes, and a month-by-month flooding assessment. Figure 7 illustrates the input and output data and how the two components are connected. As discussed in the literature review, optical remote sensing data is more sensitive to variations in land cover than variations in water content. Therefore, the land cover classification is a necessary first step to achieve more accurate monthly flood maps of wetlands. In addition, the flooding regimes

associated with each land class need to be distinguished in advance of the month-by-month flooding assessment to separate pixels into those that should be assessed for flooding and those that remain dry.

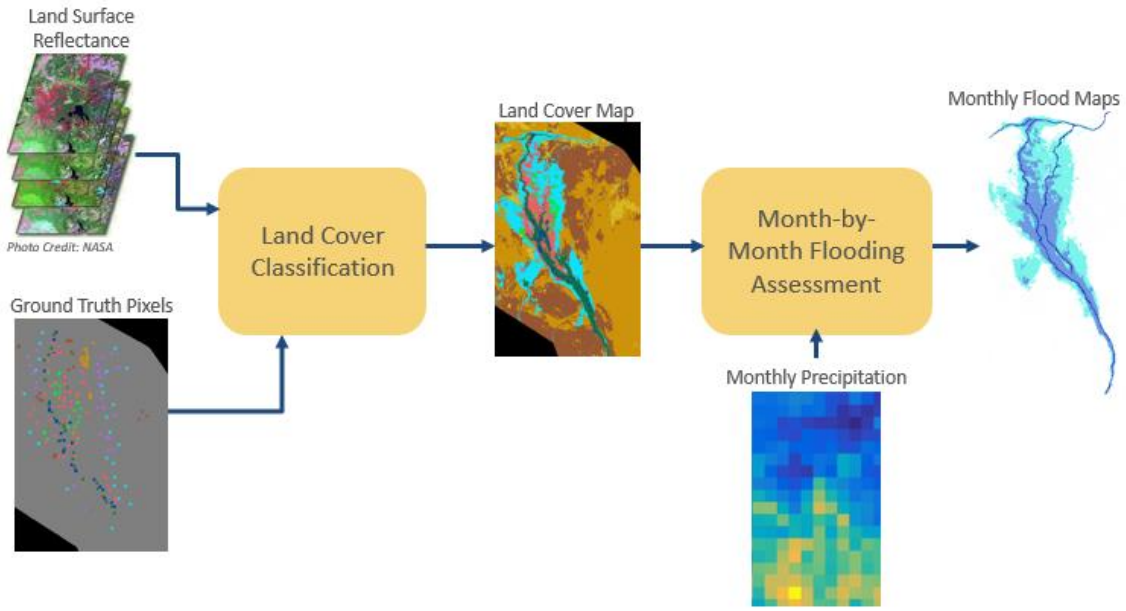

Figure 7: Flow chart describing overall approach to wetland land cover and inundation mapping procedure.

This Chapter is organized as follows: Section 3.2 describes the sources of data used in this study, Section 3.3 describes the multi-temporal land cover classification in detail, Section 3.4 presents the monthly flooding assessment, Section 3.5 explains how the results were validated, and Section 3.6 summarizes the research and key findings, and discusses the strengths and limitations of the new classification methodology.

3.2 Data

3.2.1 Land Surface Reflectance

Various remote sensing sources were evaluated for this study, and the Moderate Resolution Imaging Spectrometer (MODIS) was chosen due to its high temporal resolution and advanced atmospheric correction algorithm [*Vermote and Vermeulen*, 1999]. The MOD09A1 Collection 6, 8-day composite, 500-meter land surface reflectance product [*Vermote*, 2015] was preprocessed in Google Earth Engine (https://earthengine.google.com/) and downloaded for the years 2000-2018 over the Sudd area. This product contains layers for each band as well as a quality assurance (QA) layer that can be used to mask out erroneous pixels. Any pixels flagged for clouds, cloud shadows, cirrus clouds, or high levels of aerosols were set to null values. The images were mosaicked, masked (according the QA criteria) and projected to the geographic coordinate system within Google Earth Engine and subsequently stacked to create a time series of gridded data for each band. Each multi-temporal gridded data set was then ingested into Matlab [*The MathWorks Inc.*, 2016] and monthly mean values (weighted by the day of year each pixel was collected) were calculated and stored in data structures.

3.2.2 Ground Truth Imagery and Observations

The geographic locations of ground truth classes, used to calibrate the classification procedure, were identified using high spatial resolution imagery made freely available through Google Earth Pro. Software. As part of a study conducted on the Southeastern portion of the Sudd, water levels from seasonal floods occurring along a man-made levee

were measured from January to November 2005. This information was generously provided by Dr. Georg Petersen and was used in the validation of the final inundation maps [*Petersen and Fohrer*, 2010]

3.2.3 Precipitation

The Tropical Rainfall Measuring Mission (TRMM) 3B43 product [*Tropical Rainfall Measuring Mission Project (TRMM)*, 2011] was downloaded from GES DISC (https://disc.gsfc.nasa.gov/) for the years 2000 – 2018. This reanalysis product uses gauge data for bias correction and has a monthly temporal resolution and a 0.25 x 0.25-degree spatial resolution. However, gauge data is very limited in the Sudd region, so the uncertainty of the precipitation values is significant. In 2015, the TRMM satellite was replaced by the Global Precipitation Measurement (GMP) satellite system (https://www.nasa.gov/mission_pages/GPM/main/index.html); however, TRMM data is available through early 2018.

3.3 Land Cover Classification Methods and Results

3.3.1 Overview

The land cover classification algorithm has two data inputs: land surface reflectance data and ground truth pixels. The ground truth pixels are sets of pixels manually identified to represent each existing land class. Using the land surface reflectance data, the spectral signatures of these pixels are evaluated and statistics that maximize the separation between land classes are derived. The optimal statistics are then used to classify all pixels within the area of interest using an automated algorithm. The detailed procedure for the land cover classification is summarized in Figure 8 and is described in the following sections.

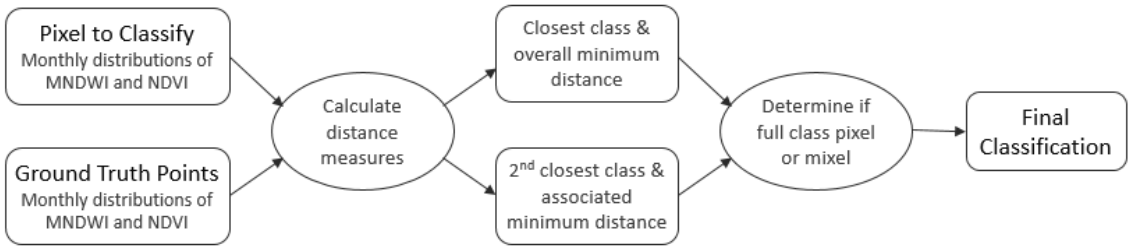

Figure 8: Flow chart describing the land cover classification procedure.

3.3.2 Ground Truth Pixels

During the Range Ecology Survey from 1979-1981, field campaigns were performed to collect data in the Sudd. The predominant vegetation types and their flooding regimes are described in *The Jonglei Canal* and summarized in Table 1 [*Howell et al.*, 1988]. It is reasonable to assume that the major land cover classes identified then are also representative of current conditions. The RES also describes the general locations of each of the land classes within the entire Sudd area. This qualitative information was used to

outline the areas of each class as viewed within Google Earth Pro, which contains high spatial resolution imagery of the Sudd during the study period. From this imagery, the exact geographic coordinates of ground truth pixels could be identified. In this classification, a seasonally flooded pixel does not necessarily flood every year, but it floods at some point over the 16-year period. Therefore, the seasonally flooded pixels represent the maximum extent of seasonal flooding. These pixels are evaluated further in the month-by-month flooding assessment.

Twenty-five pixels for each of the nine land classes were selected for a training set, and the process was repeated for a validation set of equal size. The pixels identified are shown in Figure 9 and span the full wetland area to ensure that they capture the geographic variability of each class. Separate classes for outlier pixels (from fires, human settlements, etc.) were not established because the objective was to identify pixel sets that represent a single class and its internal temporal variation.

Table 1*:* Predominant land classes within the Sudd, their flooding regime, and their abbreviations used in this document.

Flooding Regime	Land Class	Abbreviation
Permanently Flooded	Open Water	OW
	Grassland	PFG
	Papyrus	PAP
	Typha	TYP
Seasonally Flooded	Grassland	SFG
	Woodland	SFW
Non-Flooded	Grassland	NFG
	Woodland	NFW
	Sandy Soil	SS

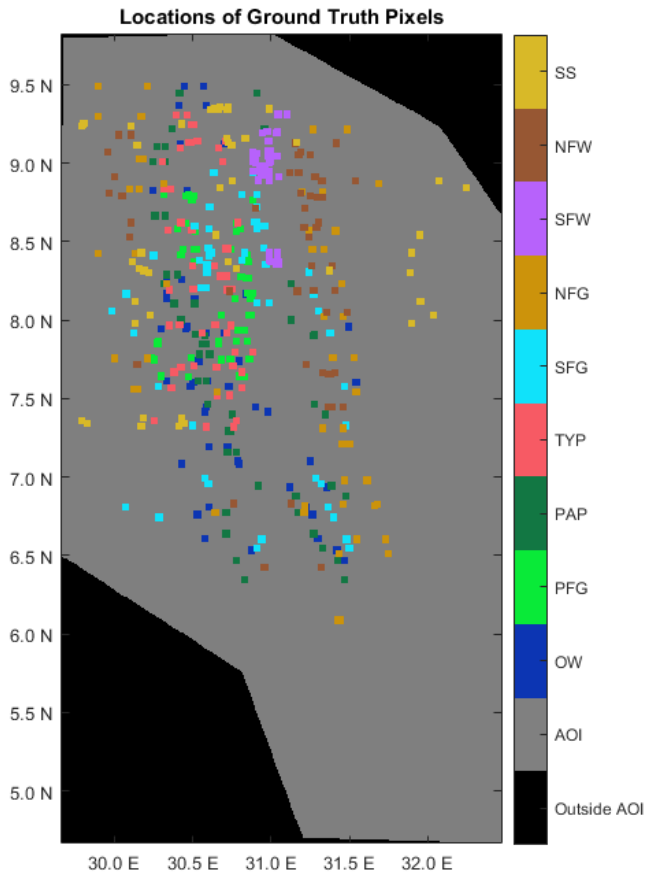

Figure 9: Locations of ground truth pixels selected for each class within the Sudd area of interest (AOI). Some of these classes, e.g., the SFW class, are naturally confined to a small portion of the full area. The wetland classes are located downstream of where the river begins to overflow into the surrounding floodplains, around 6o N; however, the upstream area (below 6o N) was maintained in the AOI to ensure that the final classified image delineated the main channel. In some areas of the Sudd, such as 7 º – 8º N and 31 º -31.5 º E, insufficient Google Earth imagery was available to identify ground truth classes.

To ensure that all ground truth pixels within each set represent a single class, and to mitigate the human error involved in this process, the land surface reflectance data associated with each pixel within a class were plotted for the full period of interest. If the behavior of a pixel exhibited an abrupt change, this indicated that the pixel might have undergone a change in land cover during the 2000-2015 period of this study. Additionally, a few pixels had a MODIS data sequence that varied significantly when compared to those of other pixels within the same class. In these cases, it was concluded that the pixel might have been improperly identified from the Google Earth imagery, or the MODIS pixel that corresponded with the selected geographic coordinates contained information from more than one class. Since the goal of this exercise was to establish ground truth information that represents a single class and its internal temporal variation, these problematic pixels were excluded, and new ground truth pixels were selected at nearby locations. To ensure that the uncertainty of the land surface reflectance data ingrained in each class was not diminished, only pixels that showed extreme variations were excluded, and those with moderate variations were maintained. Statistically, a pixel was considered an outlier and excluded if its MODIS data value was higher than the 75^{th} percentile or lower than the 25^{th} percentile of the ground truth pixel values by more than twice the interquartile range.

3.3.3 Remote Sensing Indices

As the goal of the land cover classification is to distinguish vegetation types and flooding regimes, the indices used for classification should be sensitive to moisture and vegetation and able to capture the physical relationship between land classes and their reflectance. The indices considered and their equations are shown in Table 2. Normalized

indices are commonly used in remote sensing because they result in values between -1 and 1, which are easily interpretable and compared and cancel out the variation between images from differing atmospheric conditions and satellite instrument orientations [*Jensen*, 2005]. While the Normalized Difference Vegetation Index (NDVI) [*Rouse*, 1974] is generally an agreed-upon index for measuring vegetation density and health, there are multiple interpretations of the Normalized Difference Wetness Index (NDWI). The original NDWI was developed to measure moisture within leaves of vegetation [*Gao*, 1996]. The Modified NDWI (MNDWI) was later developed to sense open water while suppressing background noise from vegetation, soil, and built-up land [*H Xu*, 2006]. Tasseled Cap (TC) indices were originally developed using Landsat data and are linear transformations derived from a principal component analysis of the full spectral signature of a global set of ground truth points [*Kauth*, 1976]. The MODIS TC indices, including the greenness and wetness indices evaluated in this study, were derived later [*Lobser and Cohen*, 2007] and represent the second and third principal components. The monthly values of all indices were calculated from 2000-2018 for each ground truth pixel. The 18 years of data were then used to derive monthly distributions of the indices.

Table 2: Summary of remote sensing indices explored in this study and the equations used to derive them

Type of Index	Name	Equation
Normalized	NDVI	$\frac{\rho_{NIR} - \rho_{RED}}{\rho_{NIR} + \rho_{RED}}$ [8]
	NDWI	$\frac{\rho_{GREEN} - \rho_{NIR}}{\rho_{GREEN} + \rho_{NIR}}$ [9]
	MNDWI	$\frac{\rho_{GREEN} - \rho_{SWIR1}}{\rho_{GREEN} + \rho_{SWIR1}}$ [10]
Tassled Cap	Greenness	$-0.4064\rho_{RED} + 0.5129\rho_{NIR1} - 0.2744\rho_{BLUE} - 0.2893\rho_{GREEN} + 0.4882\rho_{NIR2} - 0.0036\rho_{SWIR1} - 0.4169\rho_{SWIR2}$ [11]
	Wetness	$0.1147\rho_{RED} + 0.2489\rho_{NIR1} + 0.2408\rho_{BLUE} + 0.3132\rho_{GREEN} - 0.3122\rho_{NIR2} - 0.6416\rho_{SWIR1} - 0.5087\rho_{SWIR2}$ [12]

3.3.4 Best Performing Indices

To determine which remote sensing indices should be used in the classification, each index listed in Table 2 was compared using the ground truth pixels. Each pair of land classes was evaluated for the amount of overlap that existed between the monthly distributions of the set of pixels that belonged to each class. The indices that maximized the separation between these distributions were noted. In general, the permanently flooded classes were easy to distinguish, but the seasonally flooded and dry classes had more similarities. Because the rainy season and river flooding coincide, the areas that never flood still become green and wet and can be confused with river flooded pixels. The indices that most consistently separated the land cover classes and identified river flooding were the NDVI and MNDWI.

To generally illustrate how these indices can differentiate between the land classes, Figure 10 shows the monthly mean NDVI, MNDWI, and MNDWI+NDVI values for each of the nine classes averaged over all ground truth pixels. While the NDVI is helpful in distinguishing between the different land classes, the MNDWI appears to capture the occurrence of flooding on a monthly resolution. As expected, the permanently flooded classes are less variable throughout the year. Additionally, the MNDWI values of the papyrus and typha remain relatively low due to the density of the vegetation, while the grasslands can have higher MNDWI values in the wet season as the surface water is visible from above. The MNDWI of the seasonally flooded grasslands diverges from the non-flooded grasslands from July to January, which corresponds to the full flooding season, and the MNDWI of the seasonally flooded woodlands diverges from those of the non-flooded woodlands from October to December, which coincides with the latter half of the flooding season. This observation is logical considering that woodlands are located on the outer extents of the seasonally flooded area and do not flood every year. The MNDWI+NDVI index conveniently ranks the non-flooded classes as the least green and wet during the dry season.

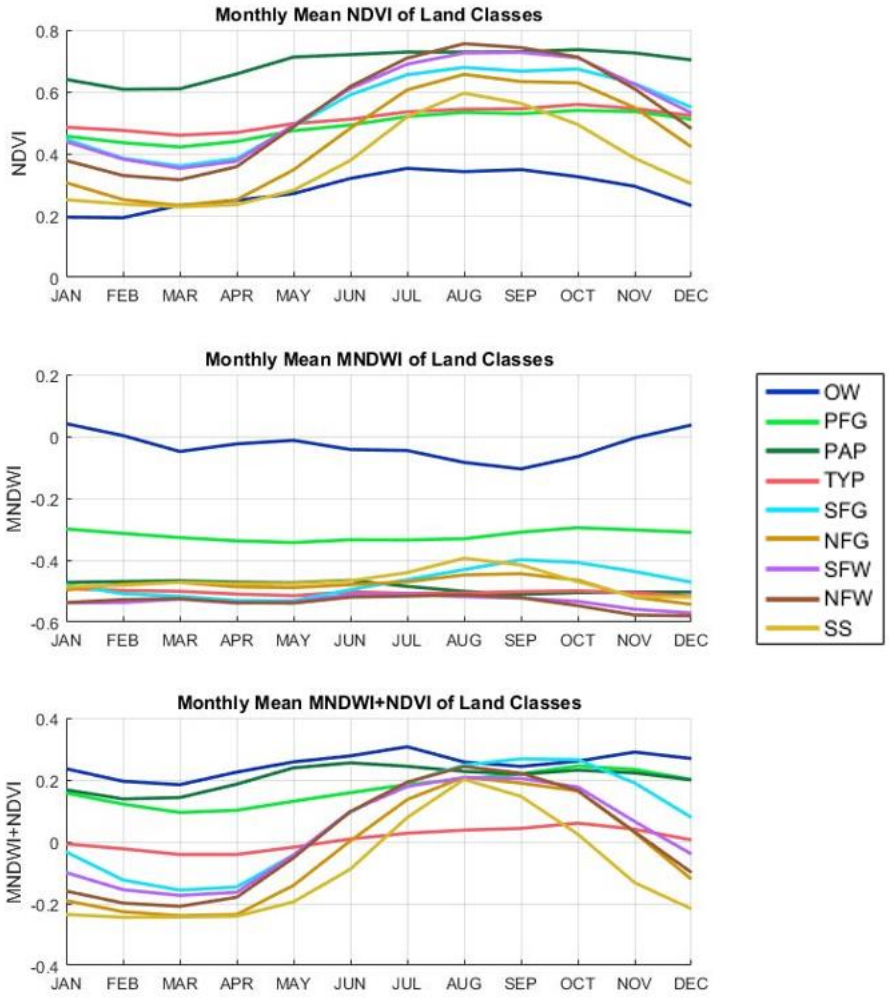

Figure 10: Monthly mean values of NDVI (top), MNDWI (middle), and MNDWI+NDVI (bottom) calculated from the full set of ground truth pixels for each land class over 2000-2018

Many combinations of the NDVI and MNDWI indices, including their orthogonal components and their changes from one month to the next, were calculated and tested in the final land cover classification procedure (which has not yet been described). Based on the accuracies measured using the ground truth pixels, the following indices were selected to be used in the final classification: (i) MNDWI+NDVI, (ii) MNDWI-NDVI, (iii)

Δ(MNDWI+NDVI), and (iv) Δ(MNDWI-NDVI). Indices (iii) and (iv) indicate change of the quantity in parenthesis, Δ( ), computed by subtracting the current month's index value from that of the previous month. The orthogonal components of the indices had an equally high accuracy level but were abandoned due to the added computation needed for their derivation.

3.3.5 Distance Measures

Distance measures quantify the difference between monthly distributions of the remote sensing indices and enable the implementation of an automated classification algorithm. An ideal distance measure would have to be robust across regions without making any assumptions about the underlying monthly distributions. Toward this goal, the following non-parametric distance measures were explored.

Absolute Difference Measures Using Sample Moments

The simplest distance measures evaluated were the absolute differences from the first and second sample moments—mean and standard deviation. The third moment, which represents the skewness of the distribution, was also tested; however, the skewness of the monthly distributions was found to be insignificant compared to the first two moments. These measures are defined as follows:

$$1^{\text{st}} \text{ Moment:} \qquad \sum_{j=1}^{K}\left(\sum_{m=1}^{12}\left|\hat{\mu}_{p,m,j} - \hat{\mu}_{q,m,j}\right|\right) \qquad [13]$$

$$1^{\text{st}} \text{ and } 2^{\text{nd}} \text{ Moment:} \qquad \sum_{j=1}^{K}\left(\sum_{m=1}^{12}\left(\left|\hat{\mu}_{p,m,j} - \hat{\mu}_{q,m,j}\right| + \left|\hat{\sigma}_{p,m,j} - \hat{\sigma}_{q,m,j}\right|\right)\right) \qquad [14]$$

where

μ = sample mean; σ = sample standard deviation;
p = distribution 1; q = distribution 2;
m = month; j = index number; K = number of indices;
"^" denotes sample estimate.

Wilcoxon-Mann-Whitney Test

This measure utilizes the empirical cumulative distribution function of each quantity and tests the hypothesis that they are two statistically different distributions [*Wilks*, 2011]. The probability that this hypothesis is true is calculated as follows:

(i) The two distributions were combined and sorted from smallest to largest, and each value was given a unique rank.

(ii) The pixel ranks were summed for each distribution, and the sums were normalized by the number of values in the distributions.

(iii) Under the null hypothesis, the summed ranks are expected to follow known distributions. The summed ranks were finally tested to determine their consistency relative to these distributions.

Kullback-Leibler Divergence

This measure utilizes the full empirical probability density function of each monthly distribution and is related to the Fisher information matrix, which quantifies the amount of information gained from an observation [*S. Kullback and Leibler*, 1951]. The symmetric form was originally introduced by Jeffreys [1946], and was popularized by Kullback

[1959]. In this application, a discretized form of the symmetric measure was used and calculated as follows:

$$D(P||Q) = \sum_{j=1}^{K}\left(\sum_{m=1}^{12}\left(\frac{1}{2}\sum_{i=1}^{N} p_{j,m,i}\ln\left(\frac{p_{j,m,i}}{q_{j,m,i}}\right) + \frac{1}{2}\sum_{i=1}^{n} q_{j,m,i}\ln\left(\frac{q_{j,m,i}}{p_{j,m,i}}\right)\right)\right) \quad [15]$$

where:

p = frequency of distribution 1;
q = frequency of distribution 2;
m = month;
i = bin number; N = number of bins;
j = index number; K = number of indices.

If the divergence value is zero, the two distributions are identical; higher values indicate more separation between the distributions. The following procedure was used to implement this calculation:

(i) The maximum and minimum values of the combined distributions were taken as the bounds for the computation.

(ii) Normalized histograms for each distribution were extracted using a bin size that resulted in the optimal classification accuracy.

(iii) The divergence from each bin was computed and summed for all bins for which the logarithm term was numerically finite.

3.3.6 Classification Methods

Using the distance measures, a decision can be made on which class a pixel most likely belongs to. There are multiple ways to approach this final step and two were evaluated here. In the first method, called "distance from ensemble member distributions," the distance measure is calculated between the pixel being classified and each individual pixel within each class. Then, the pixel is classified to the class that contains the overall minimum distance measure. For a set of 25 ground truth pixels and 9 classes, a total of 225 distance measures are calculated for each pixel to be classified. In the second method, called "distance from ensemble mean distributions," the individual pixels within each class are first aggregated into a single representative distribution for each class. Then, the distance measure between the individual pixel to be classified and each class ensemble distribution is computed, and the pixel is classified to the class with the minimum distance measure. In this method, only 9 distance measures are calculated for each pixel to be classified. The method that combines the absolute difference from the 1st moment and the distance from ensemble mean distributions is essentially the same as the "minimum distance to means" classification method that is commonly used in remote sensing classification [*Jensen*, 2005]. In most classification procedures, training pixels within a class are aggregated into a single distribution. The distance from ensemble member distributions can be used as an alternative method here because the monthly distributions are used instead of singular values.

3.3.7 Best Performing Distance Measure and Classification Method

Finally, the best distance measure and classification procedure was determined using the optimal set of combined indices for the ground truth pixels. Instead of obtaining a single accuracy measure using the validation pixels, the training and validation pixels were combined and then randomly split 25 times and each classification approach was applied. The mean overall accuracy percentages over the 25 iterations is summarized in Table 3. The overall best distance measure was the absolute difference from the 1st and 2nd moment, and the best classification procedure was the distance from ensemble member distributions. The KL divergence also performed well and was more consistent across the two classification procedures. When calculating the empirical pdf of the distributions, a bin number of 5 resulted in the highest accuracy. If more data were available, the optimal number of bins might be increased and a higher accuracy might be obtained. Additionally, the KL divergence may perform better if the monthly distributions are more asymmetric—in this case, the skewness was close to zero for all monthly distributions.

Table 3: Summary of overall accuracy calculated for each distance measure and classification procedure tested.

	Overall Accuracy Percentages	
Distance Measures	Distance from Ensemble Member Distributions	Distance from Ensemble Mean Distributions
Absolute Difference 1st Moment	96.28	92.48
Absolute Difference 1st & 2nd Moment	**98.13**	92.36
WMW Statistic	92.57	82.61
KL Divergence	97.21	94.54

A confusion matrix that represents the average of the 25 iterations of the best performing classification method is shown in Table 4, and the user's and producer's accuracy of each class are summarized in Table 5. The values along the diagonal of this matrix represent the pixels that were correctly classified and portray the overall accuracy. Each row of the matrix represents the commission error of a class and is used to derive the user's accuracy, or the probability that a pixel allocated to a class actually represents that class. Each column represents the omission error of a class and is used to derive the producer's accuracy, or the ratio of pixels correctly allocated to a class over the total number of pixels belonging to that class. The classes that had the highest amounts of misclassified pixels were the non-flooded grasslands, seasonally flooded woodlands, and non-flooded woodlands. The non-flooded grasslands were occasionally mistaken for seasonally flooded grasslands and non-flooded woodlands, and the non-flooded woodlands

were occasionally mistaken for seasonally flooded woodlands. In addition, the shallow open water pixels were sometimes classified as permanently flooded grasslands, which was somewhat expected as these water bodies are frequently covered by floating vegetation. The standard deviations of the confusion matrices from the 25 iterations were also evaluated, and the magnitudes were within 1 pixel.

Table 4: Average confusion matric from 25 iterations of best performing classification method using random combinations of training and validation ground truth pixels

		Actual Class								
		OW	PFG	PAP	TYP	SFG	SFW	NFG	NFW	SS
Predicted Class	OW	24.48	0	0	0	0	0	0	0	0
	PFG	0.52	25	0	0	0	0	0	0	0
	PAP	0	0	25	0	0	0	0	0	0
	TYP	0	0	0	24.96	0.2	0	0	0	0
	SFG	0	0	0	0.04	24.56	0.08	1.2	0	0
	SFW	0	0	0	0	0.16	24.84	0.08	1.16	0
	NFG	0	0	0	0	0.08	0	23.24	0.04	0.08
	NFW	0	0	0	0	0	0.08	0.32	23.8	0
	SS	0	0	0	0	0	0	0.16	0	24.92

Table 5: User's and producer's accuracy for each class, derived from the confusion matrix presented in Table 4.

Class	User's Accuracy	Producer's Accuracy
OW	1.000	0.979
PFG	0.980	1.000
PAP	1.000	1.000
TYP	0.992	0.998
SFG	0.949	0.982
SFW	0.947	0.994
NFG	0.991	0.930
NFW	0.983	0.952
SS	0.994	0.997

An additional analysis was performed to understand the effect that the number of ground truth pixels has on classification accuracy. The training and validation set of ground truth pixels were combined to produce a set of 50 pixels, and then random sampling was again used to create subsets from this combined set. The classification procedure was implemented on each subset, and the error was recorded. The number of pixels sampled varied from 20 to 50, in increments of 5, and 20 iterations of random sampling were performed for each sample size. The average percent errors are shown in Figure 11. The percent error is approximately 2% for a 25-pixel sample size, 1% for a 35 to 40-pixel sample size, and 0.67% for 50-pixel sample size. These results are very favorable, despite the Sudd geographic extent and land cover classes to be resolved. In general, large

geographic areas with many land cover classes (reflecting large variations of topography, precipitation, soil types, and human interventions) are expected to require more ground truth pixels to achieve a certain percent error. As a general rule, one could gradually increase the number of ground truth pixels until the desired level of accuracy is achieved. Because a lower percent error was achieved for the full combined ground truth and validation set, all 50 pixels were used in the final land cover classification of the entire Sudd area.

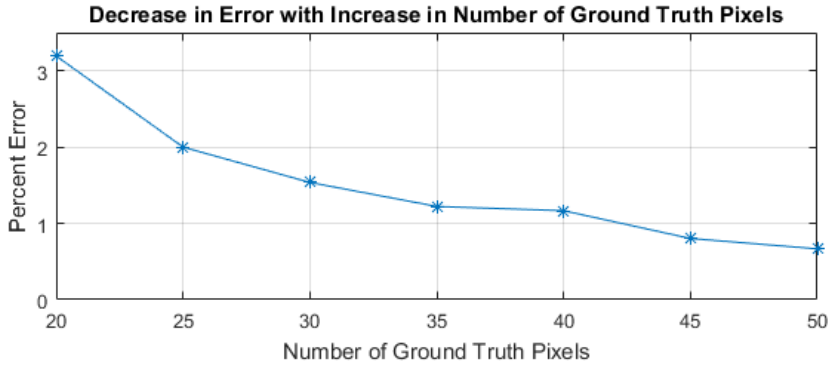

Figure 11: Relationship between number of ground truth pixels and classification error rate.

3.3.8 Uncertainty of Classification Accuracy

Remote sensing classification studies have sources of uncertainty that should be considered alongside quantitative accuracy assessments. One consideration is the geolocation accuracy of the satellite system; if this error is significant then the monthly distributions used in the classification would not consistently represent the same area. However, considering the relatively coarse resolution of MODIS pixels (500 m) compared to the along-track and along-scan errors estimated as 18 m and 4 m, respectively following

the launch of MODIS [*Wolfe et al.*, 2002], geolocation errors are not a cause for great concern. A more significant source of uncertainty relates to the way ground truth points were selected. Due to the lack of available in-situ data, this task had to be performed somewhat subjectively and there may be ground truth pixels within each class that were improperly allocated. Finally, the validation pixels ideally would have been selected using a stratified random sampling technique [*Olofsson et al.*, 2014]. This would have allowed for error bounds on accuracy measures that better represent the full wetland area versus the accuracy of the selected validation set of pixels. Unfortunately, implementing a random sampling procedure was not feasible here since the validation pixels should represent single classes in homogenous areas, and the amount of Google Earth imagery available did not allow for much flexibility in identifying seasonally flooded pixels over the entire wetland area. If more ground data and high-resolution imagery were to become available, these accuracy measures could be improved. However, to ensure that the classification results represent the entire Sudd area (versus only homogenous areas), a procedure was developed to identify pixels that contain more than one land cover class, or mixels.

3.3.9 Classification of Mixels

During the analysis of potential classification methods, the consistency of the classification results when using either the training or the validation set of ground truth pixels was evaluated. When comparing the results, there were certain classes for which a significant number of pixels were classified *differently* in the training and validation stages. For example, Figure 8 highlights the pixels that were classified to both the seasonally flooded grassland and the papyrus classes. If these pixels were simply misclassified, they

would be randomly scattered throughout the area. However, their location pattern is not random. Rather, they are consistently located *between* the two classes to which they are alternatively classified, suggesting that they are "mixels," or mixed pixels containing properties of both classes. This is contrary to common practice [*Congalton et al.*, 2014; *M. A. Friedl et al.*, 2002] which assumes that pixels that are similar to more than one class simply reflect large data uncertainties. Alternatively, these mixels contain valuable information that can be used to improve the overall land classification scheme. In this work, mixel signatures provided the means to identify other mixels within the image, using a ratio of the distance measures between the two closest classes for a given pixel. The addition of this step enabled the derivation of a more informative land cover map and improved the final inundation maps.

The classification procedure developed to identify mixels is illustrated in Figure 12 and is described next:

(i) For each class and each ground truth pixel, calculate the distance measure within its own class, D_i, and the potential mixel classes, D_j.

(ii) Take the ratio of these distance measures, D_i/D_j; a value close to 0 indicates a full class pixel and a value close to 1 indicates a mixel.

(iii) Compute the same ratio for randomly selected mixels between the two classes of interest (identified from the full area analysis) and plot the histograms of the distance ratios of both the mixels and ground truth pixels.

(iv) Identify threshold values that separate the two distributions.

This procedure was incorporated into the full image classification as follows: For each pixel being classified, the ratio between the closest and second closest pixels is calculated and compared to the threshold value that was determined for the two classes. If the ratio is less than the threshold, the corresponding pixel is considered a full class pixel; while if the ratio exceeds the threshold, the pixel is considered to be a mixel between the two closest classes.

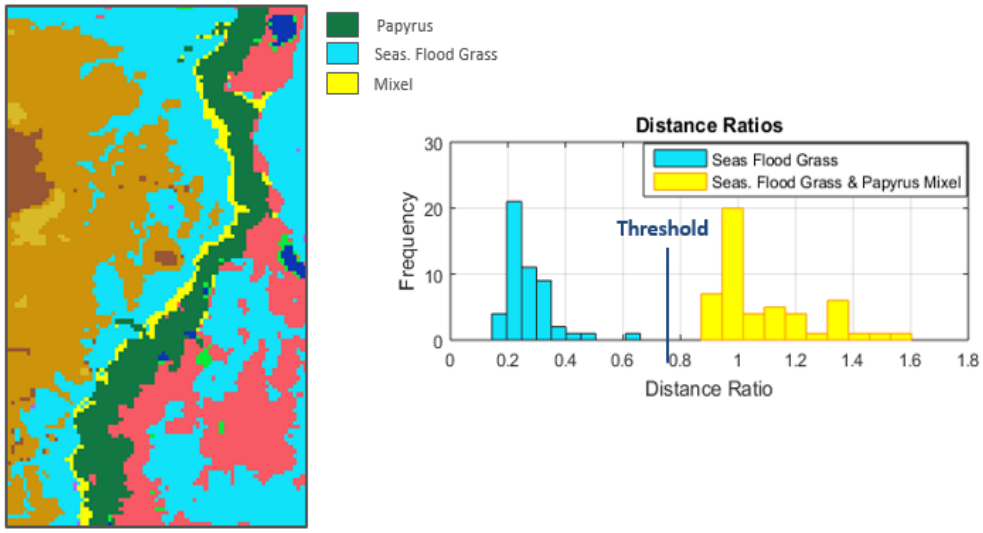

Figure 12: Left: Partial view of Sudd showing pixels that were classified as both papyrus and seasonally flooded grassland using the training and validation set of ground truth pixels. Right: Distributions of distance ratios between the seasonally flooded grassland class and the seasonally flooded grassland/papyrus mixel class.

3.3.10 Uncertainty of Mixel Classification

The mixel classification thresholds were estimated such that the type I error probability (false class assignment given the null hypothesis that the pixel belongs to a certain class) is minimized. Equivalently, the power of the test is maximized. Eighty

percent of these distributions did not overlap, and the test power was very high. The other 20% exhibited a 10% type I error, with the exception of the mixels in the flooded and non-flooded woodland class which exhibited a 20% type I error. Considering that the process of selecting the ground truth pixels is somewhat subjective, it is possible that some ground truth pixels are actually mixels, introducing the above uncertainty. Additionally, a small portion of the pixels identified as mixels may instead be outlier pixels that are affected by anomalous behavior from human activity (e.g., human settlements, fires). Identifying separate classes for these pixels was not an objective of this classification procedure.

3.3.11 Final Land Cover Map

The full area land cover map was produced using all 50 ground truth pixels. The absolute differences between the first and second moment and the distance from ensemble member distributions classification method were applied, and the thresholds on the ratio of the two closest land classes were used to identify mixels. The final land cover map is shown in Figure 13, along with a zoomed-in view in Figure 14. Even though the classification was performed on a pixel-by-pixel basis, the spatial coherency of the final image is rather high.

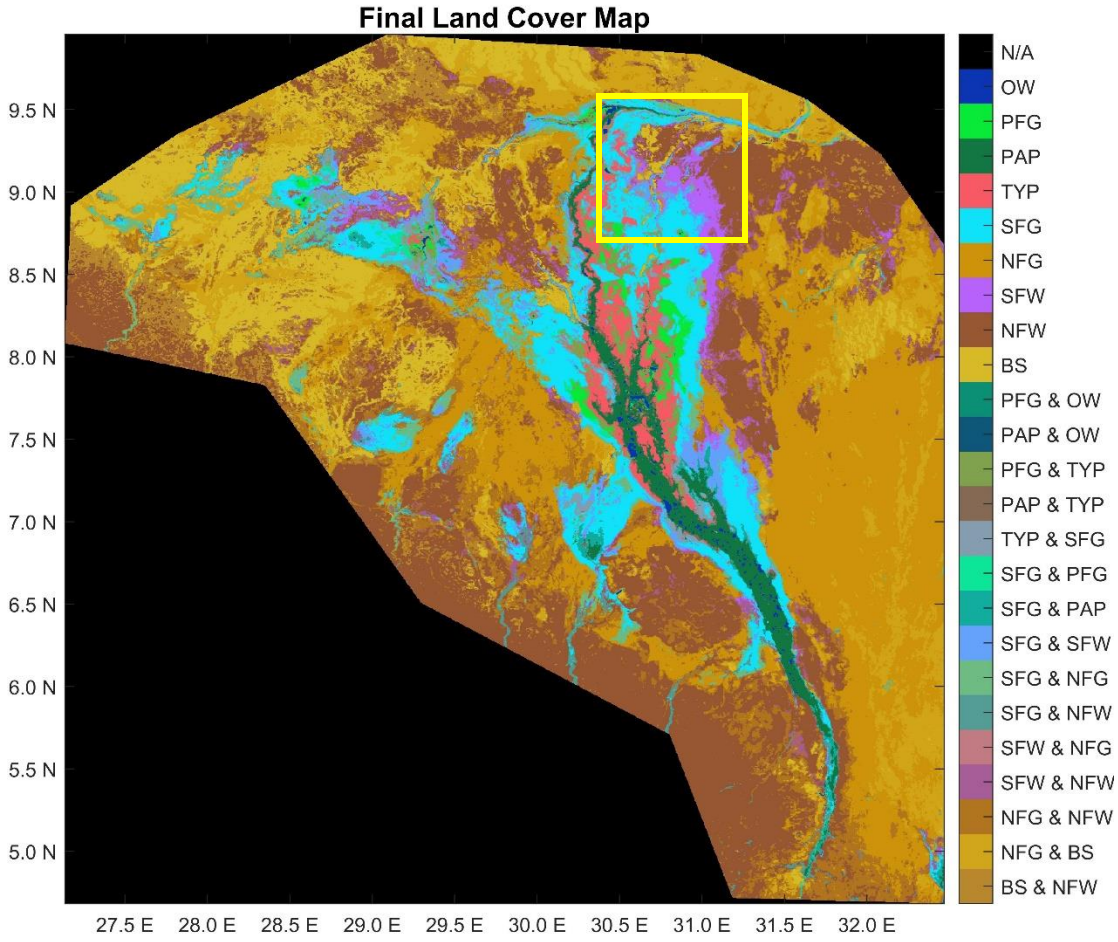

Figure 13: Final land cover map for full Sudd area.

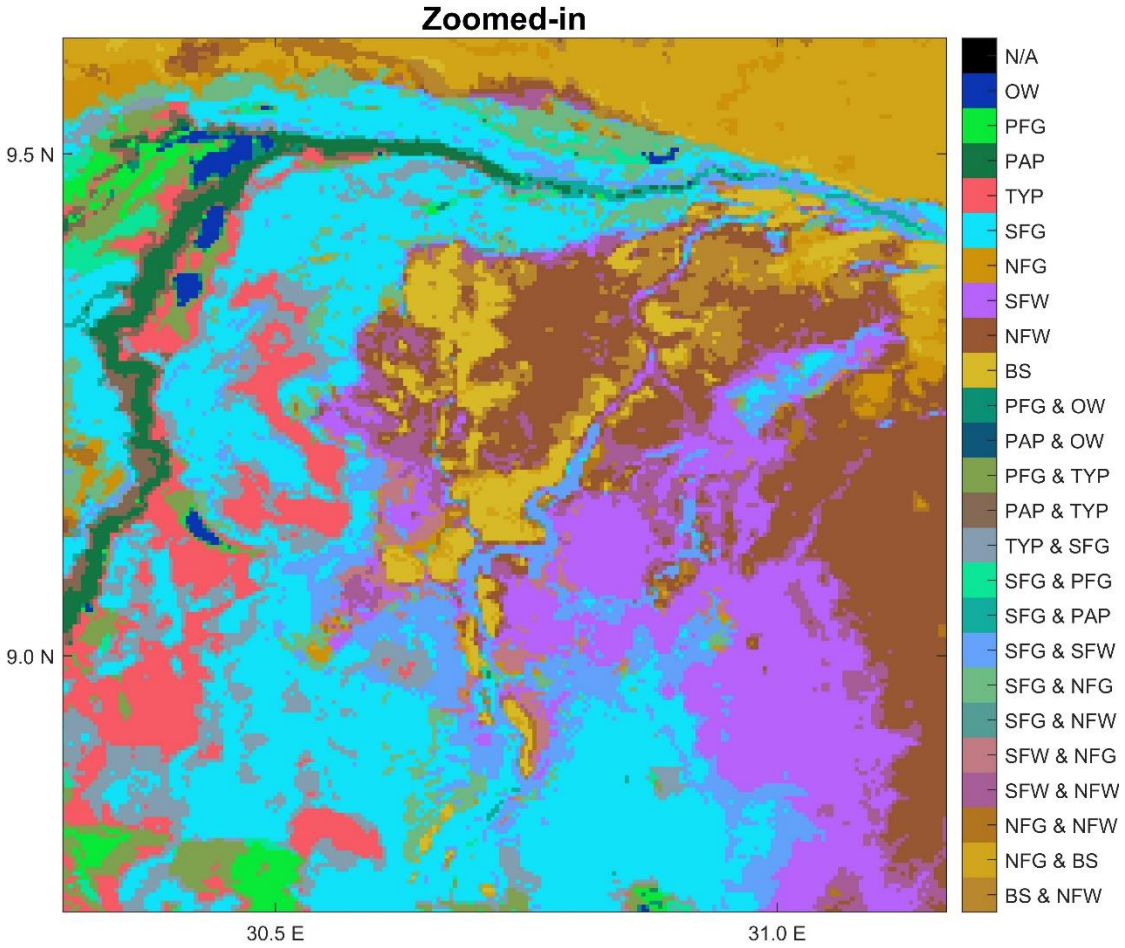

Figure 14: Close-up view of the highlighted area from Figure 10.

The area to the west of the Sudd has traditionally been considered part of the Bahr El Ghazal Basin, and hydrologic models of the Sudd have assumed that the amount of water exchanged between the Sudd and Bahr El Ghazal is negligible [*J V Sutcliffe and Parks*, 1999]. However, this assumption was based on historical flow records at Lake No from the Nile Basin Volumes in the early 1900's, before the expansion of the Sudd following the 1960's. In this study, the Bahr El Ghazal region was mapped to gain insights into the presence and magnitude of flows transferred across the two sub-basins. Based on the land cover map shown in Figure 13, there appears to be a connection during the flooding

period. However, during the dry season, there are areas of permanent swamp in the Bahr El Ghazal that are maintained by the water balance within its basin. Considering one of the objectives of the Sudd Wetland hydrologic model is to model the flooded area extents that results from variations in the Nile flows, the permanently flooded areas within the Bahr El Ghazal should not be confused with the Sudd flooding extents. Therefore, the Bahr El Ghazal region was not included as part of the Sudd flooded area in this study.

The area of each land class within the Sudd is reported in Table 6. Approximately 34% of the pixels were classified as mixels, located between their associated classes. The permanently flooded area is approximately 12,470 km^2 when neglecting the mixels, and 16,370 km^2 when including the permanently/seasonally flooded mixels. The seasonally flooded area (including the permanently/seasonally flooded mixels) is approximately 15,080 km^2, and the potentially seasonally flooded area (including the seasonally flooded and non-flooded mixels) is approximately 31,120 km^2. The locations and quantities of the land classes generally agree with those reported in the literature [*Howell et al.*, 1988]. Additionally, the total permanently and seasonally flooded areas are similar to those reported from the 1979–1980 survey, which were 16,200 km^2 and 13,600 km^2, respectively [*J V Sutcliffe and Parks*, 1999].

Table 6: Summary of land cover classification and total areas belonging to each class.

Area of Land Classes - km²										
		Permanently Flooded				Seasonally Flooded		Non-flooded		
		OW	PFG	PAP	TYP	SFG	SFW	NFG	NFW	SS
Permanently Flooded	OW	432	263	149						
	PFG		1,153		1,225	487				
	PAP			4,457	1,062	1,113				
	TYP				3,730	2,300				
Seasonally Flooded	SFG					10,098	3,170	4,234	1,487	
	SFW						1,813	337	6,077	
Non-flooded	NFG							43,121	13,877	10,452
	NFW								27,529	2,685
	SS									3,230

3.4 Month-by-month flooding assessments methods and results

3.4.1 Seasonally Flooded Pixels

After the final land cover map was obtained, the seasonally flooded grasslands, woodlands, and mixed grasslands/woodlands could be compared to their non-flooded counterparts to determine the timing and duration of flooding of each pixel. This procedure is illustrated in Figure 15. For each pixel evaluated for flooding, the 25 most similar non-flooded pixels are identified based on 3 criteria: (i) they must be of the same land cover type, (ii) they should be close to the pixel being assessed, which is determined using a radial search algorithm, and (iii) they should have a similar monthly precipitation value, which was determined using the TRMM 3B43 product.

Since the TRMM resolution is much coarser than MODIS (about 60 x 60 MODIS pixels to 1 TRMM pixel), the precipitation data was only used if the radial search exceeded 60 pixels without finding 25 non-flooded pixels. In the Sudd region, there is a vertical gradient for the onset of the rainy season and vegetation green-up [*X Zhang et al.*, 2005]. To constrain the TRMM data to an area that is more representative of the seasonality of the pixel being classified, the full TRMM image was subset to 2 rows above and 2 rows below the pixel of interest. Then an algorithm searches for the TRMM pixel with a value close to but not greater than the TRMM pixel overlaying the pixel being classified, and identifies additional non-flooded MODIS pixels. This procedure is repeated until 25 non-flooded MODIS pixels are identified.

Subsequently the MNDWI (wetness index) is plotted for both the flooded pixel and the ensemble non-flooded pixels. The duration of flooding is then determined based on

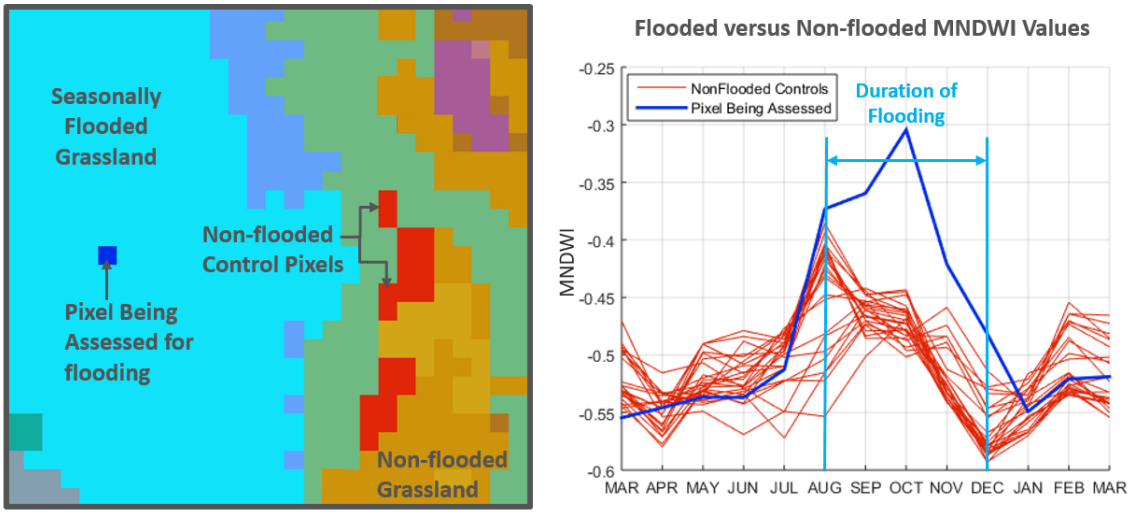

Figure 15: Left: Partial view of the Sudd demonstrating how non-flooded control pixels were selected to determine the timing and duration of flooding for a seasonally flooded pixel. Right: Comparison of MNDWI values for seasonally flooded and non-flooded pixels.

whether the wetness index of the potentially flooded pixel exceeds that of 24 or 25 of the non-flooded pixels. In Figure 9, the flooding duration of the pixel shown is from August to December. This analysis is performed from March to March of the following year, because the driest month is usually March/April which signifies the start and finish of a flooding cycle. This procedure is repeated for each seasonally flooded pixel within the image and each month from March 2000 to March 2018 (18 full flooding/drying cycles).

3.4.2 Seasonally/Permanently Flooded Mixels

Figure 15 illustrates the monthly flooding analysis performed for a seasonally flooded grassland class; however, there are many pixels in the Sudd that were classified as mixels between permanently and seasonally flooded classes. Therefore, these mixels were

first evaluated on an annual basis (from March to March) to determine which years they behave more as a seasonally flooded class and which years they behave more as a permanently flooded class. For each mixel, the 25 closest pixels from each of the potential classes were identified using the same criteria outlined for the monthly flood analysis. The mixel was then classified to the class with the most similar pixel based on the difference between monthly values summed over the year. If the mixel was classified to a seasonally flooded class, it was analyzed for flooding on a monthly basis by comparing it to its non-flooded counterpart using the same procedure as for all seasonally flooded pixels. If the mixel was classified to a permanently flooded class, then it was assessed according to the procedure outlined in Section 3.4.3, described next.

3.4.3 Permanently Flooded Pixels

Finally, the permanently flooded pixels were analyzed to determine whether they dry out at some point over the 18-year period. Because the permanently flooded pixels have dense vegetation canopies and are not expected to become dry very frequently, a set of ground truth pixels cannot be identified from Google Earth imagery. Therefore, a slightly different method was developed that relies on statistically-based threshold values. This procedure is summarized as follows:

(i) For each pixel to be evaluated, identify the 25 most similar pixels based on the same three criteria as the seasonally flooded pixel analysis (pixels must belong to the same class, be located close to the pixel being evaluated, and have similar amounts of precipitation).

(ii) Calculate the monthly median and standard deviation of the NDVI for the group of 25 pixels.

(iii) The pixel being assessed is considered dry for months when its NDVI value falls below the median minus 1.65 standard deviations (lower 5%) during the dry season, and 2.33 standard deviations (lower 1%) during the dry season.

The NDVI was chosen as opposed to the MNDWI or the MNDWI+NDVI because the dense vegetation cover of the permanently flooded classes dominates the remote sensing reflectance. When the permanently flooded vegetation is temporarily non-flooded, the vegetation responds to the lack of water and the NDVI is reduced. By using the standard deviations to identify threshold values, the NDVI is assumed to be normally distributed. The median was chosen as opposed to the mean because it is less sensitive to outlier values that are potentially representative of other permanently flooded pixels that become dry. A stricter threshold (2.33 standard deviations) was used for the wet season to eliminate commission errors; during very wet years, the water level in permanently flooded areas can increase and reduce the NDVI value. The threshold values were chosen by plotting the time series of NDVI values for sample pixels and comparing them with potential threshold values, and by evaluating images that highlighted the locations of pixels that became dry. The optimal threshold values resulted in dry pixels along the perimeter of the wetland extents while minimizing the number of dry pixels located close to the interior portion of the wetland. A comparison of the Sudd flooded areas calculated before and after the

permanently flooded pixel analysis is shown in Figure 16. The total flooded area is mostly reduced in the dry season during very dry years, such as 2010.

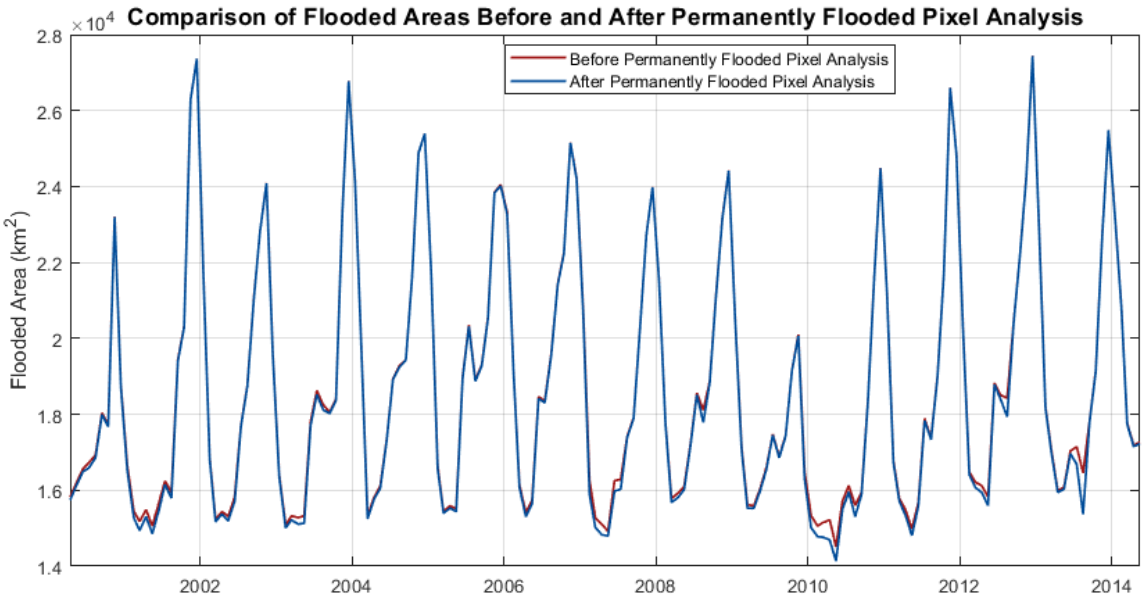

Figure 16: Comparison of the total flooded area of the Sudd calculated before and after the permanently flooded pixels were assessed for drying out.

3.4.4 Summary and Results of Monthly Flooding Assessment

Figure 17 provides a visual summary of the detailed procedures followed for the seasonally and permanently flooded monthly flood assessments, and describes how the most appropriate algorithm was selected for the mixel classes.

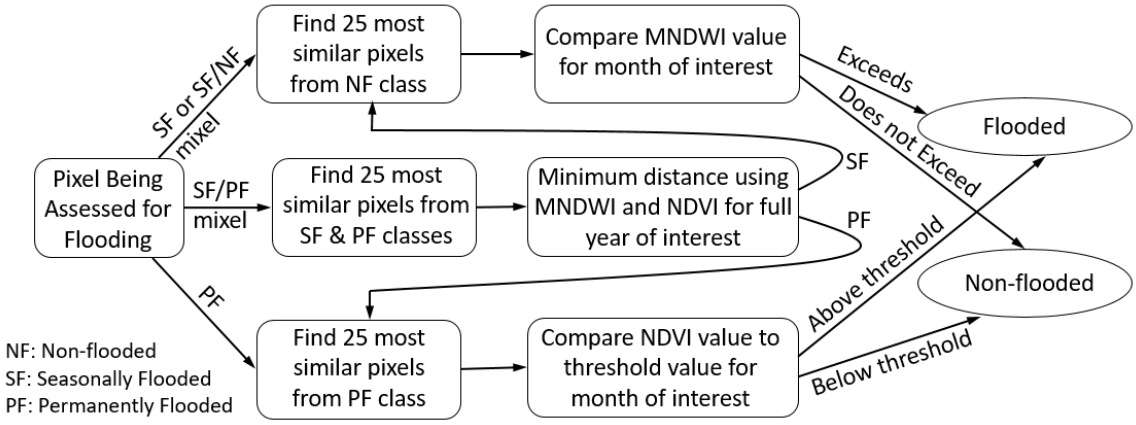

Figure 17: Flow chart describing monthly flood assessment for non-flooded, seasonally flooded, and permanently flooded pixels and mixels.

As a final step in the monthly flood assessment of the entire wetland, all pixels classified as flooded for a given month had to be connected to the main river through neighboring pixels. This was implemented to delineate flooded areas due to river spillage versus temporary and isolated flooded areas due to excessive rainfall. A slight exception was made for pixels that are permanently flooded but are temporarily disconnected from the river due to adjacent seasonally flooded pixels. In this case, the permanently flooded pixels were considered part of the flooded area as long as they were connected to the main river at some point during the same year. The rationale for this exception is that these areas are likely connected to the river through sub-surface flows or streams that are of a smaller resolution than the size of a MODIS pixel.

The results from the month-by-month flood assessment are summarized in Figure 18, which shows the time series of total flooded area along with a visual of the maximum flood extent (permanently and seasonally inundated area) for the driest year, 2009-2010,

and the wettest year, 2001-2002. This time series captures both the seasonal and annual variability of the flooded area. The minimum flooded area over the 15-year period is 13,783 km^2, and the maximum is 24,841 km^2. This result is consistent with literature accounts according to which the wetland can nearly double in size [*Howell et al.*, 1988]. However, according to the aerial survey that mapped the Sudd flooded area from 1979 to 1980, the maximum extent of flooding was estimated as 29,800 km^2 [*J V Sutcliffe and Parks*, 1999], a quantity larger than that observed during the 2000-2015 period. This apparent difference may be caused by a few factors. The historical Sudd survey estimates the maximum flooded area using a similar approach to that of a lake, where every pixel within the outer inundation extent is considered flooded. In reality, there are areas within the interior of the Sudd that remain dry throughout the year [*Howell et al.*, 1988]. Thus, it is possible that the maximum flooded area was somewhat overestimated. At the same time, 1979–1980 was a very wet year in Equatorial Africa as indicated by the significant increase in the level of Lake Victoria [*A. P. Georgakakos and Yao*, 2007]. Higher lake levels imply higher river flow and larger inundation extent. Thus, it is also possible that the higher wetland area estimate of the earlier study is consistent with these results.

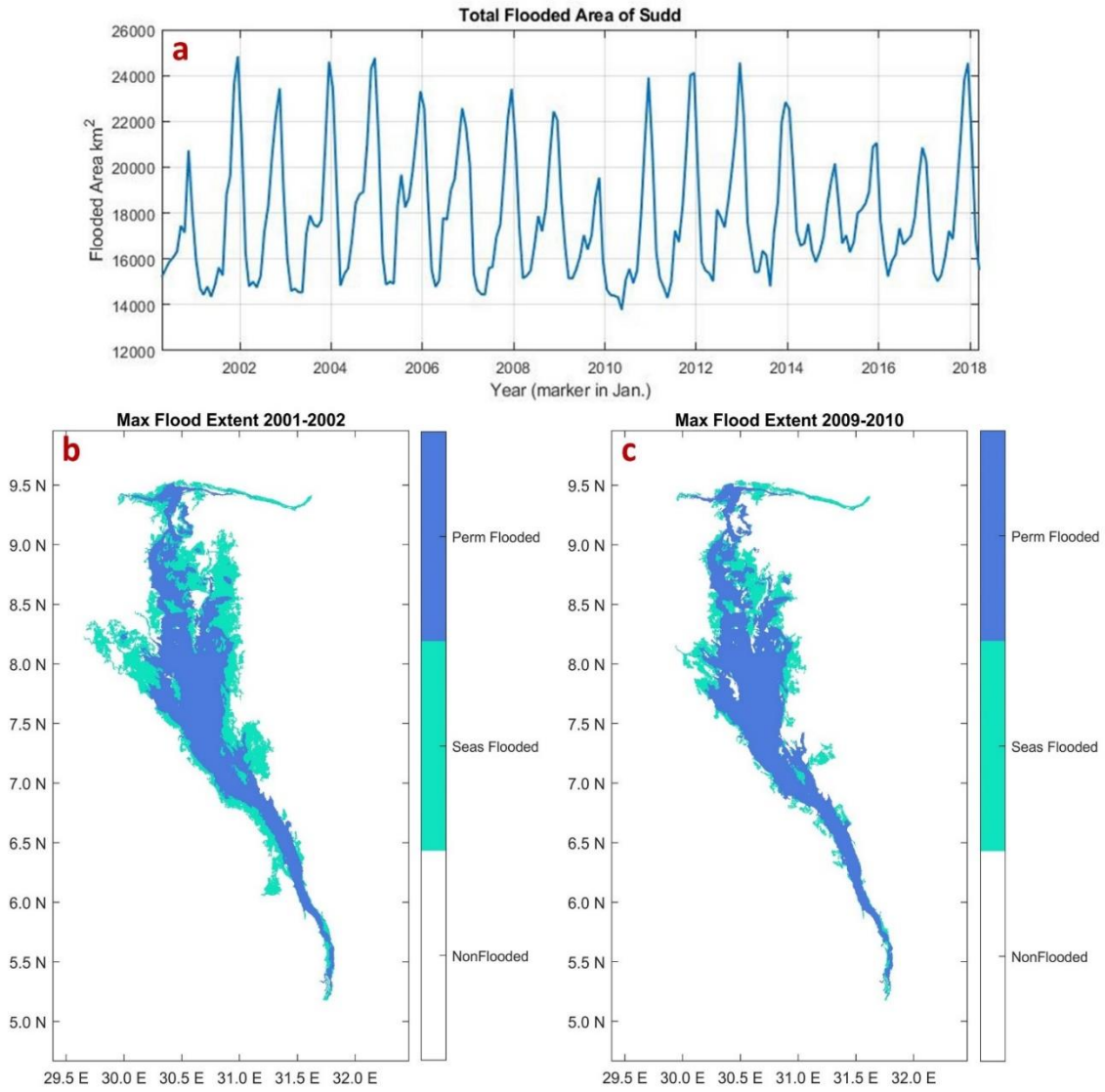

Figure 18: (a) Full time series of total flooded area; (b) maximum flood extent for 2001-2002; (c) maximum flood extent for 2009-2010.

3.5 Validation of Final Inundation Maps

Validation of these results is challenging given the lack of ground observations. However, the monthly flood maps were assessed using the following methods: (i) qualitative comparison with literature, (ii) comparison of the flooding behavior of pixels

near the levee with gauge data provided by Petersen, (iii) correlation with estimated river flow data, and (iv) spatial consistency of inundation pixels.

3.5.1 Validation with Published Literature

The results were assessed qualitatively by studying an animation of the monthly flood maps. As cited in literature, the flooding begins with the start of the rainy season, around May/June, and increases in magnitude as the river flows increase, from October to December [*Howell* 1988; *Sutcliffe and Parks* 1999]. Flooding occurs more heavily towards the southern portion of the Sudd earlier in the year and progresses northward. This observation agrees with the literature that describes the general wetland flood patterns [*Howell* 1988; *Hurst and Phillips* 1932; *Petersen and Fohrer* 2010; *Sutcliffe and Parks* 1987; *Sutcliffe and Brown* 2018] and is logical considering that the river flows from south to north and rainfall typically begins in the southern portion.

3.5.2 Validation with In-situ Observations:

As part of a study conducted on the Southeastern portion of the Sudd [*Petersen and Fohrer*, 2010], water levels from seasonal floods occurring along a man-made levee were measured in 400-meter intervals from January to November 2005. This data was shared personally by Dr. Georg Petersen. The geographic coordinates of the water level measurements could be roughly identified using Google Earth imagery, enabling a comparison of the in-situ flood observations with the MODIS-derived flood maps. Using the locations estimated from Google Earth imagery, a 3x3 pixel grid was indexed from the monthly MODIS flood maps. If more than half of the pixels in this grid were classified as

flooded for a particular month, then the gauge location was considered flooded. The resulting flood periods for each gauge are shown in Table 7 and are compared to the historical records.

All five of the locations were flooded for a continuous period in 2005, and both the satellite maps and the in-situ levels showed that these areas remained flooded in Nov. 2005, when the in-situ measurements were abandoned. However, the monthly flood maps recorded flooding earlier in the year than when water was first recorded on the gauge. This discrepancy may have resulted because the gauges were not able to record flooding below a certain water level, or because the MODIS-derived flood maps might indicate flooding prematurely when the soil is saturated but not quite flooded. This insight will be considered when developing a hydrologic model of the Sudd using the results from this study. However, the agreement shown here is promising and suggests that the MODIS flood maps are capturing in-situ flooding behavior.

Table 7: Comparison of in-situ measurements of Sudd with results from this study.

	Gauge Record	This Study	
Gauge Location	Start of Flood ('05)	Start of Flood ('05)	End of Flood ('06)
1	Jun	Jun	Dec
2	Jul	May	Dec
3	Jul	May	Jan
4	Jul	Apr	Jan
5	Jul	Apr	Jan

Dr. Petersen also provided daily water level measurements of permanently flooded reservoirs near the main channel. The longest continuous data record from these measurements is compared to the MODIS-derived total flooded area of the Sudd in Figure 19. The maximum height of this reservoir occurred in Nov. 2005 and corresponds with the month of maximum flooded area for the same year. This agreement suggests that the MODIS-derived inundation maps accurately capture the timing of the flood peak, an important characteristic for wetland modeling and management applications.

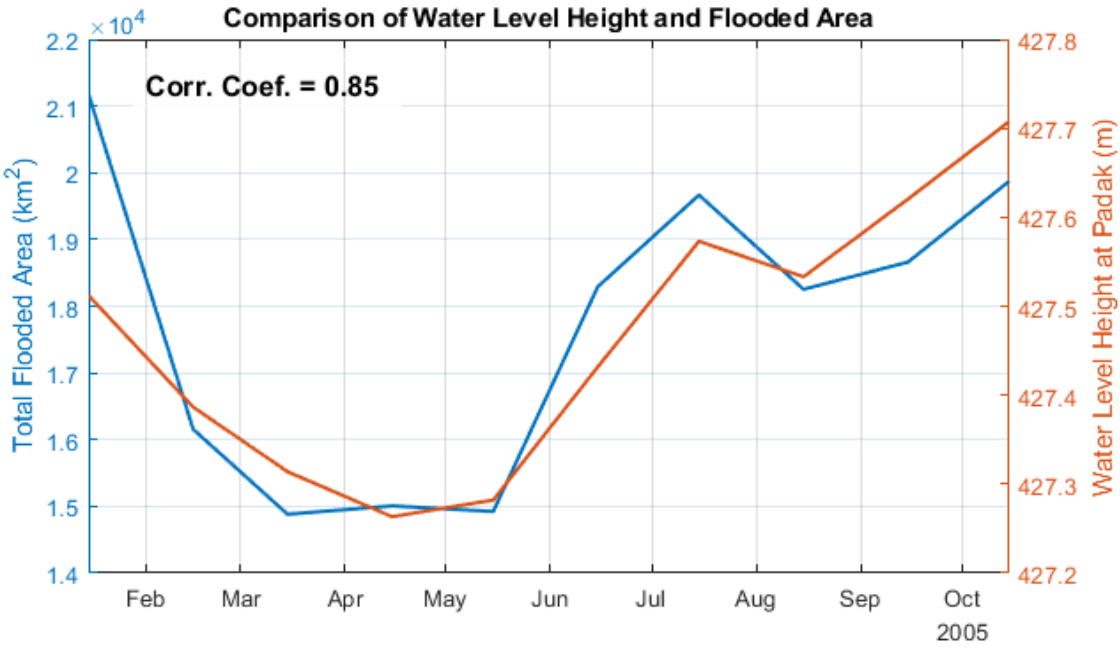

Figure 19: Comparison of water level heights (in orange) recorded at Padak (located in the Southern region of the Sudd) to the MODIS-derived total flooded area of the Sudd (in blue).

3.5.3 Correlation with the River Flow Regime:

According to historic hydrologic studies on the Sudd, much of the flooding is caused by increases in the Nile River flow and seasonal rainfall. Therefore, there should be a relationship between the aerial extent of flooding, the river flow, and net precipitation over the flooded area. To confirm that this relationship exists, the total flooded area of the Sudd was compared with estimated flows plus the net flux (precipitation - evapotranspiration) over the flooded area. The derivation of these estimated flows and water fluxes is described in detail in Chapter 4. Data was available to estimate the Sudd inflows and outflows from 2000 – 2015; therefore, the MODIS-derived flooded area after 2015 could not be used in this comparison. Additionally, the flooded area estimates in 2014 were omitted because extensive flooding to the east of the Sudd was reported that year [*Sudan Tribune*, 2014]. If some of the non-flooded pixels were actually flooded, then the satellite-derived flooded area would be underestimated using the month-by-month flooding assessment procedure that was applied in this study.

The estimated monthly Sudd water flux, defined by Equation 16, is plotted in Figure 20 and compared with the total flooded area lagged backwards by 4 months. The 4-month lag was determined to be the lag which maximized the correlation between the flux and the flooded area. This lag is somewhat consistent with Sutcliffe and Parks' finding that the best statistical relationship between inflows and outflows in the Sudd occurred when the inflows were lagged forward by 3 months [1987]. A high correlation coefficient between the flux and flooded area was observed for a 3-month lag (0.757), and the correlation coefficient was higher when a 4-month lag was applied (0.809). This 4-month lag might reflect the

travel time required for the Sudd fluxes and flows to reach to the outer extents of the wetland.

$$Flux(k) = Q_{IN}(k) - Q_{OUT}(k) + \big(P(k) - ET(k)\big)A(k) \quad [16]$$

where:

Q_{IN} = monthly Sudd inflows (m^3/month)
Q_{OUT} = monthly Sudd outflows (m^3/month)
P = monthly cumulative precipitation (m/month)
ET = monthly evapotranspiration (m/month)
A = monthly mean Sudd flooded area (m^2/month)
k: temporal index

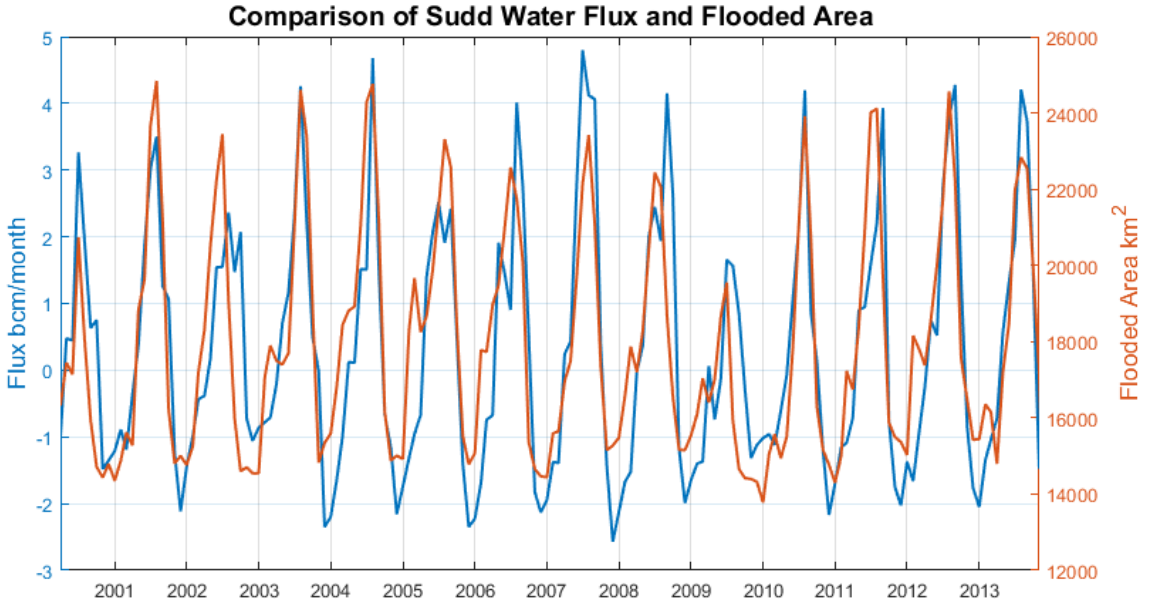

Figure 20: Comparison of time series of monthly sudd water flux and the monthly mean flooded area (estimated from MODIS imagery). The flooded area time series is lagged backwards 4 months to optimize the correlation coefficient between the two time series (0.809).

To test the significance of the correlation coefficient between the flux and flooded area, the following procedure was implemented: (i) The seasonally flooded area time

series, from April 2000 to March 2014, was split by year; (ii) 14 separate years of the flooded area were randomly sampled without replacement and then combined to create a random time series that maintains the seasonal flooding cycle; and (iii) the correlation coefficient between the random time series, lagged backwards 4 months, and the estimated water flux into the Sudd was calculated. This procedure was implemented 100,000 times in Matlab and the histogram of the resulting correlation coefficients is shown in Figure 21. Only 0.8% of the randomly generated time series have a correlation coefficient exceeding that of the true time series. Considering these time series were obtained nearly independently, the significance of the correlation over the 2000 to 2014 period further validates the flooded area derived in this study and suggests that an accurate hydrologic model of the Sudd can be developed using this data.

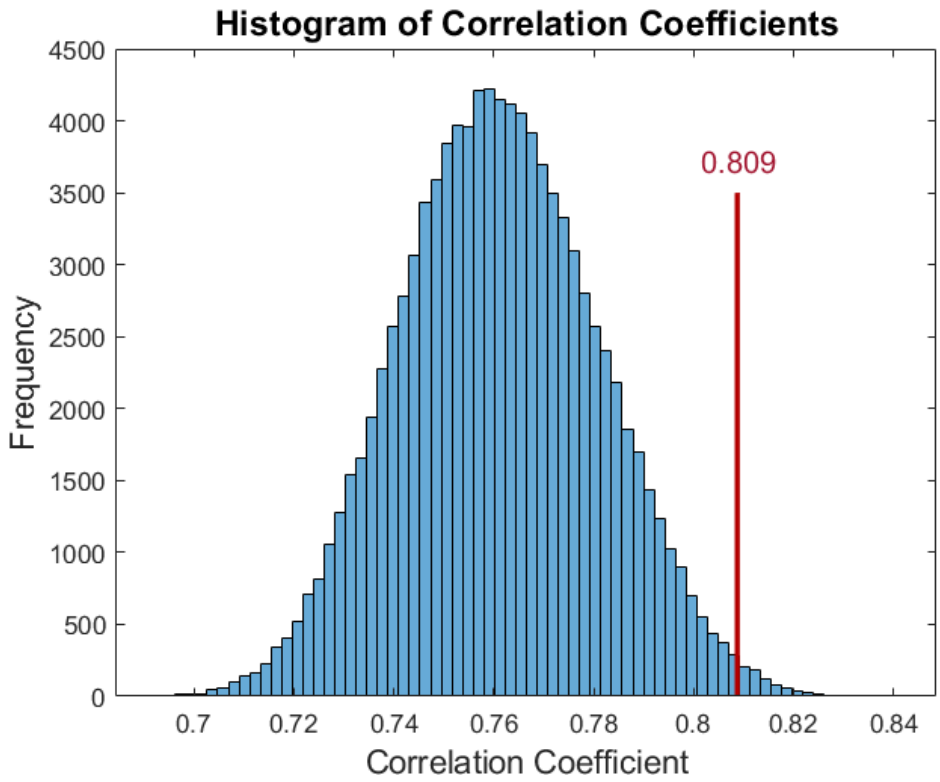

Figure 21: Histogram of correlation coefficients calculated between randomly generated flooded area time series and the Sudd water flux, compared to the correlation coefficient obtained using the true flooded area time series (0.809). 0.8% of the correlation coefficients calculated using the randomly generated time series exceed that of the true.

3.6 Summary and Conclusions

Obtaining a time series of wetland flooded areas can inform the development of reliable wetland models. This section showed that optical remote sensing imagery can be utilized to extract the flooding extent of wetlands at a monthly temporal resolution. The general method was to first derive a single land cover map that identified land classes and their flooding regime, and subsequently analyze potentially seasonally flooded pixels to determine the timing and duration of flooding.

For the land cover classification, a novel method was developed that uses common normalized difference wetness and vegetation indices with non-parametric statistical distance measures to determine the land cover class to which each pixel belongs. By evaluating the ratios of this distance measure, pixels could be further classified as mixels sharing properties of two adjacent classes. The accuracy of the classification is high for the selected ground truth pixels. Thirty-five to forty ground truth pixels yielded a percent misclassification error of about 1%. About one third of the pixels in the land cover map were classified as mixels, located adjacent to the classes they resembled.

The monthly flood maps were obtained by identifying ensembles of non-flooded pixels for each pixel that potentially floods according to the land cover map. The wetness index for each potentially flooded pixel was then compared to those of the ensemble group to identify the timing and duration of flooding. Previous literature, selected water level observations, and estimated flow data agreed well with the resulting monthly flood maps.

The classification procedure presented in this paper has many advantages for applications in data scarce areas. Characteristics of the new approach and how they differ from those commonly found in remote sensing research are summarized in Table 8.

Table 8: Summary table comparing features in existing research to the methods presented in this study.

Trends of methods in existing literature	Methods in this study
Rely on the collection of in-situ data.	Can use, but does not rely on in-situ data.
Use single images, short time periods, or compressed data in classification.	Use all data from multi-year sequences (18 years) in classification.
Make assumptions on statistical distributions.	Use non-parametric statistical measures.
Pixels are forced to fall into a single class. Ignore mixel information.	Pixels may belong to more than one class. Use mixels to delineate/verify class boundaries.
Apply uniform thresholds/decisions over entire area to identify flooded pixels.	Identify flooded pixels using local conditions.
Generate static wetland area products.	Quantify dynamic wetland area changes.

There are also limitations to this methodology and potential for improvement that can be considered for future research. A key limitation inherent to this methodology is the assumption that the land cover map does not undergo significant changes over the period of analysis. This assumption is reasonable for the Sudd Wetland from 2000-2018 but might be inadequate for other wetlands that are subject to rapidly occurring human-induced changes. The land cover map could be derived for shorter time horizons; however, the monthly distributions of the indices and their statistical measures are more stable for longer time spans.

Additionally, this method does not account for potential variations in vegetation phenology within each land cover class during the month-by-month flooding assessment. As previously mentioned, the NDWI is sensitive to moisture in vegetation in addition to the ground surface. Therefore, the monthly flood detection algorithm may be measuring differences in vegetation moisture between pixels as opposed to differences in ground

surface water content between pixels. This misclassification would not occur if all pixels within each land cover class have the same vegetation phenology. However, considering the size of the Sudd and the number of land cover classes for which a set of ground truth points could be derived, there are likely variations in phenology within each class.

The vegetation phenology also impacts the evaluation of the permanently flooded land classes. Recall that permanently flooded land classes were considered temporally non-flooded if their NDVI value dropped significantly. The NDVI was chosen instead of the NDWI because the vegetation in these areas is very dense and dominates the satellite measurements. However, the permanently flooded vegetation in the Sudd may be resilient to short-term drying of the ground surface, and consequently the NDVI cannot detect areas within the "permanently" flooded areas that are temporarily dry. If this hypothesis is correct, then the Sudd flooded areas would be overestimated during the dry season, and the magnitude of the seasonal fluctuations of the flooded areas would be underestimated.

An additional limitation of this methodology specific to the Sudd is that it does not consider the communities' burning practices. After cattle have grazed on the seasonally flooded grasslands, the communities burn the grasslands in hopes of obtaining a second growth cycle [*Howell et al.*, 1988]. These practices could affect the monthly flood assessment, where potentially flooded pixels are compared to nearby non-flooded pixels; the assumption that the non-flooded pixels have the same vegetation cover as the flooded pixels would be violated, resulting in commission errors in terms of the flooded area.

The potential limitations of this flood detection algorithm are difficult to test given the sparsity of data in the Sudd region. This method could be further tested and validated if it were applied to an area where more extensive in-situ data is available, such as the Florida Everglades, a large wetland that is actively monitored by the South Florida Water Management District (SFWMD). The SFWMD continuously records water level heights at many locations within the wetland [*Ordoyne and Friedl*, 2008], and these water level heights and variations could be compared to MODIS-derived flooded area maps. Finally, this method could be further evaluated using SAR data. Section 2.2.2 summarized some potential advantages for detecting flooding beneath vegetation using SAR imagery. However, previous studies that have attempted to map the Sudd flood extents using SAR [*Rebelo et al.*, 2012; *Wilusz et al.*, 2017] have limitations, and based on our own analysis the "double-bounce" affect is not discernable for the Sudd in freely available SAR imagery. However, future satellite missions may offer new opportunities in this area, and/or SAR may be more effective for detecting flooding beneath vegetation in other wetlands, allowing a classification procedure that utilizes both optical and SAR imagery jointly to be developed and validated.

CHAPTER 4: ESTIMATION OF SUDD FLUXES AND FLOWS

4.1 Overview

In Chapter 3, a monthly time series of inundation maps for the Sudd Wetland was derived from MODIS satellite imagery. The significant correlation between the resulting monthly flooded area time series and the monthly Sudd water flux (Section 3.5.3), calculated from the inflows, outflows, and precipitation and evapotranspiration rates, suggests that the Sudd hydrology can be modeled by simulating these basic surface water processes. The simple lumped mass balance model of the Sudd that was originally developed by Sutcliffe and Parks [*J Sutcliffe and Brown*, 2018; *J V Sutcliffe and Parks*, 1987; 1999] was summarized in Section 2.1.3 and relies on these key hydrologic fluxes. Therefore, if estimates of the Sudd inflows, outflows, precipitation, and evapotranspiration (ET) are obtained for the 2000 to 2015 period, the Sutcliffe and Parks model can be re-evaluated using the time series of flooded area maps derived in Chapter 3. Insights from this analysis can subsequently guide the development of a more accurate hydrologic model.

The data and methods applied toward estimating the Sudd fluxes and flows will be described in detail in this chapter. The chapter begins with a description of historical and current data sources for precipitation in Section 4.2. In Section 4.3, historical measurements and estimates of ET within the Sudd are summarized and discussed, and ET estimates for the 2000 to 2015 period are derived and compared. Available in-situ flow records for the 2000 to 2015 period are then presented in Section 4.4, along with historical flow records available since the early 1900's. Considering the significant data gaps in

available in-situ flow data in this region, various methods were developed and applied to obtain continuous time series estimates of the Sudd inflows and outflows. These methods are discussed in Section 4.5 and utilize supplemental satellite-based data sources and physical and statistical models.

4.2 Precipitation

4.2.1 Historical Records

The rainy season in the Sudd generally lasts from April to October and peaks in July/August. The average net annual precipitation over the Sudd from 1941 to 1970 was estimated to be 871 mm [*J V Sutcliffe and Parks*, 1999], calculated from measurements at 9 stations in the Sudd region. The monthly mean precipitation values calculated from these gauge measurements are shown in Table 9. Gauge data remains available at two locations within the Sudd, Juba (just south of Mongalla) and Malakal, through the Global Surface Summary of Day (GSOD) and the Global Precipitation Climatology Center (GPCC) datasets. This gauge data is used to develop and bias correct many gridded precipitation data products; however, there are significant data gaps that increase the uncertainty of gridded estimates in the Sudd area.

Table 9: Monthly mean cumulative precipitation (in mm) measured in the Sudd region from 1941 - 1970.

Jan	Feb	Mar	Apr	May	Jun	Jul	Aug	Sep	Oct	Nov	Dec	Net Annual
2	3	22	59	101	116	159	160	136	93	17	3	871

4.2.2 Estimates Used in This Study:

Four freely available global precipitation data products were evaluated for estimating precipitation in the Sudd over the 2000 to 2016 period:

1) **Climate Research Unit (CRU) version 4.01:**

   The CRU at the University of East Anglia provides global gridded data sets of various hydrologic and atmospheric variables that were obtained through interpolation of ground station data. The interpolation procedure is performed using an angular-distance weighting procedure. The CRU TS (time series) version 4.01 precipitation product was downloaded and clipped to the Sudd region [*University of East Anglia Climatic Research Unit*, 2017]. This gridded precipitation product has a 0.5-degree spatial resolution and a monthly temporal resolution. Because the CRU data products do not rely on satellite data, precipitation estimates can be obtained for the Sudd as early as 1901. Therefore, the CRU precipitation estimates can be used to reproduce the historical flooded areas of the Sudd using the model developed in this research. For the development of the Sudd hydrologic model over the period of time that aligns with the MODIS-derived flood maps, the monthly cumulative precipitation rates were downloaded from 2000 to 2016 and were averaged over the time-varying flooded extents of the Sudd. The resulting monthly time series is compared to the other data products evaluated in this study in Figure 22, and the monthly mean values are compared in Figure 23.

2) **Tropical Rainfall Measuring Mission (TRMM) 3B43 version 7:**

The TRMM data products use information from three instruments: the Precipitation Radar, TRMM Microwave Imager, and the Visible Infrared Scanner (VIRS) [*Tropical Rainfall Measuring Mission Project (TRMM)*, 2011]. The 3B43 Version 7 data product contains global precipitation estimates that are derived from both satellite and gauge data. This product has a monthly temporal resolution and a 0.25-degree spatial resolution and is available through the Goddard Earth Sciences Data and Information Services Center (GES DISC) from 1998 to present. TRMM has been replaced by the Global Precipitation Measurement (GPM) Mission; however, the TRMM data products are still being produced to support research and operational tools that have come to rely on this valuable data resource. Similar to the CRU product, the TRMM monthly precipitation estimates were averaged over the Sudd flooded area extents from 2000 – 2018 and the resulting time series and monthly mean values are shown in Figure 22 and Figure 23, respectively.

3) **Precipitation Estimation from Remotely Sensed Information using Artificial Neural Networks (PERSIANN) Climate Data Record (CDR):**

PERSIANN data products are developed by the Center for Hydrometeorology and Remote Sensing (CHRS) at the University of California, Irvine. The PERSIANN algorithm applies neural network procedures to brightness temperature images from geostationary satellites to produce precipitation estimates on a 0.25-degree global grid. The monthly Climate Data Record (CDR) product (ftp://persiann.eng.uci.edu/CHRSdata/PERSIANN-CDR/mthly/) was used in this

study, which is adjusted with global precipitation climatology project (GPCP) estimates. The GPCP integrates information from both satellites and ground measurements to estimate precipitation on a relatively coarse (2.5-degree) spatial scale. The PERSIANN monthly CDR data product was downloaded over the 2000 to 2018 period and averaged over the Sudd flood extents. The time series and monthly means are shown in Figure 22 and Figure 23, respectively.

4) Africa Rainfall Climatology Version 2.0 (ARCv2):

ARCv2 precipitation estimates are provided by the National Oceanic and Atmospheric Administration (NOAA) and rely on: geostationary infrared data centered over Africa from the European Organization for the Exploitation of Meteorological Satellites (EUMETSAT), and Global Telecommunication System (GTS) gauge observations. This data is available on a 0.1-degree spatial grid resolution and a daily temporal resolution [*Novella and Thiaw*, 2012]. This product combines a geostationary satellite centered over Africa and gauge observations to estimate daily precipitation on a 0.1-degree grid. Precipitation estimates were downloaded from 2000 to 2015, aggregated to a monthly temporal resolution, and then averaged over the monthly Sudd flooded area. The time series of monthly precipitation is shown in Figure 22 and shows a significant increase in precipitation

from 2012 to 2015 that is not observed in the other satellite products. The monthly mean precipitation over the 2000 to 2015 period is shown in Figure 23.

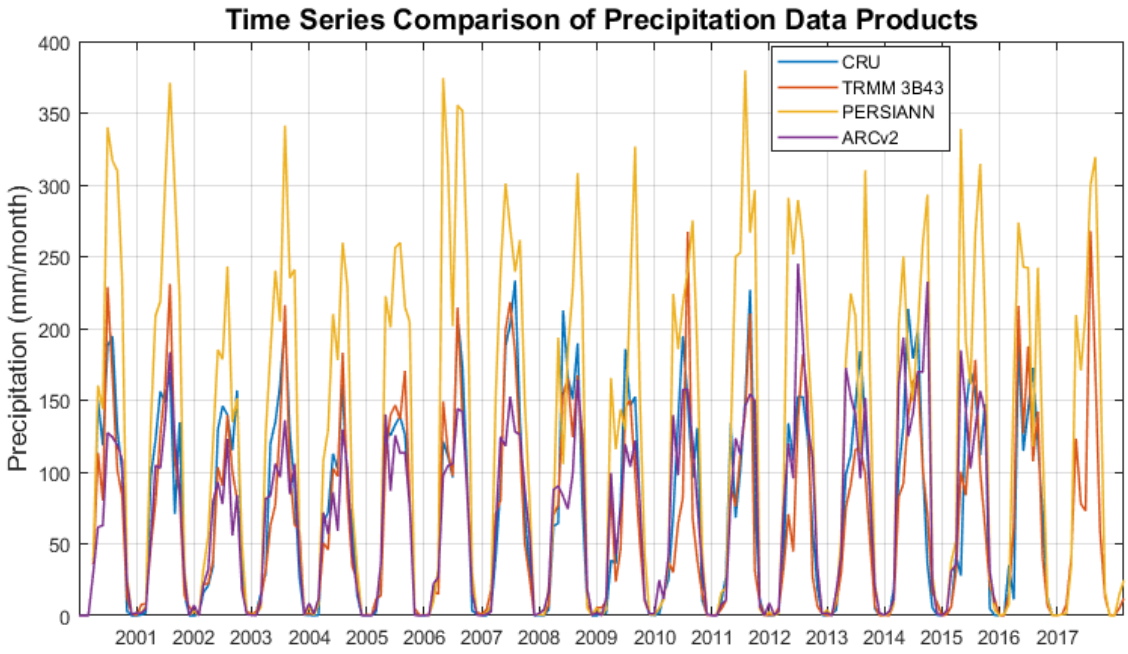

Figure 22: Time series of gridded precipitation data products evaluated in this study from 2000 to 2018.

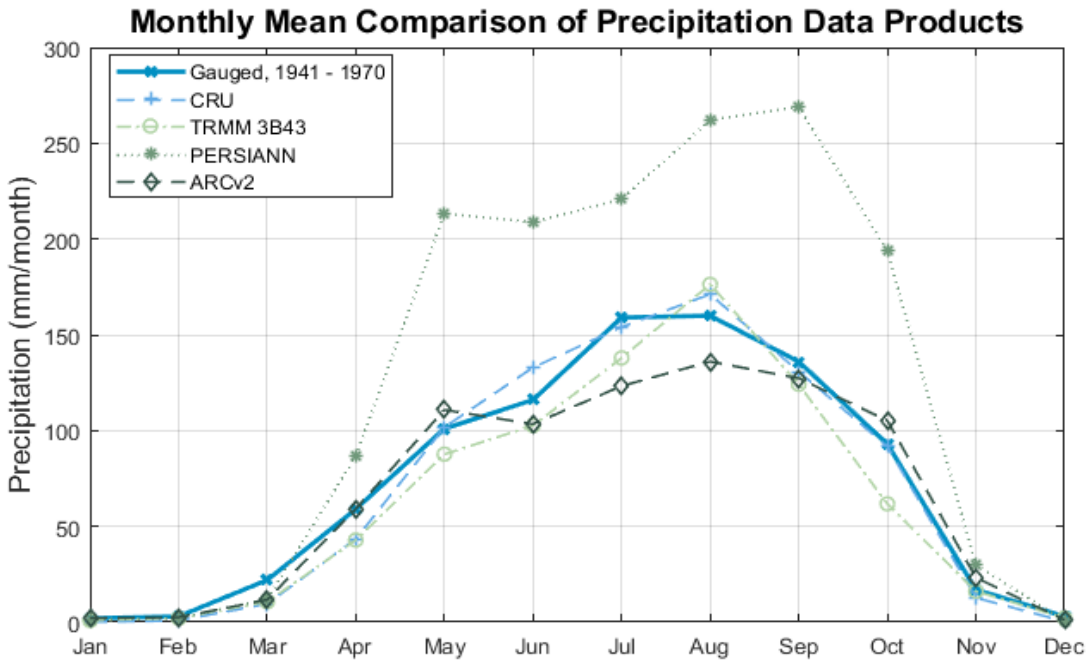

Figure 23: Monthly mean values of gridded precipitation data products evaluated in this study from 2000 - 2018, compared to the measured monthly mean rainfall from 1941 – 1970 reported in previous studies.

Figure 22 and Figure 23 show that the PERSIANN estimates are significantly greater than those of other precipitation data products, and substantially exceed the monthly mean values reported from historical in-situ gauges. The monthly mean estimates from the TRMM and CRU data products are most similar to the historical monthly means calculated from the in-situ gauges. Since current gauge data recorded at Juba and Malakal are used in the development of some of these products, they should not be used to assess relative accuracies. However, an evaluation of the Sudd performed by Petersen and Fohrer [2010] included daily rainfall measurements recorded from April 2004 to November 2005 at a station in the southern portion of the Sudd. This data was graciously provided by Dr. Georg Petersen and was compared to the corresponding pixel in the gridded precipitation data

products. The four data products evaluated in this study are compared with these in-situ measurements in Figure 24, and common statistical measures are listed in Table 10. From these measures, TRMM appears to be more consistently ranked high for accuracy. However, the spatial aggregation from point to pixel and the unknown accuracy of the gauge measurements introduces some uncertainty in this comparison. Therefore, these estimates need to be evaluated more rigorously during the iterative hydrological modelling process.

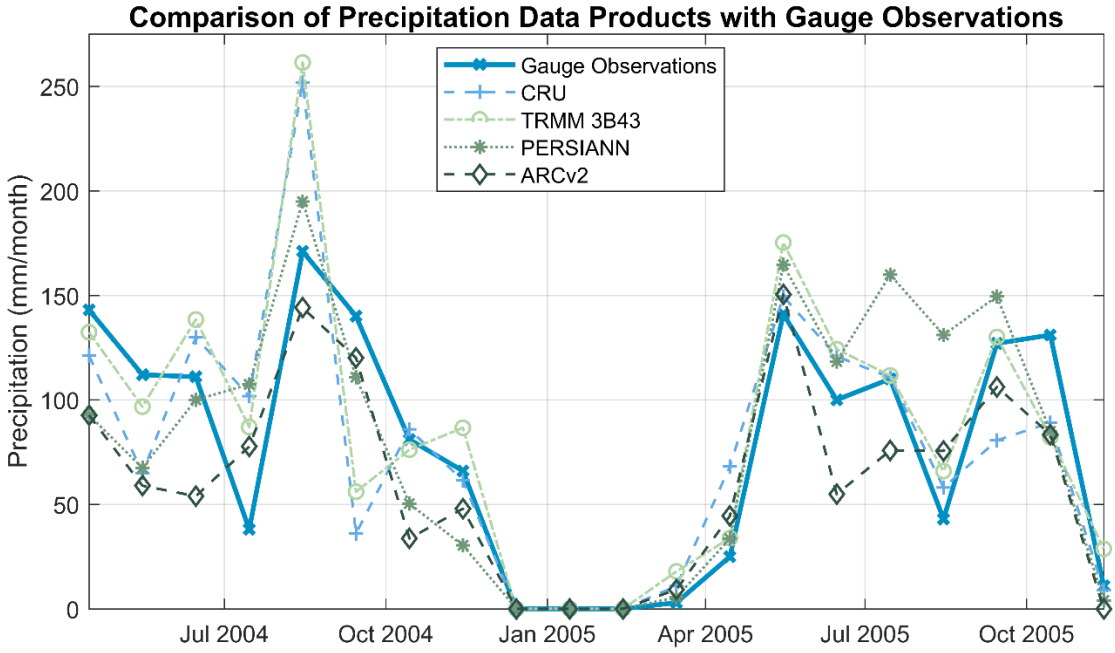

Figure 24: Comparison between monthly ground precipitation measurements from Petersen's study and satellite-based precipitation measurements evaluated in this study.

Table 10: Summary statistics in units of mm of the comparison between ground measurements from Petersen and satellite-based precipitation measurements, including mean absolute error (MAE), root mean square error (RMSE), mean bias (MB), and Pearson's correlation coefficient *(PCC)*.

	MAE	**RMSE**	**MB**	**PCC**
CRU	26.61	39.41	-0.17	0.776
TRMM	23.93	34.97	7.57	0.847
PERSIANN	28.07	36.72	2.63	0.808
ARCv2	26.95	32.77	-16.22	0.866

Global and regional assessments of the accuracy of satellite-based precipitation data products have varied widely and are sensitive to variations in geography and climate. Therefore, the data products presented in this section were chosen based on findings from previous studies that relied on remotely-sensed precipitation products in sparsely-gauged areas of Africa [*Awange et al.*, 2016; *Cattani et al.*, 2016; *Thiemig et al.*, 2012]. In these studies, TRMM products are consistently ranked highest in accuracy. However, Cattani et al. [2016] caution that these results may be biased since satellite estimates that are merged with gauge data (such as those evaluated in this study) use the same gauge data for accuracy measures. Cattani et al. also evaluated the signal-to-noise ratio of six products without using gauge data and found that PERSIANN, ARCv2, and TRMM were the top three performers (in that order). While these previous studies were helpful for identifying potential precipitation data sources, they were not relied on for accuracy assessments. The

best-performing data products were determined based on their success in modeling the Sudd wetland, according to the model performance metrics.

4.3 Evapotranspiration

4.3.1 Previous Measurements and Estimates:

Evapotranspiration (ET) is a critical hydrologic variable in the water mass balance of the Sudd and estimates have varied widely in the literature. Net annual ET rates estimated from previous studies are presented in Table 11. The historical estimates of ET rates in the early 1900's were summarized by Sutcliffe and Parks [1999]. In 1938, Butcher reported a net annual ET of 1533 mm based on a multi-year experiment with papyrus in a tank. However, he found that the corresponding amount of water lost in the entire Sudd area from this ET estimate was less than the amount needed to explain the total losses from the Sudd observed from the difference between inflows and outflows. Butcher suggested that this difference is attributed to water being transferred to the Bahr el Ghazal basin (west of the Sudd) without returning to the wetland. Hurst and Phillips believed that the ET estimated by Butcher should be approximately 30% greater if measured inflows and precipitation over the Sudd are equated to outflows and ET over the Sudd. Because flooding was shown to be more substantial downstream of where losses to the Bahr El Ghazal were potentially occurring, they surmised that these losses are insignificant in the total water balance. Migahid repeated the tank experiment in a different area of the Sudd where the papyrus was lusher and found that the mean daily ET was 80% greater than the amount reported by Butcher. Penman later reported on these findings and observed that the

ET rates for papyrus were similar those of open water. Using weather station data, he then calculated ET rates using the Penman equation and found that the resulting estimated net annual ET of 2150 mm agreed well with the mass balance of the Sudd while neglecting losses to the Bahr El Ghazal. The monthly ET rates reported by Penman are shown in Table 12 and were used in Sutcliffe and Parks' model of the Sudd [1999].

Table 11: Previous studies on the Sudd that estimated ET.

Study	Description	Time period of study	Net Annual ET (mm/yr)
Butcher*	Measured from papyrus in tanks	1927-1936	1533
Hurst & Phillips*	Estimated ET to close the water mass balance of the Sudd	1938	~2000
Migahid*	Measured from very lush papyrus in tanks	1948	2760
Sutcliffe & Parks (1999)	PET over open water calculated from Penman equation using local weather station data	1941-1970	2150
Mohammed (2004)	Surface Energy Balance Algorithm for Land (SEBAL), used satellite data	2000	1636
Petersen & Fohrer (2010)	FAO Penman-Monteith equation, calibrated using in-situ measurements	2005-2006	2077
Rebelo et al. (2012)	Simplified Surface Energy Balance (SSEB) model, used weather station data and satellite data	2007-2008	1697
Wilusz et al. (2017)	Atmosphere Land Exchange (ALEXI) land surface model, used satellite data	2007-2011	1210

**presented in Sucliffe and Parks (1999)*

Table 12: Monthly open water PET rates estimated for the Sudd and used in the Sutcliffe and Parks model.

Jan	Feb	Mar	Apr	May	Jun	Jul	Aug	Sep	Oct	Nov	Dec	Net Annual
217	190	202	186	183	159	140	140	150	177	189	217	2150

More recent studies have estimated actual ET using surface energy balance models informed with satellite data. Mohammed [2004] estimated the Sudd actual ET using the SEBAL algorithm (Surface Energy Balance Algorithm for Land) and satellite imagery from NOAA-AVHRR. The actual ET is estimated as the residual of energy balance terms, including net radiation, soil heat flux, and sensible heat flux. Unlike previous estimates of PET, the actual ET calculated here may be limited by soil moisture content. Mohammed found a net annual ET of 1636 mm/yr; monthly rates are shown in Figure 26. He subsequently estimated the flooded area of the Sudd using a threshold on ET values and delineated an area that is substantially larger than the flooded area estimated by Sutcliffe and Parks. Therefore, the increased area compensated for the reduction in ET in the water mass balance of the Sudd. However, Mohammed included areas outside the wetland area that may temporality be flooded from rainfall but are not connected to the wetland. Therefore, the flooded area he delineated is not appropriate for the mass balance analysis and the ET is likely underestimated [*J V Sutcliffe*, 2005].

As part of a study conducted by Petersen and Fohrer [2010], daily actual ET rates were measured in Oct. and Nov. of 2006 in a flooded depression in the southeast of the Sudd area. These observations along with meteorological data measured from nearby

stations from April 2005 to August 2006 were used to calibrate the Food and Agriculture Organization (FAO) Penman-Monteith equation [*Smith et al.*, 1998] for the Sudd and derive actual ET estimates for a full year. The resulting net annual ET was 2077 mm, an amount similar to Sutcliffe and Parks' estimate. However, the ET measurements and weather stations were located in the seasonally flooded area that completely dries out. Consequently, the estimated ET reduces to nearly zero during the dry season, as shown in Figure 26. Thus, these results are not representative of the flooded area of the Sudd and are therefore not suitable for the hydrologic model.

Rebelo et al. [2012] evaluated the relationship between satellite-derived ET and the flooded area of the Sudd and used the Simplified Surface Energy Balance (SSEB) model to derive monthly actual ET maps. In this model, daily reference ET was calculated using weather station datasets and were subsequently adjusted by ET fractions derived from 8-day MODIS thermal data. Between June 2007 and May 2008, the total annual actual ET was estimated as 1449 mm for the full Sudd area, shown in Figure 25. The mean annual ET over open water and flooded vegetation was estimated as 1697 mm. The monthly values were not presented in this study.

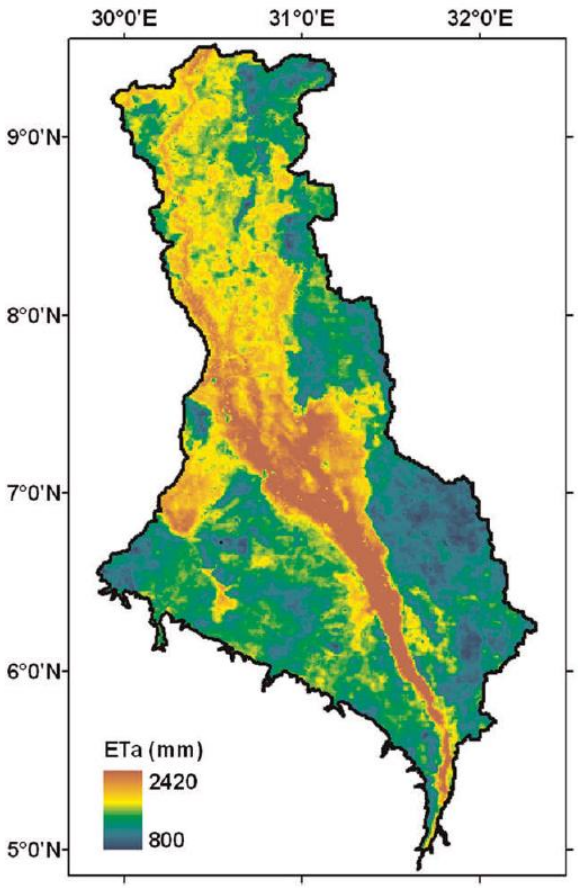

Figure 25: Total annual ET estimated over Sudd area from June 2007 to May 2008 from Rebelo at al. [2012].

Wilusz et al. [2017] evaluated ET in the Sudd region using the Atmosphere-Land Exchange (ALEXI) land surface model [*Anderson et al.*, 1997]. The ALEXI algorithm uses the surface energy balance model and partitions the surface fluxes by estimating the change in land surface temperature obtained from satellite observations. ET over the Sudd region was estimated at a daily resolution from 2007 to 2011 and yielded an average net annual ET of 1210 mm/yr. The monthly mean estimates are shown in Figure 26. Note that the ET is reduced during the dry season, suggesting that the actual ET is limited by water availability. This deviation from estimates obtained in other studies is due to the fact that

ET was estimated over an area that was delineated using a digital elevation model (DEM), identical to that shown in Figure 25. Large portions of this area are not continuously flooded; therefore, the ET rates reported in this study are substantially lower than ET rates that were calculated within the permanently flooded area.

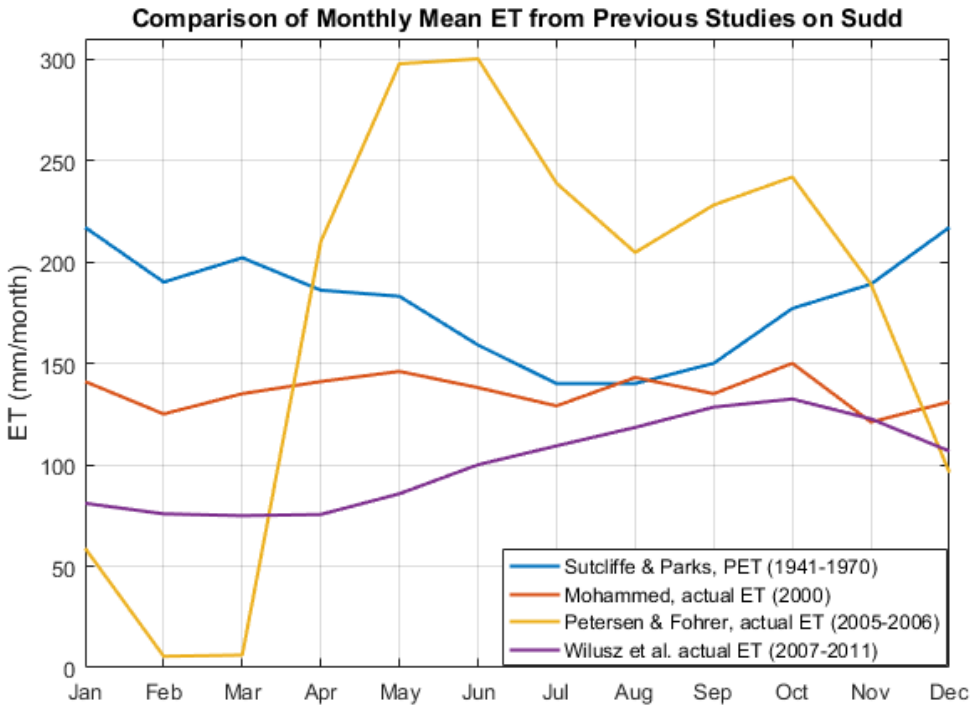

Figure 26: Comparison of monthly mean ET rates estimated in previous studies of the Sudd.

Figure 26 and Table 11 compare the ET estimates from previous studies on the Sudd and show the substantial variation in the net annual rates and the monthly time series. The minimum and maximum monthly values occur in different months, and intra-annual variation can be small (e.g. Mohammed's) or very large (e.g. Petersen & Fohrer). Some of this variation can be attributed to the fact that the ET was calculated from points in different locations, or averaged over areas with inconsistent boundaries. The lack of agreement

between previous studies suggests that estimates of ET rates in the Sudd are uncertain and should be used cautiously in modeling applications. Instead of treating ET estimates as known forcing data, they will be treated as uncertain estimates that may require adjustments through optimized model parameters.

4.3.2 Estimates Used in This Study:

For the 2000 to 2015 period of interest in this study, four different estimates of ET were evaluated or calculated over the Sudd area:

1) **Reference crop ET from the CRU:**

   The CRU distributes a global gridded ET data product for a reference crop of clipped grass with a 12 cm height [*University of East Anglia Climatic Research Unit*, 2017]. ET is calculated using a variant of the Penman-Monteith method (Equations 17 and 18) and relies on other CRU gridded data products, including average, min and max temperature, vapor pressure, and cloud cover. The monthly CRU TS (time series) version 4.01 has a 0.5-degree spatial resolution and a monthly temporal resolution. This data product was downloaded, clipped to the monthly flooded area extents of the Sudd, and averaged to obtain monthly mean ET rates over the Sudd flooded area. The vegetation in the Sudd likely has higher ET rates than the short grass reference crop. Therefore, this time series could be multiplied by a coefficient that is treated as an optimization parameter in the hydrologic model to better represent the Sudd.

$$ET = \frac{0.408\Delta(R_n - G) + \gamma \frac{900}{T + 273.16} U_2(e_a - e_d)}{\Delta + \gamma(1 + 0.34U_2)} \quad [17]$$

$$U_2 = U_{10} \frac{\ln(128)}{\ln(661.3)} \quad [18]$$

where

ET: reference crop evapotranspiration (mm d^{-1})
Rn: net radiation (MJ m^{-2} d^{-1})
G: soil heat flux (MJ m^{-2} d^{-1})
T: average temperature at 2 m height (^oC)
U2: windspeed at height of 2 m (m s^{-1})
U10: windspeed height of 10 m (m s^{-1})
$(e_a - e_d)$: vapor pressure deficit at 2 m height (kPa)
Δ: slope of vapor pressure curve (kPa $^oC^{-1}$)
γ: psychrometric constant (kPa $^oC^{-1}$)
900: coefficient for the reference crop (kJ^{-1} kg K d^{-1})
0.34: wind coefficient for reference crop (s m^{-1})

2) Reference crop ET calculated using the Hargreaves equation:

The Hargreaves method for estimating ET evolved from empirical relationships between pan evaporation and crop ET from agricultural areas in California. Farmers benefited from being able to predict ET rates of their crops, and efforts were subsequently made to apply this information to areas outside of California. This led to the 1985 Hargreaves equation (Equation 19). Similar to the CRU data product, the Hargreaves equation estimates ET for a reference crop of grass with height 8 to 15 cm. The Hargreaves equation is relatively simple and requires the daily average temperature and the daily temperature range. The temperature range is assumed to be correlated to relative humidity, a variable that is often used to estimate ET but is more difficult to measure than temperature. This

relatively simple equation has performed well when compared to more complex methods such as the Penman-Monteith [*Hargreaves and Allen*, 2003].

$$ET_o = 0.0023 R_a (TC + 17.8) TR^{0.5} \quad [19]$$

where:

ET_o: reference crop evapotranspiration (MJ m^{-2} d^{-1})
R_a = extraterrestrial radiation (MJ m^{-2} d^{-1})
TC: average temperature (^oC)
TR: temperature range (max – min)

The extraterrestrial radiation was calculated using the following equations:

$$R_a = \frac{24(60)}{\pi} G_{sc} d_r [\omega_s \sin(\varphi) \sin(\delta) + \cos(\varphi) \cos(\delta) \sin(\omega_s)] \quad [20]$$

$$d_r = 1 + 0.033 \cos\left(\frac{2\pi}{365} J\right) \quad [21]$$

$$\delta = 0.409 \sin\left(\frac{2\pi}{365} J - 1.39\right) \quad [22]$$

$$\omega_s = \arccos[-tan(\varphi)\, tan(\delta)] \quad [23]$$

where:

G_{sc}: solar constant = 0.0820 MJ m^{-2} min^{-1}
d_r: inverse relative distance between Earth and Sun
ω_s: sunset hour angle (rad)
φ: latitude (rad)
δ: solar declination (rad)
J: Julien day

To estimate the reference ET in the Sudd using the Hargreaves equation, 0.5-degree gridded monthly temperature products were obtained from the CRU version 4.01

[*University of East Anglia Climatic Research Unit*, 2017], and the mean daily ET was calculated for each month from 2000-2015. A factor of 0.408 was then applied to convert ET to mm/day, and then to mm/month. Finally, the ET was averaged over the monthly flooded areas of the Sudd.

3) Actual ET from Global Land surface Evaporation: the Amsterdam Methodology (GLEAM):

The GLEAM model [*Martens et al.*, 2017; *Miralles et al.*, 2011] estimates actual ET and partitions it into evaporation from bare soil, transpiration, open water, interception loss, and snow sublimation. Pan evaporation is first estimated with the Priestley and Taylor equation (Equation 24) using satellite observations of net radiation and near-surface air temperature Subsequently, actual ET is calculated using an evaporative stress factor that is derived from a multi-layer water balance model that simulates root-zone soil moisture. Microwave observations of soil moisture are assimilated into the soil moisture model for improved accuracy. Various satellite data products are also used to estimate net radiation and air temperature. GLEAM version 3.1 was downloaded over the Sudd area and has a 0.25 x 0.25 degree spatial resolution and daily temporal resolution. The total actual ET was aggregated to a monthly temporal resolution and averaged over the monthly flooded area of the Sudd.

$$\lambda E_P = \alpha \frac{\Delta}{\Delta + \psi}(R_n - G) \qquad [24]$$

where:

λ: latent heat of vaporization (MJ kg-1)
Ep: pan evaporation (mm day-1)
α: Priestly and Taylor coefficient, replaces aerodynamic term in Penman equation
Δ: slope of saturated water vapor-temperature curve (kPa K-1)
ψ: psychrometric constant (kPa K-1)
Rn: net radiation (W m-2)
G: ground heat flux (W m-2)

4) ET calculated using the Maximum Entropy Production (MEP) method

The MEP formulation for ET was derived by Wang and Bras [2011]. Similar to other surface energy balance approaches, net radiation is partitioned between ET, ground heat flux (G) and sensible heat flux (H). However, this method differs from traditional approaches because it utilizes maximum entropy production theory to determine the most likely surface fluxes given available information. Huang et al. [2017] calculated global ET rates using the full MEP formulation on a 1 degree grid. Their calculations relied on global land cover data from the International Geosphere-Biosphere Programme (IGBP) to identify appropriate model parameters for each grid cell. This land cover map underestimates the flooded are of the Sudd, and therefore leads to an underestimation of the ET rates in the Sudd. Therefore, the more accurate land cover map that was derived in this research (Chapter 3) (Di Vittorio & Georgakakos, 2017) was used in a modified formulation of the MEP method that is more appropriate for a permanently flooded wetland.

The full MEP formulation that considers sensible, ground, and latent heat fluxes is described in Equations 25 to 31:

$$R_n = H\left[1 + B(\sigma) + \frac{B(\sigma)}{\sigma}\frac{I_S}{I_O}|H|^{-\frac{1}{6}}\right] \quad [25]$$

$$B(\sigma) = 6\left[\sqrt{1 + \frac{11}{36}\sigma} - 1\right] \quad [26]$$

where:

R_n: Net radiation (W m^{-2})
H: Sensible heat flux (W m^{-2})
B(σ): Reciprocal Bowen ratio
σ: dimensionless parameter that describes the state of the evaporating surface
I_S: thermal inertia of soil (W m^{-2} K^{-1} s$^{-1/2}$)
I_O: "apparent" thermal inertia of turbulent air (W m^{-2} K^{-1} s$^{-1/2}$)

$$I_o = C_o\rho_a c_p\sqrt{\kappa z}\left(\frac{\kappa g z}{\rho_a c_p T_o}\right)^{1/6} \quad [27]$$

$$I_S \begin{cases} \sqrt{I_d^2 + \theta I_w^2} & bare\ soil \\ \sqrt{\rho c L_v} = 1560\ Jm^{-2}K^{-1}s^{-\frac{1}{2}} & water \\ 0 & canopies \end{cases} \quad [28]$$

where:

C_o: related to atmospheric stability, 1.7 if unstable (R_n > 0) & 1.2 if stable (R_n < 0)
ρ_a: density of air = 1.2 kg m^{-3}
c_p: heat capacity of air at constant pressure = 1005 J kg^{-1} K^{-1}
κ: von Kármán constant = 0.4
z: distance from surface for which Monin-Obukhov similarity holds, 2.5 m for bare soil, 4.5 m for short vegetation, 9.5 m for tall trees
g: gravitational constant = 9.81 m s^{-2}
T_o: reference temperature = 273 K
I_d = thermal inertia dry soil = 900 W m^{-2} K^{-1} s$^{-1/2}$
I_w = thermal inertia liquid water = 1600 W m^{-2} K^{-1} s$^{-1/2}$
θ = volumetric water content = porosity for saturated soil = 0.45

$$\sigma \equiv \frac{L_v^2}{c_p R_v}\frac{q_s}{T_s^2} \quad [29]$$

where:

L_v: latent heat of vaporization = 2.5x10^6 J kg^{-1}
c_p: heat capacity of air at constant pressure = 1005 J kg^{-1} K^{-1}

R_v: gas constant of water vapor = 461 J kg^{-1} K^{-1}
q_s: surface specific humidity
T_s: surface temperature (K)
Δ: Slope of saturation water vapor pressure curve at Ts
γ: psychrometric constant

$$\Delta = \frac{de^*(T_s)}{dT_s} = \frac{L_v}{R_v T_s^2} e^*(T_o) \exp\left[\frac{L_v}{R_v}\left(\frac{1}{T_o} - \frac{1}{T_s}\right)\right] \quad [30]$$

$$\gamma = \frac{c_p P_o}{0.622 L_v} \quad [31]$$

where:

e(T): saturation vapor pressure as a function of temperature*
e(To) = 611 Pascals*
Po: surface air pressure = 101,300 Pa

For the Sudd Wetland, the following methodology was followed to calculate ET rates:

- Because the ET rates are calculated over the Sudd flooded area only, assume that the soil is always saturated. Therefore, σ in Equation 29 can be replaced with the ratio of the surface temperature gradient to the psychrometric constant: $\sigma \rightarrow \frac{\Delta}{\gamma}$. This adjustment eliminates the dependence on specific humidity.
- For areas with very dense vegetation cover, the ground heat flux can be assumed negligible. The permanently flooded vegetation in the Sudd is believed to have very dense coverage near the soil surface, minimizing the amount of radiation that can be absorbed by the ground surface. Therefore, the transpiration method can be used to estimate Evapotranspiration (E) rates, according to Equation 32:

$$E = \frac{R_n}{1 + \left(B(\sigma)\right)^{-1}} \quad [32]$$

- Ground heat flux was calculated for the seasonally flooded vegetation since it dries out every year and these areas likely have more exposed soil at the ground surface. Therefore, the full energy balance equation (Equation 25) was used to calculate ET.
- The time-varying inputs in this formulation are the net radiation and surface temperature. These were obtained from the Clouds and Earth's Radiant Energy System (CERES) SYN1deg data product (Level 3, Edition 4A), on a 3-hourly temporal resolution (https://eosweb.larc.nasa.gov/project/ceres/ceres_table).
- ET rates in the Sudd were calculated every for 3 hours from 2000 – 2016 for each MODIS (500-m) pixel. Subsequently the 3-hourly rates were converted from W/m^2 to units of mm/3-hr using a factor of 0.00440816, aggregated to monthly rates, and averaged over the flooded area for each month.

The full time series of monthly ET rates over the Sudd flooded area for the four estimates described above are plotted and compared in Figure 27. The monthly mean values of these four time series for the 2000 to 2018 period are shown in Figure 28 and are compared to the monthly ET rates estimated by Sutcliffe and Parks.

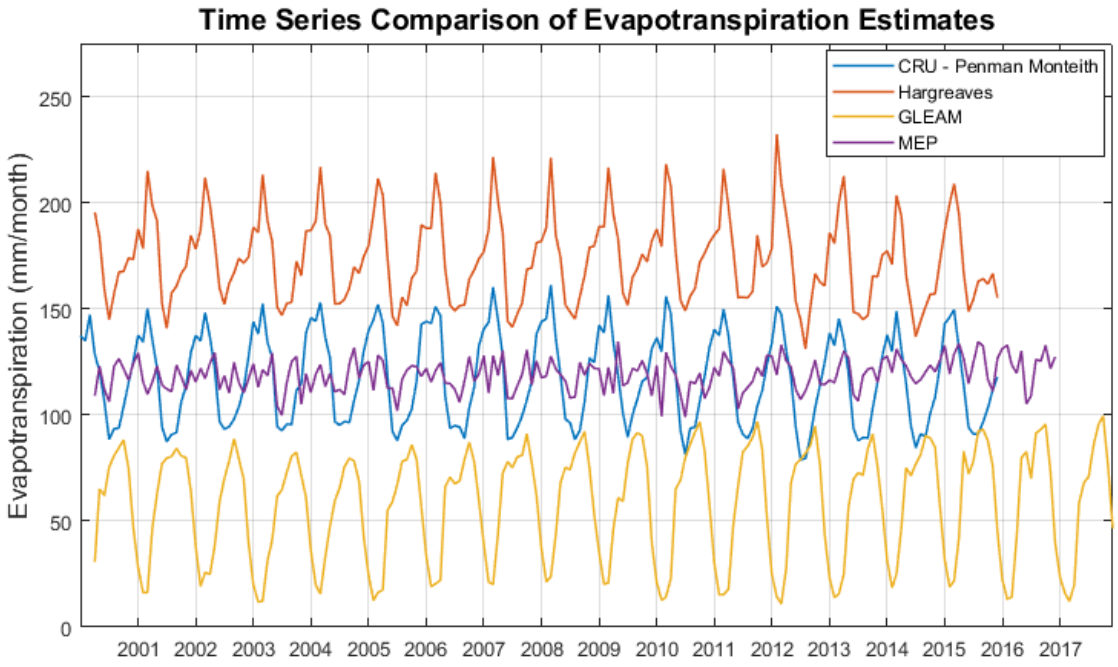

Figure 27: Time series of gridded evapotranspiration estimates averaged over the Sudd flooded area evaluated in this study from 2000 to 2018.

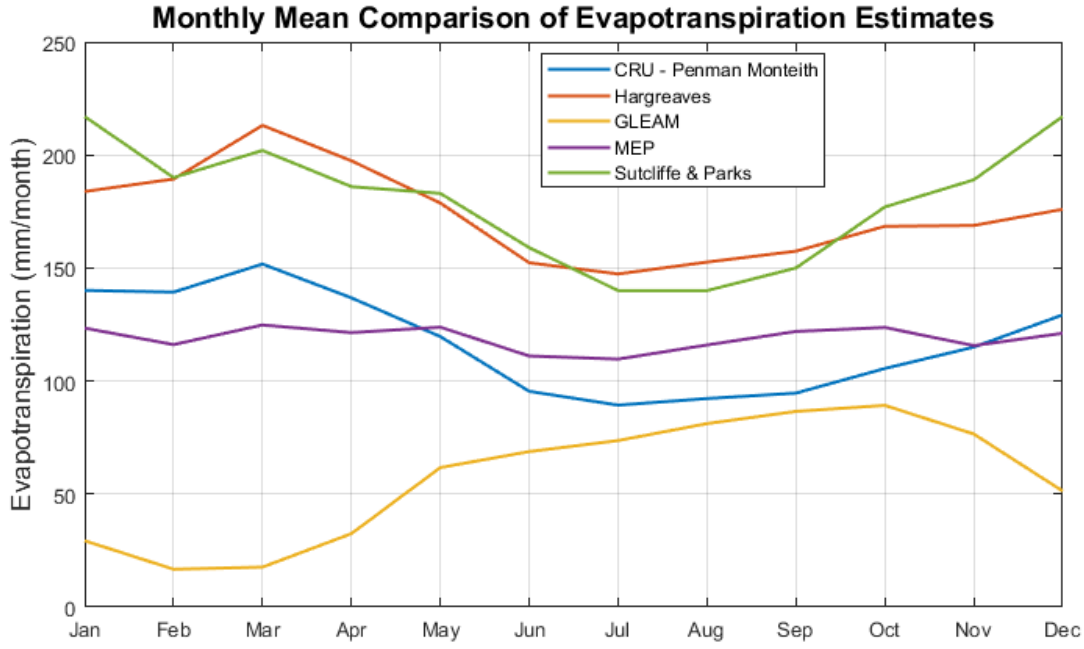

Figure 28: Comparison on monthly mean evapotranspiration rates estimated over Sudd flooded area.

Figure 27 and Figure 28 highlight the substantial differences between the ET estimates. In general, the Sutcliffe and Parks and CRU monthly mean estimates have the highest correlation, which is not surprising considering they are both based on the Penman (and Penman-Monteith) formulations. However, there is a significant bias of 50-100 mm per month due to the assumptions made on vegetation type. The Sutcliffe and Parks estimates assume that papyrus is representative of the entire wetland area and the ET rates are similar to those to open water, and the CRU estimates are for those of a reference crop that would be most similar to the seasonally flooded grassland class. The Hargreaves estimate is similar in magnitude to that of Sutcliffe and Parks, but has a slightly different seasonality. The Hargreaves estimates are more sensitive to errors in remotely sensed temperature differences but require less meteorological data, which is scarce in the Sudd area. The MEP values are similar in magnitude to those of the CRU; however, the time series lacks a distinct seasonal fluctuation. Finally, the GLEAM estimates contrast greatly with the others. The reduction of ET in the dry season is most likely induced by a water limitation calculated in the soil moisture accounting module of the GLEAM model. However, since ET was calculated over the flooded area only, ET should not be moisture limited. Consequently, the GLEAM estimates of actual ET are likely inaccurate, demonstrating that remotely sensed data sources must be carefully chosen and assessed prior applying them in hydrologic models.

The Sutcliffe and Parks, CRU, and Hargreaves estimates represent potential ET, whereas the MEP and GLEAM models estimate actual ET. Typically, potential ET is assumed larger than that of actual ET; however, this is a subject of debate for wetland areas.

Lott and Hunt [2001] compared in-situ ET measurements from a natural wetland to concurrent ET rates calculated according to the Penman equation. They found that actual ET rates were consistently higher than the theoretical ET, and nearly doubled the ET rates during the middle of the growing season. A potential explanation for this behavior is that the non-uniform height of vegetation in a natural wetland makes the air flow more turbulent, thereby increasing ET.

To understand the behavior of the MEP estimates, the input data sources were evaluated. The most influential variable in this model is the net radiation obtained from CERES. The full time series is shown in Figure 29. Starting in 2011, there is an upward trend in the radiation. This trend influences the MEP estimates as well and should be further evaluated to determine whether it is representative of actual conditions. The monthly mean net radiation calculated over the 2000 to 2016 period is presented in Figure 30, along with the monthly mean surface temperature and final monthly mean MEP ET rates. This comparison explains why the MEP ET rates have a very different seasonality than the other estimates. The CRU, Hargreaves, and Sutcliffe and Parks estimates have higher ET rates during the dry season (Dec. to Mar.), when the temperature is higher and fewer clouds are present. However, the CERES net radiation is showing low radiation rates during the dry season, and an increase in radiation during the rainy season. The high surface temperature during the dry season compensates for the low radiation and increases the ET rates. However, as a result, the final MEP estimates have a relatively low seasonal fluctuation compared to the other estimates.

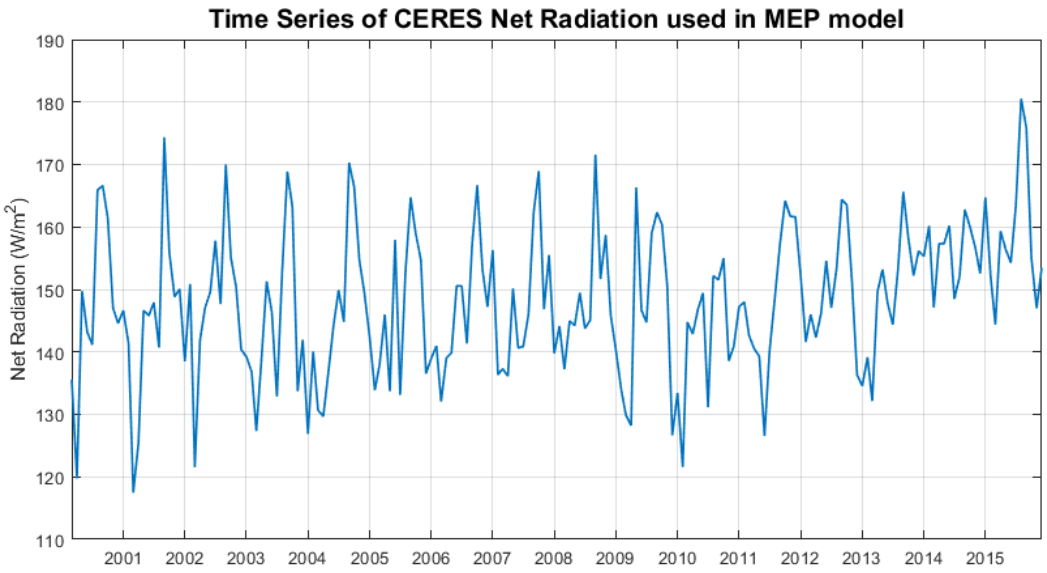

Figure 29: Time series of net radiation obtained from the CERES data product over the Sudd area from 2000 to 2016.

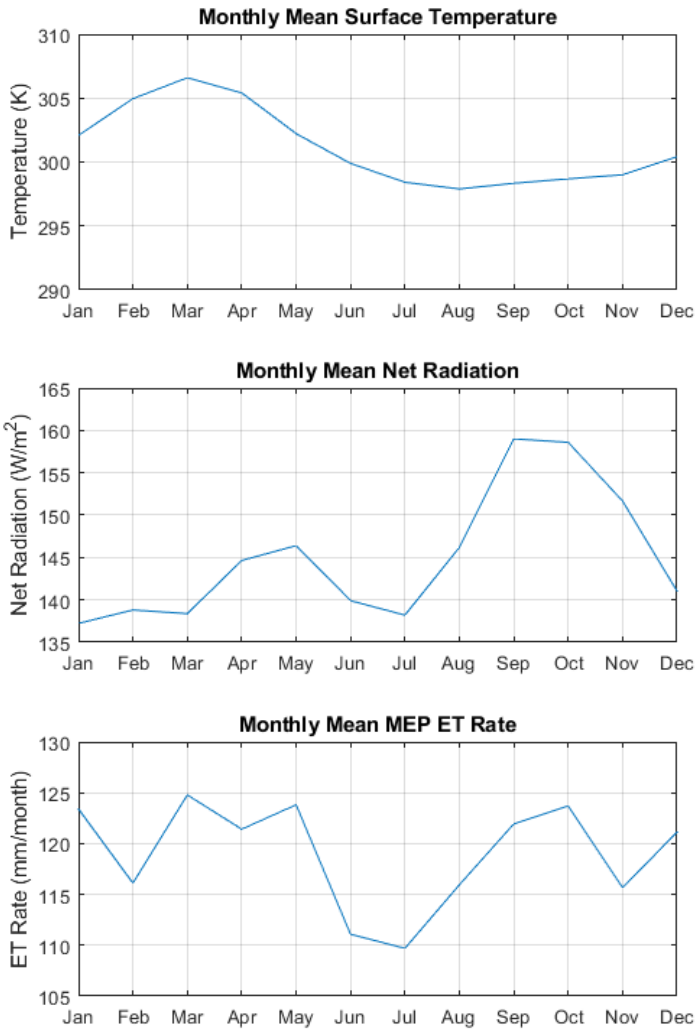

Figure 30: Comparison of monthly mean surface temperature (top), monthly mean net radiation from CERES (middle), and monthly mean MEP ET rate (bottom).

Theoretically, the ET rates should not exceed the available net radiation. Therefore, another comparison was made between the ET estimates evaluated in this study and the CERES net radiation, converted to units of mm/month. This comparison is presented in Figure 31 and shows that the Hargreaves and Sutcliffe and Parks estimates exceed the CERES net radiation during the dry season. The net radiation could be used in this way to assess how realistic various ET estimates are; however, the accuracy of the CERES data

product is suspect considering the trend observed in the time series and the low radiation rates during the dry season.

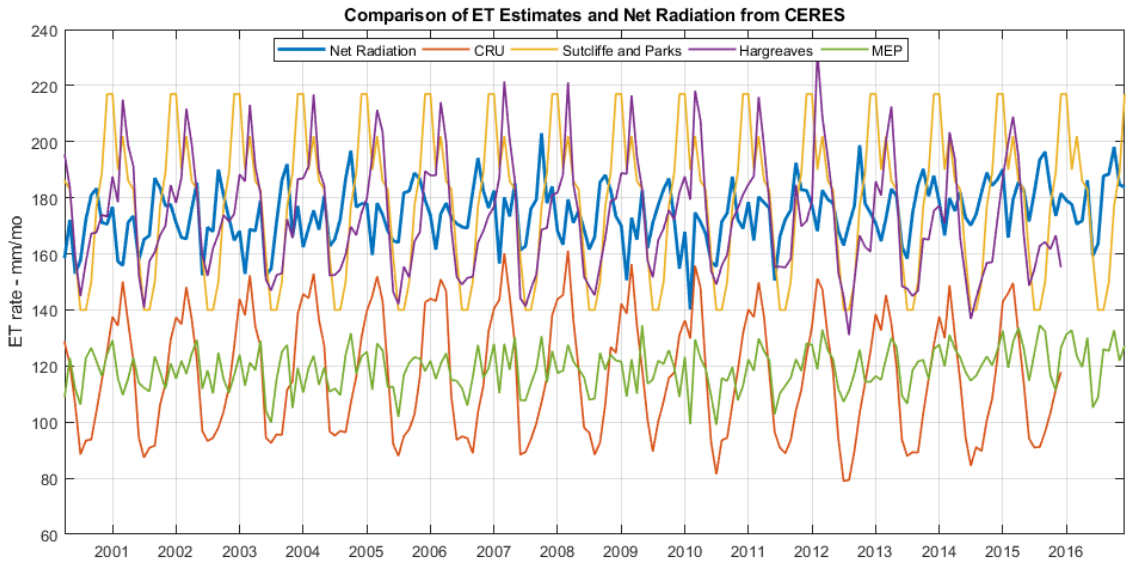

Figure 31: Comparison of ET estimates evaluated in this study to total net radiation from CERES data product.

This evaluation of estimates of ET in the Sudd over the 2000 to 2018 period again highlights the difficulty of estimating this hydrologic variable. Unfortunately, the large amount of variability in these estimates is not a challenge that is unique to the Sudd. In a global comparison study, Jiménez et al. found standard deviations of 50% or larger when comparing five different satellite-based ET models [2011]. Similar levels of uncertainty were found by Mueller et al. when comparing forty different ET products [2013]. Previous studies on the Sudd emphasize the important of ET rates in the hydrologic mass balance. Therefore, when using these ET estimates to develop a hydrologic model of the Sudd, they should be considered uncertain and adjusted during the modelling process to achieve consistency between multiple data sources and logic underlying the physically-based

model. An example of this approach is implemented in Section 5.5, where these ET estimates are evaluated along with other data sources to identify which estimates provide the highest correlation between the net water flux in the Sudd and the MODIS-derived flooded area extents.

4.4 In-situ Flow Records

The development of a hydrologic model of the Sudd requires estimates of the wetland inflows and outflows that align temporally with the MODIS-derived flood maps (2000 to 2018). Unfortunately, countries within the Nile Basin have not shared flow data publically since the 1980's. Additionally, data records in Sudan and South Sudan have not been well maintained due to recent political turmoil. However, the GWRI has worked with the Nile Basin countries for decades and has acquired a limited amount of in-situ flow data within the Nile Basin that was used in this study. This in-situ data is presented here, and the gaps that must be filled in order to obtain estimates of the Sudd inflows and outflows are identified. The actual derivation of the Sudd inflows and outflows is described in detail in Section 4.5.

The Nile Basin upstream of the Sudd Wetland is presented in Figure 32. The sub-basins in this figure were obtained from HydroSHEDS (www.hydrosheds.org), a global database that provides shape files of watersheds derived primarily from the Shuttle Radar Topography Mission (SRTM) 3 arc-second spatial resolution Digital Elevation Model (DEM). Key points along the Nile River that are referenced in this study are indicated in Figure 32. Mongalla is considered the entrance to the Sudd, and Malakal is the

location closest to the Sudd exit where the Nile flows have been measured. Just upstream of Malakal, the Sobat River enters the White Nile; therefore, the Sobat flows must be subtracted from Malakal flows to obtain the Sudd outflows. The area to the west of the Sudd (known as the Bahr el Ghazal) is delineated from Lake No. Historical field measurements suggest that the flows between the Bahr el Ghazal and the Sudd are negligible and can be ignored [*J V Sutcliffe and Parks*, 1987; 1999].

Figure 32: Nile Basin and sub-basins upstream of the Sudd Wetland, showing locations considered for estimation of inflows and outflows.

A very important source of flow data in this study was acquired at Laropi, located in Uganda near the border of South Sudan, courtesy of the Ugandan Ministry of Water and Environment. The raw data is shown in Figure 33 and has a daily temporal resolution and

spans from Feb. 2000 to Mar. 2013. This hydrograph shows seasonal and inter-annual variations and is strongly influenced by outflows from the upstream Great Equatorial Lakes. The data record after 2012 is suspect considering it does not show much variation and was therefore discarded.

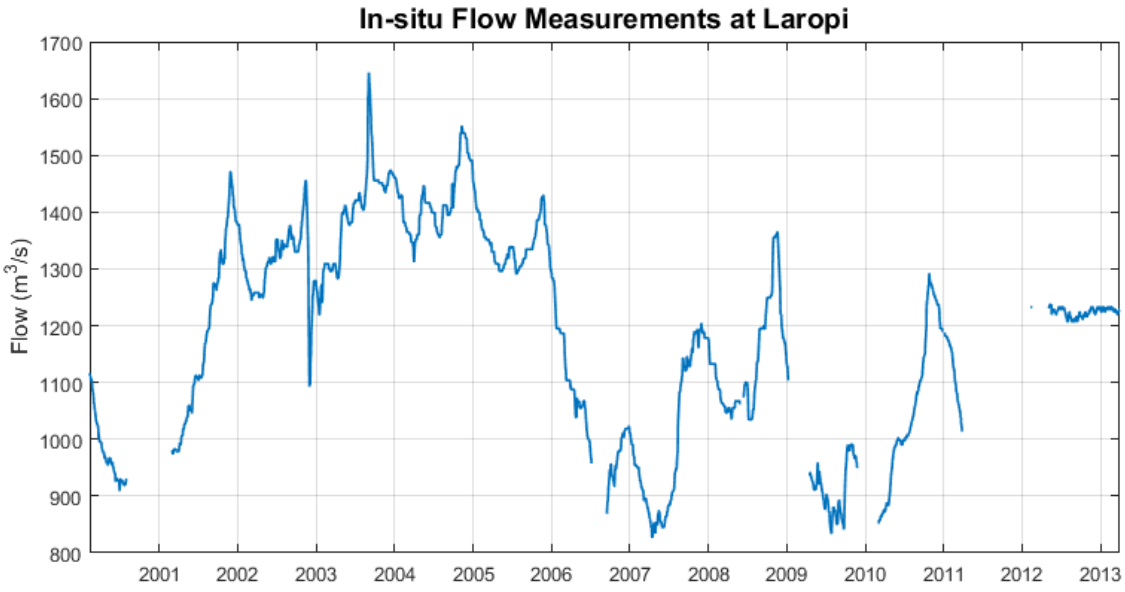

Figure 33: In-situ flow measured at Laropi, obtained from the Ugandan Ministry of Water and Environment.

In order to gap-fill the Laropi flow data, additional flow data was sought upstream of Laropi. The flow at Laropi is known to be highly correlated to outflows from Lake Albert, located at Packwach. Therefore, the Ugandan Ministry also provided us with measured water levels of Lake Albert from Jan. 2000 to Dec. 2015. The raw data was measured twice daily and was available from Jan. 2000 to Dec. 2015. This record was averaged over 10-day intervals for alignment with historical flow records and previously-derived statistical hydrologic routing models that are used in the Nile DST [*A P*

Georgakakos et al., 2003]. The 10-day Lake Albert levels are shown in Figure 34. In addition, the Ugandan Ministry provided the lake release rules that can be used to relate the water level heights of Lake Albert to outflows at Packwach. Similar to the Laropi flow data, there were some gaps in this data record that needed to be filled. A continuous time series of the Lake Albert levels was obtained using satellite altimetry data, described in Section 4.3.

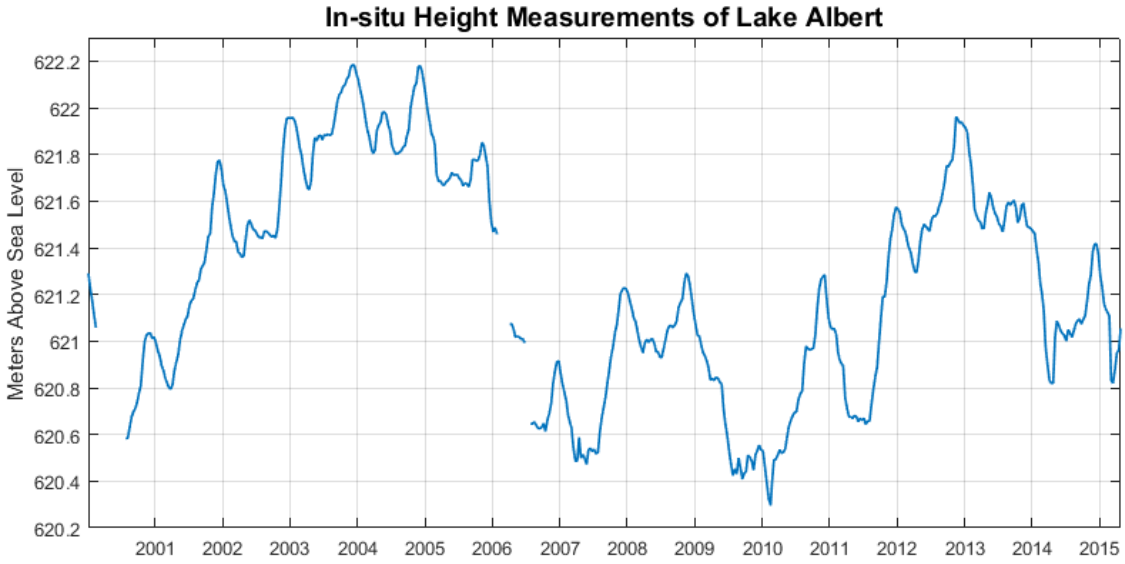

Figure 34: In-situ height measurements of Lake Albert, in meters above sea level, obtained from the Ugandan Ministry of Water and Environment.

The final source of in-situ flow data that was available after 2000 was located at Malakal, just downstream of the Sudd, within South Sudan but close to the Sudan border. This data, presented in Figure 35, was provided by the Sudanese Ministry of Irrigation and Water Resources on a 10-day temporal resolution and was available from Jan. 2000 to July 2011. This information was used to evaluate the outflows from the Sudd; however, in between the Sudd exit and Malakal, the Sobat River enters the Nile. This river is substantial

and drains the entire Sobat sub-basin, shown in Figure 32. Therefore, the Sobat flows need to be removed from the Malakal flows in order to estimate the Sudd outflows.

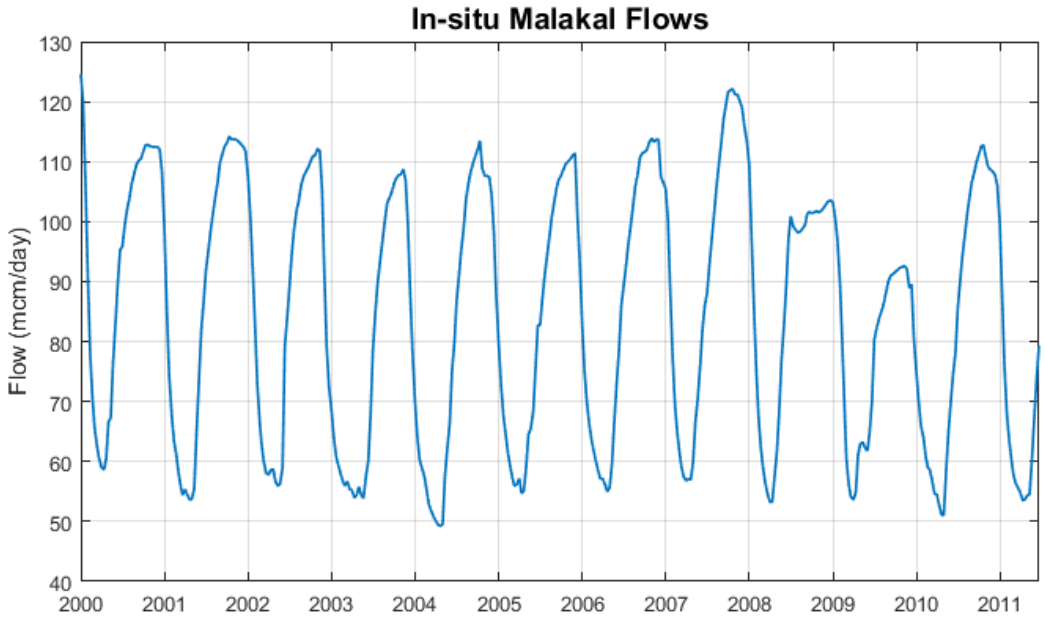

Figure 35: Measured in-situ flows at Malakal, downstream of the Sudd exit, provided by the Sudanese Ministry of Irrigation and Water Resources.

The in-situ data for Laropi, Lake Albert, and Malakal were critical for estimating the Sudd inflows and outflows during the period for which the MODIS flood maps were derived. However, historical flow data was also required to develop the statistical and physical relationships that could be used to gap-fill flow records and route them to the Sudd's entrance and exit. Historical flows in the Nile River from the early 1900's through the 1980's are available through the Nile Basin Volumes [*Hurst and Phillips*, 1932] and its supplements. The GWRI maintains hard copies of these volumes. Some of these records are also publically available through a global river discharge database, the GRDC (www.bafg.de/GRDC).

Historical flow records for locations upstream of the Sudd are shown in Figure 36. Nimule is located very close to Laropi, and inflows and losses between these two locations can be considered negligible based on an inspection of this reach using satellite imagery. However, Nimule flows were no longer recorded after 1960. An important feature of these upstream flows is the significant increase that occurred in the early 1960's. This increase in was caused by an increase in rainfall climatology over the Great Equatorial Lakes [*Mohamed et al.*, 2005; *J V Sutcliffe and Parks*, 1999]. As a result, the flows upstream of the Sudd approximately doubled, as did the flooded area extent of the wetland. This shift in the flows must be considered when using historical data to derive statistical relationships; the relationship may change before and after the 1960's, and the period after the 1960's is more representative of the 2000 to 2018 period for which the wetland model is being developed and calibrated.

The increase in flow between Packwach and Mongalla is attributed to run-off from seasonal rivers that enter the Nile in this reach, known as the Torrents. The Nile Basin Volumes contain monthly estimates of the Torrents flows. However, these flows were not measured directly and instead were calculated by subtracting the Packwach flows from the Mongalla flows. Therefore, measuring the accuracy of statistical models that rely on historical estimates of the Torrents flows is challenging due to the dependency of these estimates on the downstream Mongalla flows. The Torrents flows used in this study were provided by the Egyptian Ministry of Water Resources and Irrigation and have a 10-day temporal resolution. These flow estimates are not exactly equivalent to the difference

between the historical Mongalla and Packwach flows, but they are very similar and must have been derived similarly.

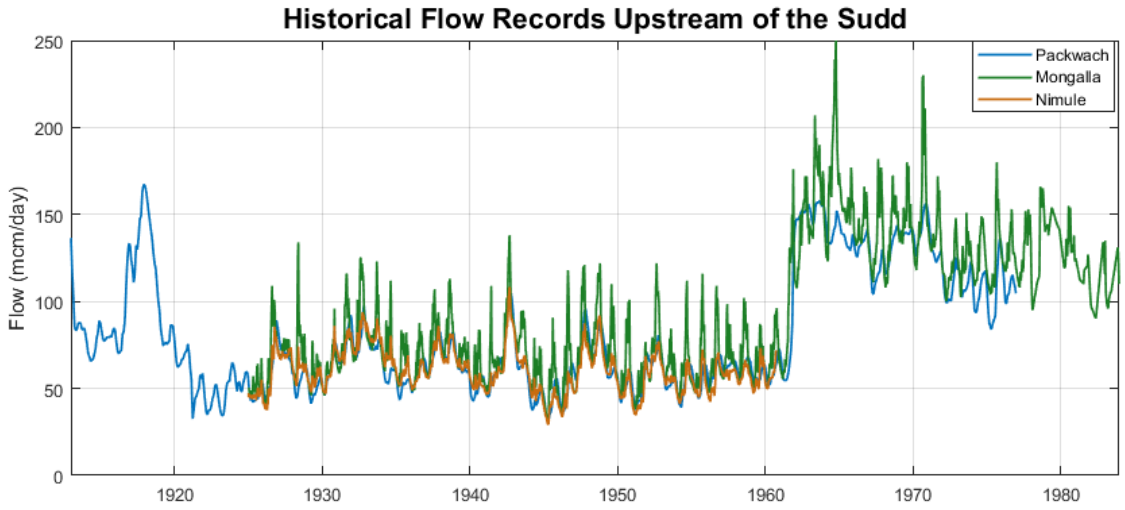

Figure 36: Historical 10-day flow records for locations upstream of the Sudd, taken from the Nile Basin Volumes.

The Nile Basin Volumes also contain flow records for the interior of the Sudd. Boats operated by the Egyptian Ministry of Irrigation traveled up and down the Sudd and recorded water level heights at locations throughout the wetland where flow measurements might provide insights into where losses occur. In many cases, multiple measurements were made in an effort to capture all of the flows that travel across a transect of the wetland where the Nile is split into multiple channels. The locations of the transects that were evaluated in this research are identified in Figure 37.

These interior flow records have not be utilized to a great extent in previous studies. However, in a recent study, Sutcliffe and Brown [2018] used some of these flows to split the wetland into multiple sub-basins, enabling them to apply the Sutcliffe and Parks mass

balance model to each sub-basin and calculate the associated flooded area. They concluded that this strategy was appropriate for the interior flows collected from 1936 to 1963; however, following the increase of the Nile flows and the Sudd flooded area, these measurements no longer captured all of the flows across each transect. Despite the conclusions of the Sutcliffe and Brown study, the interior Sudd flow records were further evaluated in this research to determine if flows within the interior of the Sudd could be produced for the 2000 to 2018 period. These estimated interior flows could then be used to calibrate a hydrologic model of the Sudd that is split into two separate sub-basins. The time series of the interior Sudd flows obtained from the Nile Basin Volumes are displayed in Figure 38 and compared to the inflows at Mongalla.

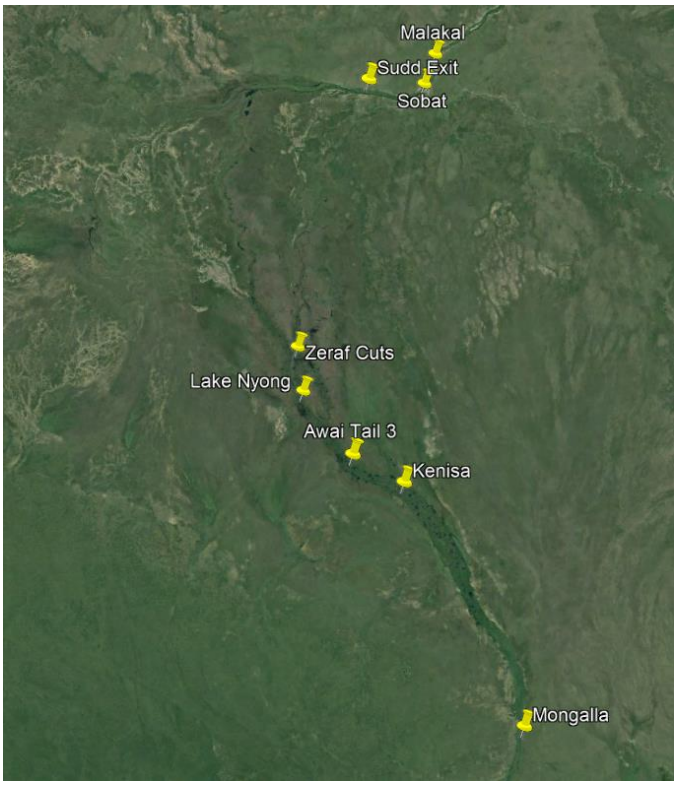

Figure 37: Landsat satellite image from Google Earth with locations within interior of Sudd where historical flow records are available.

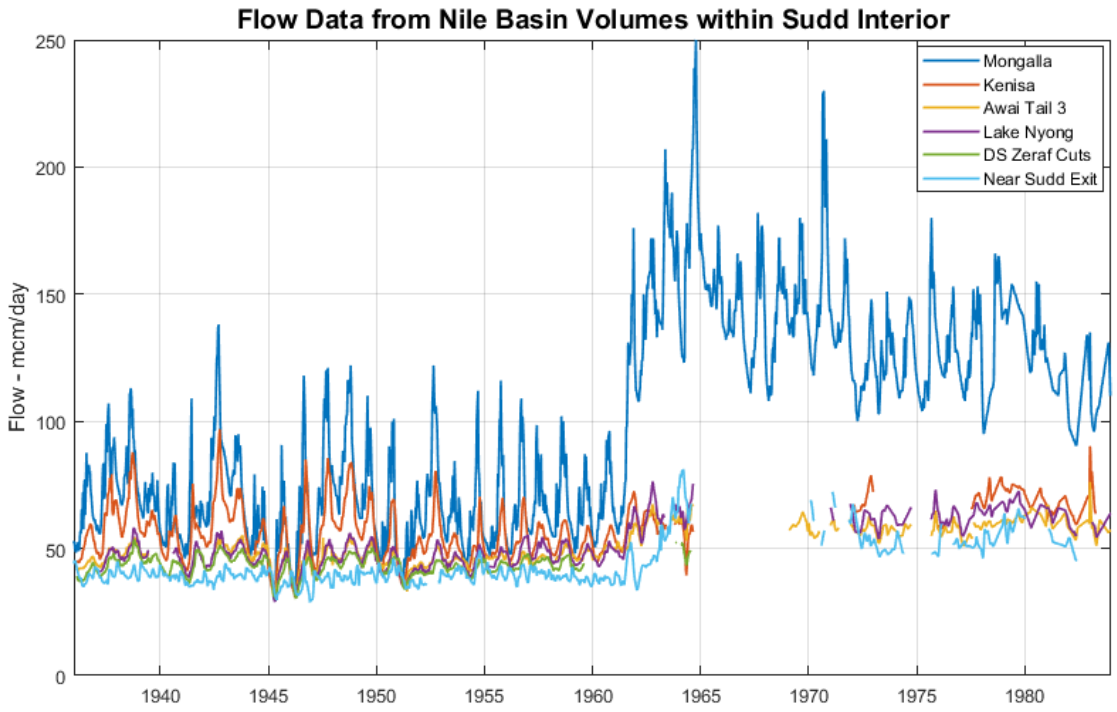

Figure 38: Historical 10-day flow records for locations within the interior of the Sudd, from the Nile Basin Volumes.

As mentioned when discussing the in-situ Malakal flows (Figure 35), the Sobat flows must be removed to obtain the Sudd outflows. To explore the relationships between the Malakal, Sobat, and Sudd outflows, historical flow records at Malakal and Sobat were also collected from the Nile Basin Volumes. These flows are shown in Figure 39 along with the estimated Sudd exit flows, calculated simply be subtracting Sobat from Malakal. Historical estimates of the Sudd outflows reported in previous literature were calculated using this same methodology.

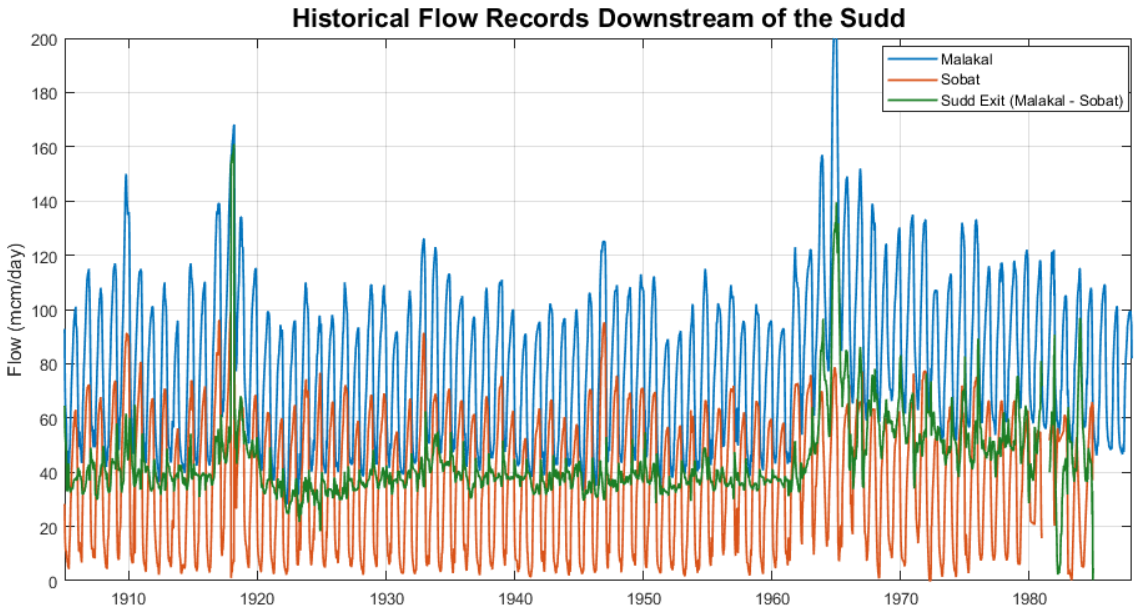

Figure 39: Historical 10-day flow records for locations downstream of the Sudd, from the Nile Basin Volumes.

Based on in-situ flow records available during the 2000 to 2018 period obtained from the Ugandan and Sudanese Ministries, and the long-term historical flow records obtained from the Nile Basin Volumes, the following tasks need to be performed to estimate the Sudd inflows and outflows from 2000 to 2018:

1. Gap-fill the Laropi flows using upstream flow estimates at Packwach and a statistical routing model developed with historical flows.
2. Estimate the Torrents flows from the 2000 to 2018 period using a rainfall-run-off model calibrated to historical Torrents flows.
3. Route the flows from Laropi to Mongalla using a regression model developed using historical flows for Mongalla, Nimule, and Torrents.

4. Assess whether the in-situ Malakal flows can be used to estimate the Sudd outflows if the Sobat flows can be produced for the 2000 to 2018 period using historical flows and regression models.

The implementation of these tasks and the resulting estimated Sudd inflows and outflows are discussed and presented in Section 4.5.

4.5 Estimation of Sudd Inflows and Outflows

4.5.1 Gap-filled Laropi Flows

As discussed in Section 4.2 and shown in Figure 33, there are gaps in the Laropi flow data that need to be filled to obtain a continuous time series of Sudd inflows. This can be achieved by using the upstream flows at Packwach and a simple linear regression model. Measured in-situ lake levels for Lake Albert were presented in Figure 34 and can be converted to outflows at Packwach using the reservoir release rules. However, the lake levels also have data gaps that need to be filled. To fill in the missing values, satellite altimetry data was downloaded from HYDROWEB [*Crétaux et al.*, 2011]. This database was developed by LEGOS (Laboratoire d'Etude en Géophysique et Océanographie Spatiale) and merges data from Topex/Poseidon, Jason-1 and 2, ENVISAT, and GFO to obtain water levels of large lakes. Levels for Lake Albert are available on a monthly temporal resolution and each measurement represents a linear scan across a portion of the Lake. The monthly satellite-based lake levels were converted to 10-day levels using linear interpolation to align with the desired temporal resolution of the final inflows and outflows. The measured lake levels obtained from the Ugandan Ministry were aggregated from the

raw twice-daily measurements to 10-day levels by calculating the mean lake levels over a 10-day period. The resulting 10-day measured and satellite-based lake levels are shown in Figure 40.

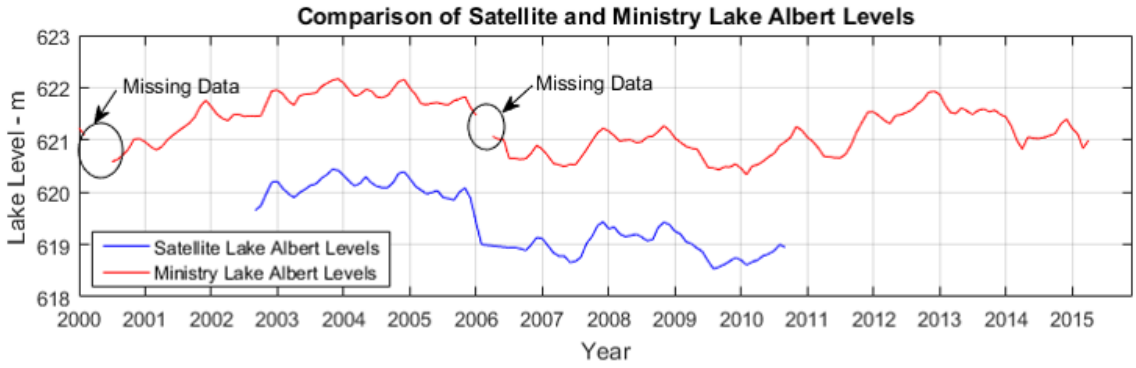

Figure 40: Comparison of monthly lake levels for Lake Albert from the Ugandan Ministry of Water and Environment and the HYDROWEB satellite altimetry database.

The Ministry's readings for January, May, and June of 2006 were removed as they are believed to be outliers based on the fact that they straddle a period of missing data and are irregular when observing the differences between the two data sources. The Pearson's correlation coefficient between the two time series is very high (0.994), but the satellite-based measurements have a bias close to 2 meters. Therefore, a statistical relationship for the lake level was derived as a function of the satellite measurement using a simple linear model and least squares regression. The resulting relationship is displayed in Equation 33. The lake levels are measured in meters, the root mean squared error of this model is 0.0631 meters, and the r^2 value is 0.987. A scatter plot comparing the measured lake levels to the modeled lake levels using the satellite estimates is shown in Figure 41; there is no trend in the residuals.

$$Lake\ Level = 34.909 + 0.94653 * Altimetry\ Lake\ Level \quad [33]$$

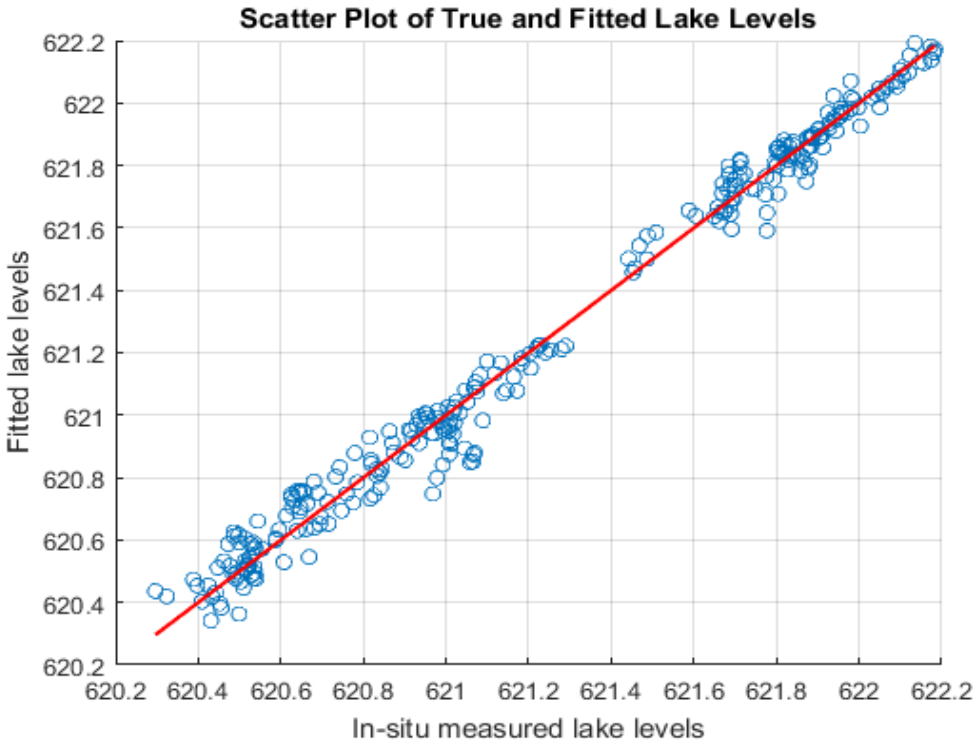

Figure 41: Scatter plot of true and fitted Lake Albert levels using linear model between measured lake levels and satellite-estimated lake levels.

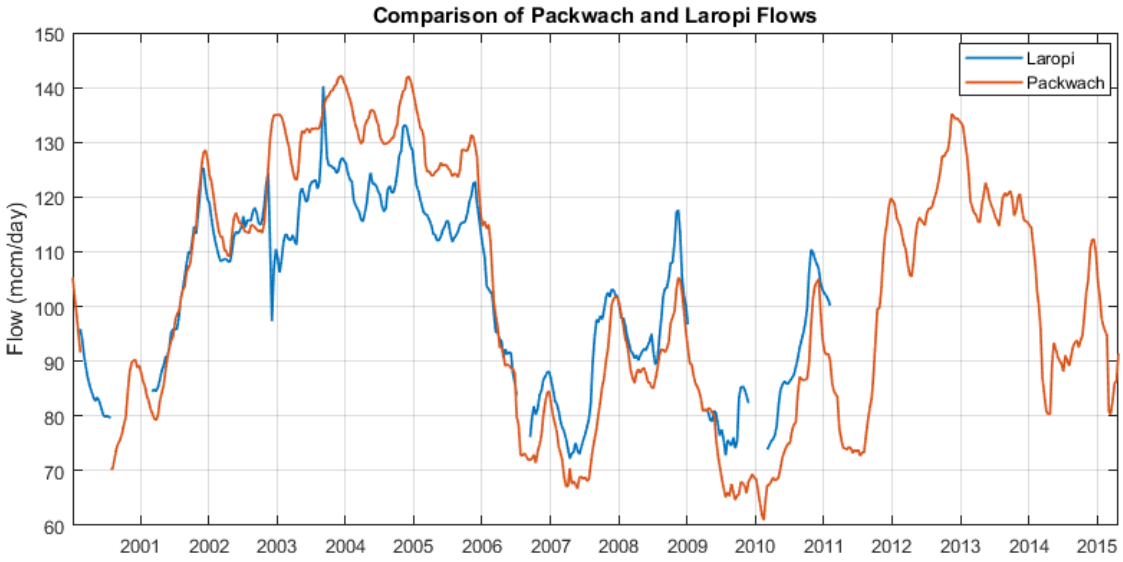

Figure 42: Comparison of gap-filled flows at Packwach to measured Laropi flows, in units of million cubic meters per day.

The reservoir release rules were provided in 0.1 meter increments. These values were interpolated to align with the measured Lake Albert levels and subsequently used to convert the gap-filled measured lake levels to outflows at Packwach. The resulting flow at Packwach is compared to the flows at Laropi in Figure 42. Note that these flows were converted from cubic meters per second to million cubic meters per day to align with historical flow records from the Nile Basin Volumes and the previously derived statistical routing relationships used in the Nile DST.

The Laropi and Packwach flows have a high linear correlation coefficient of 0.934. The comparison in Figure 42 suggests that the Laropi flow record from Nov. 2002 to Jan 2003 is not accurate; therefore, this portion of the flow record was removed, and the correlation coefficient increased to 0.9627. Figure 42 also shows that there is a reduction in flow rate between Packwach and Laropi during high flows, and an increase in flow rate

between Packwach and Laropi during low flows. During high flows, water may exit the main channel and evaporate or seep into the ground. A statistical model for Laropi as a function of Packwach was fit using least squares regression. A third order polynomial model provided an acceptable fit and eliminated a trend in the residuals that was observed for a simple linear model. The resulting model is displayed in Equation 34, where flows are measured in million cubic meters (mcm) per day. The root mean square error is 4.3 mcm/day and the r^2 value is 0.934. The intercept term and the term for the third power Packwach flows have p-values of 0.123 and 0.075, respectively, indicating that they are mildly significant. P-values for the other terms were very close to 0. Figure 43 is a scatter plot comparing the true and fitted Laropi flows, and the final gap-filled time series of Laropi flows is shown in Figure 44 and compared to the original measured flows. The gap-filled time series now provides flow estimates from Jan. 2000 to April 2015. These estimates cannot be extended beyond 2015 because neither the measured nor satellite-derived Lake Albert levels are available.

$$Q_{LAR} = -39.7 + 2.6598(Q_{PAC}) - 0.016958(Q_{PAC})^2 + 4.5786 * 10^{-5}(Q_{PAC})^3 \quad [34]$$

where:

Q_{LAR} = *Laropi Flow (mcm/day)*
Q_{PAC} = *Packwach Flow (mcm/day)*

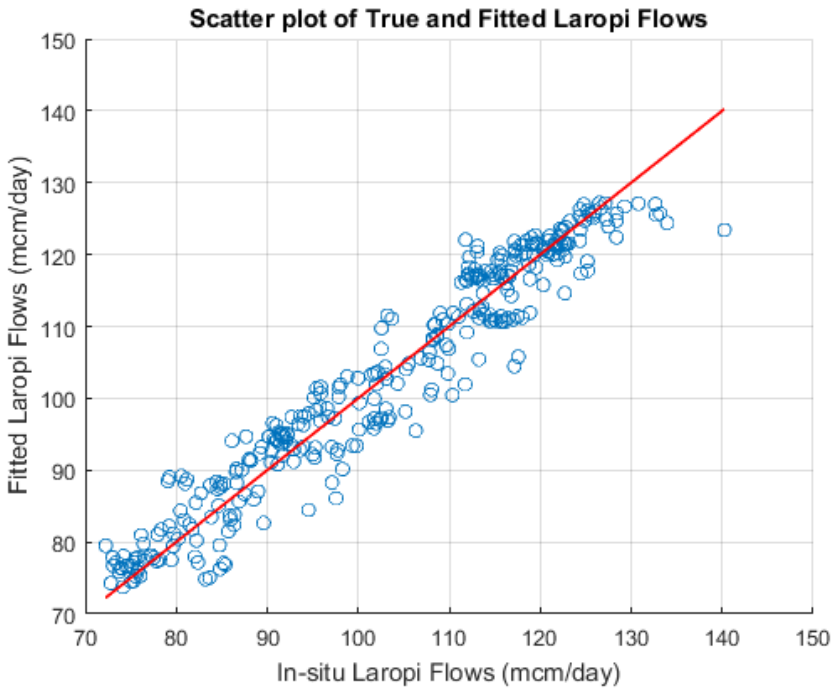

Figure 43: Scatter plot comparing the true and fitted Laropi flows using the non-linear regression model.

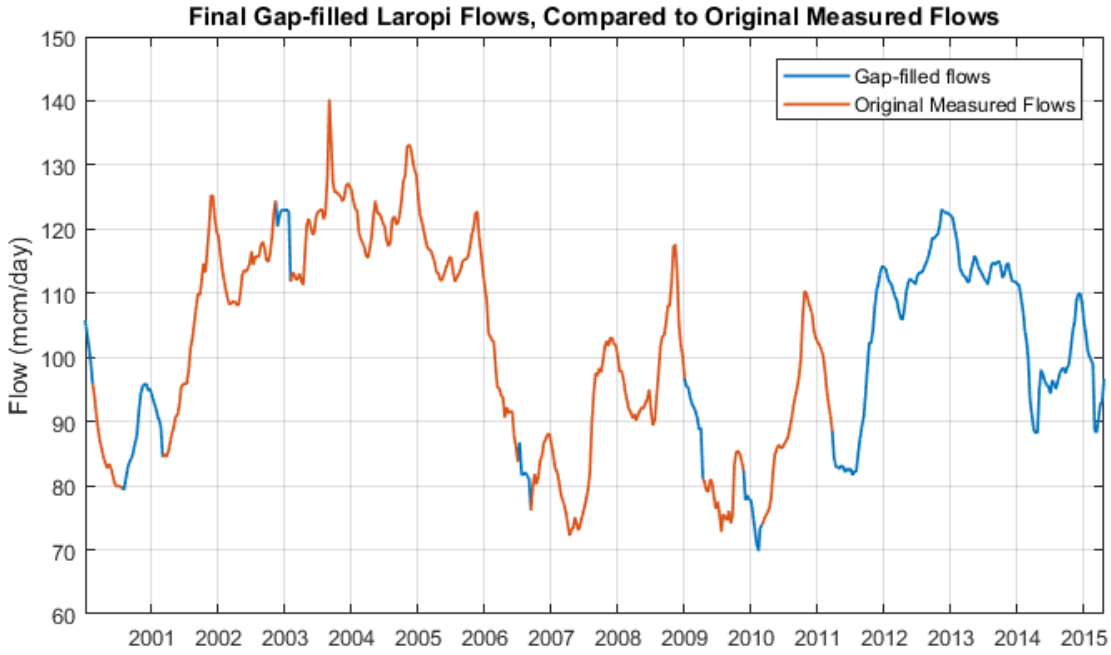

Figure 44: Time series of final gap-filled Laropi flows, compared to original measured flows, in units of million cubic meters per day.

4.5.2 Estimation of Torrents Flows

Prior to reaching the Sudd's entrance at Mongalla, the White Nile receives runoff from seasonal rainfall, known as the Torrent flows. Based on historical flow data from 1961-1980, the Torrents account for approximately 10% of the total annual Sudd inflows. The seasonality of the Torrents aligns with the period of extensive flooding within the Sudd, and this additional inflow is believed to impact the extent of the seasonally flooded wetland area [*J V Sutcliffe and Parks*, 1999]. Therefore, the Torrents flows are believed to be an important component of the hydrology of the Sudd.

As mentioned in Section 4.2.3, historical 10-day Torrents flows were obtained from the Egyptian Ministry of Water Resources and Irrigation and cover the period from January 1912 to December 1977. A hydrologic rainfall-runoff model was calibrated to these historical flows, enabling the estimation of the Torrents flows during the 2000-2015 period. The rainfall-runoff model applied was a modified version of the Sacramento Soil Moisture Accounting Model (SAC-SMA). The SAC-SMA model is a rainfall-runoff model that considers the soil mantle and the amount of tension water (water that can only be removed by evapotranspiration), and free water (water that eventually drains out of the soil column). Given forcing data for rainfall and ET, water storage is modeled in an upper and lower zone to allow for the estimation of runoff and return flows at varied temporal scales. The SAC-SMA model requires a minimum of 20 input parameters, assuming the ground is not frozen [*Burnash and Ferral*, 1996]. In data scarce areas, obtaining accurate estimates of such a large amount of parameters is not feasible, and multiple optimal solutions may exist

that do not accurately reflect the physics of the watershed. Therefore, the model has been modified to require only six calibration parameters.

To calibrate this model for the Torrents sub-basin, the historic Torrents flows were aggregated to a monthly temporal resolution and monthly rainfall and ET were obtained from the CRU, the same data source discussed in Sections 4.2.1 and 4.2.2 to estimate precipitation and ET for the 2000 to 2018 period. During the calibration process, the period from 1948 to 1977 provided the most consistent results. The Torrents flow record after 1977 shows little inter-annual variation appears to be filled with historical monthly averages. Figure 45 shows the observed and simulated Torrents flows during this period, and Figure 46 compares the observed and simulated flows using a scatter plot. Note the results circled in red in Figure 45 from 1963-1964 are considered outliers, as the data points deviated from the mean by more than three standard deviations. This time period was known to be unusually wet; however, the CRU input data did not reflect this.

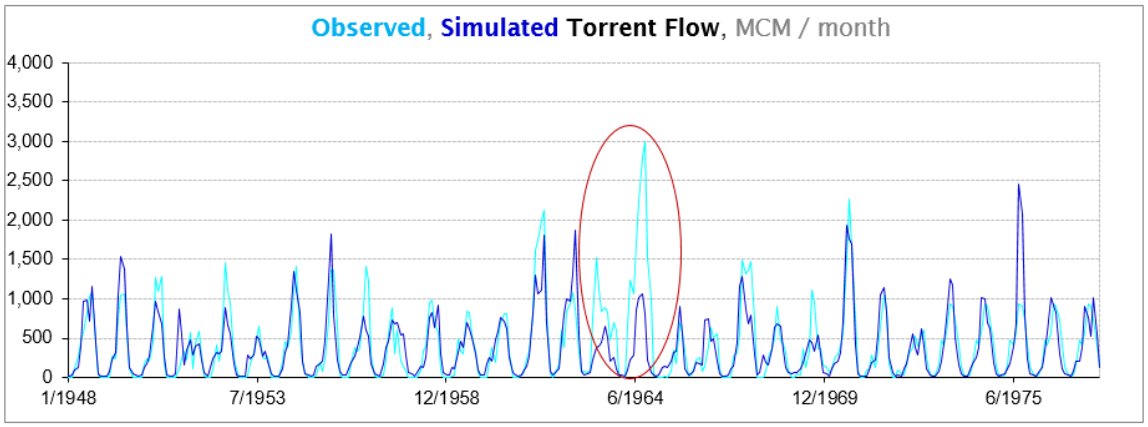

Figure 45: Comparison between observed and simulated Torrents flows for the 1948-1977 period using the SAC-SMA rainfall-runoff model. Outlier values are shown in the red circle.

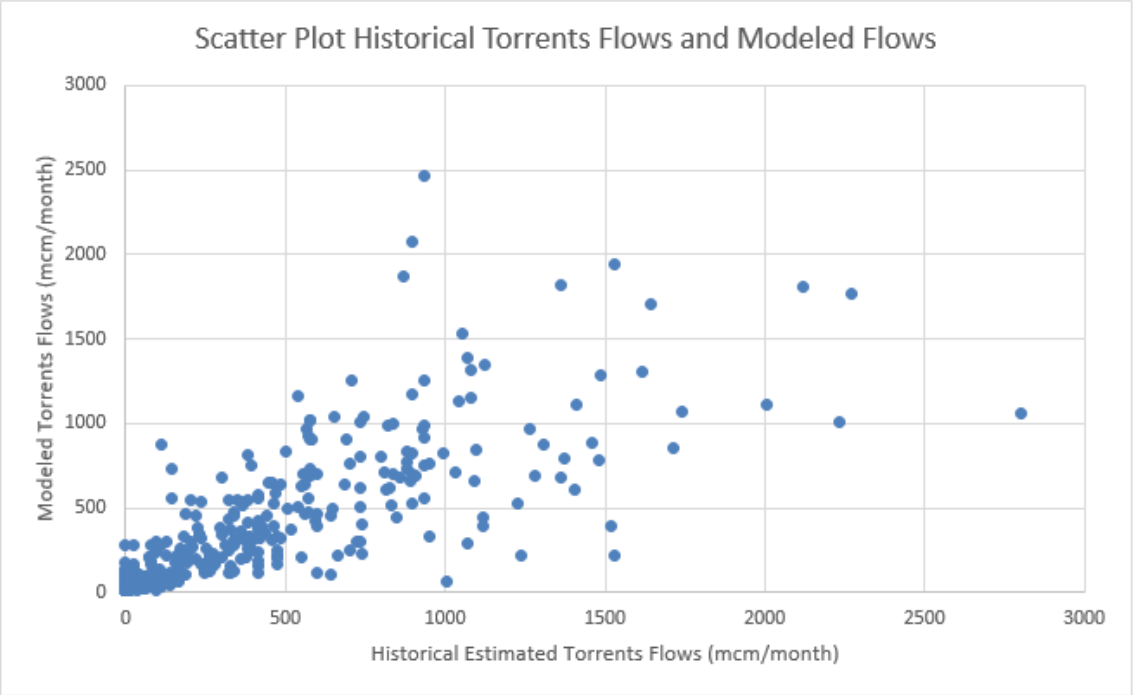

Figure 46: Scatter plot comparing historical estimated monthly Torrents flows to Torrents flows modeled using SAC-SMA rainfall-runoff model.

The Pearson's correlation coefficient between the observed and simulated flows is 0.823, the Spearman's rank correlation coefficient is 0.892, and the Nash Sutcliffe Efficiency coefficient is 0.621. The differences between the estimated and modeled flows are more significant for higher magnitude flows.

Using the calibrated rainfall-runoff model, the monthly Torrents flows were simulated for the 2000-2015 period using the same CRU precipitation and ET data products and the results are presented in Figure 47.

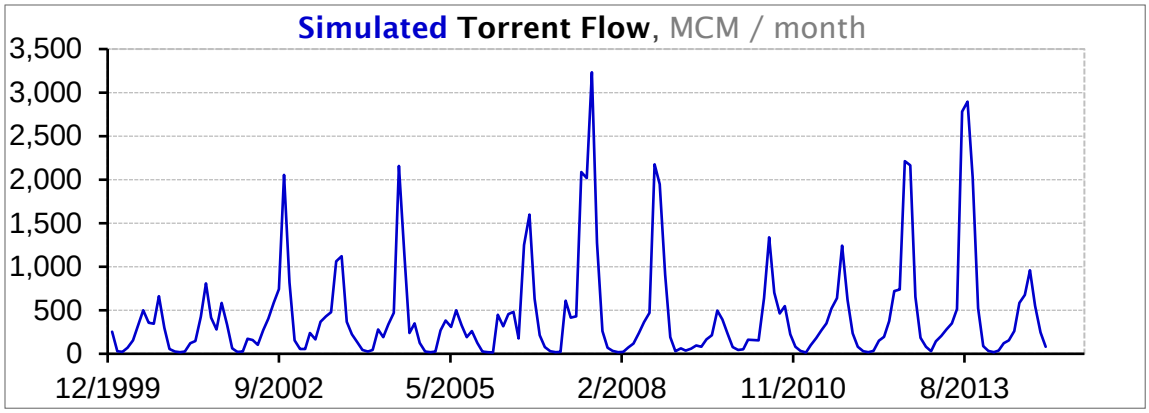

Figure 47: Simulated Torrent flows from 2000 - 2015 period, in units of million cubic meters per month.

The Torrents runoff model has a monthly temporal scale; however, a 10-day temporal resolution is desired to align with the upstream flow estimates. Therefore, the monthly Torrents flows were with disaggregated using the TRMM 3B42 daily precipitation data product. The daily precipitation product was downloaded for the 2000 – 2015 period, clipped to the Torrents sub-basin, and averaged. Subsequently the daily mean areal precipitation was aggregated to 10-day cumulate precipitation. The monthly Torrents flows were then disaggregated to a 10-day resolution using the 10-day TRMM precipitation as weighting factors. Finally, the Torrents flows were converted to units of mcm/day to align with the upstream flow estimates. The final estimated Torrents flows for the 2000 – 2015 period are shown in Figure 48.

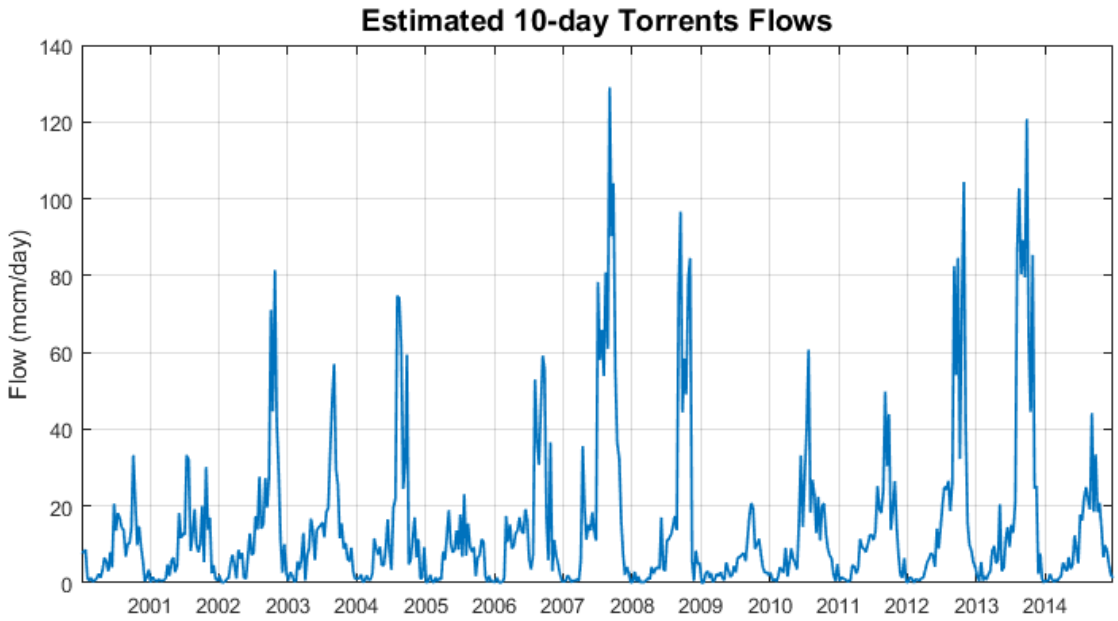

Figure 48: Final estimated 10-day Torrents flows, obtained by disaggregating monthly Torrents flows with daily TRMM precipitation.

4.5.3 Estimation of Mongalla Flows

The final step in estimating the Sudd inflows is to use the upstream Nile flows at Laropi and the inflows from the seasonal Torrents to estimate the Nile flows at Mongalla. A similar task was required for the Nile DST, and an autoregressive model was developed using historical flow records from the Nile Basin Volumes and the Egyptian Ministry of Water Resources and Irrigation [*A P Georgakakos et al.*, 2003]. This model is summarized in Equation 35. The Pearson's correlation coefficient between observed and fitted flows was reported as 0.99, and the standard deviation of the error was 6.3 mcm/day. The lag-1 autocorrelation coefficient of the model residuals was found to be 0.3.

$$Q_{MON}(k) = 7.318 + 0.163Q_{PAC}(k) + 0.739Q_{MON}(k-1) + 0.330Q_{TOR}(k) + \varepsilon(k) \quad [35]$$

where:

Q_{MON} *= Mongalla flow (mcm/day)*
Q_{PAC} *= Packwach flow (mcm/day)*
Q_{TOR} *= Torrents flow (mcm/day)*
ε *= error (mcm/day)*
k: temporal index

Note that Equation 35 relies on the flows at Packwach, but for the 2000 to 2015 period, we have derived flows at Laropi, a location downstream of Packwach and closer to the Sudd's entrance. Therefore, historical flows at Nimule (refer to Figure 36), a location just upstream of Laropi, were used instead of Packwach flows. As a first attempt to estimate the Mongalla flows, an autoregressive model similar to the model used in the Nile DST was calibrated using historical flow records from Jan. 1925 to Sep. 1960. This model is summarized in Equation 36. Figure 49 presents a scatter plot comparing the measured and modeled Mongalla flows, and the time series of the model residuals. The model achieved a high Pearson's correlation coefficient between the fitted and observed Mongalla flows (0.985), a model r^2 value of 0.97, and the RMSE was 3.06 mcm/day. Additionally, the p-values of all model parameters were very close to zero. However, Figure 49 shows that the model residuals are correlated, and the lag-1 autocorrelation coefficient of the residuals was found to be 0.714. This autocorrelation coefficient is significant and suggests that additional terms with longer lag times need to be added.

$$Q_{MON}(k) = 5.8328 + 0.73297Q_{NIM}(k) + 0.1555Q_{MON}(k-1) + 0.69892Q_{TOR}(k) + \varepsilon(k) \quad [36]$$

where:

Q_{NIM} *= Nimule flow (mcm/day)*

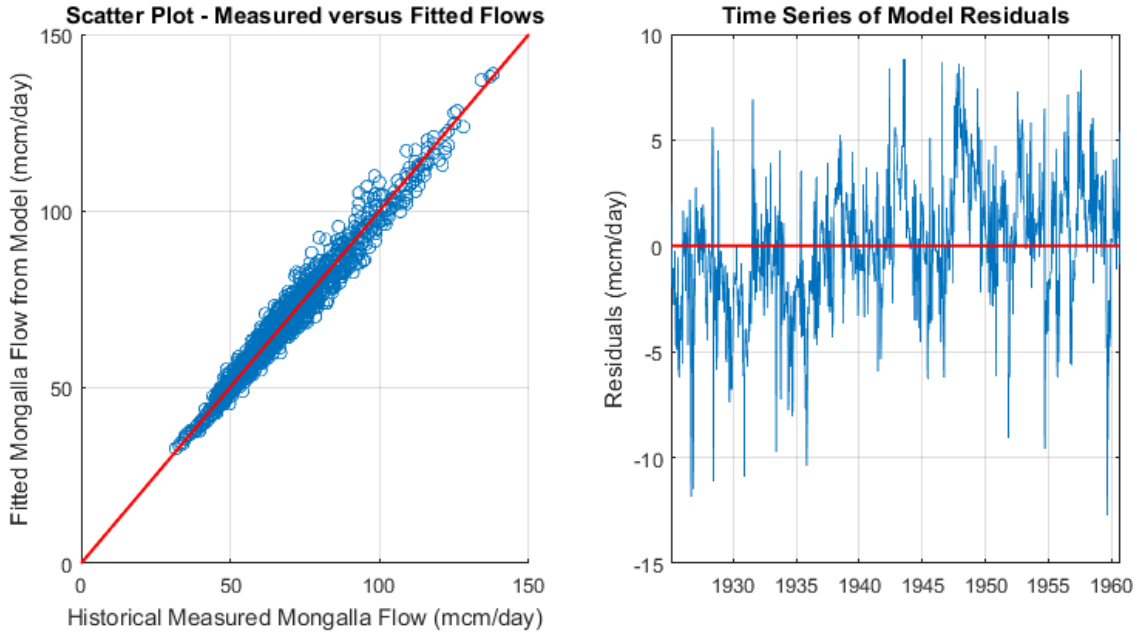

Figure 49: Autoregressive model for Mongalla flows calibrated to historical data, where there is temporal autocorrelation in the residuals.

To reduce the autocorrelation in the residuals, a revised autoregressive model that includes an additional term for both the Laropi and Torrents flows was calibrated. This model is summarized in Equation 37. Figure 50 presents a scatter plot comparing the measured and modeled Mongalla flows, and the time series of the model residuals. The model achieved a high Pearson's correlation coefficient between the fitted and observed Mongalla flows (0.999), a model R^2 value of 0.997, and the RMSE was 0.91 mcm/day. Except for the intercept, which is nearly zero, the p-values of all model parameters were very close to zero. The lag-1 autocorrelation coefficient of the residuals was reduced to 0.1345. A drawback of this model compared to the previous model (Equation 36) is that the coefficients have less physical meaning since some of the terms are negative. However, all of the terms are less than one, indicating that the model is stable.

$$Q_{MON}(k) = -0.060643 + 0.19474Q_{NIM}(k) - 0.13171Q_{NIM}(k-1)$$
$$+ 0.93112Q_{MON}(k-1) + 0.99677Q_{TOR}(k)$$
$$- 0.90984Q_{TOR}(k-1) + \varepsilon(k) \quad [37]$$

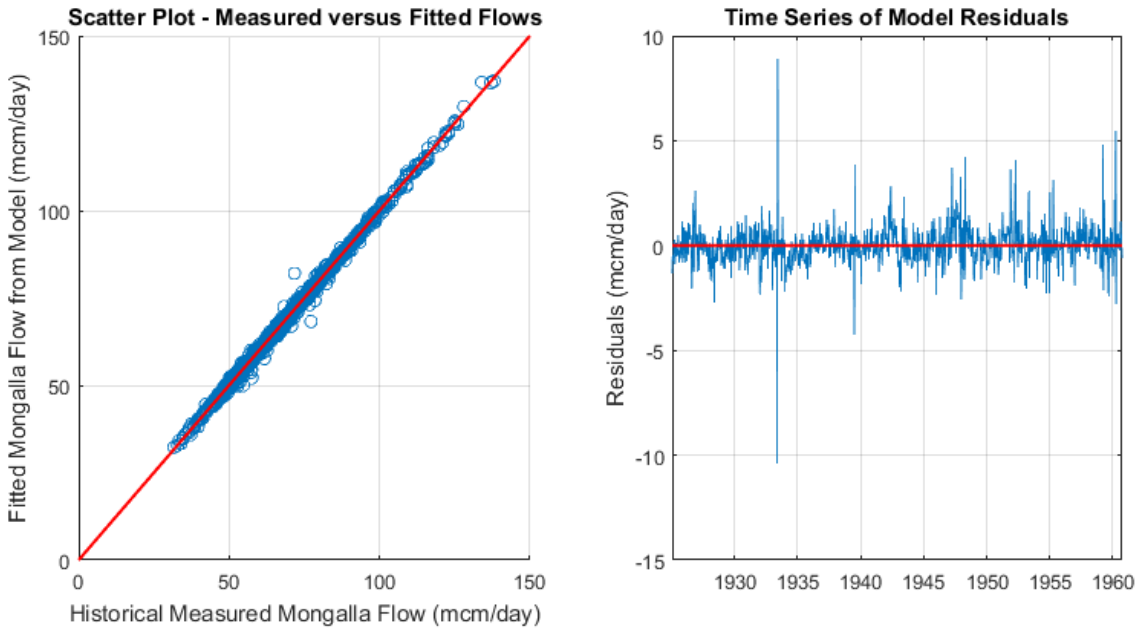

Figure 50: Revised autoregressive model for Mongalla flows calibrated to historical data, where the temporal autocorrelation of the residuals has been reduced.

To calibrate the parameters in Equation 37, the measured Mongalla flows were used for the response variable. However, to obtain a more realistic measure of the model performance, the Mongalla flows should be simulated from one time step to the next, without replacing the predicted flow with the measured flow. The simulated time series of historical Mongalla flows is compared to the measured Mongalla flows in Figure 51. The Pearson's correlation coefficient between these two time series is 0.971, and the RMSE is 4.23 mcm/day.

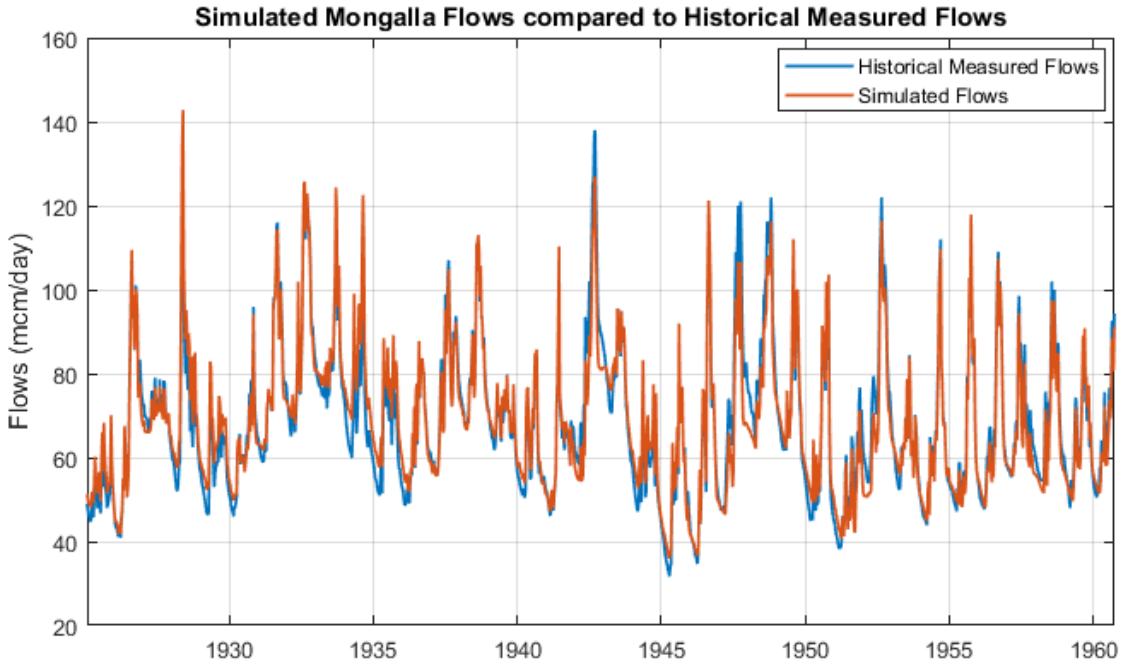

Figure 51: Time series of historical measured Mongalla flows and historical simulated Mongalla flows using autoregressive model.

The most accurate data available was used to calibrate the parameters of the Mongalla regression model. However, the corresponding performance metrics from this model are misleading because, as discussed in Section 4.4, the Torrents flows used in the model were estimated directly from the historical measured Mongalla flows. The simulation of the Mongalla flows during the 2000 to 2015 period depends on Torrents flows produced by the calibrated rainfall-runoff model. Therefore, the modeled Torrents flows that are independent of the Mongalla flows should be used to assess the uncertainty of the Mongalla flows estimated during the 2000 to 2015 period.

Consequently, the modeled Torrents flows from 1925 to 1960 were applied to Equation 37, in place of the Torrents flows from the Egyptian Ministry. The resulting

model performance is depicted in Figure 52 and shows that the variance of the model residuals has increased significantly. The simulated time series of the Mongalla flows is displayed in Figure 53. The Pearson's correlation coefficient between the time series is 0.777, and the RMSE is 11.64 mcm/day, a notable change from 0.971 and 4.23 mcm/day.

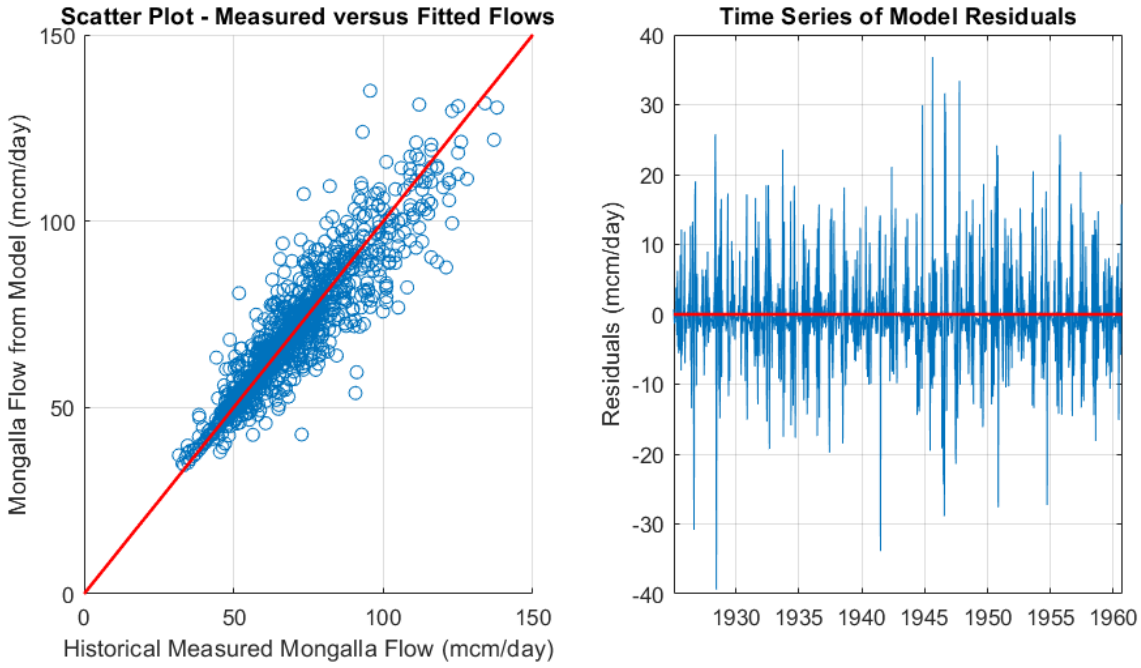

Figure 52: Performance of autoregressive model for Mongalla flows when Torrents flows from the calibrated rainfall-runoff model are used in place of the measured Torrents flows from the Egyptian Ministry.

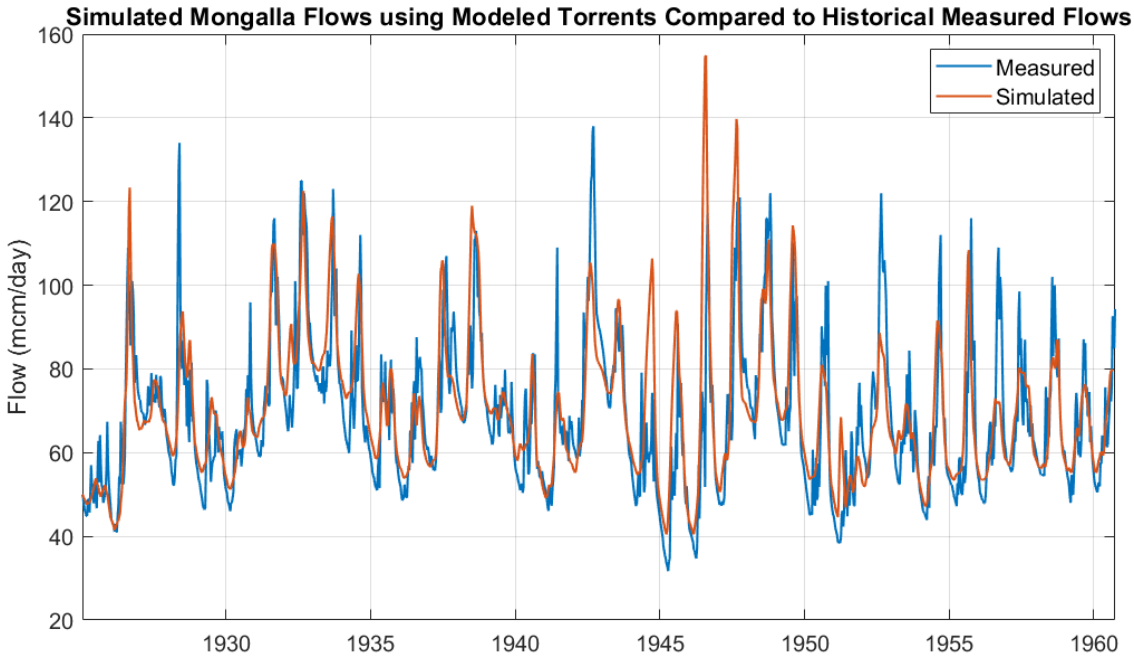

Figure 53: Simulated Mongalla flows when using the Torrents flows produced by the rainfall-runoff model instead of the measured Torrents flows.

The more realistic performance metrics for the Mongalla flow model can be used to assess the uncertainty of Mongalla flows simulated for the 2000 to 2015 period. Figure 53 shows that the model errors tend to be greater during peak flows. Therefore, the magnitude of the uncertainty likely varies seasonally. To explore the temporal dependence of the model errors, the full time series of the measured and modeled flows from 1925 to 1960 were partitioned by month. Figure 54 presents estimates of the monthly error distributions, in terms of the means and standard deviations. Figure 55 provides histogram plots for each distribution. The errors were calculated by subtracting the measured flows from the modeled flows, so values greater than zero indicate that the model overestimated the flow. Although the monthly mean errors are not exactly zero, the distributions appear to follow the normal distribution, and the deviations of the means from zero are not very

substantial. If the error distributions are assumed to be normally distributed, then the first and second standard deviations bracket the 68% and 95% confidence intervals, respectively. Note that the largest variances and biases (from 0) occur during months with heavier rainfall. This result reflects the previously stated observation that the errors in the Torrents flows are more significant during the heavier parts of the rainy season. While a portion of the model errors can be attributed to the regression models used to gap-fill the Laropi flows, the errors from the Torrents rainfall-runoff model are much more significant and dominate the uncertainty of the Mongalla flows.

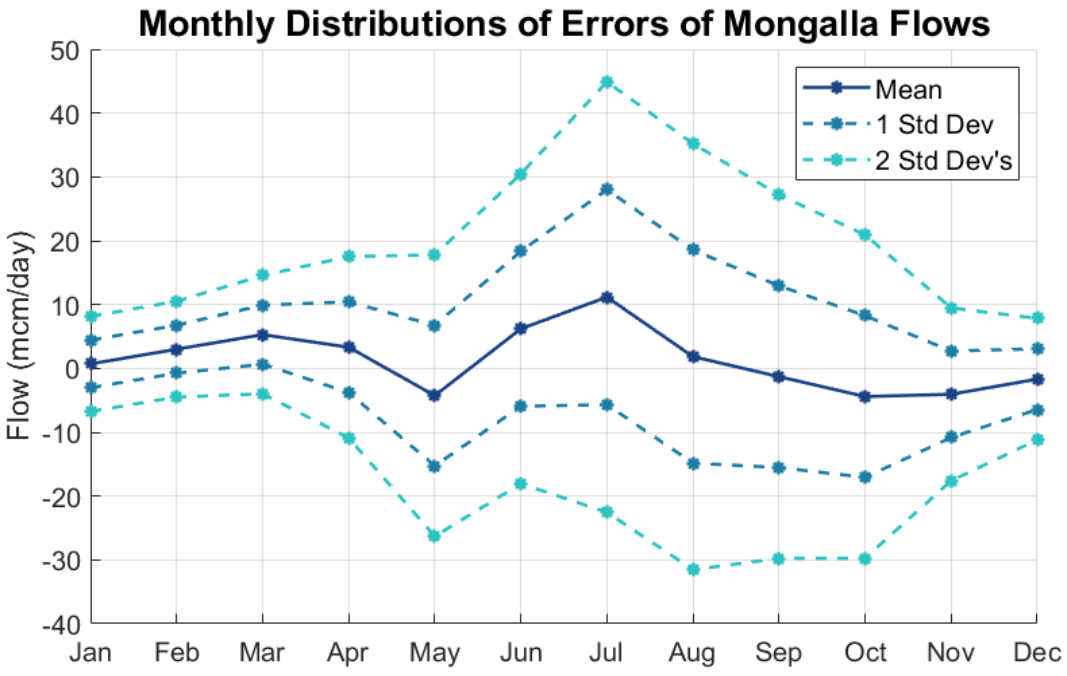

Figure 54: Monthly error distributions of Mongalla flows, estimated from the differences in measured and modeled Mongalla flows from 1925 to 1960.

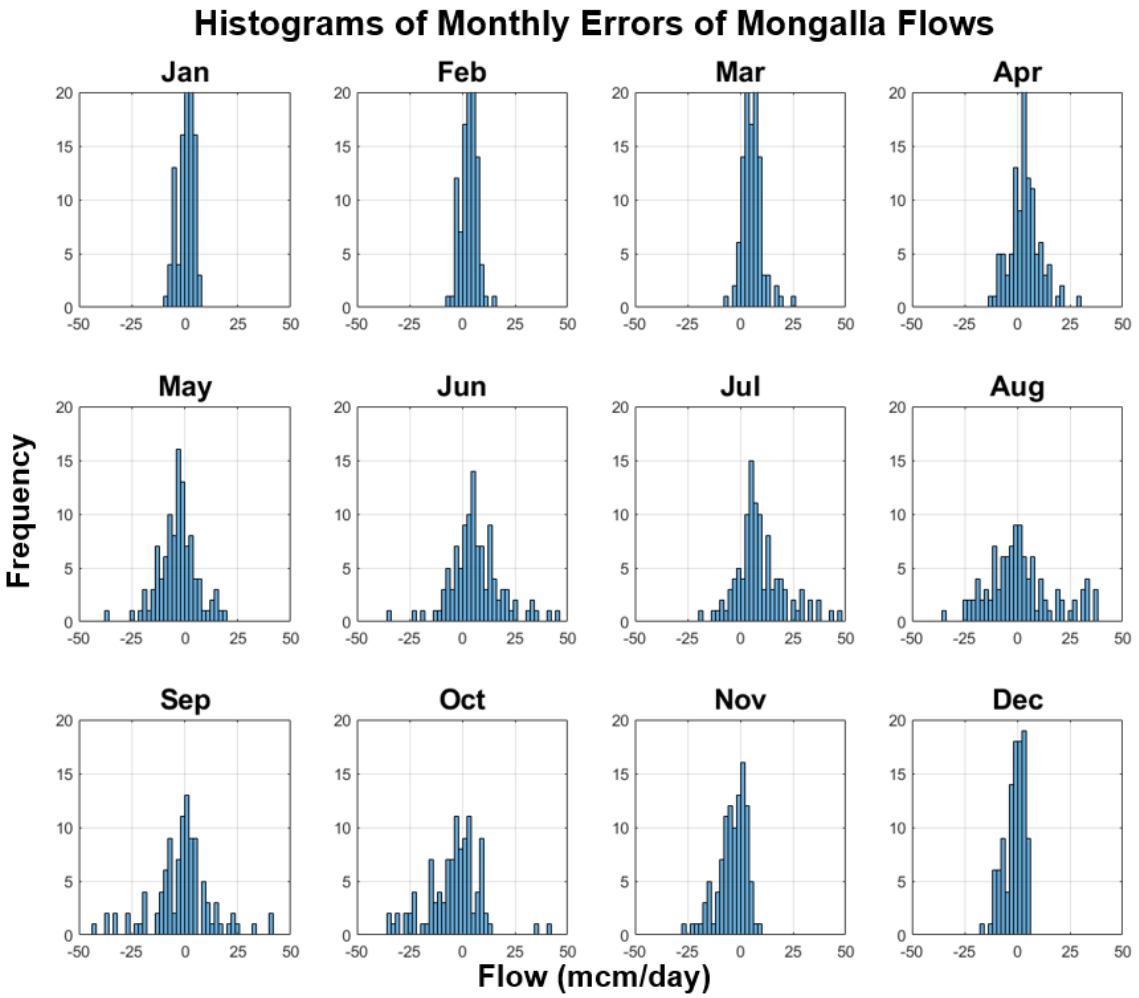

Figure 55: Histogram plots of monthly error distributions for modeled Mongalla flows, estimated from the 1925 to 1960 records.

Finally, the flows at Mongalla can be simulated for the 2000 to 2015 period by using the flows at Laropi (instead of Nimule) and the Torrents flows produced from the hydrologic rainfall-runoff model. Because an autoregressive model is being applied, the initial value of the Mongalla flows had to be specified to initiate the simulation. This initial value was calculated by simply adding the flow at Laropi and the Torrents inflow for the

first time step. The resulting simulated Mongalla flows are shown in Figure 56 and will be used as the Sudd inflows for the hydrologic model development.

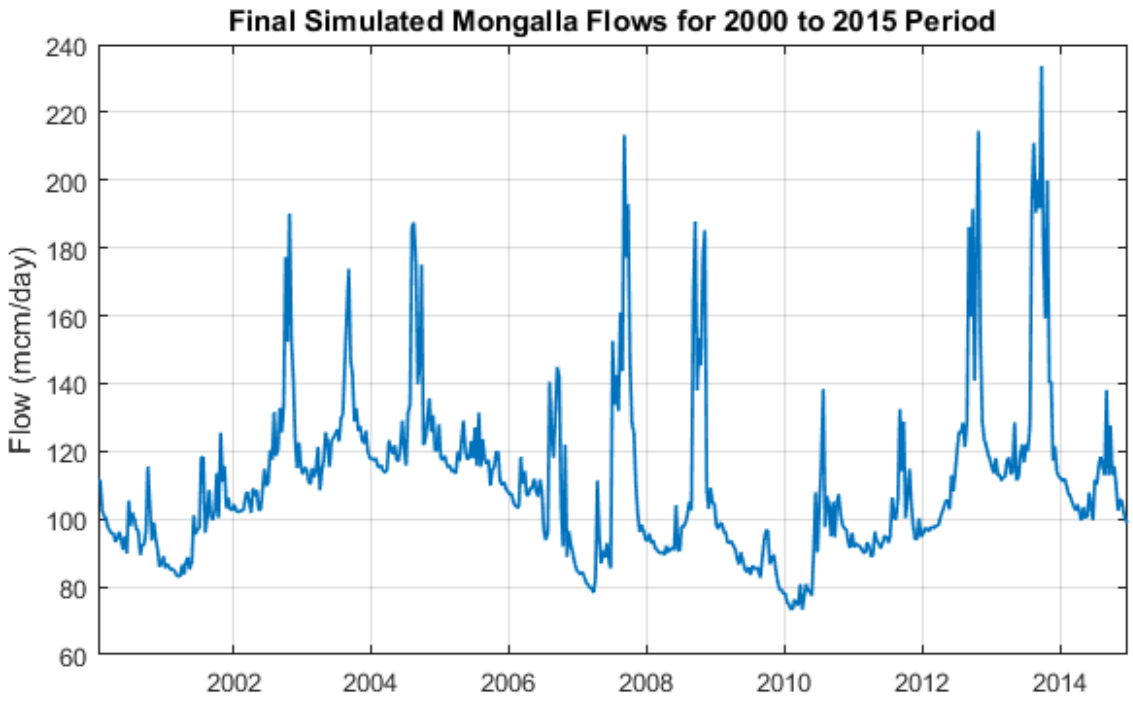

Figure 56: Final simulated Mongalla flows for 2000 to 2015 period using flows at Laropi instead of Nimule. These are the Sudd inflows that will be used to develop the hydrologic model.

The monthly error distributions from Figure 54 were applied to the simulated Mongalla inflows for the 2000 to 2015 period to assess the uncertainty of the estimated inflows. Figure 57 presents the monthly Mongalla flows (in units of billion cubic meters per month) with the monthly error standard deviations applied to represent the uncertainty of the inflow estimates. The uncertainty analysis is important for applications of a hydrologic model of the Sudd because it enables simulations of ensemble inflow time series. These ensembles will demonstrate how the uncertainty of the Sudd inflows propagates through the final hydrologic model.

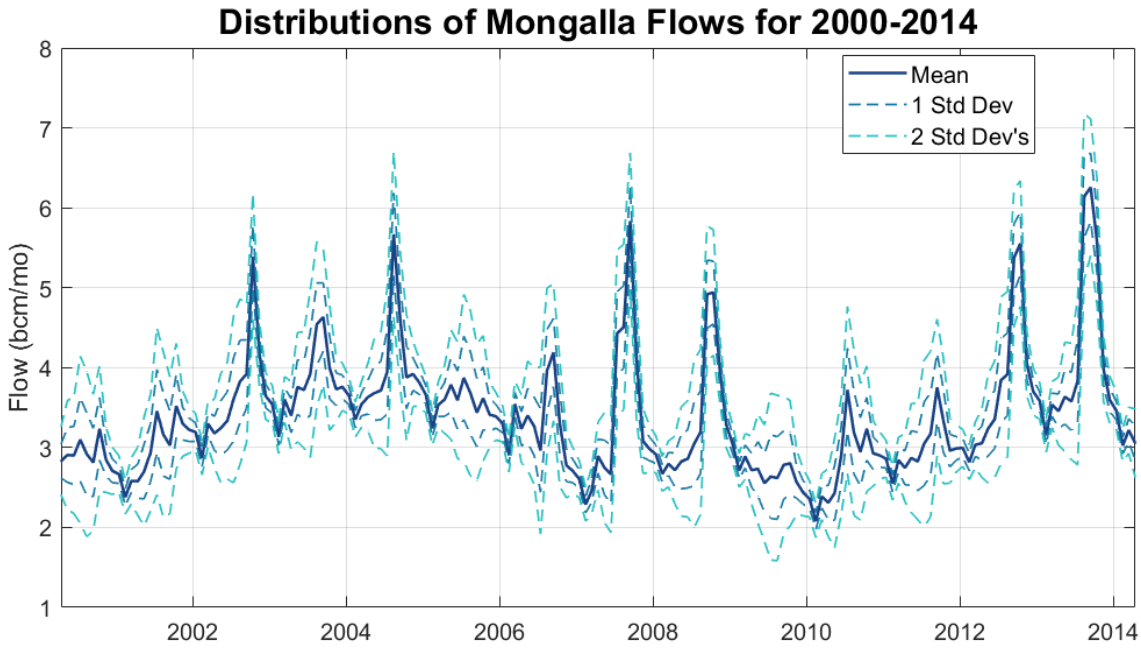

Figure 57: Monthly Mongalla flows from 2000 to 2015, with monthly error standard deviations applied to depict the magnitude of uncertainty.

4.5.4 Estimation of Sudd Outflows from Malakal

As discussed in Section 4.2.3, the measured Sobat River flows can be subtracted from the measured Nile River flows at Malakal to obtain the Sudd outflows. The full historical record of the Sobat, Malakal, and Sudd exit flows were shown in Figure 39 for the 1905 to 1984 time period. Measured flows at Malakal were obtained for 2000 to 2011 (Figure 35); however, Sobat River flows have not been measured for this same time period. Therefore, in order to estimate the Sudd outflows during the 2000 – 2011 period, the Sobat flows first need to be estimated. The scatter plot shown in Figure 58 shows that there is a significant linear correlation between the Sobat and Malakal flows, suggesting that the Malakal flows could be used to estimate the Sobat flows. The Pearson's correlation coefficient for the full record is 0.856. If the data is split before and after the increase in

flows that occurred in the early 1960's, also shown in Figure 58, then there appears to be two different relationships. The period after the 1960's is more representative of the 2000 to 2011 period for which the Sudd outflows need to be estimated.

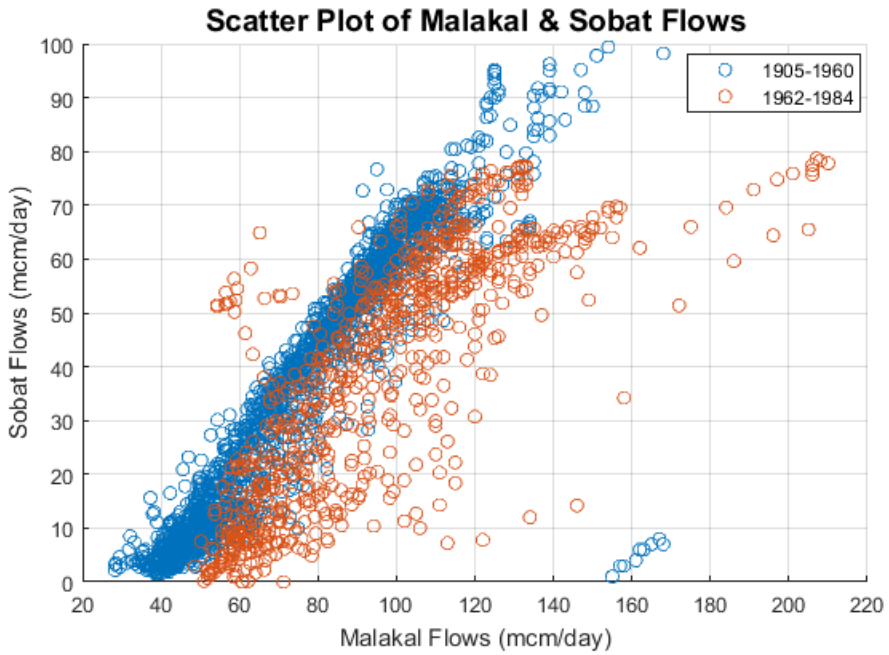

Figure 58: Scatter plot between historical Sobat and Malakal flows, split before and after the early 1960's.

A comparison of the historical Malakal and Sobat flows for the 1962 to 1984 period, presented in Figure 59, shows that the Sobat flow record after 1981 (where there is a data gap) is somewhat irregular. Additionally, 1965 appears to be an outlier year, where the hydrology of the Nile is likely in a transition period due to the increased upstream flows. Figure 60 presents a scatter plot of the historical flow records isolated to the 1966 to 1980 period. This portion of the flow record appears to have a stronger relationship and a more significant Pearson's linear correlation coefficient (0.91) and will be used to calibrate a model for the Sobat flows.

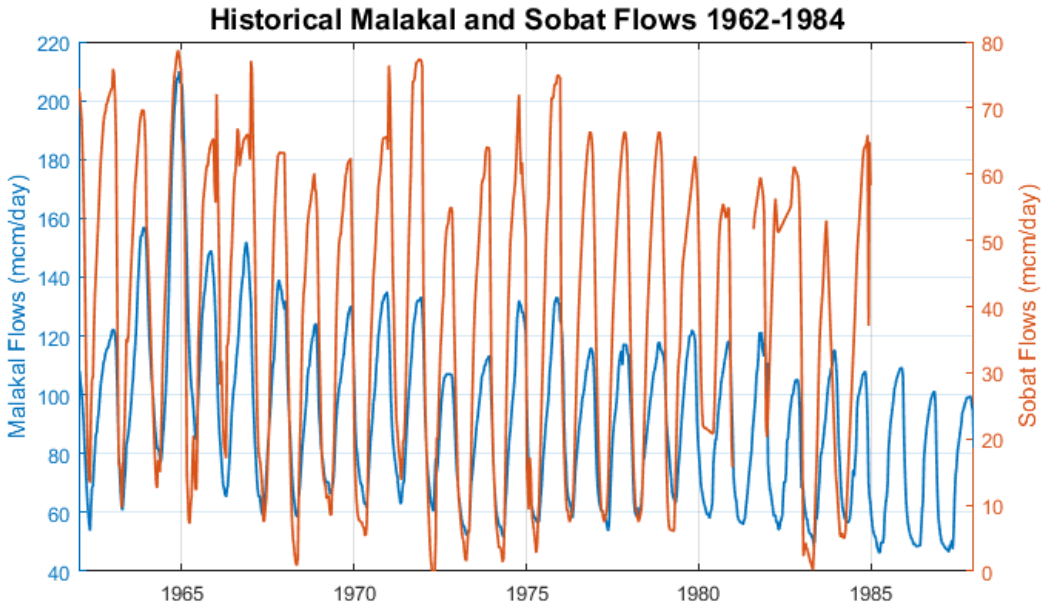

Figure 59: Time series of historical Sobat and Malakal flows for 1962 to 1984 period.

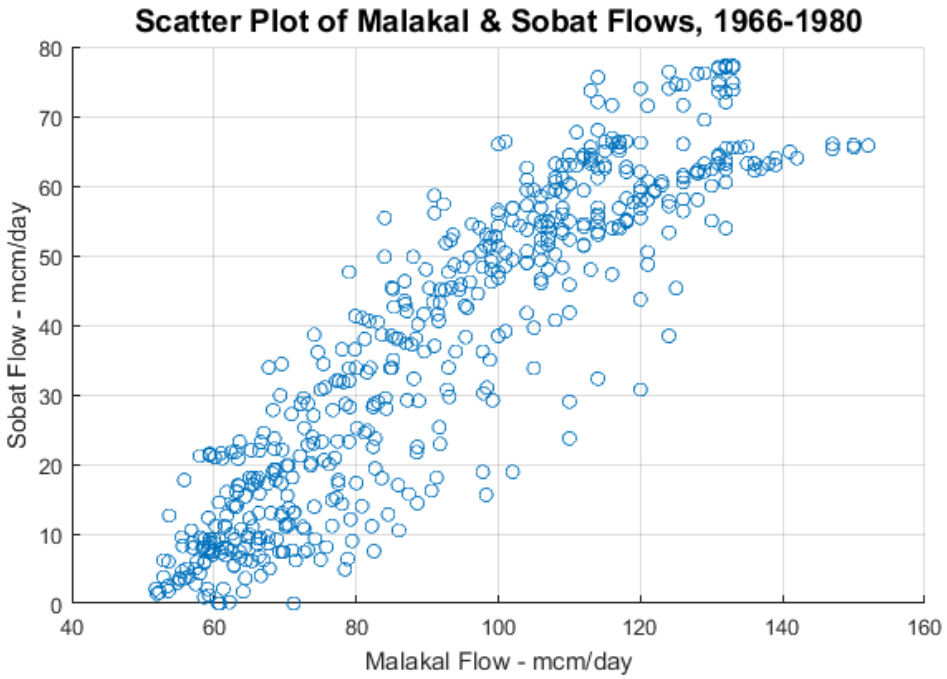

Figure 60: Scatter plot comparing Malakal and Sobat flows for the 1966 to 1980 period.

In addition to the Malakal flows, the Sobat hydrologic fluxes – the precipitation and ET – should help predict the Sobat flows. Historical monthly precipitation and ET from the CRU database were downloaded and clipped to the Sobat sub-basin (see Figure 32 for sub-basin outline). The Sobat River drains an area of approximately 214,000 square kilometers and has wetland areas that store water. Therefore, there is likely a lag between precipitation and ET rates over the sub-basin and outflows. The highest linear correlation coefficients were found between the Sobat flows and the hydrologic fluxes when a two and three month lag was applied. Figure 61 displays scatter plots of the Sobat flows and precipitation, ET, and Precipitation minus ET for both temporal lags and lists the corresponding correlation coefficients. This result suggests that a model for the Sobat River outflows should include the precipitation and ET fluxes at both two and three month lags.

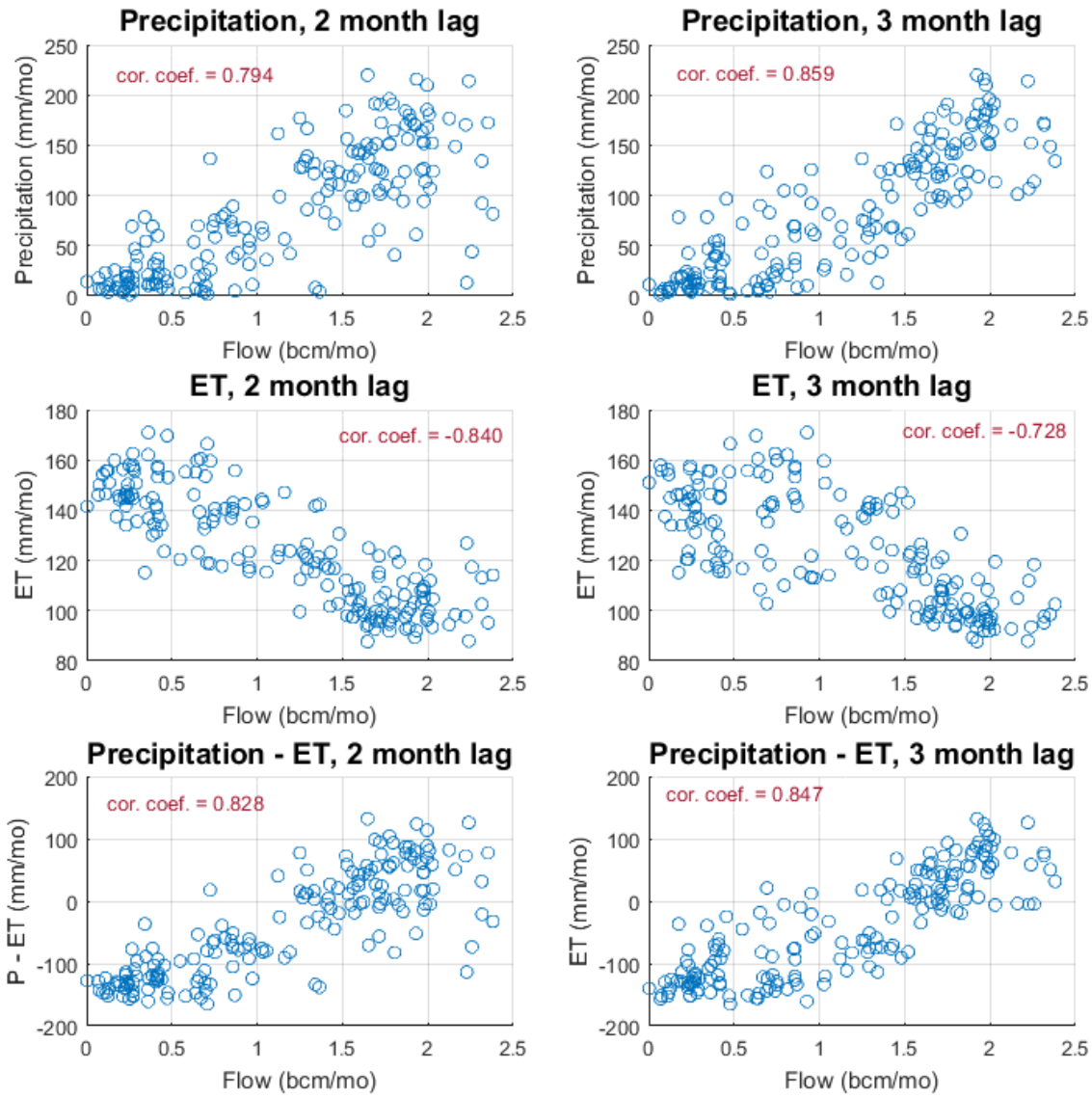

Figure 61: Scatter plots between monthly Sobat flows and monthly CRU precipitation and evapotranspiration (ET) fluxes. The left column plots have a temporal lag of 2 months, and the right column plots have a temporal lag of 3 months. The Pearson's correlation coefficient between the time series used in each scatter plot is shown in red on the each plot.

A model for the Sobat flows that depends on the Malakal flows and all hydrologic fluxes shown in Figure 61 for the 1966 to 1980 period is displayed in Equation 38, where flow units are in billion cubic meters (bcm) per month, and the precipitation and ET rates

are in meters/month. This model has an r^2 value of 0.858 and a RMSE of 0.26 bcm/month. The Malakal flows and the precipitation term with the two month lag have p-values less than 0.05, but the remaining p-values range from 0.14 to 0.22.

$$Q_{SOB}(k) = -0.58862 + 0.59141Q_{MAL}(k) + 1.3607P_{SOB}(k-2) - 3.7532ET_{SOB}(k-2) + 1.4177P_{SOB}(k-3) + 2.4458ET_{SOB}(k-2) + \varepsilon(k) \quad [38]$$

where:

Q_{SOB} = *Sobat flows (bcm/month)*
Q_{MAL} = *Malakal flows (bcm/month)*
P_{SOB} = *Monthly mean precipitation in Sobat basin (m/month)*
ET_{SOB} = *Monthly mean ET in Sobat basin (m/month)*

A variety of modifications to Equation 38 were attempted, including a model based on the monthly anomalies of the flows and fluxes, and the model chosen to move forward with in this analysis (Equation 39) is relatively simple and relies on the Malakal flows and precipitation terms only. Again, the units of flow are bcm/month and the units of precipitation are m/month. This model has an r^2 value of 0.856, the RMSE is again 0.26 bcm/month, and all of the terms have relatively low p-values. A scatter plot comparing the measured and fitted Sobat flows and the time series of residuals is shown in Figure 62, and a comparison of the historical record and the fitted Sobat flows is shown in Figure 63. The correlation coefficient between the measured and fitted Sobat flows is 0.925. The lag-1 autocorrelation of the residuals is 0.641; however, there does not appear to be a significant trend in the residuals.

$$Q_{SOB}(k) = -0.79455 + 0.58766Q_{MAL}(k) + 2.1549P_{SOB}(k-2)$$

$$+ 1.2675P_{SOB}(k-3) \ + \varepsilon(k) \qquad [39]$$

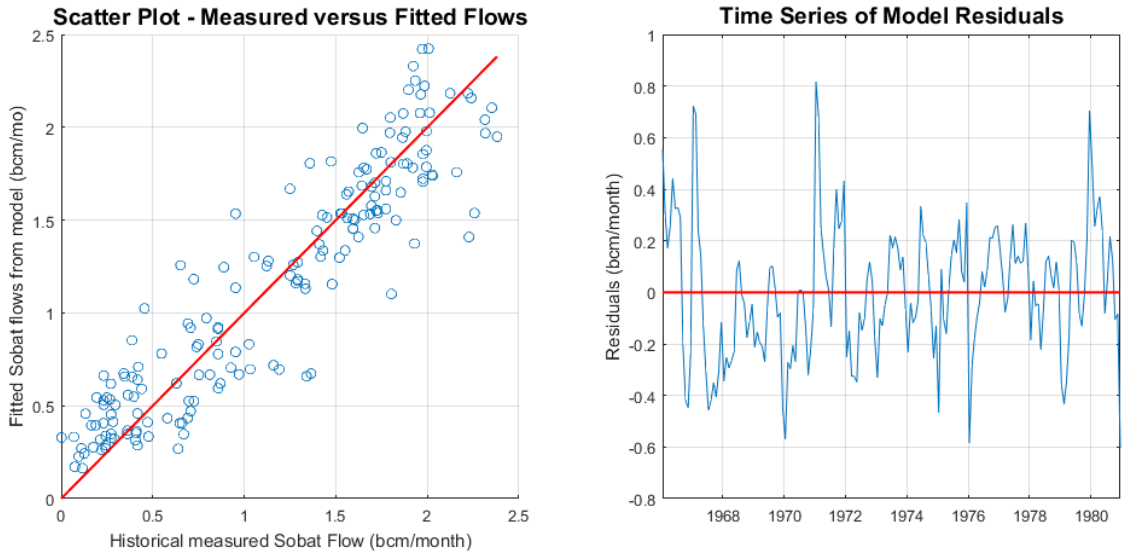

Figure 62: Scatter plot comparing measured and fitted Sobat flows and time series of model residuals for the statistical model of the Sobat flows during the 1966 to 1980 period.

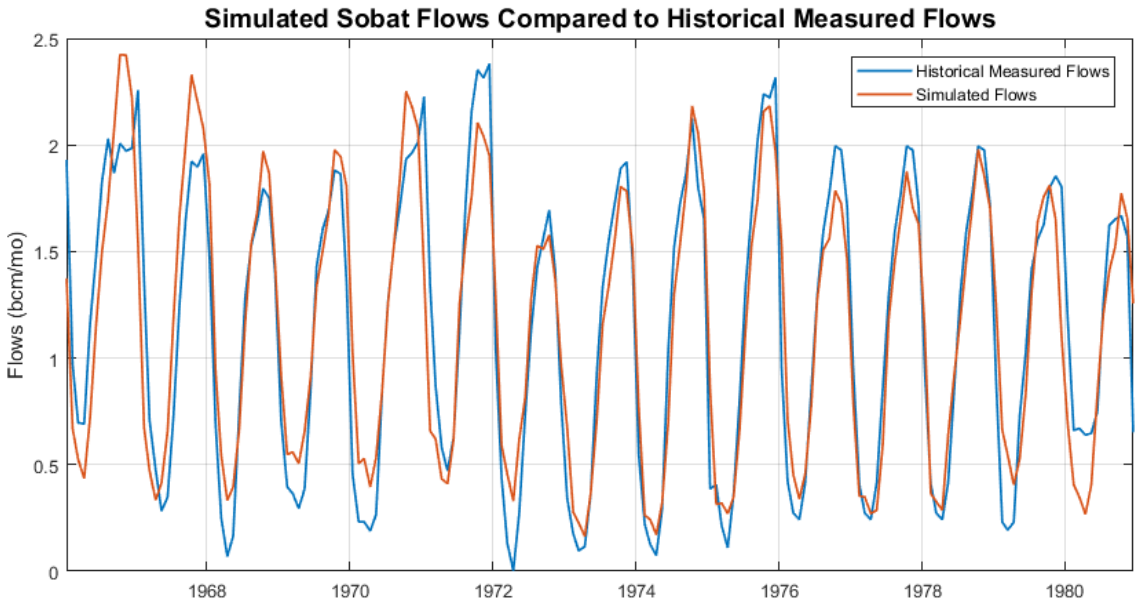

Figure 63: Time series comparison of historical measured and modeled Sobat flows for the 1966 to 1980 period.

To assess this simple Sobat flow model in terms of its utility in simulating the Sudd outflows, the modeled Sobat flows can be used to model the historical Sudd outflows by subtracting them from the measured historical Malakal flows. The simulated Sudd outflows are compared to the historical outflows in Figure 64. The monthly mean standard deviations were obtained from the differences between the two time series and added/subtracted from the simulated outflows to represent error bounds. The modeled Sudd outflows typically miss the extreme values, often by a magnitude larger than that of the monthly standard deviation, which represents the 68% confidence interval if the errors are normally distributed.

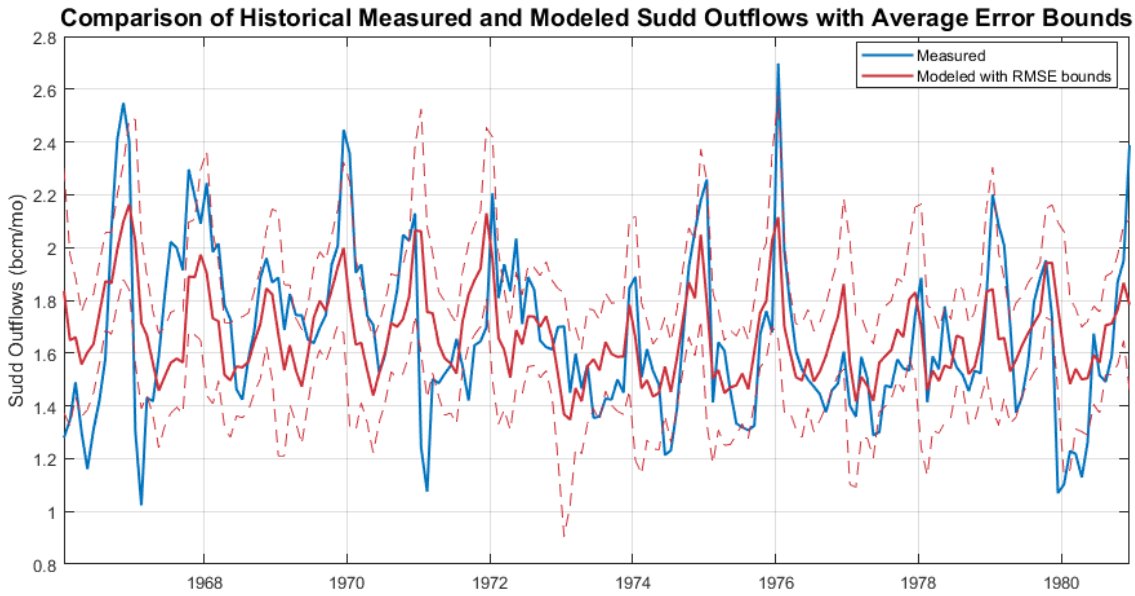

Figure 64: Comparison of measured and simulated Sudd outflows using Sobat modeled flows and measured Malakal flows. The error bounds on the modeled flows were calculated by adding and subtracting the monthly mean standard deviations.

The Sobat flow model derived in this section has acceptable performance metrics; however, when the estimated Sobat flows are subtracted from the Malakal flows, the errors between the measured and simulated Sudd outflows are significant. Despite the uncertainty of the estimated Sudd outflows using the in-situ Malakal flows and the Sobat model, the Sudd outflows have been estimated for the 2000 to 2011 period and are displayed in Figure 65. The time series lacks a distinct seasonal trend and has limited inter-annual variation. A more complex, physically based rainfall-runoff model for the Sobat basin could be developed in an attempt to improve the Sudd outflows, but would be challenging considering the lack of data and in-situ observations in this region. Additionally, this region is relatively flat and has a complex hydrologic balance, similar to the Sudd. Therefore, developing an entirely separate model for the Sobat basin is beyond the scope of this

research and is unlikely to result in a significant improvement with regards to modeling the Sudd.

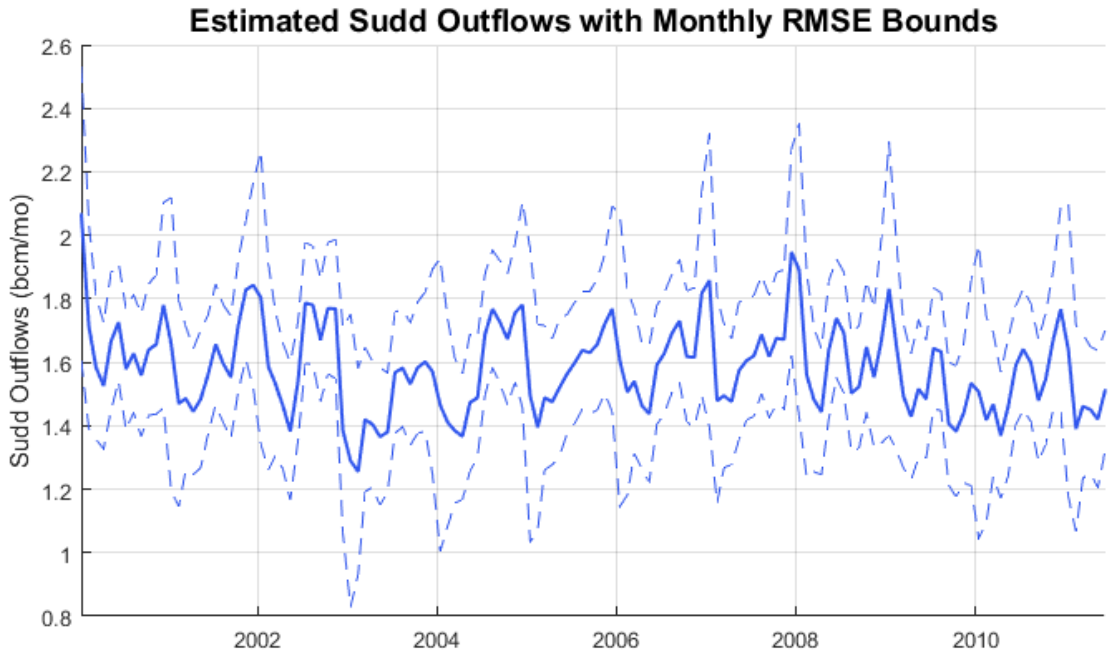

Figure 65: Estimated Sudd outflows for 2000 to 2011 using the in-situ Malakal flows and the Sobat regression model. The upper and lower bounds represent the monthly RMSE.

4.5.5 Estimation of Sudd Outflows from Mongalla

Due to the uncertainty of the Sudd outflows estimated in Section 4.3.4, an alternative approach was also explored. Section 2.3.2 presented a statistical autoregressive model that is used in the Nile DST to estimate the losses in the Sudd. This model, shown again here for convenience (Equation 6), estimates the losses in the Sudd as a function of the inflows at Mongalla and the losses in the previous time step.

$$Q_{LSS}(k) = 0.9923Q_{MON}(k) - 0.9522Q_{MON}(k-1) + 0.9435Q_{LSS}(k-1) - 1.0379 + \varepsilon(k) \quad [6]$$

where:

$Q_{LSS}(k)$ = *Sudd losses at time k (mcm/day)*
$Q_{MON}(k)$ = *Sudd inflows at time k (mcm/day)*
$\varepsilon(k)$ = *error at time (mcm/day)*

A scatter plot comparing the historical measured Mongalla flows to the Sudd losses (calculated by subtracting the historical outflows from the inflows) is presented in Figure 66. Similar to the analysis of the Sobat and Malakal flows presented in Section 4.3.4, there appears to be two different relationships before and after the increase in flows that occurred in the 1960's. Again, the outlier points correspond to 1965, when the region was transitioning to the higher flow regime. Therefore, Equation 6 was recalibrated using the 1966 – 1980 period only to be more representative of the current relationship between the inflows and losses. The modified relationship is presented in Equation 40. This model has an r^2 value of 0.97, a RMSE of 3.98 mcm/day, and all terms have p-values close to zero. A scatter plot comparing the measured and modeled Sudd losses in shown in Figure 67, along with the time series of residuals. The lag-1 autocorrelation of the residuals is 0.284.

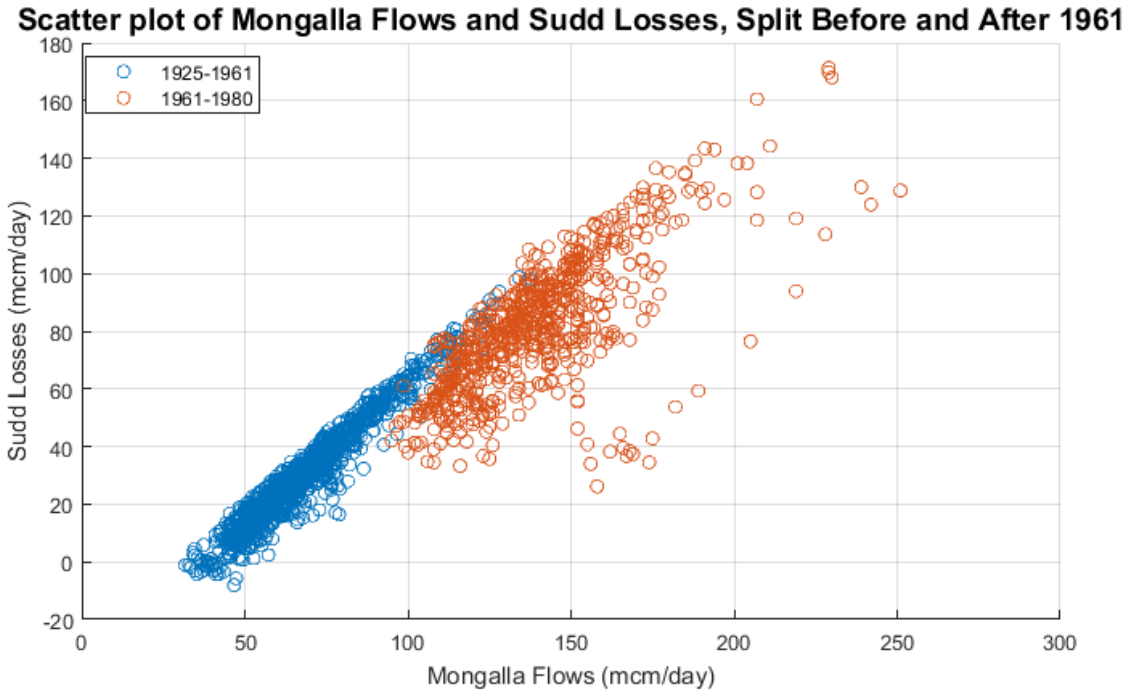

Figure 66: Scatter plot comparing Mongalla inflows to Sudd losses, split into two time periods before and after the 1960's increase in flow.

$$Q_{LSS}(k) = 2.6224 + 0.98756Q_{MON}(k) - 0.97603Q_{MON}(k-1) + 0.94755Q_{LSS}(k-1) + \varepsilon(k) \quad [40]$$

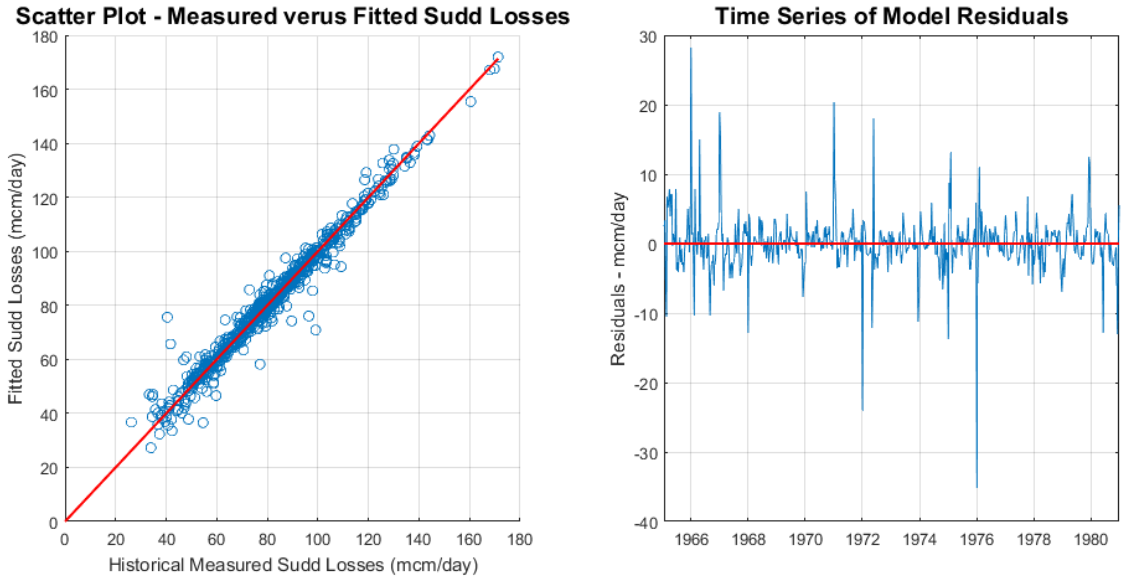

Figure 67: Scatter plot comparing measured and fitted Sudd losses for 1965 - 1980 period and time series of model residuals.

To obtain a more representative estimate of the model error, the Sudd losses should be simulated without using the historical measured flows. The resulting time series of the simulated Sudd losses is compared to the measured losses in Figure 68. The Pearson's correlation coefficient between the fitted and observed time series is 0.980, and the RMSE is 4.0783 mcm/day. The RMSE is very low compared to the magnitude of the Sudd losses.

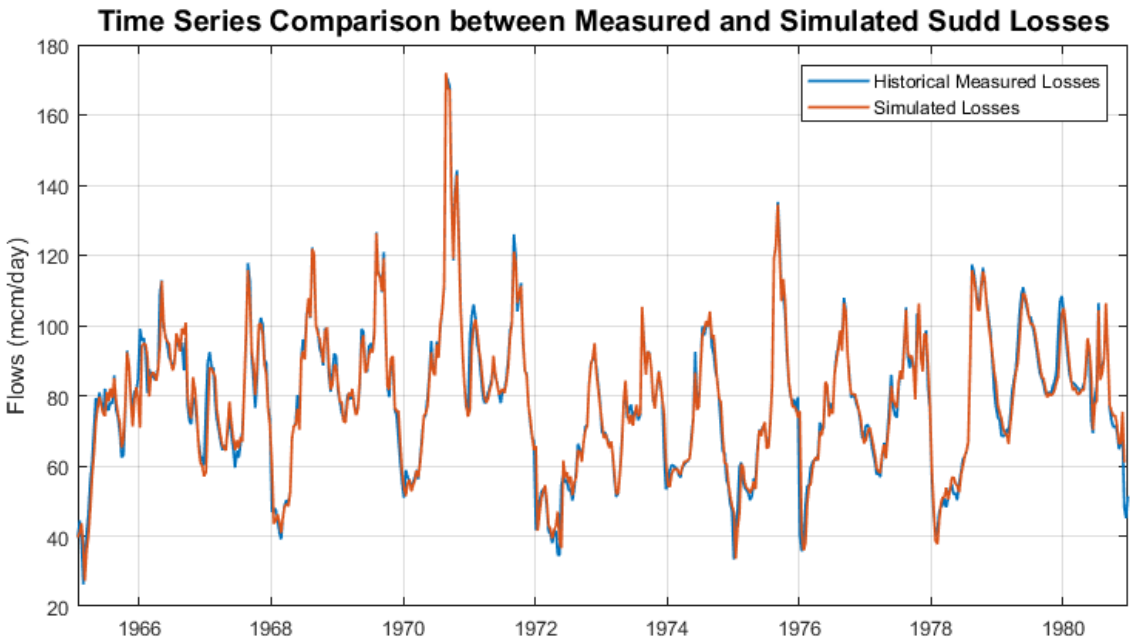

Figure 68: Time series comparison between the historical measured losses of the Sudd and the simulated losses using the autoregressive model, for the 1966 to 1980 period.

Section 4.5.4 discussed and demonstrated the impact of using the modeled Torrents flows instead of the Torrents provided by the Egyptian Ministry. The modeled Torrents flows also impacts the estimation of the Sudd losses, because the losses depend on the Mongalla flow estimates. Therefore, an uncertainty analysis similar to that of Section 4.5.4 should be completed for the Sudd losses. However, the flows at Nimule are available only until 1960, and the Mongalla flows therefore cannot be simulated for the 1966 to 1980 period that was used to calibrate Equation 40. To complete the uncertainty assessment despite this limitation, an additional model (Equation 41) for the Sudd losses was calibrated using data from 1925 to 1960, when the Nimule flows are available. The r^2 of this model is 0.99, and the RMSE is 1.81 mcm/day. The slight improvement in the performance metrics compared to the model presented in Equation 40 results from the hydrodynamics

of the Sudd changing after the 1960's, when the wetland approximately doubled in size. Therefore, the uncertainty assessment from this model will slightly underestimate the true uncertainty when applied to the 2000 to 2015 period.

$$Q_{LSS}(k) = -2.92728 + 0.99996Q_{MON}(k) - 0.915221Q_{MON}(k-1) + 0.905630Q_{LSS}(k-1) + \varepsilon(k) \quad [41]$$

The Mongalla flows produced from the modeled Torrents flows (using the rainfall-runoff model) were subsequently applied to the Sudd loss model (Equation 41), and the losses were simulated without using the measured losses for the previous time step. The resulting simulated losses are shown in Figure 69 and compared to the measured losses obtained from the Nile Basin Volumes. The correlation coefficient between the time series is 0.739, and the RMSE is 12.56 mcm/day.

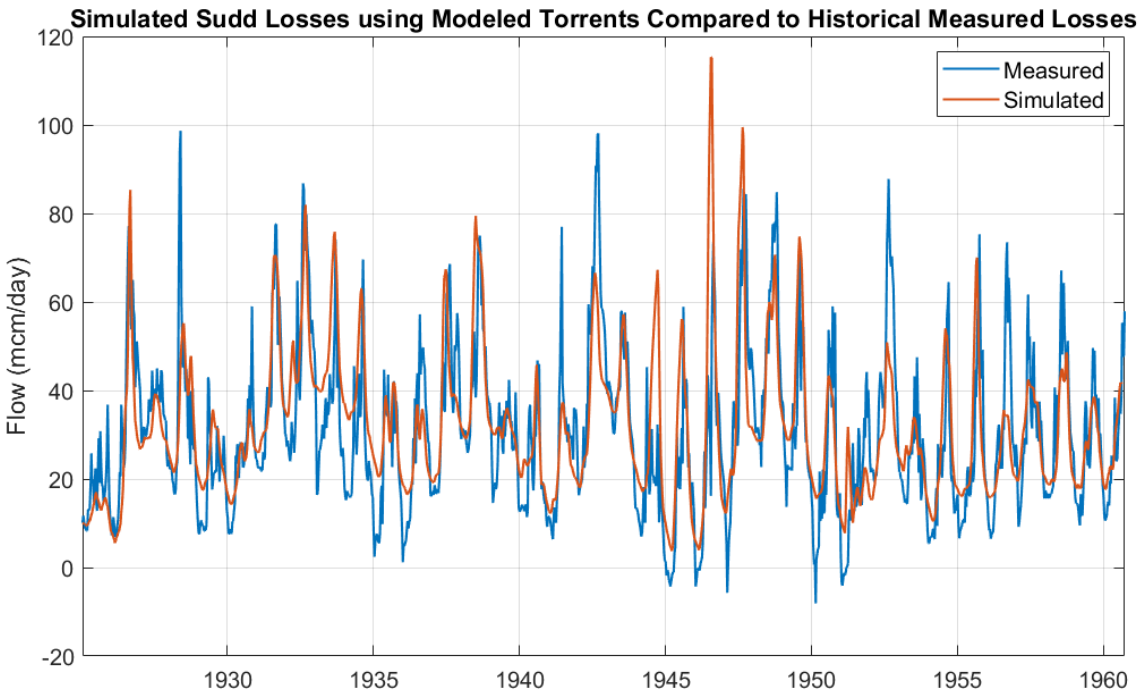

Figure 69: Simulated Sudd losses using autoregressive model from Equation 41. The Mongalla flows used in this model were obtained using the Torrents flows simulated from the rainfall-runoff model.

The model errors shown in Figure 69 can be used to assess the uncertainty of the Sudd losses estimated for the 2000 to 2015 period. The monthly mean errors and the first and second standard deviations are shown in Figure 70, and histogram plots of the error distributions are shown in Figure 71. Similar to the inflow errors, these distributions are approximately normally distributed around zero, and the bias and variance are greater during the rainy season.

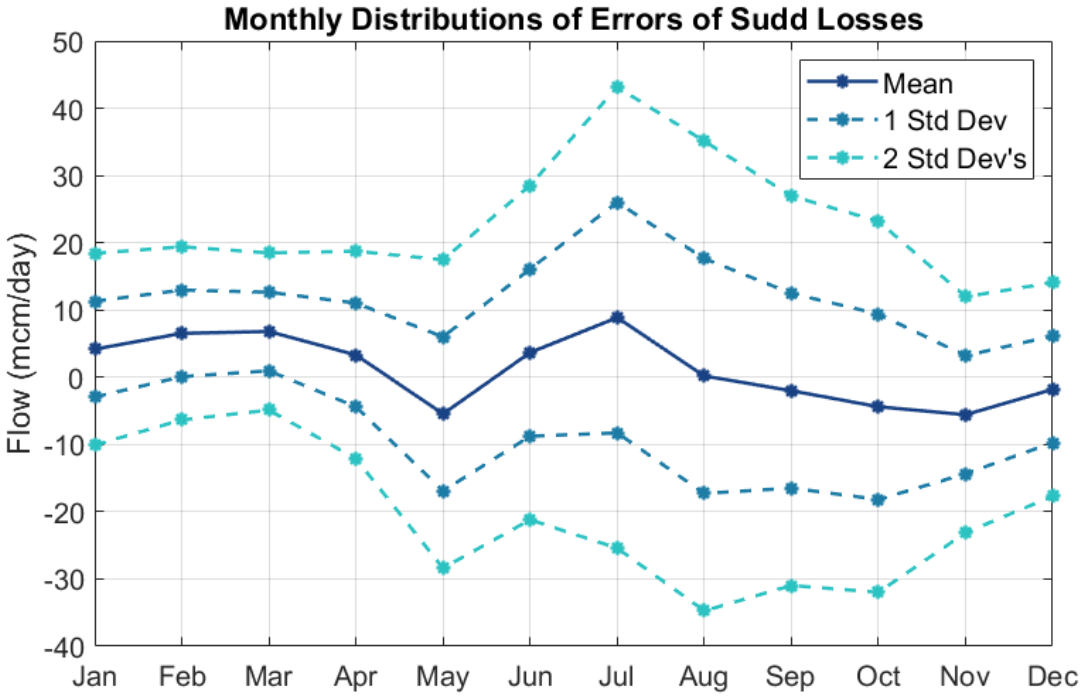

Figure 70: Monthly distributions of errors estimated by comparing the simulated losses to the difference in inflows and outflows provided in the Nile Basin Volumes, using data from 1920 to 1965.

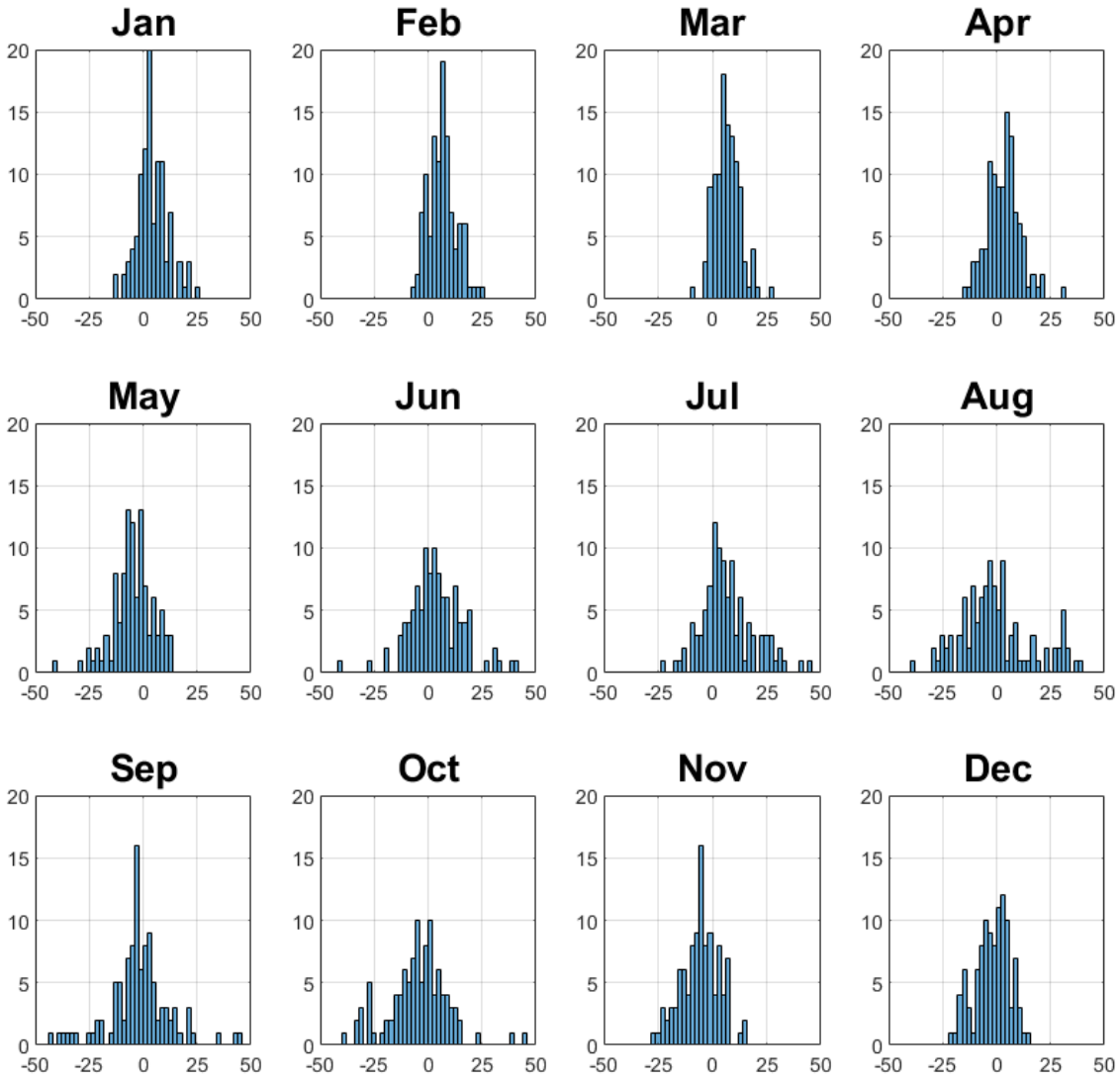

Figure 71: Histogram plots of monthly error distributions for modeled Sudd losses, estimated from the 1925 to 1960 records.

The 10-day Sudd losses can now be simulated for the 2000 – 2015 period that is of interest for the hydrologic model. Again, because this is an autoregressive model, the first value of the Sudd losses had to be estimated to initiate the simulation. Therefore, the Sudd outflow in Jan. 2000 estimated in Section 4.3.4 (using Sobat and Malakal flows) was

subtracted from the Mongalla inflow for Jan. 2000. The final simulated Sudd Losses are presented in Figure 72.

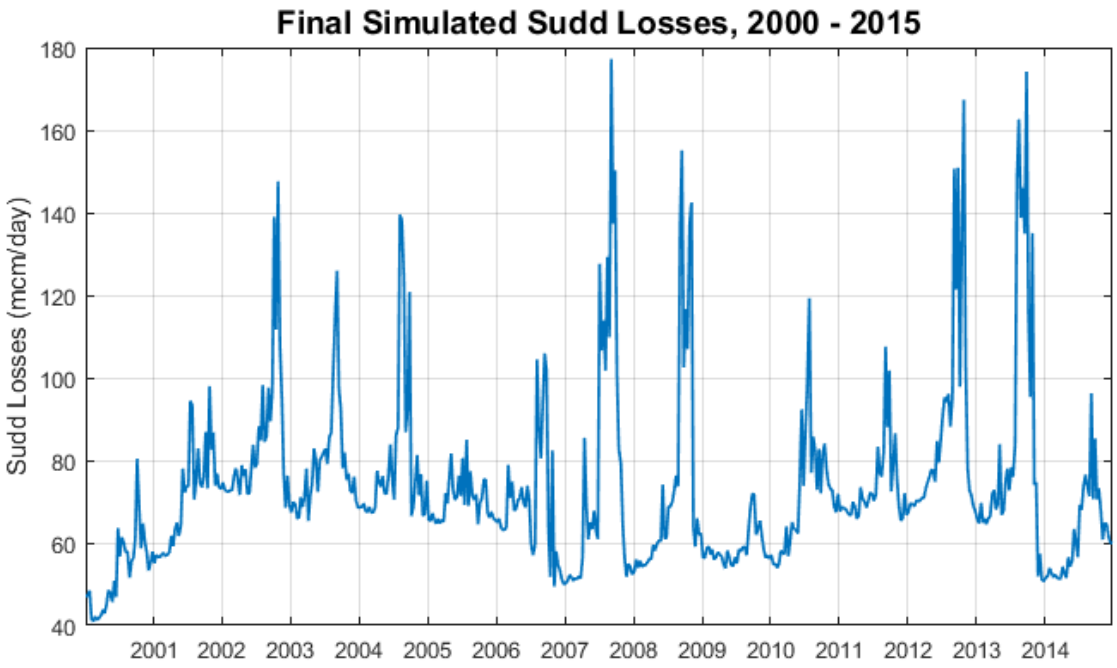

Figure 72: Final 10-day simulated Sudd losses for the 2000 to 2015 period.

The 10-day losses were then aggregated to monthly flows, and the error standard deviations from Figure 70 were added and subtracted to evaluate the uncertainty of the losses. The Monthly mean flows and their distributions are presented in Figure 73.

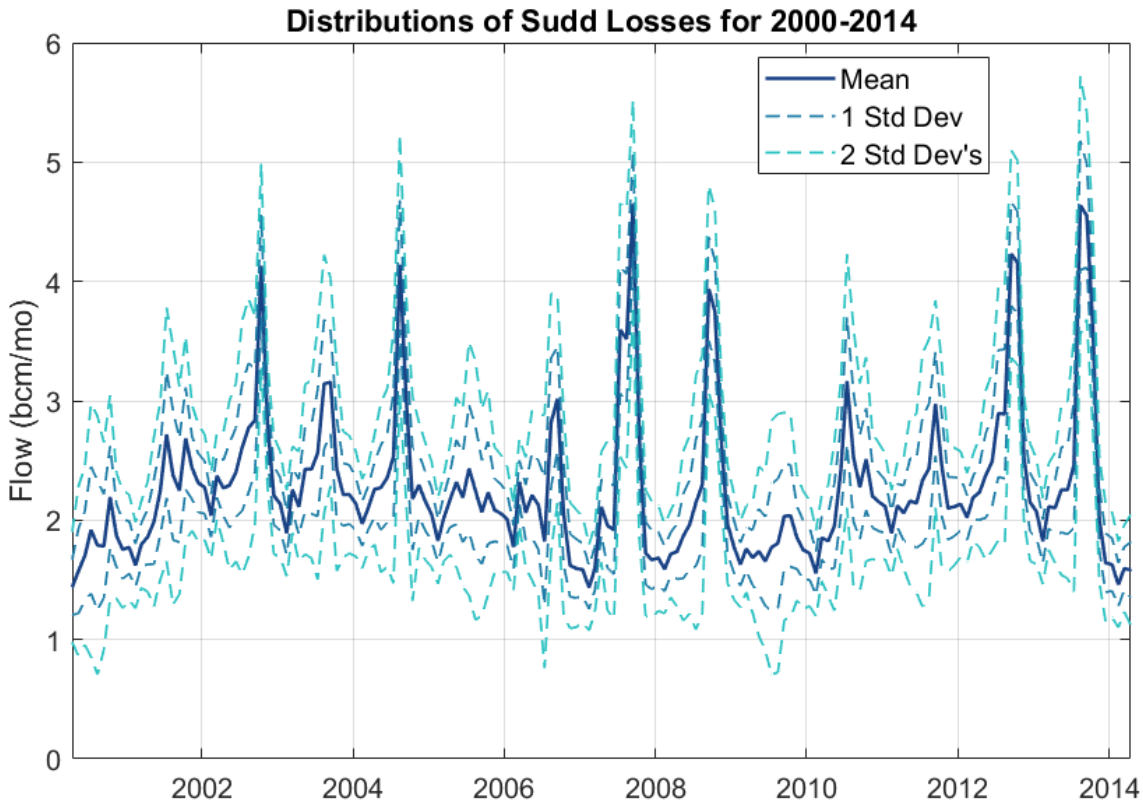

Figure 73: Monthly Sudd losses from 2000 to 2014, with standard deviations from estimated error distributions to evaluate the uncertainty of the losses.

Finally, the monthly outflows from the Sudd can be estimated by simply subtracting the Sudd losses from the inflows. The monthly Sudd outflows and inflows are compared in Figure 74. This comparison shows the extent to which the wetland attenuates the Nile flows. The uncertainty of the outflows can be determined analytically using the monthly error estimates of the inflows and losses and Equation 42.

$$Var[Q_{OUT}] = Var[Q_{MON} - Q_{LSS}] = Var[Q_{MON}] + Var[Q_{LSS}] - 2Cov[Q_{MON}, Q_{LSS}] = \sigma^2_{Qmon} + \sigma^2_{Qlss} - 2\rho_{Qmon,Qlss}\sigma_{Qmon}\sigma_{Qlss} \quad [42]$$

The correlation coefficient between the inflows and losses ($\rho_{Qmon,Qlss}$) was assumed not to vary seasonally and was found to be 0.939 when calculated from the monthly mean inflows and losses. The magnitude of the correlation is not surprising considering the dependency of the autoregressive loss model on the inflows at Mongalla. The resulting monthly mean standard deviations were applied to the estimated outflows and are shown in Figure 75. Similar results would be obtained if the errors were determined empirically, according to the procedure demonstrated with the inflows and losses. The estimated uncertainties of the outflows will be informative when evaluating the performance of the hydrologic model of the Sudd, which will produce outflows using a physically based model.

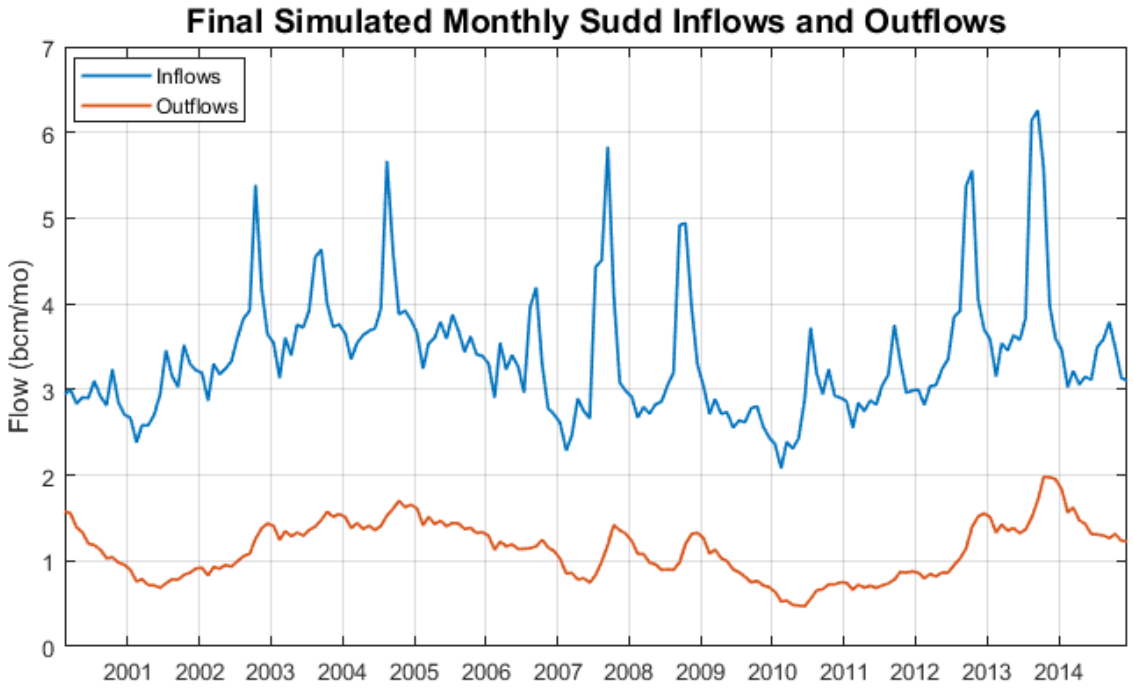

Figure 74: Final simulated monthly Sudd inflows and outflows, in units of billion cubic meters per month, for the 2000 to 2015 period.

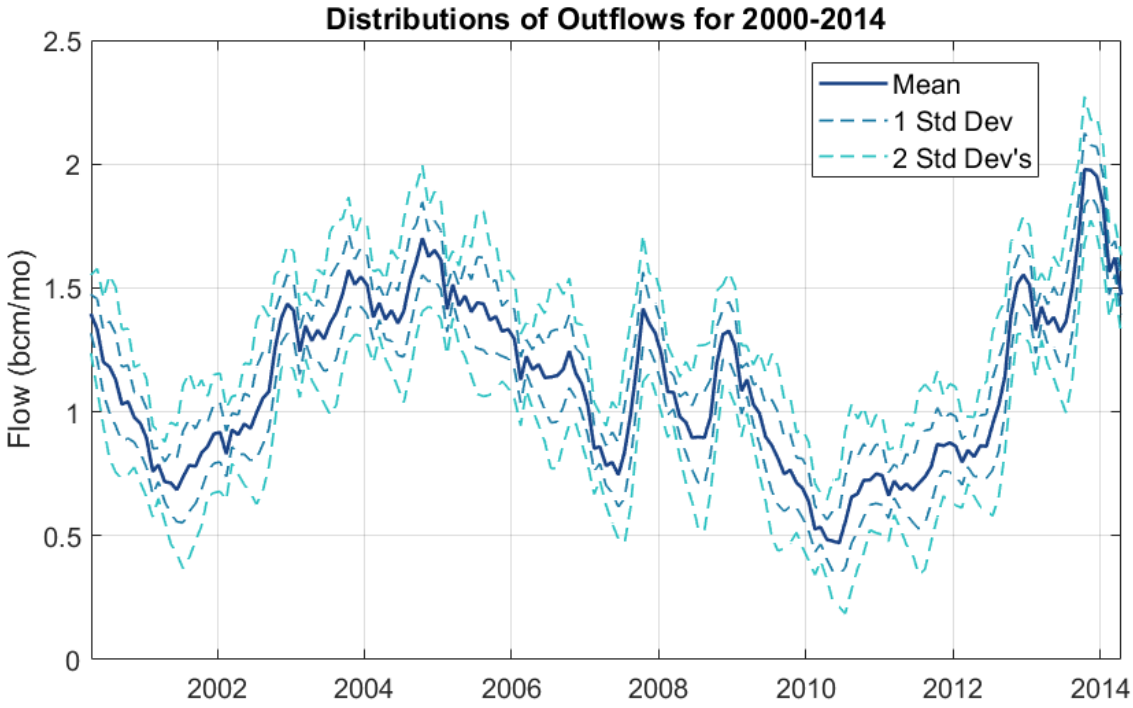

Figure 75: Estimated monthly Sudd outflows calculated from the simulated inflows and losses, with estimated standard deviations of error applied.

CHAPTER 5: CONSISTENCY BETWEEN FLUXES AND MODIS-DERIVED FLOODED AREAS

5.1 Overview

Recall the iterative modeling process outlined in Chapter 1 and Figure 1. The MODIS-derived flooded areas derived in Chapter 3 and the hydrologic fluxes estimated in Chapter 4 should be coherent with one-another and should inform the structure of the hydrologic model. Therefore, prior to identifying a physically based model of the Sudd, these hydrologic variables should first be viewed holistically through an analysis of the overall water budget of the wetland. A more accurate and robust hydrologic model can be developed if input data sources can be selected or adjusted to optimize the consistency between hydrologic processes.

In Section 3.5.3, before the Sudd fluxes and flows were described in detail, a quick comparison was shown between the net water flux in the wetland and the MODIS-derived flooded areas to support the validation of the flood maps. This Chapter includes a more thorough analysis of the relationship between the water balance and the flooded area extents of the Sudd. During this analysis, inconsistencies in the connectivity of the wetland were identified, and a procedure for adjusting the MODIS-derived flood maps was developed and applied. The Chapter concludes with an analysis of the correlation between the adjusted flooded areas and the net water flux for all combinations of the precipitation and ET estimates presented in Chapter 4 to identify the most accurate data sources.

5.2 Comparison of Net Water Flux to MODIS-derived Flooded Areas

Figure 20 from Chapter 3 is shown again here for convenience and compares the time series of net water flux in the Sudd to the MODIS-derived flooded area extents. The net water flux was calculated according to Equation 16 and is also shown again here. The TRMM precipitation and the Sutcliffe and Parks climatology ET estimates were applied to Equation 16. If a 4 month lag is applied to the flooded area extents, there is a correlation coefficient of 0.809 between the net flux and the flooded areas. The high correlation coefficient obtained from this simple representation of the Sudd water balance suggests that the hydrology of the Sudd can be modeled using these key fluxes (flows, precipitation, and ET).

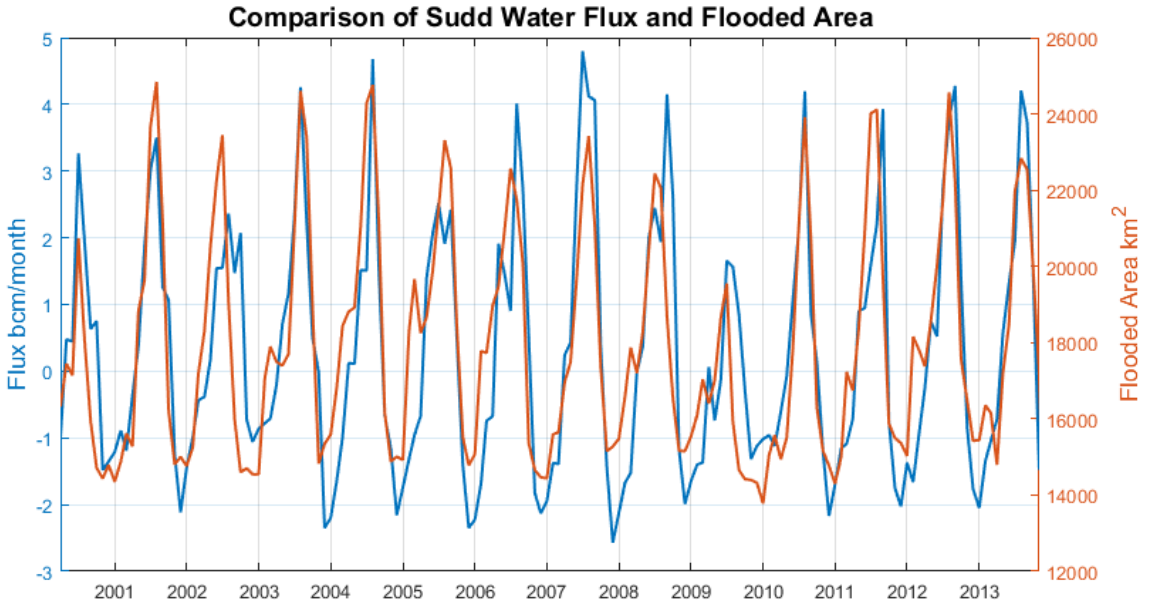

Figure 76: Comparison of time series of monthly sudd water flux and the monthly mean flooded area (estimated from MODIS imagery). The flooded area time series is lagged backwards 4 months to optimize the correlation coefficient between the two time series (0.809).

$$Flux(k) = Q_{IN}(k) - Q_{OUT}(k) + \big(P(k) - ET(k)\big)A(k) \quad [16]$$

where:

Q_{IN} = monthly Sudd inflows (m^3/month)
Q_{OUT} = monthly Sudd outflows (m^3/month)
P = monthly cumulative precipitation (m/month)
ET = monthly evapotranspiration (m/month)
A = monthly mean Sudd flooded area (m^2/month)
k: temporal index

An additional assessment of the consistency between the MODIS-derived flooded area extents and the Sudd flux is to compare the cumulative fluxes and areas on an annual basis. The mild slopes and dense vegetation in the Sudd results in slow travel times, causing the expansion of the wetland to lag behind the period of heavy rainfall and flow. This temporal lag makes direct time series comparisons of the fluxes and flooded areas problematic. However, over the course of an annual cycle, larger flows and heavier rainfall should result in more extensive flooding. Therefore, the annual net fluxes and flooded area extents should be correlated. These annual net fluxes are shown in Figure 77 and were calculated from April to March of the following year since March or April is typically the driest month and the wetland area is close to its minimum extent. The minimum flooded area was subtracted from the flooded area time series to highlight the changes in flooded area as the wet season progresses. Similar to the previous flux calculation, TRMM precipitation and the Sutcliffe and Parks climatology ET estimates were applied to Equation 16.

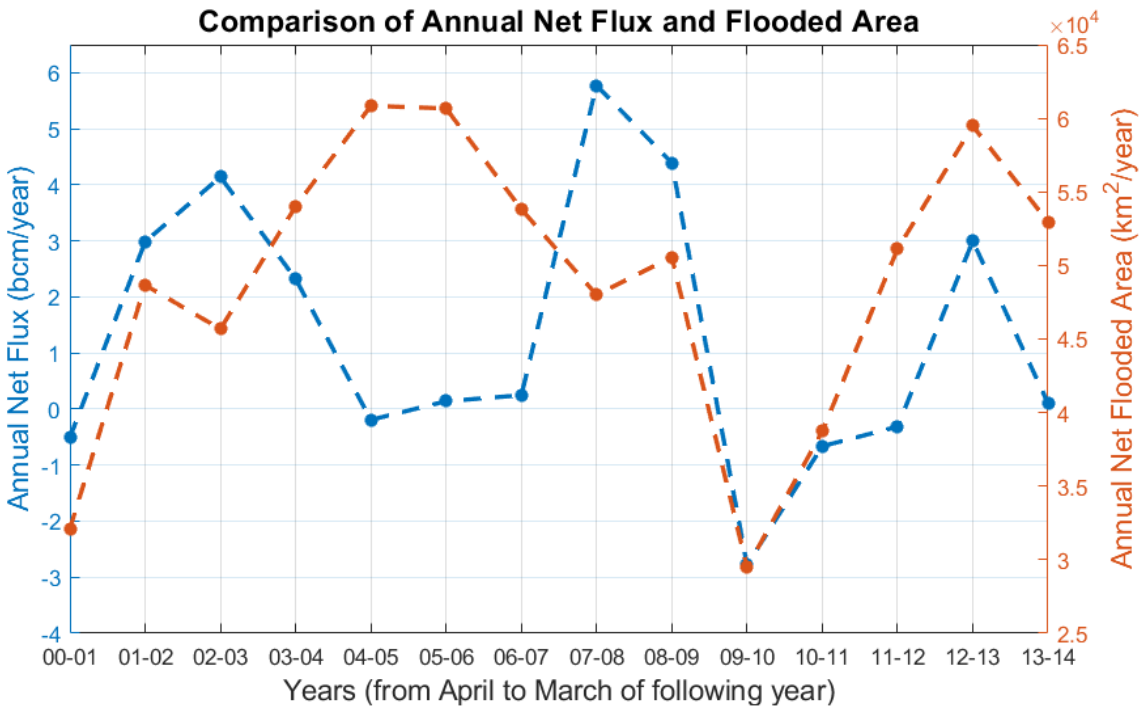

Figure 77: Comparison between annual net fluxes and flows over 2000 to 2014 period. Each data point is a summation from April to March of the following year, starting and ending in the dry season.

Visually, Figure 77 suggests that some years have higher correspondence between the fluxes and areas than others. The years 2002 – 2003 and 2004 – 2008 in particular should be evaluated to understand why there are large differences in magnitude. The accuracy of the estimated flows, precipitation, and ET is largely dependent on the amount of in-situ data available. Until more ground data is available, opportunities to improve these estimates are limited. However, the satellite-based flood mapping algorithm presented in Chapter 3 could potentially be adjusted to improve the accuracy of the final estimated flooded areas, where more accurate flooded areas are assumed to be more correlated to the hydrologic fluxes in the Sudd.

5.3 Connectivity of MODIS-derived Flooded Areas

To begin to explore how the MODIS-derived flooded area maps could be adjusted to align more closely with the hydrologic fluxes, the time series animation of the flooded area maps was revisited. Figure 78 shows the flooded area from May to July of 2006, a year where there is low correspondence between the area and net annual hydrologic flux. Note that there is a large area that floods in June (highlighted in red box) and is no longer flooded in July. This pattern deviates from patterns observed in other years, where the expansion of the wetland is more gradual and large flooded areas are sustained throughout the remainder of the expansion period.

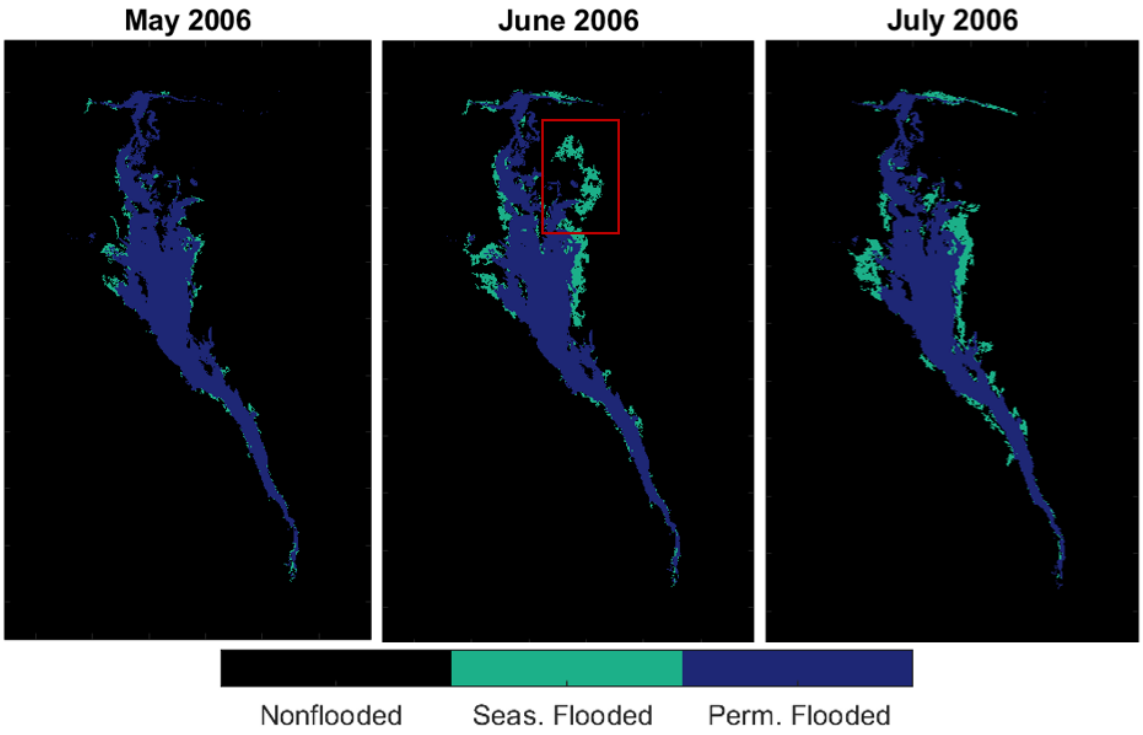

Figure 78: Time series animation of flood maps from May 2006 to July 2006, with potential area inconsistency highlighted in the red box. The geographic coordinates are not shown here to improve readability, but the area is approximately located from 5 to 10 degrees North, and from 29 to 32 degrees East.

If the area highlighted in Figure 78 is a commission error, the source of the error could be in the flood detection algorithm. Recall from Section 3.3.3 that the NDWI (wetness index) is an aggregate measure of moisture from the land surface and the vegetation. The area highlighted in Figure 78 aligns closely with a transition in land cover classes between seasonally flooded grasslands and seasonally flooded woodlands. Therefore, the increase in the NDWI value that resulted in these pixels being classified as flooded could be related to a change in the amount of moisture in the vegetation as opposed to flooding beneath the canopy. The monthly flood assessment procedure described in Section 3.4 was designed to normalize the NDWI values of pixels for variances caused by differences in vegetation and precipitation; however, the algorithm must be able to identify a set of non-flooded pixels that have similar vegetation and precipitation and are located nearby the pixel being assessed for flooding. Depending on the location of the pixel being assessed and the spatial heterogeneity of precipitation for a given month, the non-flooded pixels selected by the algorithm may have different conditions, preventing them from being able to accurately normalize the NDWI values.

Alternatively, the flood detection algorithm may provide an accurate representation of flooding. However, large areas of the wetland could be temporarily flooded from excessive local rainfall, and this rainfall may not become part of the Sudd water budget if it becomes disconnected from the wetland in the following month. In both potential scenarios described, this portion of the flooded area should be removed from the total flooded area of the Sudd to calibrate a hydrologic model of the wetland.

Multiple options were explored for adjusting the flooded area maps to correct for inconsistencies. An observation from the time series animation of flood maps was that the recession patterns of the wetland appeared more consistent then the advancing patterns. This observation is not surprising considering the wetland recedes during the dry season, so the flooding behavior is not influenced by spatial and temporal variations from rainfall. Therefore, the receding flood patterns of the wetland could potentially be used to correct the advancing flood patterns within a particular year.

To test whether this correction procedure is justified, the advancing and receding flood patterns were plotted for each year. Figure 79 illustrates these patterns for a year with low correspondence between the flooded areas and hydrologic fluxes, 2006 to 2007 (the same year shown in Figure 78), and a year with high correspondence between flooded areas and hydrologic fluxes, 2012 to 2013. The advancing period begins when the wetland size is at a minimum and ends when the wetland size is at a maximum for a particular year. Similarly, the receding period begins when the wetland size is at a maximum and ends when the wetland size is at a minimum for a particular year. The month that corresponds to each pixel in Figure 79 indicates the month when the pixel was flooded for the first time since it reached its minimum extent (during the advancing period), or when the pixel became non-flooded since it reached its maximum extent (during the receding period).

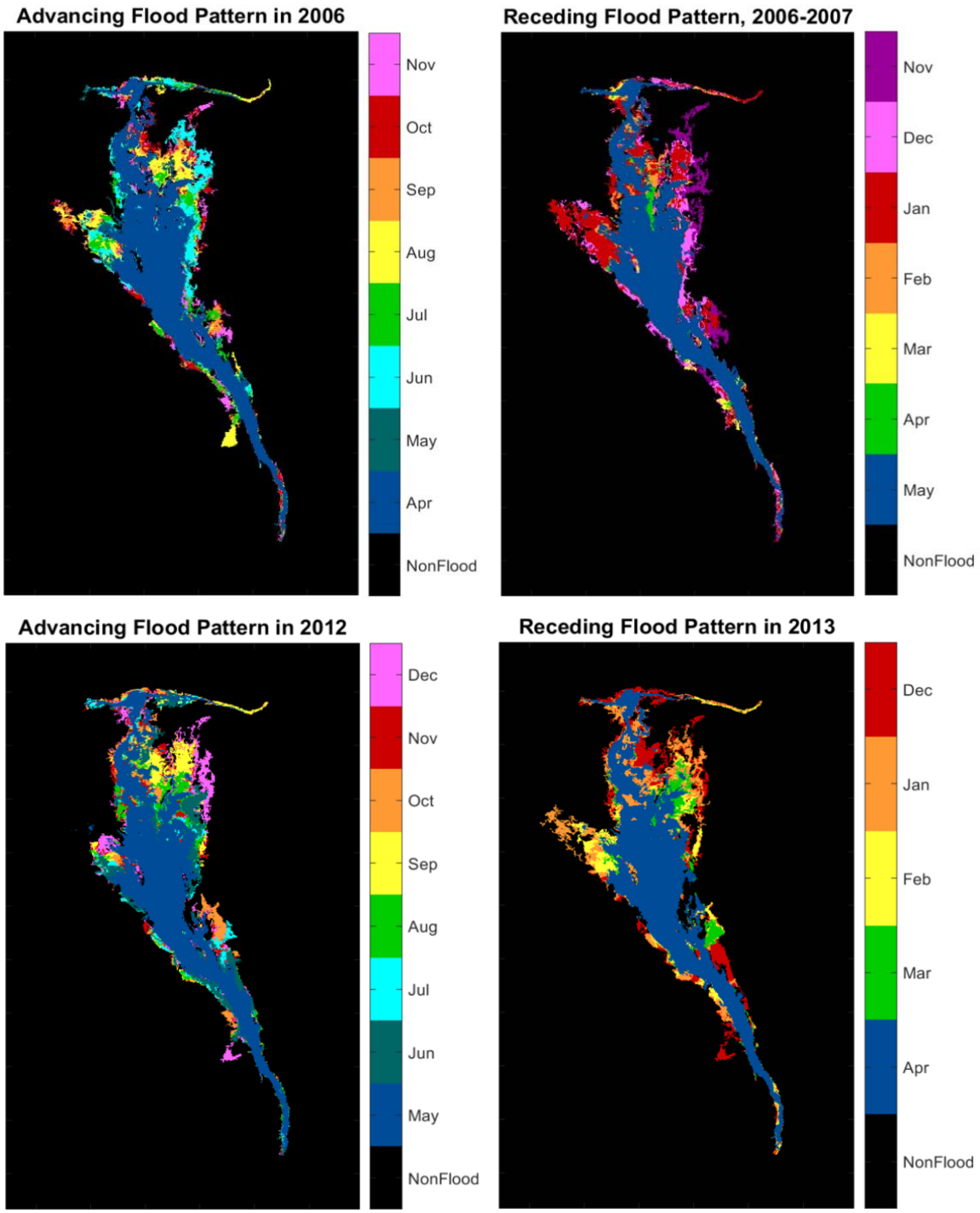

Figure 79: Illustration of advancing and receding flood patterns in the Sudd the 2006 to 2007 flood cycle, and the 2012 to 2013 flood cycle. The month assigned indicates when a pixel was flooded for the first time since the wetland size was smallest (during the advancing phase), or non-flooded for the first time since the wetland size was largest (during the recession phase). The colorbar legend changes with each plot to account for the fact that the timing of the minimum and maximum extents of the wetland changes each year. The geographic coordinates are not shown here to improve readability, but the area is approximately located from 5 to 10 degrees North, and from 29 to 32 degrees East.

Figure 79 shows that there are some similarities between the advancing and receding flood patterns; however, in general these images do not provide a convincing argument that the recession patterns could be used to correct the advancing patterns. Within each of the years, with both high and low correspondence between the areas and fluxes, many of the areas separated by months do not align spatially. Additionally, the spatial and temporal patterns vary for different parts of the Sudd. For example, the western region is believed to partially drain into the Bahr El Ghazal basin, which has a lower elevation. Consequently, this portion of the Sudd appears to still be expanding when the rest of wetland is receding, and the flooding and drainage hydrodynamics seem to vary based on the progression of the flooded area footprint. Another observation from analyzing these plots is that the recession patterns have more consistency from year-to-year compared to the advancing patterns, and the year-to-year recession patterns tend to be more similar than the advancing and receding patterns within a year. This observation supports the idea that the advancing pattern of the wetland is strongly influenced by spatial and temporal variations of rainfall and the associated variations in surface runoff patterns.

Another method of evaluating the MODIS-derived flooded areas is to plot the areas that cause the wetland to advance or recede in an inconsistent manner. Whether or not the wetland behavior is considered consistent is based on the idea that once a large area of the wetland floods, it should stay flooded as the wet season progresses. Similarly, once a large area of the wetland recedes, it should remain dry as the dry season progresses. Therefore, the wetland advancement is considered inconsistent if an area is not flooded in a current month but was flooded in a previous month since the wetland first began to expand. The

wetland recession is considered inconsistent if an area is flooded in a current month but was not flooded since the wetland first began to recede.

These inconsistent areas were plotted for the full time series of flood maps and were carefully studied. Based on the previous analysis illustrated in Figure 79, the Sudd was first split into four quadrants that are believed to have different flooding behavior. The occurrence of the minimum and maximum extent of flooding were identified for each quadrant and each year, allowing the start and end month of the advancement and recession period to vary spatially and temporal. Areas classified as inconsistent for the advancing phase in July 2006 (a year with low correspondence between flooded areas and hydrologic fluxes) and July 2013 (a year with high correspondence between flooded areas and hydrologic fluxes) and shown in Figure 80.

Plots for the recession period are not shown here because very few areas were classified as inconsistent. Because there is no precipitation during the recession period, this result further supports the idea that discrepancies in the flooded area maps during the advancing phase are associated with rainfall. Additionally, areas were identified as being inconsistent during the advancing phase for all years of the period of study, as opposed to only the years when there was low correspondence between the flooded areas and fluxes. This result suggests that the "inconsistent" areas are not necessarily erroneous and removing them from the total flooded area is not justifiable according to this analysis. As an additional test, the inconsistent areas were removed from the total flooded areas and the net annual flooded areas and hydrologic fluxes were recalculated. Not surprisingly, the correspondence between the areas and fluxes did not improve, and the correlation

decreased.

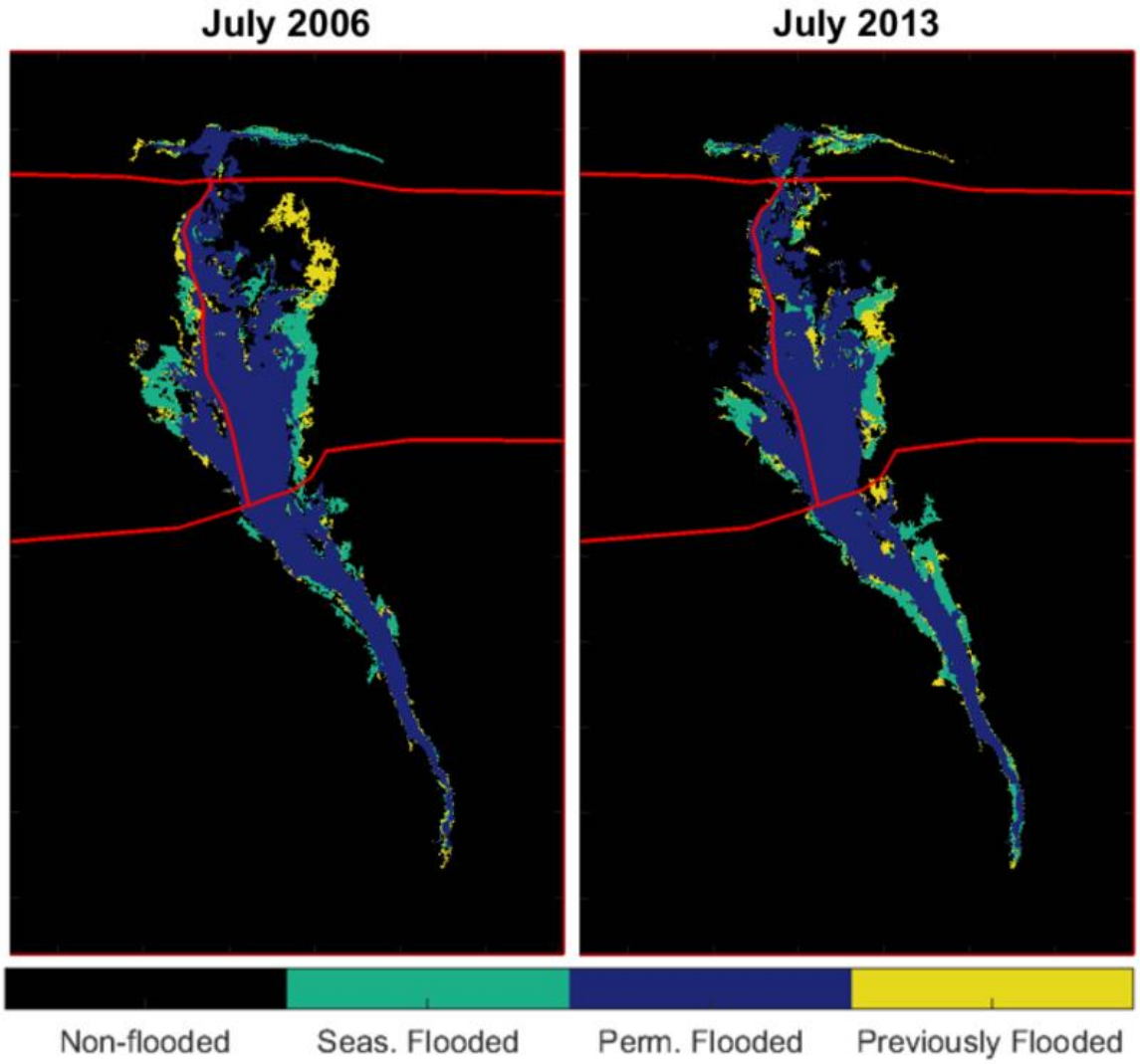

Figure 80: Example plots highlighting inconsistent flooding patterns when the wetland is expanding. Plots are show for July 2006 and July 2013. The red lines show the 4 quadrants that split the Sudd into areas with different occurrences of minimum and maximum extents. The geographic coordinates are not shown here to improve readability, but the area is approximately located from 5 to 10 degrees North, and from 29 to 32 degrees East.

Based on the advancing and receding patterns of the flooded areas, and the "inconsistent" areas analysis, a procedure for adjusting the flooded areas to align more

closesly with the hydrologic fluxes should focus on the advancing periods and should incorporate precipitation estimates. Therefore, differences in the flooded area maps during the advancing phase were evaluated along with TRMM precipitation estimates in an effort to identify patterns that could be used to adjust the flooded areas.

The occurance of surface water flooding from heavy rainfall events would not necessarily be reflected by high cumulative monthly precipitation. Therefore, the TRMM 3B42 Version 7 Research Derived Daily Product with 0.25 degree spatial resolution was downloaded from the Goddard Earth Sciences Data and Information Services Center (GES DISC) (https://disc.gsfc.nasa.gov/). The maximum daily precipitaiton rate for each pixel within the Sudd area and each month from 2000 to 2014 was extracted from the the daily TRMM dataset. The monthly differences in these maximum daily precpitation rates along with the monthly precipitation rates were superimposed on the differences in flooded area maps, as shown in Figure 81. The red ares in these images denote areas that are flooded in June but not July in 2006 (similar to Figure 78 and Figure 80), and areas that are flooded in September but not October in 2013. Similarly, the TRMM monthly and max daily precipitation rates in July 2006 were subtracted from the rates in June 2006, based on the idea that areas that were temporarily flooded in the previous month should have higher precipitation rates in the previous month. Sample plots from the years 2006 and 2013 are shown here to compare a years where there is low (2006) and high (2013) correspondence between the flooded area maps and hydrologic fluxes. However, these plots were produced and evaluated for every month in the 2000 to 2014 period.

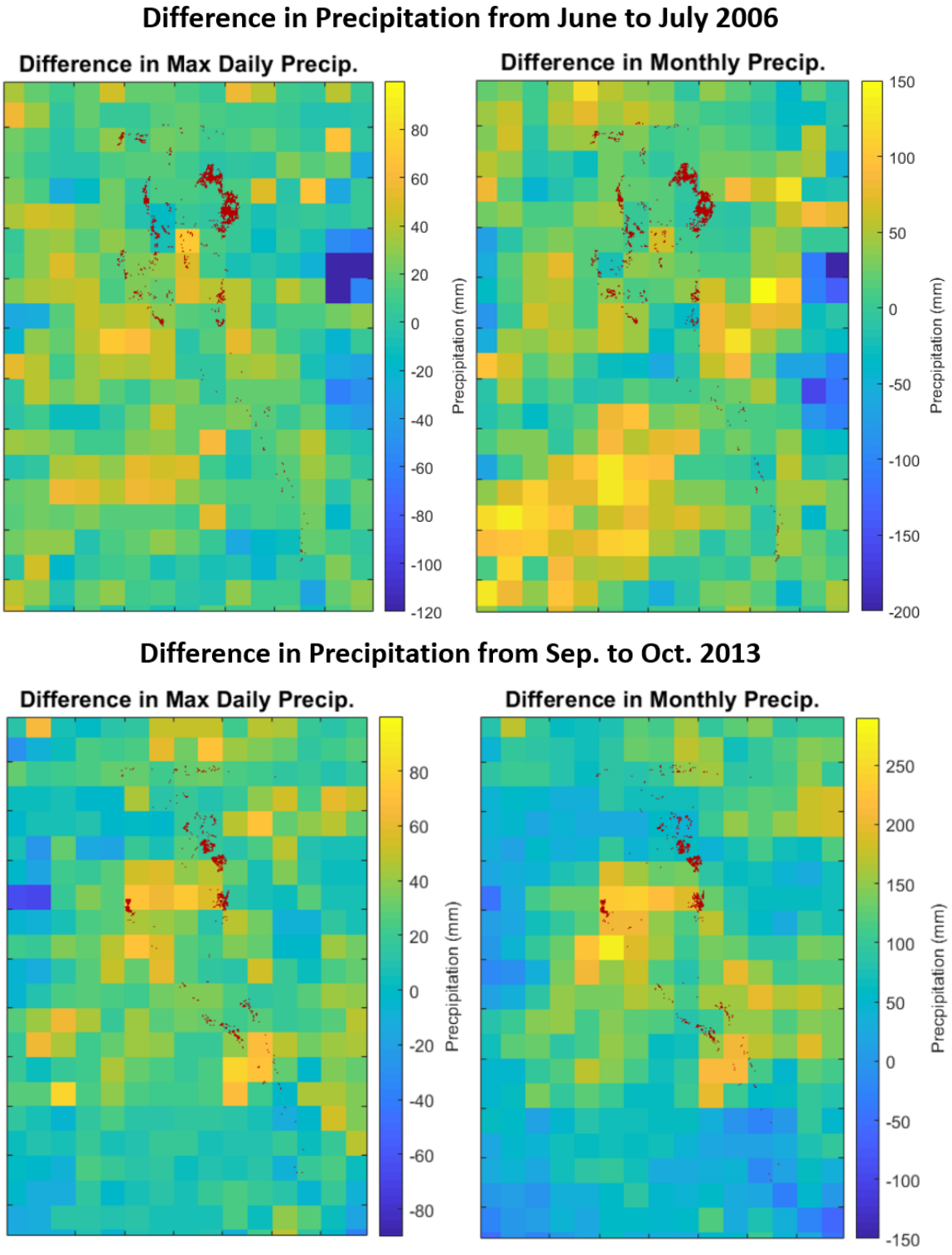

Figure 81: Differences in maximum daily and monthly mean precipitation rates obtained from TRMM, with corresponding differences in flooded area maps shown in red. The geographic coordinates are not shown here to improve readability, but the area is approximately located from 5 to 10 degrees North, and from 29 to 32 degrees East.

Unfortunately, a clear relationship between precipitation and flood patterns that could be applied to adjust the MODIS-derived flooded area maps could not be discerned from these plots. Additionally, there was not a clear difference between patterns observed in years with high or low correspondence between flooded areas and hydrologic fluxes. Figure 81 shows that the differences in precipitation are fairly neutral near the areas with significant differences in flooded area for in each subplot. Although the TRMM precipitation data product performed well based on the analysis in Section 4.2, there are still large uncertainties in these estimates due to an extremely sparse in-situ observation network in the Sudd region. Therefore, the accuracy of these data products may not be sufficient to capture the spatial rainfall variations. Additionally, there are spatial and temporal lags between rainfall and flooding in the Sudd that cannot realistically be modeled.

In this section, the connectivity of the MODIS-derived monthly flooded area maps was evaluated graphically by looking at differences in flooded areas as the wetland expands and contracts. Although a clear and simple pattern that could be used to improve the correspondence between the flooded areas and hydrologic fluxes could not be identified, these analyses provided the following valuable insights:

1. The wetland does not expand and contract in a similar spatial pattern within an annual flood cycle.
2. The timing of the maximum and minimum wetland extents varies for different areas of the Sudd.

3. The flooded area recedes in a consistent manner during the dry season, in the absence of precipitation.
4. There are some inconsistencies in the flooded area patterns when the wetland advances, and these inconsistencies are likely influenced by precipitation.
5. The inconsistencies in the flooded area patterns when the wetland advances are not necessarily errors; these areas could be temporarily flooded from heavy rainfall events.

Ideally, the analyses performed in this section would have led to a procedure for improving the flooded area maps for the full 2000 to 2014 period. However, an alternative approach is to assume that the flooded area maps are accurate if the net annual flooded areas and hydrologic fluxes are correlated (according to Figure 77), and to use the accurate flooded area maps to correct the less accurate flooded areas, corresponding with years where the net fluxes and flows are not correlated. The abovementioned insights were used to develop a procedure that follows this strategy and is presented in Section 5.4.

5.4 Adjustment of MODIS-derived Flooded Areas

The exploratory analysis of the flooded area maps presented in Section 5.3 emphasized that the extent of the wetland as it is advancing is influenced by precipitation. Because precipitation varies spatially and temporally, the advancement of the flooded area should not necessarily follow a consistent spatial pattern from year-to-year, nor expand outward in a chronological sequence. However, the magnitude of the extent of flooding over a full flood cycle should be consistent with the magnitude of the hydrologic fluxes.

This consistency was observed for the years 2000 to 2002 and 2008 to 2014, based on the analysis presented in Figure 77. Therefore, the flood maps from 2000 to 2002 and 2008 to 2014 could potentially be used to adjust the flood maps for years where this consistency was not observed, 2002 to 2008.

The following procedure was developed, evaluated, and implemented to adjust the 2002 to 2008 flood maps with flood maps from the 2000 to 2002 and 2008 to 2014 period:

1. For each monthly flood map that is being evaluated during the 2002 to 2008 period, the full Sudd area was split into the 4 sub-areas, as shown in Figure 80. Recall that these quadrants appear to have distinct spatial and temporal flooding dynamics within the full Sudd region.
2. For each sub-area and each month under consideration, the month when the wetland sub-area begins to increase from its minimum extent, and the month when it reaches is maximum extent was identified.
3. For each month under consideration when the wetland is expanding, the 3 months that have the most similar hydrologic characteristics from the 2000 to 2002 and 2008 to 2014 period were identified, according to the metric presented in Equation 43. The first term represents the difference in flow magnitude for the current month, the second term represents the difference in flow magnitudes for the previous 2 months, and the third and fourth terms represent differences in precipitation rates for the current month and previous 2 months over the same sub-areas. The flow rate in the previous 2 months were incorporated into the metric to account for the time it takes for the river water to reach the outer extents of the wetland. The

precipitation rates in the previous 2 months were incorporated to measure how much rain has accumulated in the area surrounding the wetland extent, representing water that could be running off into the outer wetland extents. The denominator of each of these terms normalizes for variations in magnitude, ensuring all terms are weighted equally. The monthly TRMM precipitation rates were used for the *P* terms. The comparison flood maps being considered (from the 2000 to 2002 and 2008 to 2014 period) must occur within a 3-month interval around the month being adjusted; for example, a flood map in June can be compared with flood maps from May to July. This constraint was enforced to ensure that the flood maps being compared are within the same season. Therefore, for each monthly flood map being evaluated and for each sub-area, 24 similarity metrics were calculated. The sub-area flood maps associated with the 3 lowest values of this metric are then extracted and compared with the flood map being considered for adjustments.

$$c_{i,j,a} = \frac{|Q_i(k)-Q_j(k)|}{Q_i(k)} + \frac{\left|\left(Q_i(k-1)+Q_i(k-2)\right)-\left(Q_j(k-1)+Q_j(k-1)\right)\right|}{Q_i(k-1)+Q_i(k-2)} + \frac{|P_{i,a}(k)-P_{j,a}(k)|}{P_{i,a}(k)} + \frac{\left|\left(P_{i,a}(k-1)+P_{i,a}(k-2)\right)-\left(P_{j,a}(k-1)+P_{j,a}(k-1)\right)\right|}{P_{i,a}(k-1)+P_{i,a}(k-2)} \quad [43]$$

where:

i = month index of flood map being adjusted
j = month index of comparison flood map
a = index for sub-area within Sudd
k = temporal index (month)
$c_{i,j}$ *= similarity measure between month i and month j*
Q = monthly Sudd inflows (m^3/month)
P = monthly mean areal precipitation over sub-area (m/month)

4. The alignment between the flood maps under consideration for adjustments and the three most hydrologically similar flood maps were then evaluated. Figure 82 shows this alignment for the June 2006 flood map that has been referred to throughout this Chapter. The white lines delineate the four sub-areas, the blue areas show where the flood maps were in agreement, the red areas show where the June 2006 map was flooded but the comparison map was not flooded, and the yellow areas show where the June 2006 flood map was not flooded but the comparison map was flooded. According to the net flux and flooded area analysis in Figure 77, a reduction in the total flooded area extents would improve the correlation between the areas and fluxes. The fact that there are far more red areas than yellow areas in Figure 82 supports the idea that the June 2006 flood map overestimates the true flooded area. These plots were produced and evaluated for all months that were considered for adjustments, and the ratios of red and yellow areas were generally in agreement with the bias in the flooded area extents observed from the net flux and flooded area comparison (Figure 77). However, the correction algorithm itself should not be biased in the manner that it adjusts the flooded area maps, so both red and yellow areas were considered in the algorithm.

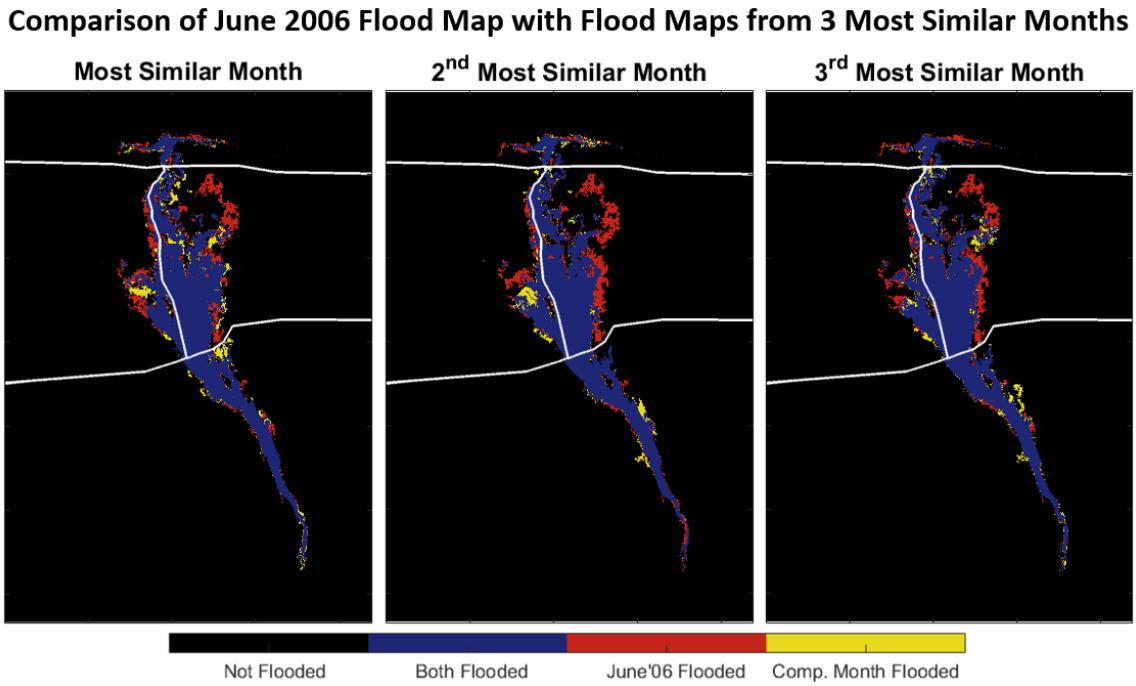

Figure 82: Alignment of June 2006 MODIS-derived area map with 3 most hydrologically similar flood maps, according to the metric presented in Equation 41.

5. If the highlighted areas in all three of the comparison flood maps aligned, and the size of the connected area was at least 100 pixels (approximately 200 km^2), then the flood map in question was adjusted accordingly. For example, the large areas that are red in all 3 plots in Figure 82 were removed from the June 2006 flood map, and the large areas that are yellow in all 3 plots in Figure 82 were added to the June 2006 flood map. A threshold was set on the size of the area to allow for minor differences between the images; however large areas that are inconsistent across the three hydrologically similar flood maps are more likely to be inaccurately classified. The resulting corrected flood map for June 2006 is compared to the original flood map in Figure 83, and the series of flood maps from May 2006 to July 2006 is shown in Figure 84. Note that the large area highlighted in Figure 78

has been removed, and the expansion of the flooded area is more consistent across sequential flood maps.

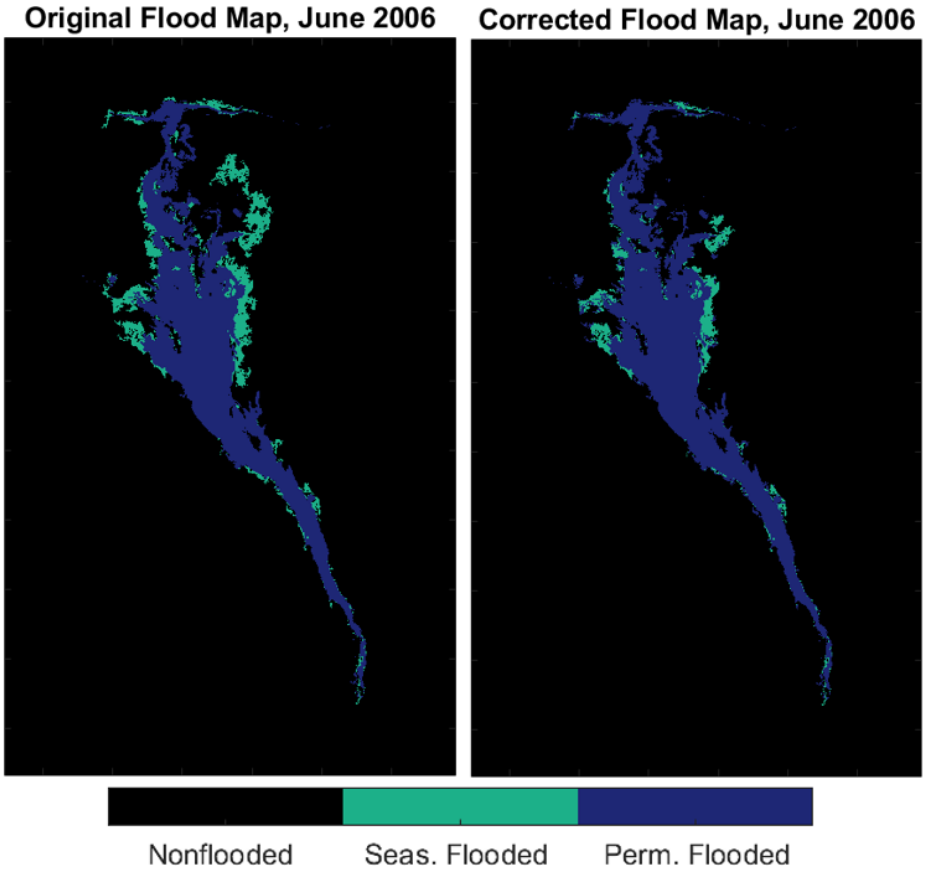

Figure 83: June 2006 flood map before and after application of correction procedure.

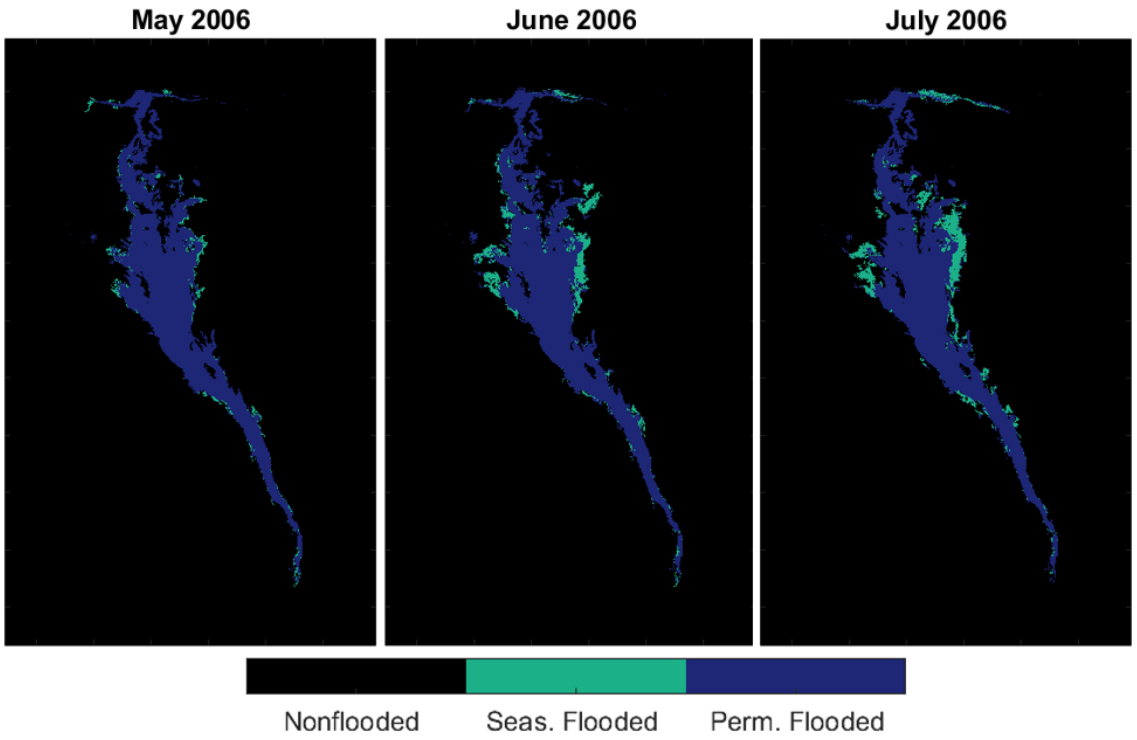

Figure 84: Corrected flooded area maps from May 2006 through July 2006 showing more consistent flood pattern.

6. After the adjustments were made to all months within the 2002 to 2008 period, the total annual change in the flooded areas over the full wetland extent were inspected. With the exception of 2002 to 2004, the direction of the adjustment in the flooded areas agreed with that suggested by the net flux and flooded area analysis (Figure 77). Note that the bias between the areas and fluxes was less significant from 2002 to 2004 period compared to the 2004 to 2008 period. Therefore, the adjustments were kept only for the 2004 to 2008 period.

The final time series of total flooded area for the original and corrected MODIS-derived flood maps are shown in Figure 85. The net annual flux and flooded area

comparison presented in Figure 77 was repeated, and the revised fluxes and areas are compared to the original in Figure 86. The correlation coefficient between these time series increased from 0.32 to 0.44. The adjustment of the flooded area did not have a significant influence on the net flux, supporting the statement made earlier that these measurements of the Sudd are nearly independent.

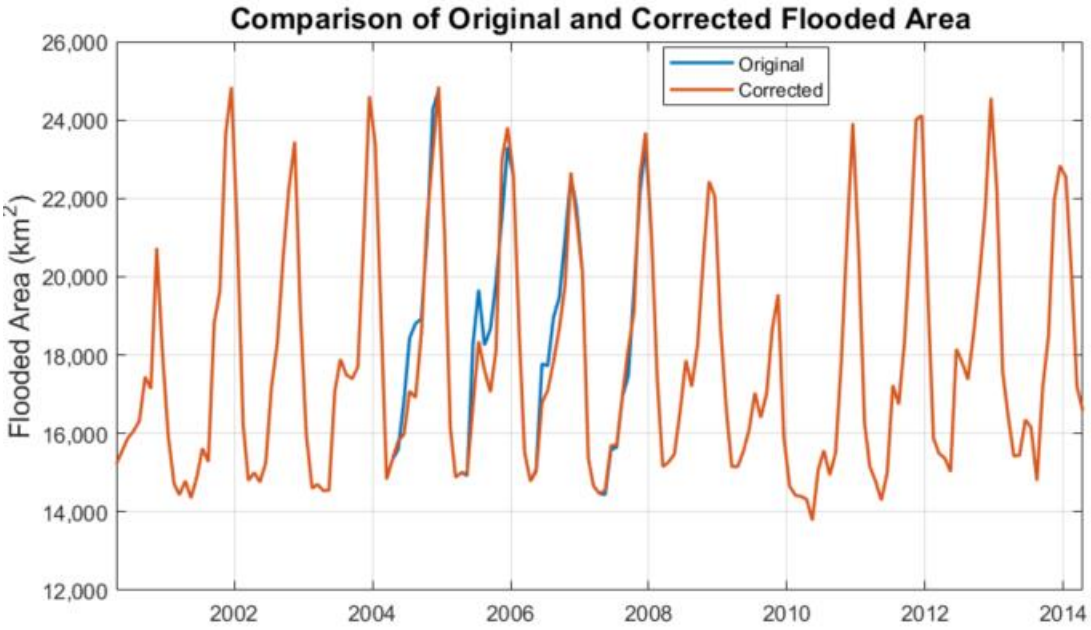

Figure 85: Time series comparison of original and corrected MODIS-derived flooded areas.

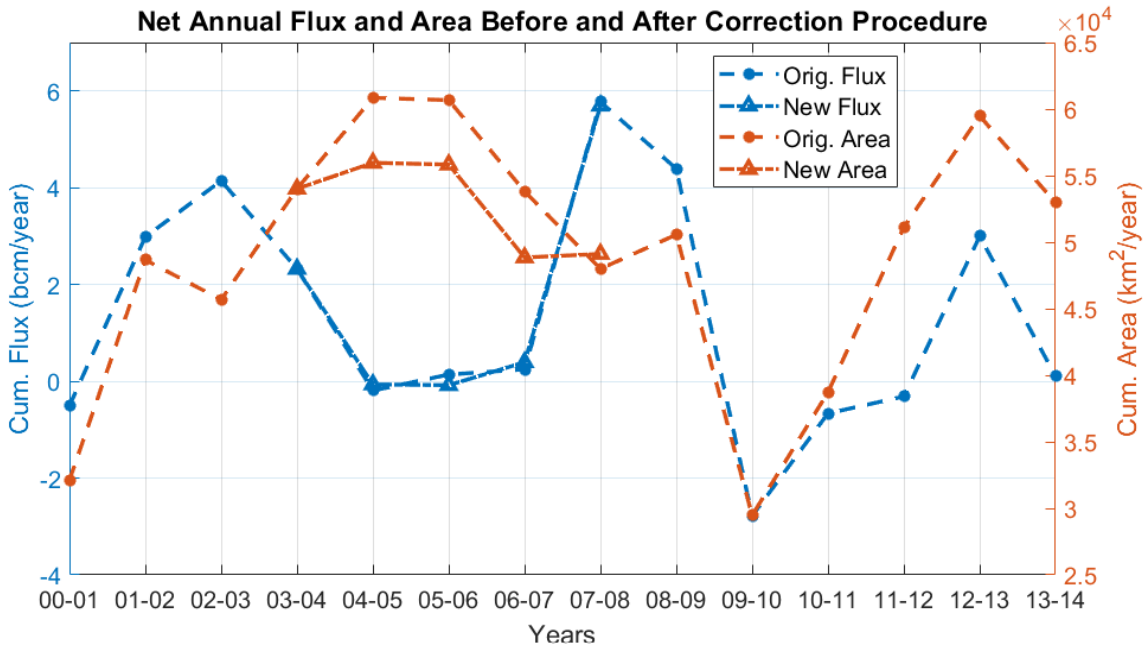

Figure 86: Comparison of net annual fluxes and flooded areas for orginal and corrected MODIS-derived flooded area maps.

This flooded area correction algorithm could potentially be fine-tuned and improved. For example, ET rates could be used in Equation 43, the statistical distributions of the similarity metric could be evaluated to develop a more statistically robust procedure for selecting flood maps that are hydrologically similar, or alternative decision criteria for making the final corrections could be tested and evaluated. However, the biggest limitation to this methodology is the relatively short time series of flood maps that can be used for comparisons. Requiring that all three hydrologically similar flood maps agree with one-another is a strict criterion. Consequently, the resulting changes in the flooded area extents are relatively minor. However, this algorithm was designed to be conservative considering the limited amount of "correct" flood maps available to implement the procedure. The final flooded area maps appear to have eliminated major anomalies, such as those observed for

the June 2006 flooded area; however, there are likely outstanding errors related to the connectivity of the wetland and the influence of rainfall and runoff on the outer wetland extents during the rainy season. Further evaluation and correction of these errors would be beneficial for the development of a hydrologic model, but more research is needed to develop an improved flood detection algorithm that focuses on the wetland connectivity. The algorithm could be significantly improved if a large amount of field observations of flooding or in-situ precipitation records were made available, or if more accurate satellite-based estimates of precipitation and topography (Digital Elevation Model) were available.

5.5 Comparison of Net Water Flux to Adjusted MODIS-derived Flooded Areas for Various Precipitation and ET Estimates

In Section 3.5.3, the net water flux in the Sudd was used to validate the MODIS-derived wetland flood maps. Figure 20 compared the time series of flooded area to the net water flux using the TRMM precipitation and Sutcliffe and Park's climatology ET estimates, and a Pearson's correlation coefficient of 0.809 was found between the two series.

In addition to validating the MODIS-derived flood maps, this correlation analysis was used to compare the precipitation and ET estimates evaluated in this study, using the adjusted flooded area estimates from Section 5.4. However, a slight modification was made to the original equation for the flux calculation (Equation 16) to account for the bias between ET data sources. The ET parameter described in Equation 44 and 45 forces the mean annual ET of each data product to be equal to the mean annual ET used by Sutcliffe

and Parks, thereby ensuring that the resulting net water flux allows for a stable, non-negative water volume storage in the Sudd. This ET parameter will also be applied to the hydrologic model of the Sudd and will be fine-tuned during the model calibration process.

$$Flux(k) = Q_{IN}(k) - Q_{OUT}(k) + \big(P(k) - \alpha_{ET} ET(k)\big)A(k) \quad [44]$$

where:

Q_{IN} = monthly Sudd inflows (m^3/month)
Q_{OUT} = monthly Sudd outflows (m^3/month)
P = monthly cumulative precipitation (m/month)
α_{ET} = ET parameter for bias reduction (unitless)
ET = monthly evapotranspiration (m/month)
A = monthly mean Sudd flooded area (m^2/month)
k: temporal index

$$\alpha_{ET} = \frac{\sum_{m=1}^{12} \overline{ET_{SP}}(m)}{\sum_{m=1}^{12} \overline{ET_D}(m)} \quad [45]$$

where:

$\overline{ET_{SP}}$ = monthly mean ET from Sutcliffe and Parks (m)
$\overline{ET_D}$ = monthly mean ET from alternate data sources (m)
m = month index

Each of the precipitation and ET estimates discussed in Sections 4.2.2 and 4.3.2 were substituted into Equation 44 along with the monthly Sudd inflows and outflows derived in Section 4.3. The net water flux was lagged backwards to account for the time it takes for floodwaters to travel across the wetland in this very large, flat area. The Pearson's correlation coefficients between the net water flux and the MODIS-derived flooded areas were recorded for each combination of precipitation and ET estimates. As mentioned in Section 3.5.3, higher correlation coefficients were generally found for a lag of 4 months. These correlation coefficients are listed in Table 13. The significance of the correlation

coefficients was tested according to the procedure outlined in Section 3.5.3, and the resulting p-values are listed in Table 14.

Table 13: Pearson's correlation coefficient between the inflows minus outflows and net precipitation minus ET, and the MODIS-derived flooded area, lagged backwards 4 months for various precipitation and ET data products. The calculations were performed on data spanning from April 2000 to March 2014.

Correlation Between Flooded Area and Net Flux					
		Precipitation			
		TRMM	CRU	PERSIANN	ARCv2
Evapotranspiration	Sutcliffe and Parks	0.815	0.773	0.753	0.770
	CRU	0.797	0.756	0.738	0.749
	Hargreaves	0.808	0.762	0.743	0.758
	MEP	0.801	0.753	0.737	0.744
	GLEAM	0.504	0.493	0.666	0.424

Table 14: p-values obtained through significance test on correlation coefficients between net flux and flooded area estimates. Artificial time series were created by combining annual flooded area subsets that were randomly sampled, without replacement. 100,000 trials were performed for each test.

p-values from Significance Test on Correlation Coefficients					
		Precipitation			
		TRMM	CRU	PERSIANN	ARCv2
Evapotranspiration	Sutcliffe and Parks	0.0105	0.2052	0.0573	0.0239
	CRU	0.0136	0.1761	0.0557	0.0262
	Hargreaves	0.0074	0.1439	0.0411	0.0153
	MEP	0.0126	0.1964	0.0585	0.0265
	GLEAM	0.0031	0.0826	0.0200	0.0060

The overall highest correlation coefficient in Table 13 is 0.815 and is associated with the Sutcliffe and Parks climatology ET and the TRMM precipitation. Note that this is slightly higher than what was reported in Section 3.5.3 (0.809), which was calculated using the flooded area estimates before the adjustment procedure was applied. The performance metrics shown in Table 13 and Table 14 are generally more sensitive to the precipitation data sources as opposed to the ET data sources, and TRMM has the highest and most significant correlation coefficients. TRMM also performed well according to the comparison with in-situ precipitation measurements in Section 4.2.2 (Table 9). Based on its consistent high performance according to multiple tests, TRMM precipitation estimates will be used to develop and test the hydrologic model of the Sudd.

The metrics listed in Table 13 and Table 14 also indicate that the Sutcliffe and Parks climatology and Hargreaves ET estimates perform well relative to the alternative data sources. Note that although the GLEAM estimates resulted in the lowest correlation coefficients, they have the highest statistical significance. This behavior could potentially be explained by the reverse seasonal trend reducing the impact of heavy precipitation during the rainy season on the net flux. The Sutcliffe and Parks ET resulted in the highest correlation coefficient, followed closely by the Hargreaves ET. However, the Hargreaves ET was slightly more significant. The CRU and MEP ET estimates also performed well and should not be entirely ruled out as potential data sources.

Finally, the annual net fluxes and flows (Figure 77) can be compared again using the new flooded areas and alternative estimates of precipitation and ET. Only TRMM precipitation was evaluated based on the performance metrics that have already been presented. The cumulative fluxes and areas using four alternative ET sources (Sutcliffe and Parks, CRU, Hargreaves, and MEP) are shown in Figure 87. The flux was calculated according to Equation 44, where the ET rates were bias corrected using the α_{ET} parameters. The correlation coefficients between the data series are 0.44, 0.49, 0.58, and 0.44 for Sutcliffe and Parks, CRU, Hargreaves, and MEP ET estimates, respectively. Therefore, the Hargreaves ET estimates result in higher correlations between the fluxes and flows according to both tests.

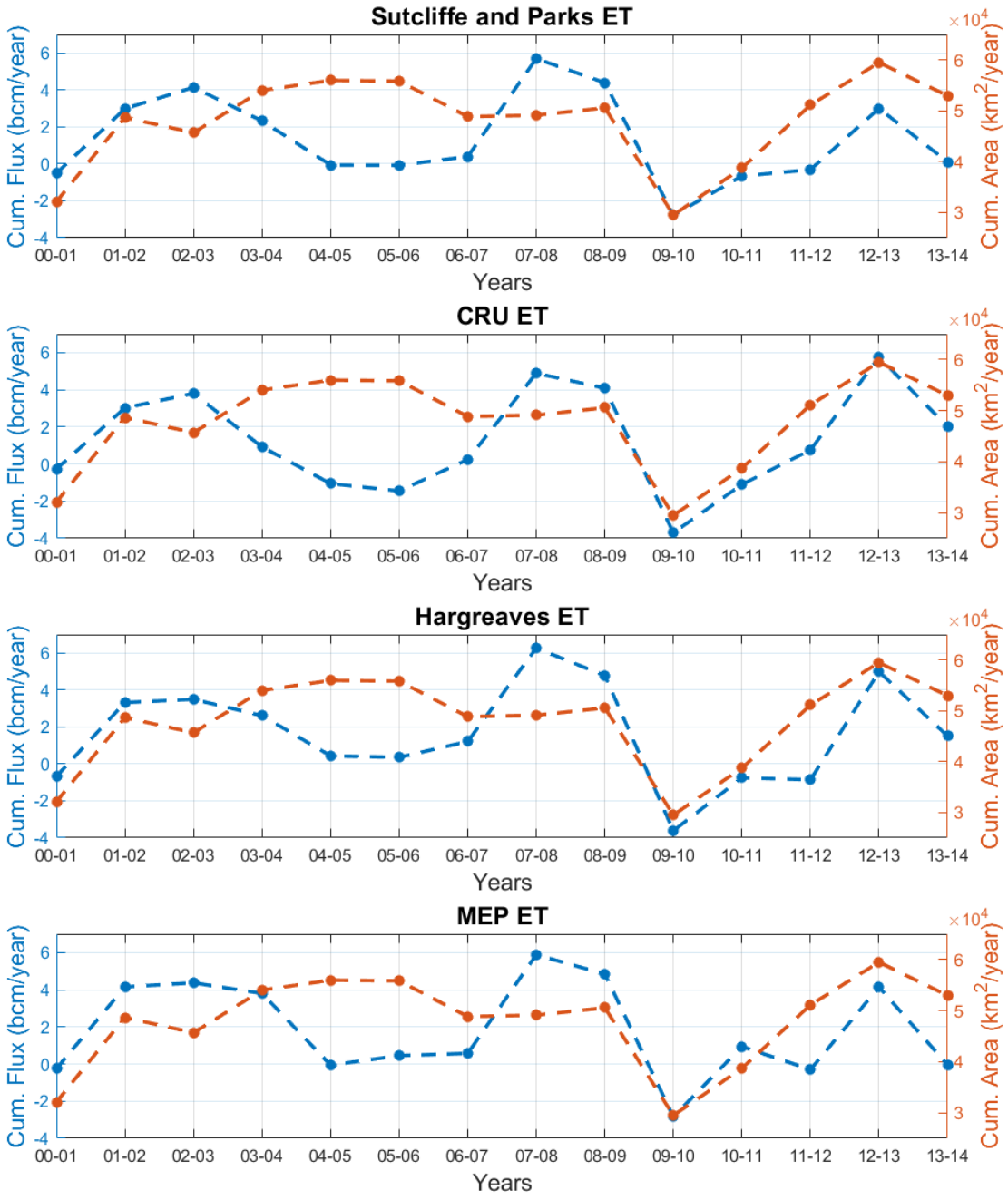

Figure 87: Comparison of annual net hydrologic fluxes and flows using TRMM precipitation and 4 different sources of ET estimates. Each annual interval uses data from April to March of the following year.

These analyses do not provide a final conclusion on which precipitation and ET estimates are most accurate, but it does provide insight into which estimates should be more consistent with the MODIS-derived flooded area estimates. This approach aligns with the modelling flow chart introduced in Figure 1 of Section 1.1.3; the satellite-based information is evaluated in an iterative manner and used to gain insights into the general hydrologic behavior of the Sudd. Depending on the complexity of the hydrologic model, it may not be feasible to iterate on each of these combinations to determine which estimates have the best model performance. Therefore, the TRMM precipitation and the Hargreaves ET will primarily be used in the development of the Sudd hydrologic model.

CHAPTER 6: DEVELOPMENT OF SUDD HYDROLOGIC MODEL

6.1 Overview

A hydrologic model of the Sudd can now be developed using the time series of flooded area maps derived in Chapter 3 and adjusted in Chapter 5, and the fluxes and flows derived in Chapter 4. Referring back to Figure 1, the research flow chart introduced in the Introduction, the model conceptualization and development process should begin with a simple model that is incrementally improved to more accurately represent the Sudd, according to the performance criteria. Therefore, the model development process will begin with an application of the original Sutcliffe and Parks model, evaluated with the MODIS-derived flood maps. This model relies on measured outflows and was not evaluated for its ability to simulate outflows from the wetland, a feature that is required for integrating models into long-term water resources planning tools, such as the Nile DST. Therefore, the Sutcliffe and Parks model will also be modified, reformulated, and optimized to estimate the Sudd outflows in addition to the flooded area extents. Insights from this analysis will guide the development of an improved hydrologic model of the Sudd.

Many of the wetland modeling approaches summarized in literature review on wetland models (Section 2.3) first assume a model structure, subsequently identify and acquire required data inputs, and then calibrate model parameters by minimizing the error between observed and simulated outflows. The approach taken in this research is to begin with a relatively simple model structure and only add hydrologic processes and more complex structures if they are required to improve the model performance. Throughout this

iterative process, the uncertainties ingrained in the model structure, input data sources, and model parameters are considered jointly. As more modeling processes and parameters and additional data sources are introduced into the model, the risk of overfitting and moving further from the true model structure increases. Therefore, changes are introduced to the basic model incrementally, and are considered improvements only if the data, hydrologic processes, and the model conceptualization are consistent with each other, and result in better performance measures.

In this chapter, Section 6.2 compares the flooded area extents produced by the original Sutcliffe and Parks to the MODIS-derived flood maps. Section 6.3 presents the modified and reformulated version of the Sutcliffe and Parks model and evaluates its ability to simulate both the flooded area extents and the outflows. Section 6.4 presents an exploration of how the model can be improved by evaluating the relative magnitudes of fluxes and the relationships between storage, area, and outflow. Section 6.5 presents a revised model that incorporates the insights derived from Section 6.4. Section 6.6 evaluates the uncertainties and sensitivities of this model related to the model parameters and hydrologic data inputs. Finally, Section 6.7 summarizes the key findings gathered through this model development process and discusses how the model might be improved.

6.2 Performance of Original Sutcliffe and Parks Model

Using the Sudd inflows, outflows, and precipitation and ET rates derived in Chapter 4 for the 2000 to 2015 period, the lumped mass-balance model of the Sudd originally developed by Sutcliffe and Parks [1987] can be applied and evaluated. This model was

summarized in Section 2.1.3. The general mass balance equation (Equation 1), and the final discretized form that was used to simulate the flooded area of the Sudd (Equation 5) are shown again in this section for convenience.

$$\delta V = [Q - q + A(R - E)]\delta t - r\delta A \quad [1]$$

$$V_{i+1} = \frac{V_i\left[1+k\left\{r_i-\frac{1}{2}(E_i-R_i)\right\}\right]+Q_i-q_i}{1+k\left\{r_i+\frac{1}{2}(E_i-R_i)\right\}} \quad [5]$$

where:

V = volume of flooding (m^3)
Q = inflow into the Sudd (m^3/month)
q = outflow from the Sudd (m^3/month)
R = average rainfall over the flooded area (m)
E = average evaporation over the flooded area (m)
A = total flooded area (m^2)
r = soil moisture recharge depth (m)
i = temporal index

There are only two parameters in this model. *k* comes from the linear volume-area relationship (A = kV) and represents the inverse of a constant depth that is representative of the entire wetland, and *r* is related to the infiltration of water into the ground over the newly flooded area and represents the maximum soil water recharge depth that is reduced by net rainfall over a season. Sutcliffe and Parks calibrated this model to just four estimates of the flooded area extents of the Sudd that were calculated using vegetation maps derived from aerial and satellite images on different dates. They concluded that there was a reasonable fit if k = 1 meter and r = 0.2 meters. Sutcliffe and Parks used historical estimates of the Sudd outflows as data inputs and did not evaluate the model's ability to estimate the Sudd outflows.

For an initial assessment of the Sutcliffe and Parks model, the volume of water stored in the wetland was simulated according to Equation 5 for the 2000 to 2015 period. To keep the simulation as similar to the original model as possible, the parameters k and r were set to the same values used in their study ($k = 1$ meter^{-1}, $r = 0.2$ meters), the same climatology monthly ET values were applied, monthly TRMM precipitation rates were used, and the estimated monthly inflows and outflows derived in Section 4.3 were input directly into Equation 5.

The maximum soil water recharge depth (parameter r) is assumed invariant with time. However, this depth should decrease by the net precipitation received during the rainy season. Therefore, the gridded monthly TRMM precipitation values were averaged over areas where seasonal flooding occurs (also where recharge into the soil would occur as the wetland expands) using the MODIS-derived land cover map. For each month of the 2000 to 2015 period, the cumulative precipitation over the seasonally flooded area since the beginning of the rainy season (assumed to occur in March) was calculated and subtracted from the maximum soil water recharge depth to obtain a time series of recharge depths.

Once the Sudd water volume is simulated, the flooded areas can be calculated from the simulated volume using the assumed linear relationship. However, V(k) in Equation 5 corresponds to the volume at the beginning or end of each month, and the MODIS-derived flooded area maps represent flood conditions over the duration of each month. Therefore, the simulated volumes were linearly interpolated, allowing the simulated areas to correspond with the middle of each month.

The simulation was initiated for the first time step by calculating the volume of water stored in the wetland from the MODIS-observed flooded area (where V = A/k). The resulting simulated flooded area time series is compared to the MODIS-derived flooded area time series in Figure 88, and a scatter plot comparing the data is shown in Figure 89. In general, the model over-estimates the flooded area extents, especially for the maximum flood extents from 2006 to 2009 and 2012 to 2014. Additionally, the maximum simulated flooded area typically occurs one month too early. However, this model does appear to capture the minimum flooded area for most years, and the drought from 2009 to 2010 adequately.

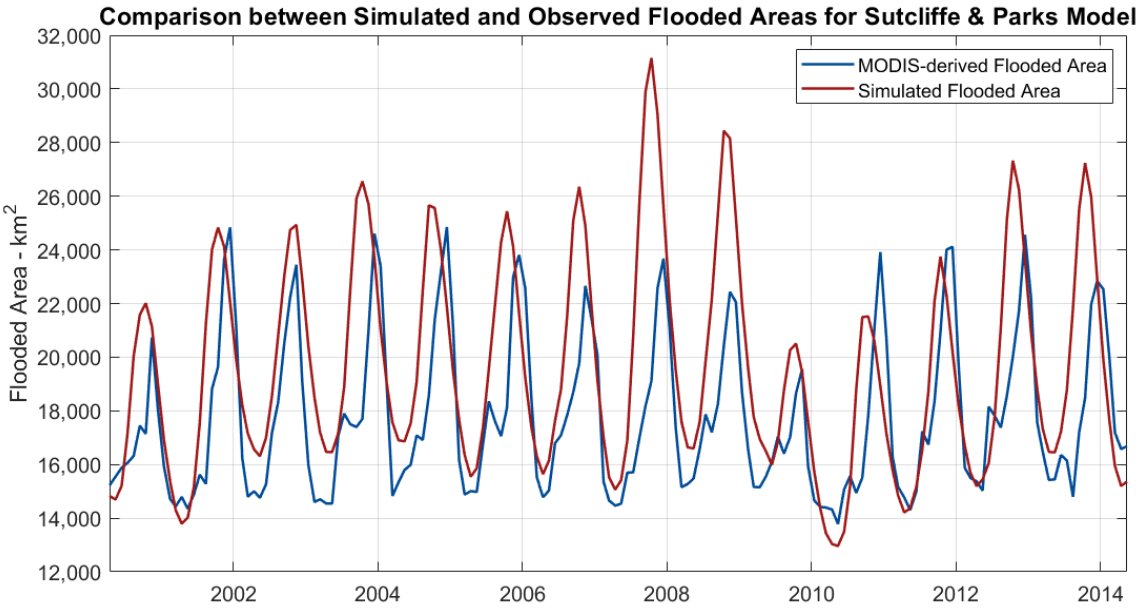

Figure 88: Comparison of simulated flooded area using original Sutcliffe and Parks model and parameters to the MODIS-derived flooded area maps.

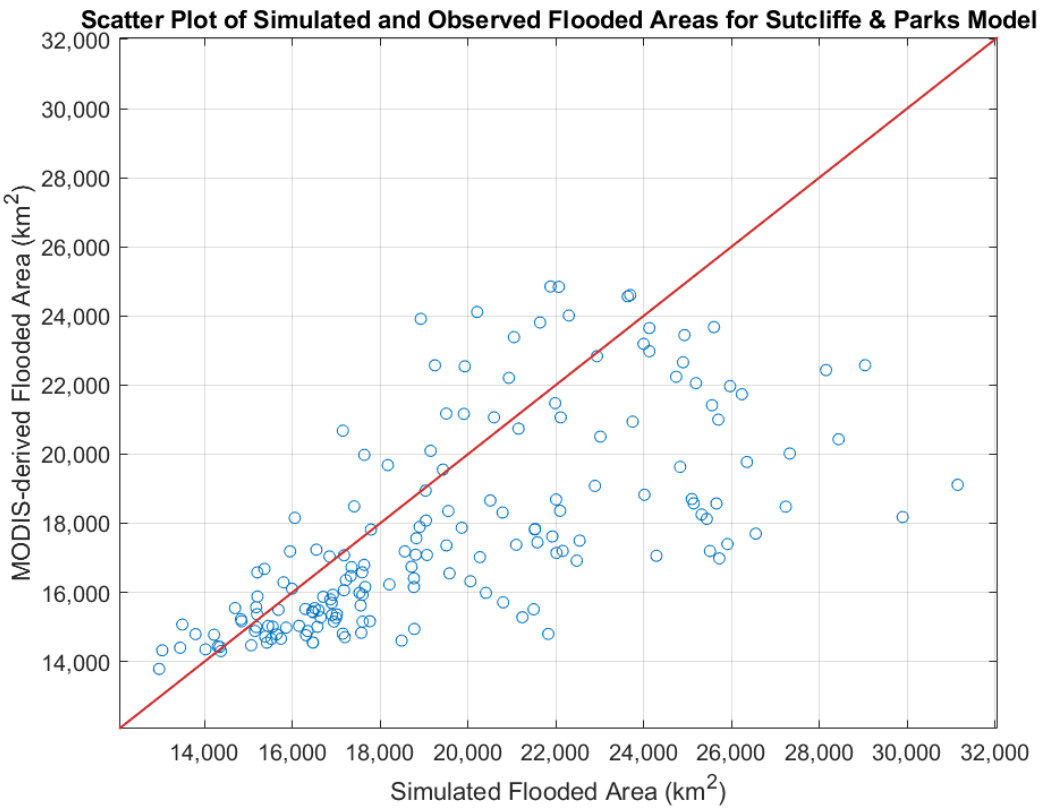

Figure 89: Scatter plot comparing the simulated Sudd flooded areas using original Sutcliffe and Parks model and parameters to the MODIS-derived Sudd flooded areas.

6.3 Reformulation and Calibration of Sutcliffe and Parks Model

6.3.1 Model Overview

A limitation of the original Sutcliffe and Parks model is that it relies on observed outflows as opposed to being able to simulate the outflows given an inflow time series. Consequently, this model cannot be integrated into water resources management tools that simulate future flow conditions that have not been observed in the past, allowing the impacts of alternative water management scenarios on the wetland to be explored. Therefore, the model should be reformulated to simulate the outflows, starting with a

simple linear relationship between the outflows and the wetland water storage. This reformulated model is presented in Equations 46 to 48. Note that a slightly different notation is being used than that of the original Sutcliffe and Parks model. A parameter was also introduced to adjust the ET rates (α_E), allowing them to be bias corrected to more accurately represent the ET rates of the Sudd vegetation. The precipitation, ET, and flow terms represent the cumulative flux throughout each monthly time step, whereas the state variables (storage and area) are simulated at the beginning and end of each month. Therefore, in Equation 46, the areas are averaged over two time steps to align with monthly cumulative fluxes. Similar to Section 6.2, the final monthly flooded areas are linearly interpolated (or averaged over two time steps) to allow for comparison with the MODIS-derived flood maps.

$$S(k+1) = S(k) + [P(k) - \alpha_E E(k)]\frac{1}{2}[A(k) + A(k+1)] - r(k)[A(k+1) - A(k)] + Q_{IN}(k) - Q_{OUT}(k) \quad [46]$$

$$A(k) = \frac{S(k)}{d} \quad [47]$$

$$Q_{OUT}(k) = \frac{\alpha_{QOUT}}{2}[S(k) + S(k+1)] \quad [48]$$

where:

k = Temporal index
S = Storage (m^3)
d = average depth of water (m)
r = soil water recharge depth (m)
α_E = parameter to correct bias in ET rates
E = Evapotranspiration over flooded area (m/month)
P = Precipitation over flooded area (m/month)
Q_{IN} = Sudd inflows (m^3/month)
Q_{OUT} = Sudd outflows (m^3/month)
A = Flooded area of wetland (m^2)
α_{QOUT} = linear outflow-storage term

Equations 47 and 48 can be substituted into Equation 44, and the terms can be re-arranged to solve for S(k+1) explicitly, yielding Equation 49. This model has four parameters that can be calibrated: d, r (max soil-water recharge depth), α_E, and α_{QOUT}. The optimal parameters are those that minimize the objective function, or cost, presented in Equation 50. The first two terms of this cost function quantify how well the simulated and observed flooded areas and outflows match, and the second two terms account for the differences in the timing of the maximum and minimum flooded areas. Each term is normalized by its maximum range to account for differences in units and the range of variation for each term, and each term has a weight to adjust its influence on the total cost. Through trial-and-error, a value of 1 for the 1st two weights and a value of 0.25 for the 2nd two weights resulted in each term having relatively equal magnitudes.

$$S(k+1) = \frac{\left[1 + \frac{1}{d}\left[r(k) - \frac{1}{2}\left(\alpha_E E(k) - P(k)\right)\right] - \frac{1}{2}\alpha_{Qout}\right] S(k) + Q_{IN}(k)}{1 + \frac{1}{d}\left[r(k) + \frac{1}{2}\left(\alpha_E E(k) - P(k)\right)\right] + \frac{1}{2}\alpha_{QOUT}} \quad [49]$$

$$J = \alpha_{J1}\sqrt{\frac{1}{T}\sum_{k=1}^{T}\left(\frac{A_{OBS}(k) - A_{SIM}(k)}{\max\{A_{OBS}\} - \min\{A_{OBS}\}}\right)^2} + \alpha_{J2}\sqrt{\frac{1}{T}\sum_{k=1}^{T}\left(\frac{Q_{OUT,OBS}(k) - Q_{OUT,SIM}(k)}{\max\{Q_{OUT,OBS}\} - \min\{Q_{OUT,OBS}\}}\right)^2} + \alpha_{J3}\sqrt{\frac{1}{N}\sum_{k=1}^{N}\left(\frac{t_{MAX,OBS}(k) - t_{MAX,SIM}(k)}{2}\right)^2} + \alpha_{J4}\sqrt{\frac{1}{N}\sum_{k=1}^{N}\left(\frac{t_{MIN,OBS}(k) - t_{MIN,SIM}(k)}{4}\right)^2} \quad [50]$$

where:

J = cost
k = temporal index
T = total number of observations/simulations
N = number of years of observations/simulations
A_{OBS} = observed flooded area (derived from MODIS)
A_{SIM} = Simulated flooded area from model
$Q_{OUT,OBS}$ = observed outflows (estimated from flow routing models)
$Q_{OUT,SIM}$ = simulated outflows
$t_{MAX,OBS}$ = month when maximum observed flooded area occurs
$t_{MAX,SIM}$ = month when maximum simulated flooded area occurs
$t_{MIN,OBS}$ = month when minimum observed flooded area occurs
$t_{MIN,SIM}$ = month when minimum simulated flooded area occurs
α_{J1} = weight for 1st term
α_{J2} = weight for 1st term
α_{J3} = weight for 1st term
α_{J4} = weight for 1st term

6.3.2 Model Calibration Procedure

The optimal calibrated parameters should be consistent with the physical model and support a stable water balance. Therefore, the parameter values chosen in the Sutcliffe and Parks study (water depth, *d* = 1 meter, maximum soil water recharge depth, *r* = 0.2 meters)

should be included in the range of parameters tested. When applying the same climatology ET that was used by Sutcliffe and Parks, the ET parameter (α_E) should be somewhat close to unity, and ET parameters applied to alternative ET estimates should adjust the magnitude of the ET rates to reduce the bias between estimates and ensure that the water balance is stable. The outflow parameter (α_{QOUT}) is highly dependent on the depth parameter; the depth determines the magnitude of the storage, and the outflows are a linear function of the storage. Therefore, an initial guess of the outflow parameter was determined after the depth parameter was specified. The wetland "observed" storage was estimated by simply multiplying the MODIS-derived flooded area by the specified depth, and then a linear model with zero intercept was fit between the observed outflows and storage. The coefficient from the fitted linear model was used as an initial guess of the outflow parameter. Ranges of each parameter were simulated, and the resulting objective function value was recorded. If any of the optimal parameters occurred at an upper or lower bound of its range, then the boundaries were adjusted, and the calibration was repeated. However, the maximum soil water recharge depth was constrained to 1 meter, based on previous studies that estimated this depth is approximately 0.2 to 0.35 meters. Therefore, if the optimal value of this parameter is 1 meter, then the physical structure of the model should be reconsidered.

Additionally, the specified resolution (or discretization) of the model parameters should be determined through a sensitivity analysis on the model outputs (flooded area and outflow). This sensitivity analysis could be done analytically by evaluating the partial derivatives of the model outputs with respect to each model parameter. However, these

derivatives can be difficult to compute (especially as the model increases in complexity), and the derivatives must be evaluated at a single value for each of the model fluxes and parameters. Considering the temporal variations of the fluxes and the range of the parameter space, a numerical approach provides a more holistic analysis of the sensitivity of parameters. Therefore, the following procedure was implemented to decide on the appropriate discretization of parameters:

1. For each parameter, a range of potential discretizations was identified.
2. For each potential discretization, a range of parameter values was generated to bracket a probable value of the parameter, according to previous studies.
3. For each parameter value, the Sudd water storage (Equation 49) was simulated from April 2000 to March 2014.
4. The average percent change in each of the model outputs (flooded area and outflow) were calculated from the average differences between subsequent simulations, according to Equations 51 and 52. The denominators in Equations 51 and 52 normalize the differences between simulations by the maximum fluctuation of the variable. The resulting metrics therefore measure the *normalized percent change* of the flooded areas and outflows and represent the change resulting from the discretization increment compared to the overall fluctuation of the variable.

$$AS_{\alpha,\delta} = \frac{\frac{1}{J}\sum_{j=2}^{J}\frac{1}{K}\sum_{k=1}^{K}\left|A_{SIM,k,j} - A_{SIM,k,j-1}\right|}{\max(A_{OBS}) - \min\left(A_{OBS}\right)} \quad [51]$$

$$QS_{\alpha,\delta} = \frac{\frac{1}{D}\sum_{j=2}^{J}\frac{1}{T}\sum_{k=1}^{K}\left|Q_{SIM,k,j} - Q_{SIM,k,j-1}\right|}{\max(Q_{OBS}) - \min\left(Q_{OBS}\right)} \quad [52]$$

where:

AS = Flooded area sensitivity, a normalized percent change, for parameter α and discretization δ (%)

QS = Outflow sensitivity, a normalized percent change, for parameter α and discretization δ (%)

J = Total number of increments applied for discretization δ

j = index for discretization increment.

K = Total number of time steps

k = index for time step

A_{SIM} = Simulated flooded area, from Equations 47 and 49 (m^2)

A_{OBS}= Observed flooded area, estimated in Chapter 3 (m^2)

Q_{SIM} = Simulated outflow, from Equations 48 and 49 (m^3/mo)

Q_{OBS}= Observed outflows, estimated in Chapter 4 (m^3/mo)

The results from this numerical approach are presented in Figure 90. The discretizations required for a 1% maximum normalized percent change are 0.025 meters for the water depth and maximum soil water recharge depth, 0.005 for the ET parameter, and 0.001 for the outflow parameter. The discretizations required for a 0.1% maximum normalized percent change are 0.001 meters for the water depth, 0.02 meters for the maximum soil water recharge depth, 0.0005 for the ET parameter, and 0.0001 for the outflow parameter. The computing time required to calibrate the model increases by an order of magnitude for each additional parameter and is scaled by the number of iterations; therefore, finer discretizations result in substantial increases in computing costs. One strategy to reduce computation time is to begin with a coarse discretization to bracket the optimal parameters, and subsequently apply a finer discretization to obtain a more optimal solution.

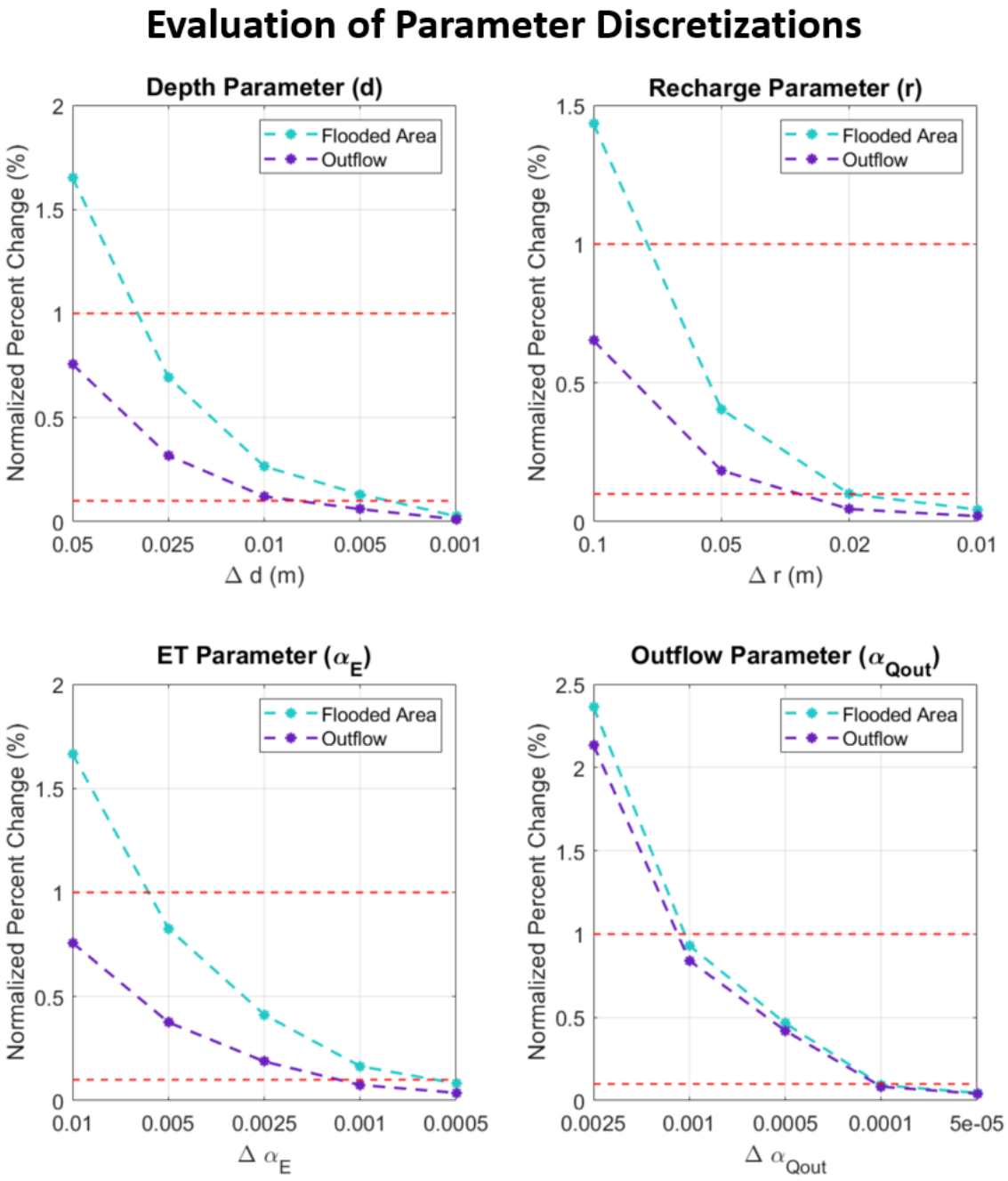

Figure 90: Results from the numerical simulation procedure that evaluates the sensitivity of model outputs to the discretization of parameters. Changes of 1% and 0.1% are highlighted with the red dashed line to aid in identifying appropriate discretization values.

6.3.3 Model Results and Discussion

For the current model with four parameters, the fine resolution discretization that corresponds with a 0.1% normalized change was applied. The Sudd water storage (Equation 49) was simulated for each parameter set using TRMM precipitation and Hargreaves ET estimates, and the parameters that minimized the objective function are listed in Table 15. Note that the maximum soil water recharge depth reached the upper boundary of 1 meter, indicating that infiltration during the rainy season is likely playing a larger role than the model currently allows.

Table 15: Optimal parameter set that minimized the cost function (Equation 50) of the reformulated Sutcliffe and Parks model (Equation 49), using TRMM precipitation and Hargreaves ET estimates.

Optimal Model Parameters			
d (m)	r (m)	α_{ET}	α_{Qout}
1.821	1.00	1.0205	0.0349

The optimal parameters were applied to Equation 49, and Figure 91 compares the resulting time series of simulated flooded areas and outflows and shows the simulated storage in the wetland. Scatter plots comparing the simulated and observed flooded areas and outflows are presented in Figure 92. These figures indicate that this model cannot adequately simulate both the Sudd flooded areas and the outflows, and there is typically a trade-off between the two. For example, during the low-flow period from 2009 to 2012, the model overestimates the outflows and underestimates the flooded area. Additionally,

the intra-annual variation of the simulated flooded area is significantly lower than that of the MODIS-observed area. This misalignment could be reduced by decreasing the depth parameter, but the magnitude of the errors between the simulated and observed maximum flood extents would increase. Additionally, because both the flooded areas and the outflows are functions of the storage, the intra-annual variations of the simulated outflows would also increase and align poorly with the estimated outflows.

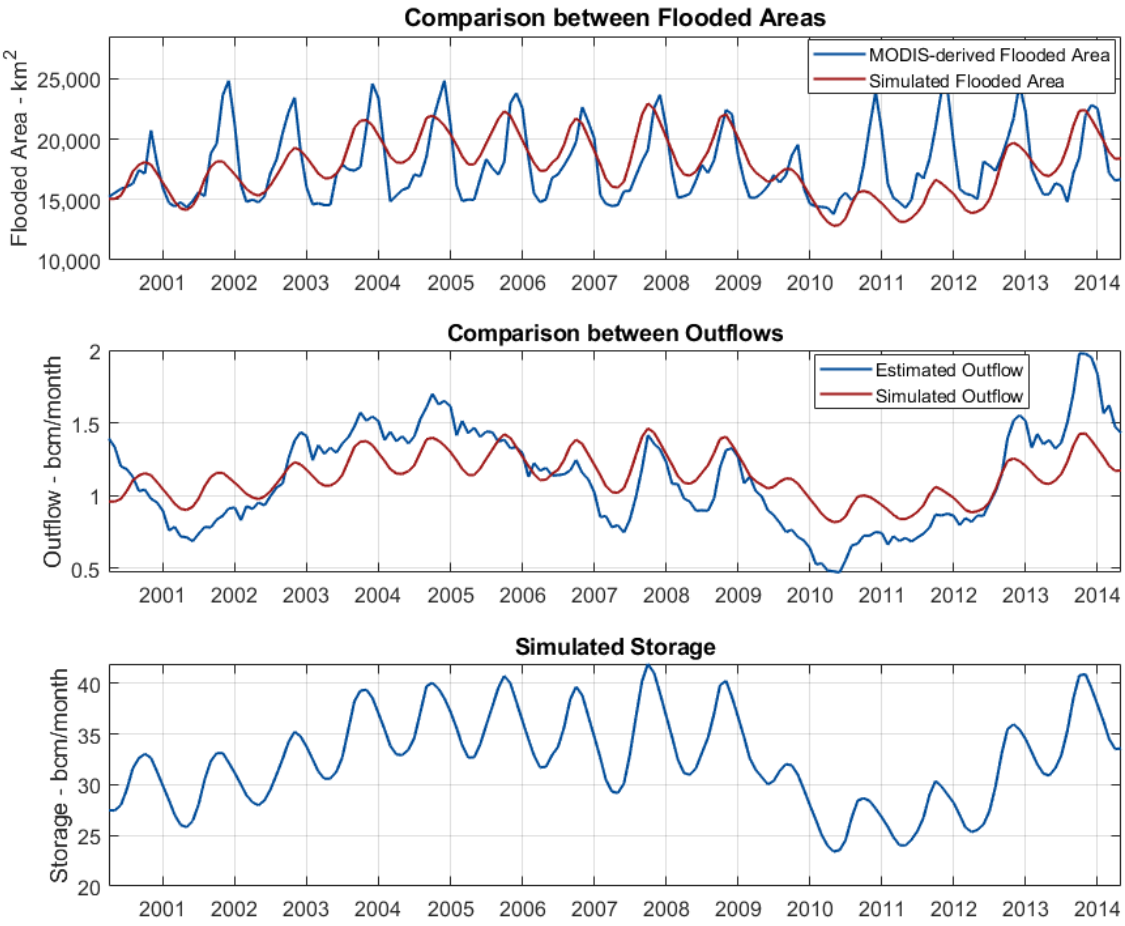

Figure 91: Time series simulation results for the reformulated and calibrated Sutcliffe and Parks model, using TRMM precipitation and Hargreaves ET estimates.

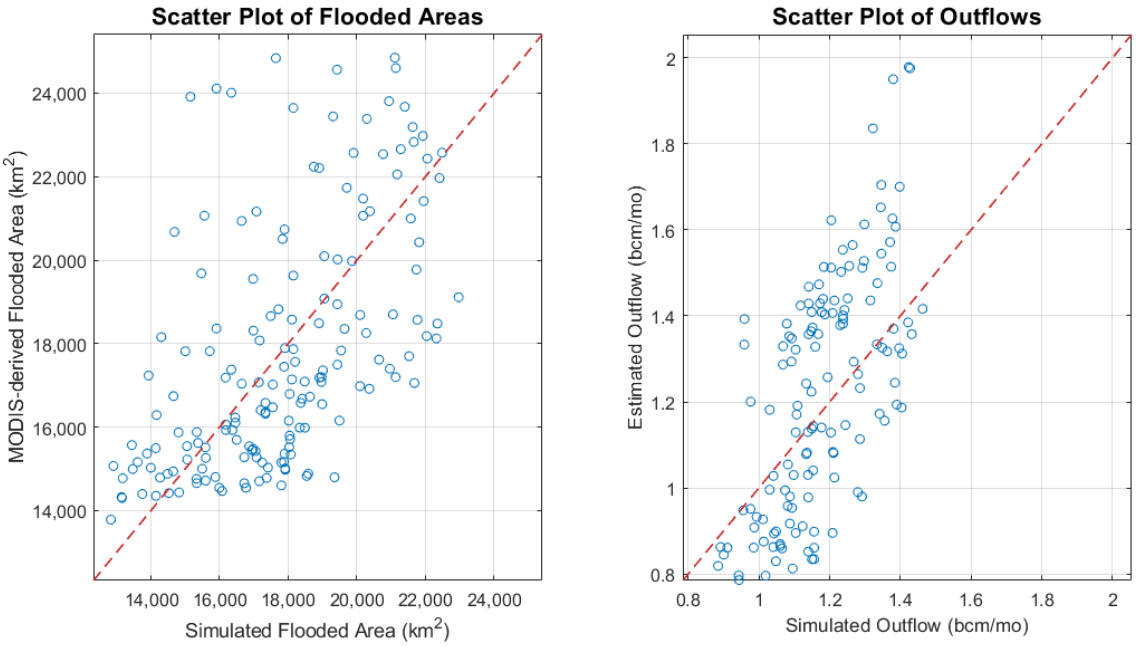

Figure 92: Scatter plots comparing the simulated and observed flooded areas and outflows for the reformulated and calibrated Sutcliffe and Parks model, using TRMM precipitation and Hargreaves ET estimates.

The sum of the objective function terms was 0.759, and the individual values are listed in Table 16. Note that the terms associated with the flooded area extents (1 and 3) are greater than the terms associated with the outflows (2 and 4), but as mentioned previously there is a trade-off in performance between the flooded areas and outflows. Some standard statistical metrics quantifying the fit between the flooded areas and outflows are listed in Table 17, including the root mean square error (RMSE), mean absolute error (MAE), Pearson's correlation coefficient (PCC), mean absolute bias (MAB), and Nash-Sutcliffe Efficiency (NSE) coefficient. These metrics will be calculated for alternative model simulations and can be used to compare the performance of different model structures, in addition to the object function.

Table 16: Individual vales of the objective function (Equation 50) from the calibrated and reformulated Sutcliffe and Parks model using TRMM precipitation and Hargreaves ET estimates.

Objective Function Terms			
J(1)	J(2)	J(3)	J(4)
0.225	0.153	0.209	0.166

Table 17: Statistical metrics calculated between the simulated and observed flooded areas and outflows, from the calibrated and reformulated Sutcliffe and Parks model using TRMM precipitation and Hargreaves ET estimates.

	Statistical Metrics				
	RMSE	MAE	PCC	MAB	NSE
Flooded Area (km^2)	2,542	1,983	0.56	18	-
Outflow (bcm/mo)	0.231	0.199	0.78	0.016	0.52

This model was also calibrated for different combinations of precipitation and ET fluxes. There were notable differences in the optimal parameter sets and performance metrics; however, the general model performance and limitations were similar for all flux combinations. The optimal recharge parameter for all model runs reached the upper bound of 1 meter, and none of optimal simulations accurately produced both flooded areas and outflows.

The inability of the model to produce both the flooded areas and outflows is not surprising. The MODIS-derived area and estimated outflow time series are assumed to be linear functions of the same surface water storage, yet they behave very differently. The flooded area time series has a strong seasonal fluctuation and a minimal multi-year trend, whereas the estimated outflows generally have lower seasonal fluctuations and more significant multi-year trends. Therefore, capturing the behavior of both time series is difficult when they are dependent on the same state variable (total surface water storage) and have similar mathematical relationships. To test whether the simulations would improve with non-linear relationships, two additional parameters were introduced, and the relationships shown in Equations 53 and 54 were calibrated. The resulting optimal non-linear terms (*m1* & *m2*) were very close to a value of 1, and there was not a significant decrease in the objective function.

$$S(k) = dA(k)^{m1} \quad [53]$$

$$Q_{OUT}(k) = \frac{\alpha_{QOUT}}{2}[S(k) + S(k+1)]^{m2} \quad [54]$$

Therefore, this model cannot be significantly improved solely by using alternative input data sources or implementing more complex, non-linear relationships. Alternatively, the model is likely misrepresenting hydrologic processes, in terms of both magnitude and timing. To further investigate these model limitations and identify an improved model structure, the Sudd water fluxes and the relationships between them were closely examined. Key findings from this investigation are presented and summarized in Section 6.4.

6.4 Evaluation of Sudd Fluxes and Storage-Area-Outflow Relationships

6.4.1 Sudd Fluxes

To develop strategies for improving the hydrologic model presented in Section 6.3, the Sudd water storage was simulated according to Equation 55 using the observed flooded areas and outflows. The structure of Equation 55 differs slightly from that of Equation 46 because the observed flooded area represents the middle of the month as opposed to the beginning or end of the month. When using the *observed* fluxes as opposed to the *simulated* fluxes, the associated storage values should more accurately represent the true water storage of the Sudd if the observations are accurate. The climatology ET and TRMM precipitation rates were applied to limit the complexity of this initial model, based on Sutcliffe and Parks' finding that these ET rates provided a stable mass-balance of the system and did not require any bias correction. However, the simulated storages shown in Figure 93 have a significant upward trend. This instability could be attributed to limitations of the MODIS flood detection algorithm described in Section 3.6. Specifically, detecting when the areas with permanently flooded vegetation become dry is challenging, and consequently the minimum flooded area each year may be overestimated. This overestimation might accumulate over a multi-year simulation and result in an upward trend in storage. The upward trend may also be attributed to errors in the TRMM precipitation data product or the flow estimates, which relied on uncertain data sources and both physical and statistical models. Alternatively, the instability of the simulated storage could indicate that the structure of the model does not accurately portray the Sudd or that the model parameters need to be adjusted.

$$S(k+1) = S(k) + [P(k) - E(k)]A_{OBS}(k) - \frac{r(k)}{2}[A_{OBS}(k+1) - A_{OBS}(k-1)] + Q_{IN}(k) - Q_{OUT,OBS}(k) \quad [55]$$

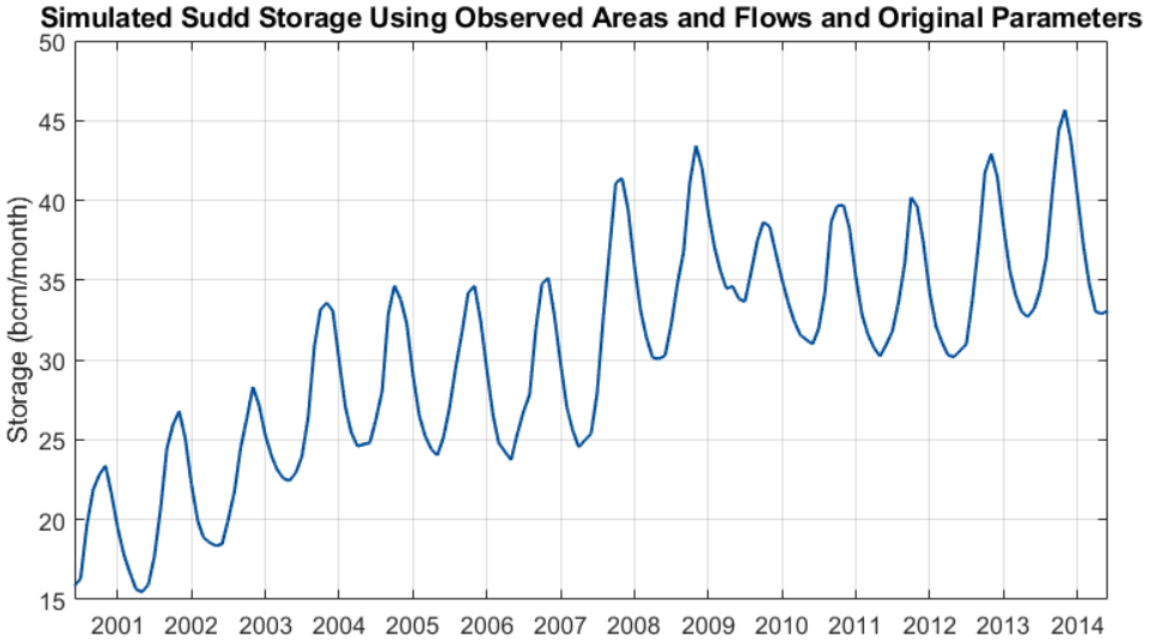

Figure 93: Simulated water storage in the Sudd using the observed flooded areas and outflows, the climatology ET and TRMM precipitation rates, and original model structure and parameters from Sutcliffe and Parks.

To correct the upward trend in Figure 93, a parameter was applied to the climatology ET (α_E). A value of 1.03 provided a more stable storage, as shown in Figure 94. While the storage stabilizes by the end of the 2000 to 2014 period, the minimum storage varies each year, conflicting with the MODIS-derived flooded areas that suggest the wetland returns to a similar state each year during the dry season. This disagreement between the observed flooded areas and the simulate storage is problematic considering the flooded areas are modeled as a function of the storage in the predictive model.

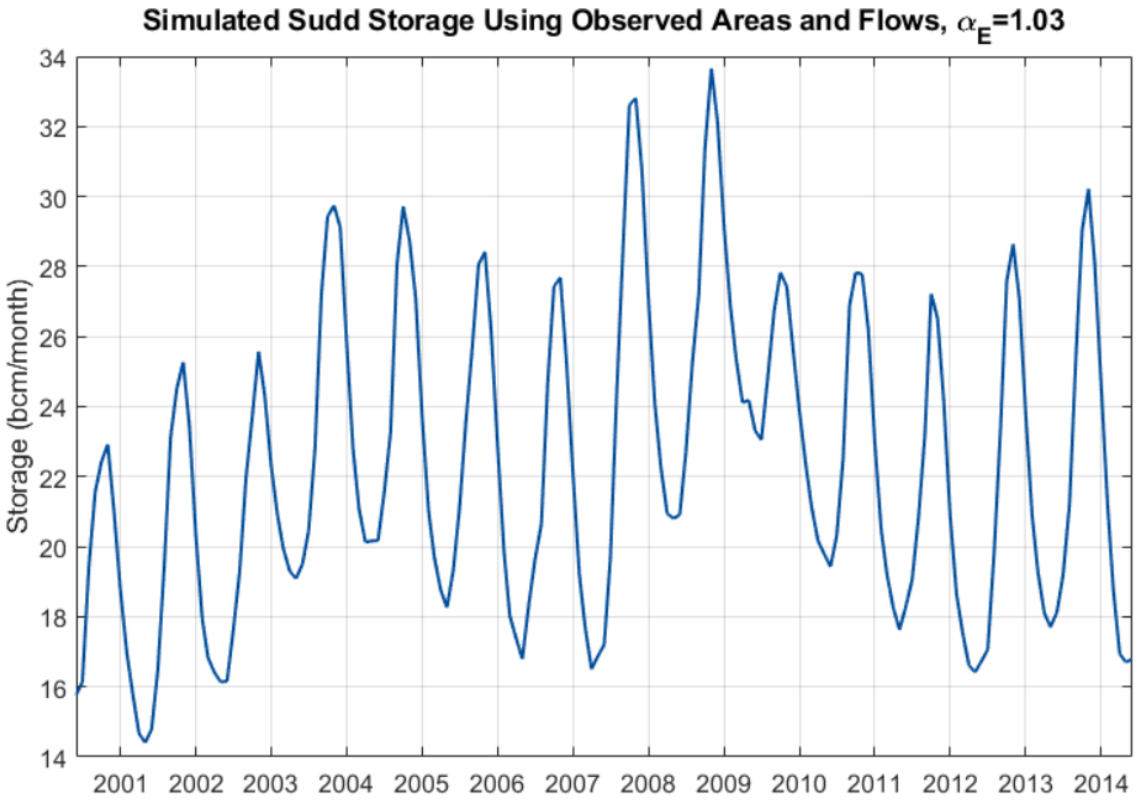

Figure 94: Simulated water storage in the Sudd using the observed flooded areas and outflows, climatology ET and TRMM precipitation rates, the original model structure, and an ET parameter to correct for the upward trend in storage.

The individual flux terms in Equation 55 are plotted in Figure 95. This Figure illustrates the relative importance of fluxes in the water mass balance equation. According to this simulation, the net precipitation minus ET flux plays a significant role in the Sudd balance. Because the precipitation and ET fluxes are weighted by the Sudd flooded area extents, the flooded area extents are largely responsible for the variability in surface water storage. Therefore, the form of the physical relationship between the storage and flooded area is a critical component of the hydrologic model and should be closely evaluated.

Additionally, the precipitation and ET fluxes account for nearly all the losses in the Sudd, and the soil water recharge flux is almost negligible. When this model was calibrated using the observed areas and outflows in Section 6.3, the maximum recharge depth reached the upper boundary of the parameter space allowed, suggesting that infiltration is more important than the current model allows. Therefore, alternative model formulations should allow infiltration to play a larger role in the Sudd water balance. An additional limitation of the current model with regards to infiltration is that the groundwater flux is one-way; surface water from the wetland can vertically infiltrate into the soil while the wetland is expanding, but shallow sub-surface groundwater cannot re-enter the wetland when it is contracting. Alternative models should also consider horizontal groundwater fluxes and whether a two-way flux between the surface water and groundwater is warranted.

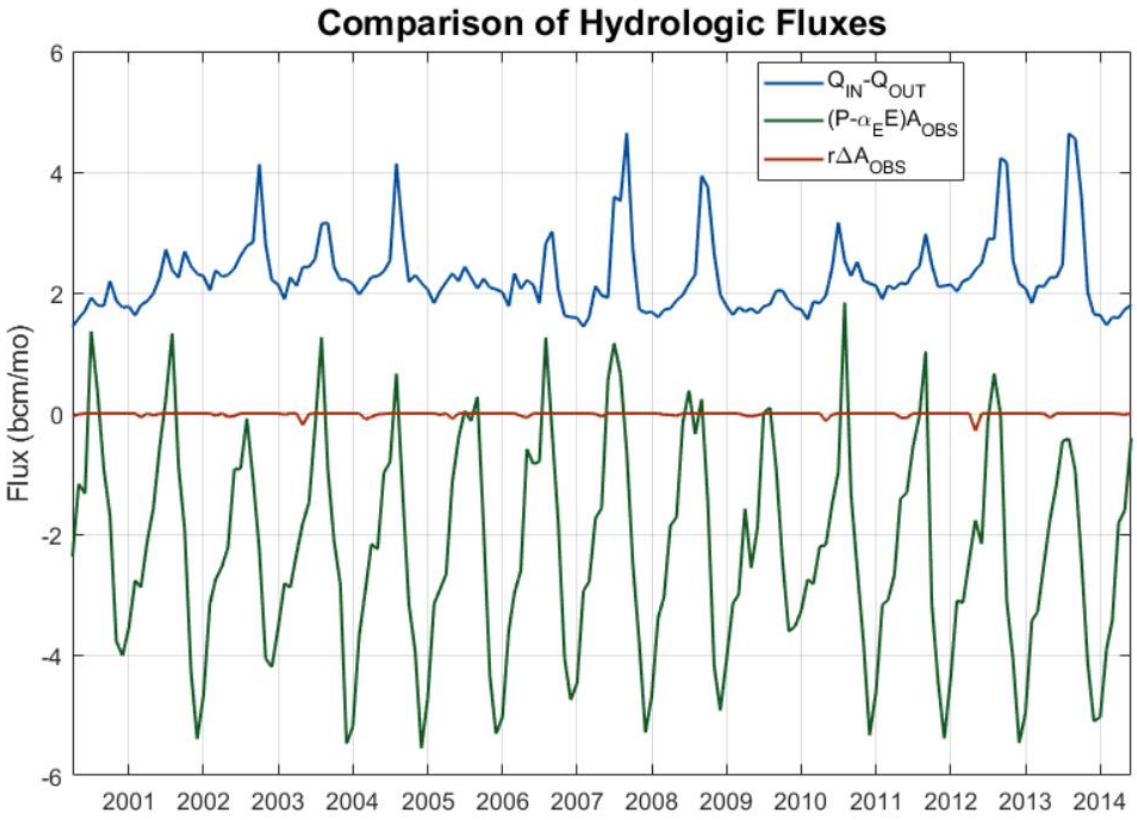

Figure 95: Comparison of individual fluxes in the Sudd water storage simulation, calculated according to Equation 51.

6.4.2 Area-Storage Relationship

Considering the primary objective of the Sudd model is to generate the flooded area and outflow time series, the mathematical forms of the relationships between the storage, flooded area, and outflow should be closely examined. A comparison between the MODIS-derived areas and the simulated storage (calculated from Equation 55) is provided in Figure 96. The MODIS-derived areas were first adjusted to align temporally with simulated storages, occurring at the beginning or end of each month as opposed to the middle of the month, using linear interpolation. The simulated storage was derived from a model that is

likely misrepresenting or ignoring important hydrologic processes. However, the MODIS-observed flooded areas were directly applied to the simulation, so these are the storage values that would exactly match the MODIS-observed flooded areas using the current model. Therefore, the relationship between these simulated storages and the MODIS-observed flooded areas should provide insight on the true relationship between the storage and area. This relationship is a critical component of the predictive model that will simulate the Sudd flooded areas.

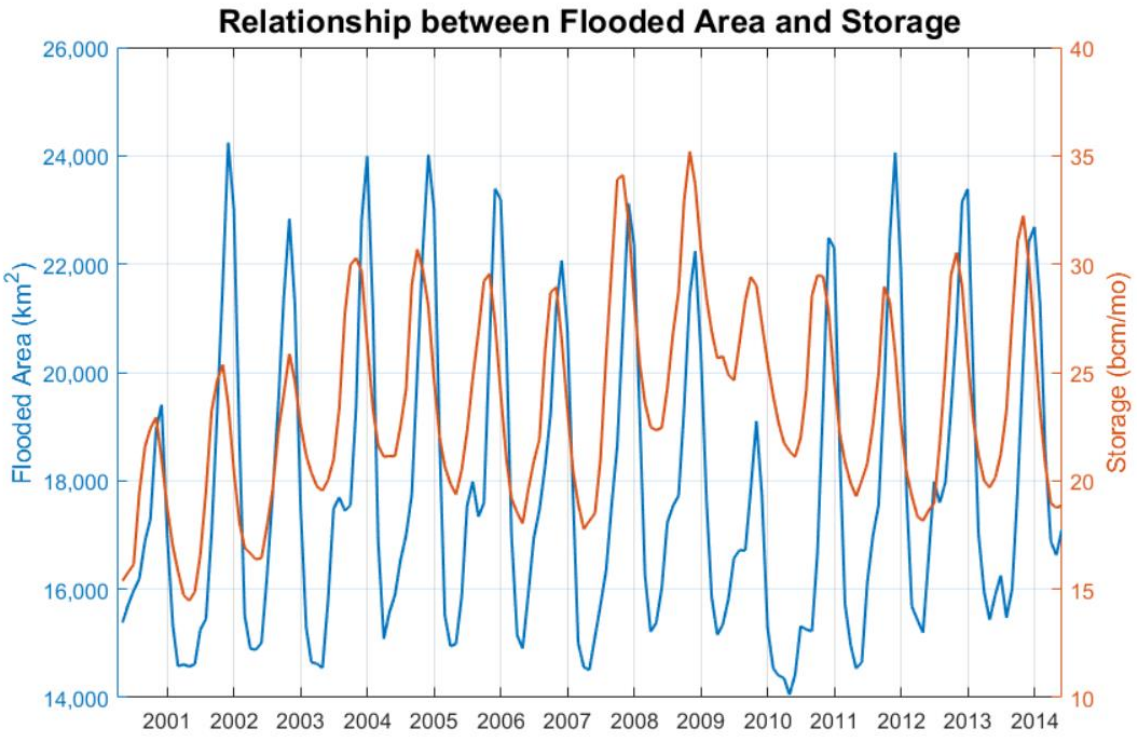

Figure 96: Comparison between the simulated storage in the Sudd and the MODIS-derived flooded area to evaluate the model representation of the storage-area relationship.

Figure 96 shows that there is clearly a temporal lag between the simulated storages and the flooded areas. The peak in the storage typically occurs before the peak in flooded

area. Several lags were applied to the flooded area time series, and the resulting Pearson's correlation coefficients are listed in Table 18. The maximum correlation occurs for a lag of 1.5 months. The physical reason for this behavior is that the surface water in the Sudd moves very slowly through the dense vegetation, and travel times could easily exceed one month based on the distance the water must travel to reach the outer extents of the wetland. Petersen and Fohrer [2010] estimated that the velocity of water through the papyrus and reed areas was approximately 0.001 to 0.01 meters per second. Based on a visual interpretation of satellite imagery available in Google Earth and using the built-in distance tool, the distance between some of the Sudd channels and the outer extents of the wetland can exceed 40 kilometers. Assuming a velocity of 0.001 to 0.01 meters per second, the travel time between the channel and outer wetland extents could take anywhere from 2 months to several years (by which time the water would have evaporated). Petersen and Fohler also estimated that the velocity of water in the channels is approximately 0.5 meters per second. A rough estimate of the length of the river reach between the Sudd entrance and exit is 550 kilometers (also inferred from Google Earth imagery and ignoring river meanders). Using this crude, conservative estimate, it could take an additional 12 days for water to flow through the Sudd channels before it reaches a point where it begins to spill into the floodplains. Therefore, the observed lags between the simulated storage and MODIS-observed flooded areas seems realistic.

Table 18: Pearson's correlation coefficients (PCC) for temporal lags applied between the MODIS-observed flooded areas and simulated water storage time series.

Lag	*0*	*0.5 months*	*1 month*	*1.5 months*	*2 months*
PCC	0.493	0.603	0.681	0.708	0.687

To begin exploring the "true" form of the relationship between the Sudd water storage and the flood area, various simple linear models were fit to the data using least squares regression. These models are presented and summarized in Table 19. In each of these models, all terms were considered highly significant according to the p-value. The best performing model used a combination of the storage for all three monthly lags. For the single variable models, the model parameters associated with the storage terms can still represent the depth of the water in the wetland, but this physical meaning is lost for the multivariate models. Instead, the parameters for the multivariate models represent the fraction of the flooded area that results from fluxes during the current and previous months. However, the parameters in the multivariate models should all be positive to align with this physical interpretation, which is not the case. The intercept terms in all models could be considered to represent the minimum flooded area of the wetland (typically 8,000 to 9,000 km^2). Scatter plots between the storage and area for different monthly lags are shown in Figure 97, along with the fitted single variable linear models. These plots show that there is a significant amount of scatter in the relationship between the storage and area, and it does not appear that a nonlinear model would provide a significant improvement.

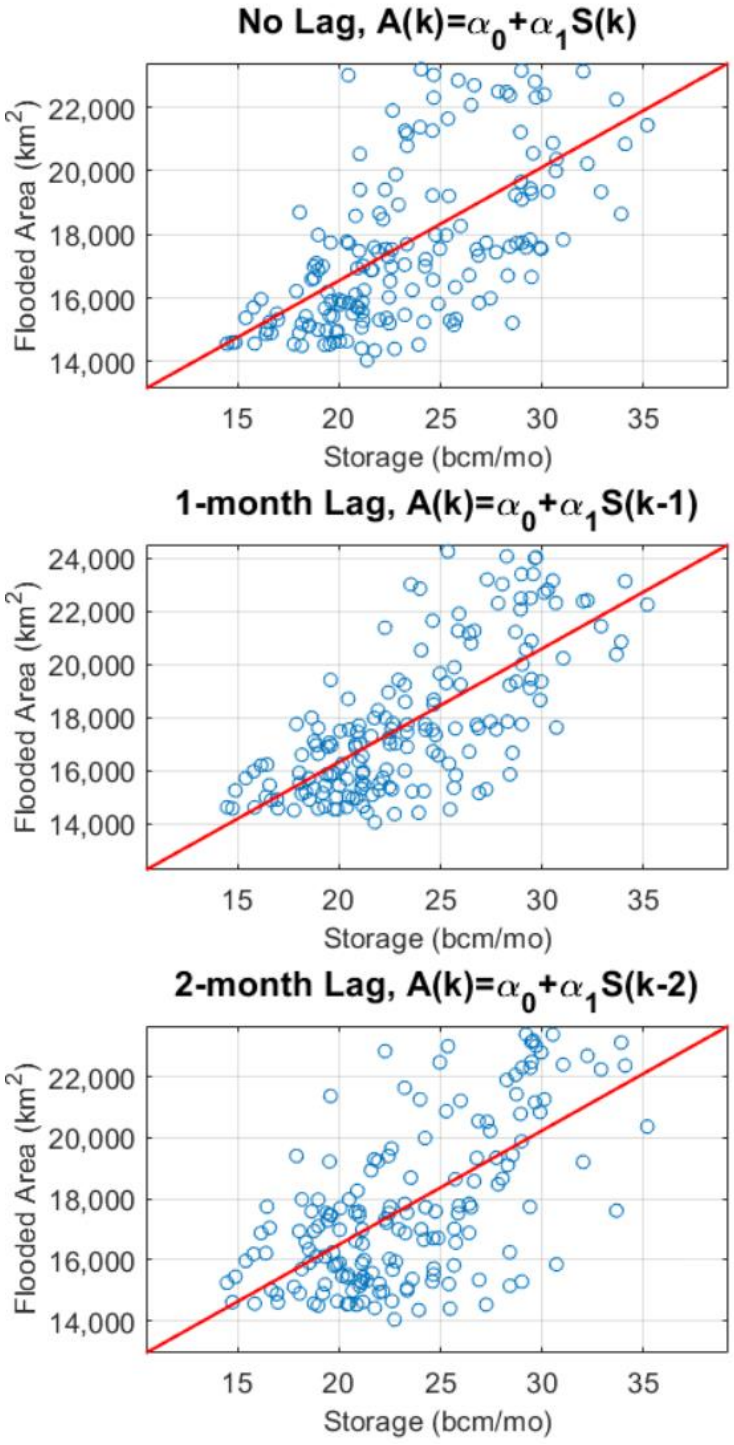

Figure 97: Scatter plots between simulated storages and MODIS-observed flooded areas for different monthly lags, with fitted linear models shown in red.

Table 19: Summary of linear models tested for different lags between the MODIS-observed areas (A) in units of m^2 and the simulated storages (S) in units of m^3, where k corresponds to a monthly time step, the alpha terms are fitted model coefficients, and RMSE represents the root mean square error of the model.

Model	α_0	α_1	α_2	α_3	r^2	RMSE (km^2)
$A(k) = \alpha_0 + \alpha_1 S(k)$	$9.443*10^9$	0.356	-	-	0.352	2,210
$A(k) = \alpha_0 + \alpha_1 S(k-1)$	$7.798*10^9$	0.426	-	-	0.508	1,930
$A(k) = \alpha_0 + \alpha_1 S(k-2)$	$9.050*10^9$	0.373	-	-	0.389	2,140
$A(k) = \alpha_0 + \alpha_1 S(k) + \alpha_2 S(k-1)$	$8.134*10^9$	-0.144	0.556	-	0.520	1,910
$A(k) = \alpha_0 + \alpha_1 S(k) + \alpha_2 S(k-1) + \alpha_3 S(k-2)$	$9.343*10^9$	-0.632	1.511	-0.576	0.572	1,810

Close examination of the time series comparison in Figure 96 led to the observation that the temporal lag between the flooded area and storage varies seasonally. The lag is shorter during the dry season and longer during the wet season. Again, this observation makes sense physically considering there is less water spilling outward into the farthest reaches of the wetland during the dry season. This seasonal variation in the temporal lag is also supported by the fact that the best performing linear regression models depend on the storage at multiple lags. Therefore, an analysis of the storage and area time series was performed to determine whether the form of the relationship between the flooded area and storage should change seasonally. The following three options were explored:

1) There are no temporal lags between the storage and flooded area.
2) There is no temporal lag between the storage and area during the dry season, but there is suddenly a **one-month lag** that is sustained at least until the wetland reaches its maximum extent. This lag ends during the dry season the following year.

3) There is no temporal lag between the storage and area during the dry season, but there is suddenly a **one-month lag, followed by a two-month lag** that is sustained at least until the wetland reaches its maximum extent. The two-month and subsequently the one-month lag end during the dry season in the following year.

The optimal months when the temporal lags should begin and end for each of the two options were identified for each year of 2000 to 2014 period. The monthly sequences are considered optimal if they maximize the correlation between the flooded area and lagged storage annual time series. A flood year is assumed to begin in March and end in April of the following year, to align with the driest time of year, when the wetland is at its minimum extent. However, the year 2000 to 2001 was omitted because the MODIS-observed flooded area maps are not available until March, and there is not enough data to simulate the storage when accounting for the temporal lags. The resulting Pearson's correlation coefficients for each of these options and the associated optimal months are listed in Table 20.

Table 20: Summary of results from the analysis of whether the relationship between storage and area should change seasonally. The Pearson's correlation coefficients (PCC) are shown for the optimal months for each lag. The lags with the optimal correlation coefficients and the associated optimal months are highlighted in yellow.

Year	Lag-0 PCC	Lag-1 PCC	Lag-1 Start	Lag-1 End	Lag-2 PCC	Lag-1 Start	Lag-2 Start	Lag-2 End	Lag-1 End
01-02	0.773	0.962	Aug	Mar	0.979	Aug	Sep	Dec	Mar
02-03	0.854	0.824	Nov	Jan					
03-04	0.657	0.876	Sep	Apr	0.958	Sep	Oct	Feb	Mar
04-05	0.729	0.950	Aug	Mar	0.984	May	Sep	Feb	Mar
05-06	0.580	0.868	Aug	Apr	0.960	Aug	Sep	Feb	Apr
06-07	0.862	0.973	Sep	Mar	0.973	Sep	Dec	Jan	Mar
07-08	0.821	0.958	Aug	Mar	0.977	Aug	Oct	Feb	Mar
08-09	0.908	0.925	Sep	Jan	0.907	Sep	Dec	Jan	Feb
09-10	0.853	0.889	Sep	Jan	0.887	May	Jun	Sep	Jan
10-11	0.507	0.836	Aug	Apr	0.954	Aug	Sep	Feb	Mar
11-12	0.776	0.971	Jun	Apr	0.980	Jun	Dec	Feb	Mar
12-13	0.800	0.947	Sep	Mar	0.961	Sep	Nov	Feb	Feb
13-14	0.564	0.887	Jun	Apr	0.968	Jun	Aug	Jan	Mar

Apart from 2002 to 2003, the correlation between the flooded area and storage increased substantially if temporal lags were introduced at the associated optimal months. A one-month lag was optimal for years that generally had lower flows and smaller flooded area extents, and a two-month lag was optimal for more typical flood cycles. Again, this result supports the idea that the lag between the storage and area should be greater when the flood water must travel longer distances.

Using the information in Table 20, an adjusted storage time series was constructed that would optimize the correlation between the area and storage. This adjusted time series is compared to the original flooded area time series in Figure 98, and a scatter plot comparison along with a fitted linear relationship is presented in Figure 99. The optimal linear model is displayed in Equation 56, where S_{CON} represents the constructed storage

time series (in units of cubic meters). The model r^2 is 0.618, and the RMSE is 1,750 km^2. This model outperforms all models presented in Table 19 and has only two parameters. Additionally, the scatter plot in Figure 99 has less scatter than those presented in Figure 97, and the area-storage relationship is more linear.

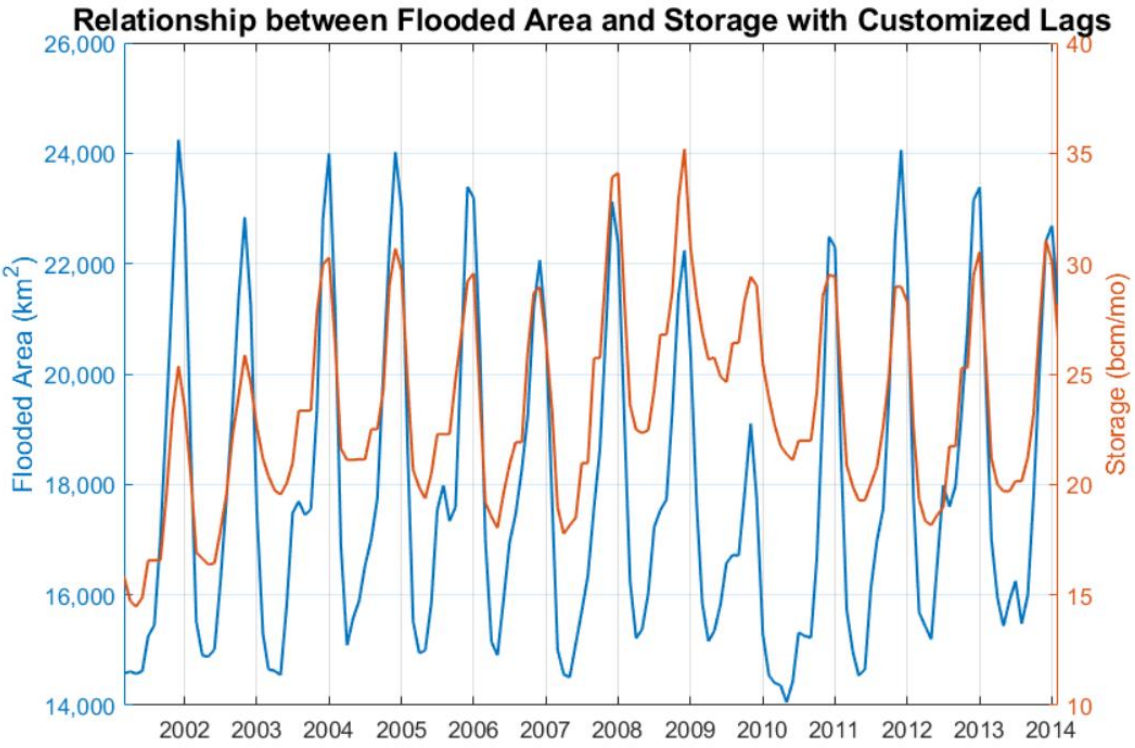

Figure 98: Comparison between the original MODIS-observed flooded areas and the constructed storage time series with optimal temporal lags applied.

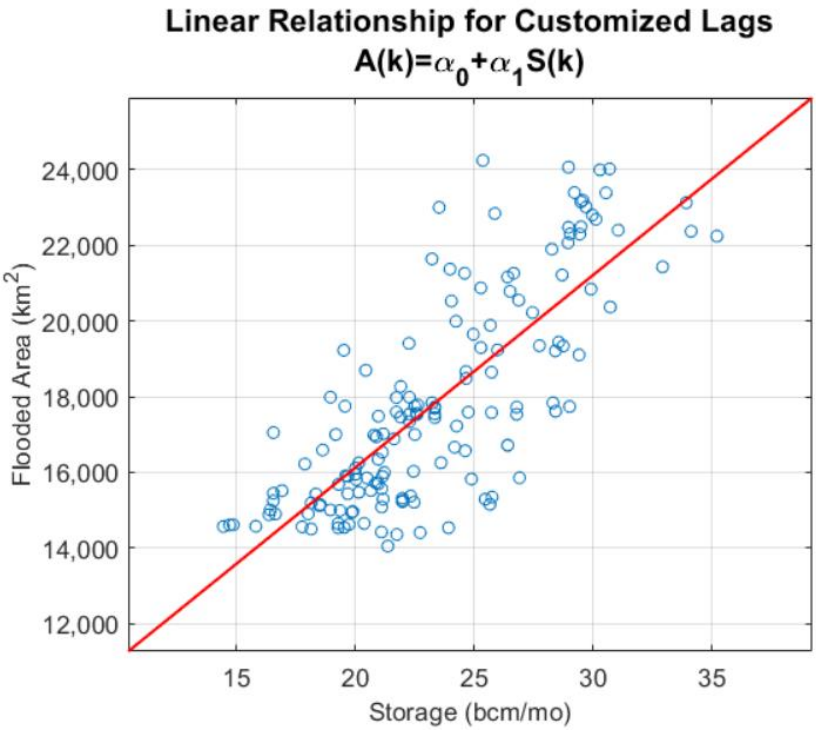

Figure 99: Scatter plot comparing optimal constructed storage values to original MODIS-observed flooded areas, with fitted linear model shown in red.

$$A(k) = 5.943 \times 10^9 + 0.5091\left(S_{CON}(k)\right) \quad [56]$$

While this lag correlation analysis resulted in an improved model, it cannot directly be applied to the simulated storages in the predictive hydrologic model. The predictive hydrologic model must simulate the flooded areas when observations are not available, and the observed flooded areas were required to determine the optimal lags. Additionally, the model may be overfit to the relatively short time period of available observed flooded areas if the temporal lags were applied to the storages with the level of detail described in this analysis. Ideally, the temporal lags could be determined according to information that is independent of the flooded area observations, such as the flows or precipitation values or the magnitude of the simulated storage. Therefore, various representations of the Sudd

fluxes were evaluated for the optimal months listed in Table 20 with the goal of identifying a consistent pattern. This pattern could then be exploited to establish rules for determining series of area-storage relationships that vary for each flood year. However, a consistent pattern across all years could not be identified.

A pattern might emerge once the structure of the model is more representative of the Sudd hydrology, or if the Sudd could be split into multiple sub-basins that have different storage-attenuation characteristics. Another option is to determine the area-storage relationships for all flood years using the results in Table 20. If the average optimal months were selected for the two-month lag option, then the first lag would take effect in July, the second lag would take effect in October, the second lag would end in January, and the first lag would end in March. A lagged storage time series was constructed using these standardized transitions, and a new linear model was fit between the flooded area and storage. The resulting scatter plot and fitted linear model is presented in Figure 100. The model r^2 decreased substantially from that of the customized lags, from 0.62 to 0.51, which is also reflected in the increased amount of scatter in Figure 100. This model no longer outperforms those listed in Table 19. Therefore, unless a reliable pattern can be exploited that can inform the monthly lag transitions, the area-storage models should not vary temporally.

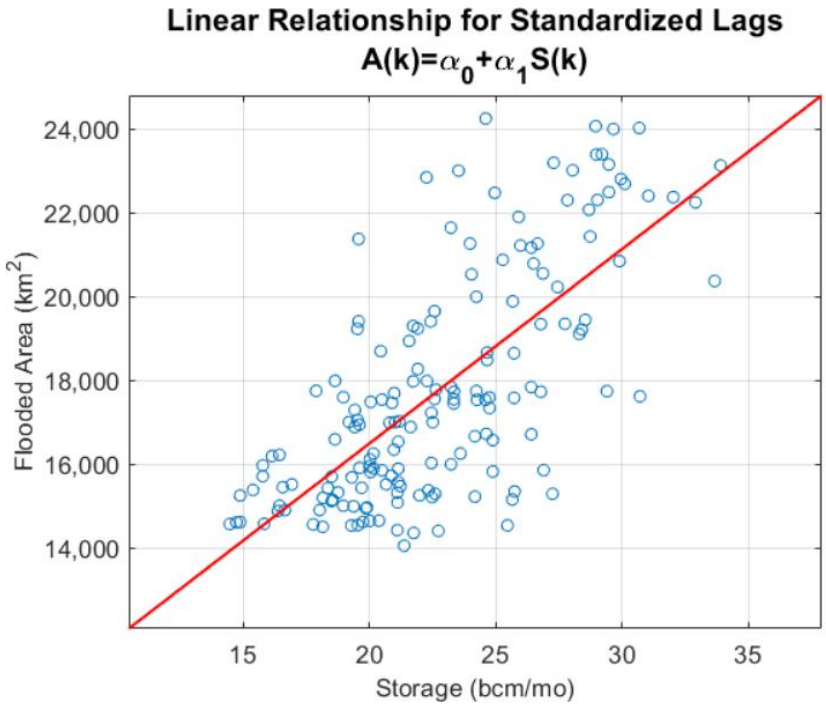

Figure 100: Scatter plot and fitted linear relationship between the lagged storage time series that was standardized across all years and the MODIS-observed flooded areas.

The analysis of the sequential lag relationships and the fitted models listed in Table 19 suggest that the flooded areas should ideally be dependent on storages from multiple time steps. However, if a single time step were to be chosen to reduce the model complexity, then the storage should be lagged by one month. Therefore, the second and fifth models listed in Table 19 will be tested in a revised model of the Sudd. As mentioned previously, the intercept terms in these models could be considered the minimum flooded area. If this substitution was made, then one of the model parameters could be eliminated. The two models of interest were therefore recalibrated using the minimum flooded area as the intercept term, and the minimum storage value was subtracted from storages to be consistent. These calibrated models and presented in Equations 57 and 58, where the area

is in units of square meters. An updated scatter plot for the single variable model is shown in Figure 101. The r^2 value associated with the single variable model increased from 0.51 to 0.53, and the r^2 value for the multivariate model increased from 0.57 to 0.61. Both area-storage models will be tested in the revised hydrologic model, and the model parameters will be treated as calibration parameters. However, for the multi-variate model, the parameters values will be restricted to positive values to ensure that the storage-area relationship has physical meaning. Any improved accuracy from applying the multivariate model will be balanced against its increased complexity to ensure model parsimony.

$$A(k) = 13.783 * 10^9 + 0.4422(S(k-1) - 14.464 * 10^9) \quad [57]$$

$$\begin{aligned} A(k) = {} & 13.783 * 10^9 - 0.3857(S(k) - 14.464 * 10^9) \\ & + 1.1459(S(k-1) - 14.464 * 10^9) \\ & - 0.3337(S(k-2) - 14.464 * 10^9) \end{aligned} \quad [58]$$

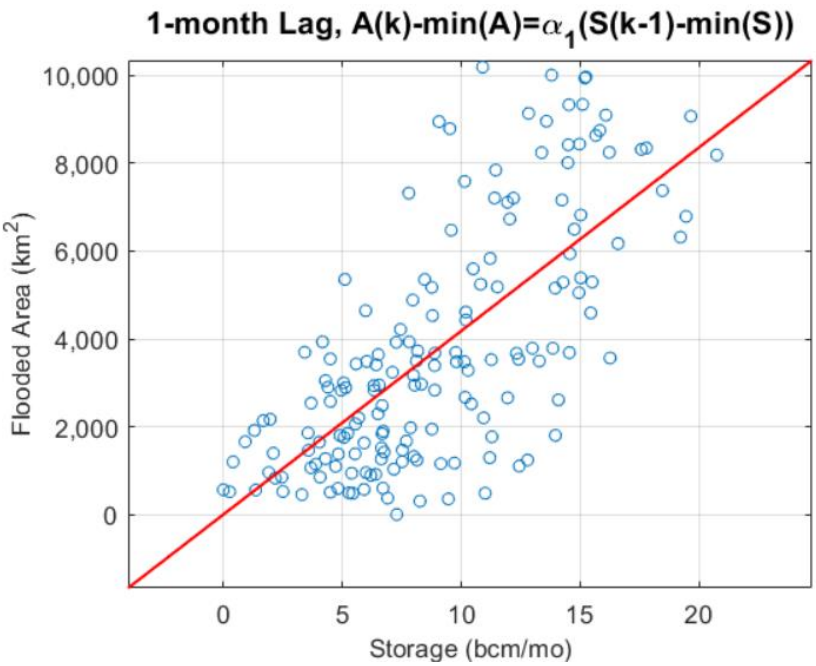

Figure 101: Scatter plot between simulated storages and MODIS-observed areas for the single variable model with a one-month lag applied.

6.4.3 Outflow-Storage Relationship

The hydrologic model presented previously in Section 6.3 also models the Sudd outflows as linear function of the storage. The relationship between the outflow and storage should therefore be assessed. Similar to the MODIS-observed flooded areas, the outflows were first interpolated to align temporally with the simulated storages (the beginning or end of the month as opposed to the middle of the month). A comparison between the outflow and storage time series in presented in Figure 102. Like the flooded area time series comparison, the peak in the outflows tends to occur after the peak in the simulated storage. The Pearson's correlation coefficients between the time series with various lags applied

are listed in Table 21. The maximum correlation occurs for a 1-month lag. This temporal lag is realistic considering the long flow travel times that were previously discussed.

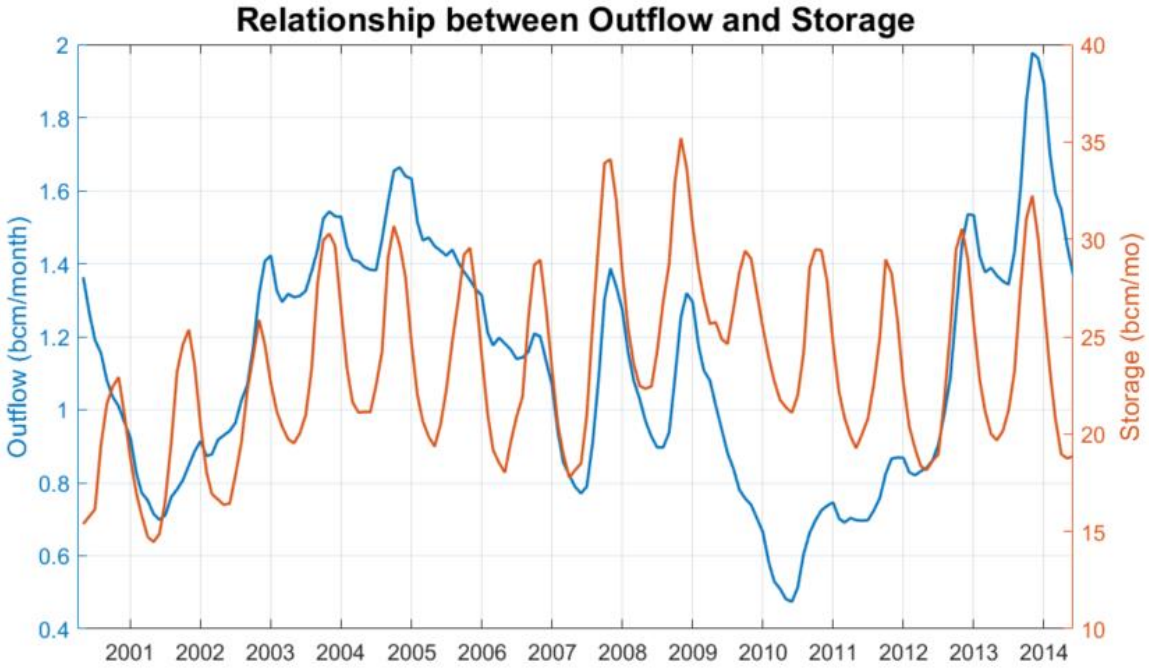

Figure 102: Comparison between the simulated Sudd water storage and the Sudd outflows to assess whether a relationship exists.

Table 21: Pearson's correlation coefficients (PCC) between observed outflows and simulate water storage for various temporal lags.

Lag	*0*	*0.5 months*	*1 month*	*1.5 months*	*2 months*
PCC	0.320	0.339	0.342	0.324	0.293

A scatter plot comparing the estimated outflows and simulated storages with a 1-month lag is shown in Figure 103, along with a fitted linear model. The r^2 value for this model is only 0.11, and the lack of correlation is visible in Figure 103. The modeling exercise in Section 6.3 discussed how the MODIS-observed flooded areas and the outflows have very different behaviors and should not be modeled from the same state variable. Considering the poor relationship between the outflow and simulated storage, the outflow should be modeled from a new state variable that can account for the temporal lag between the simulated storage and the outflow. This state variable will represent the water stored in a routing compartment. The routing compartment will receive a fraction of the water in the main surface water storage compartment that is used to model the flooded area each month and will have the ability to store this water prior to releasing it as the Sudd outflow. Similar to the area-storage relationship, the outflow-storage relationship should have an intercept term that represents the minimum Sudd outflows. The mathematical formulation of the routing compartment is presented in Section 6.5.

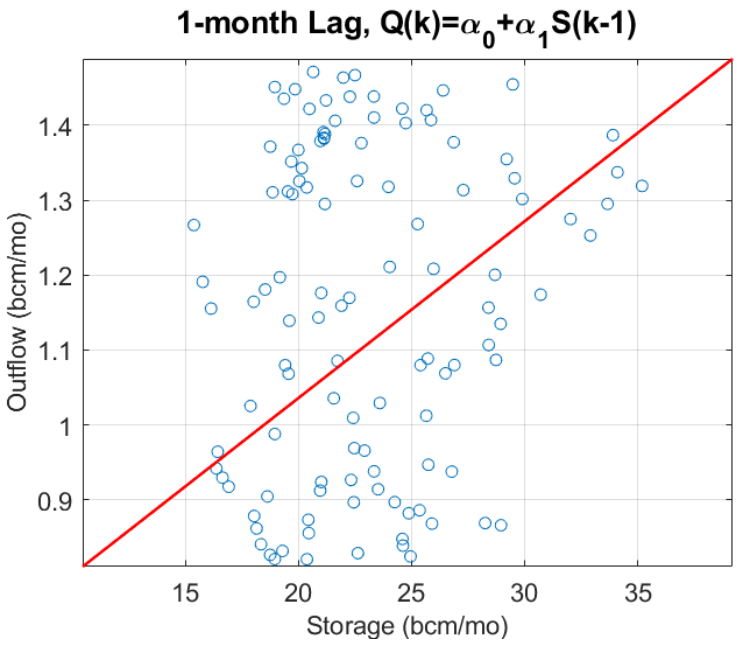

Figure 103: Scatter plot between observed outflows and the simulated storage, lagged backward 1 month. A fitted linear model is shown in red.

The evaluation of the Sudd fluxes and storage-area-outflow relationships presented in this Section lead to the following three key insights that have informed the revised model presented in Section 6.5:

1) The flux between the surface water and groundwater is likely more significant than the current model allows, and this flux should be evaluated in both directions, when the wetland is both expanding and contracting.
2) The Sudd flooded area at time k should be modeled as a function of the simulated storage from time k-1, or from a combination of time k, k-1, and k-2, and the intercept term should be the minimum observed flooded area.

3) The Sudd outflows should be modeled from a new state variable that represents a routing compartment of the wetland. The outflow-storage relationship should also have an intercept term that is the minimum Sudd outflow.

6.5 Revised Hydrologic Model

6.5.1 Model Overview

The governing mass balance equations for the revised Sudd hydrologic model are presented in Equations 59 through 63. The second storage simulation (*S2*) described in Equation 59 represents a flow routing compartment that is used to model the Sudd outflows. The routing compartment receives water from the surface water storage compartment (*S1*), and the amount is determined by the linear α_{Q12} parameter shown in Equation 58. The flux between the two compartments (Q_{12}) represents the total amount of water exchanged in a one-month interval and is therefore a function of the *S1* storage at the beginning and end of the month. The relationship between the simulated storage and flooded area is shown in Equation 61, and is based on the simpler of the two relationships explored in Section 6.4.2 (the second model in Table 19). The multivariable storage-area model (the fifth model in Table 19) was also formulated and tested. The outflow-storage relationship is represented in Equation 63 and utilizes the minimum outflow as an intercept term, and is dependent on the monthly mean fluctuation of the volume of water in *S2* from the minimum ($S2_{MIN}$).

There are now two parameters for the soil water recharge depth, which accounts for the water exchanged between the surface water and groundwater. When the wetland is

advancing, $r_A\,(k)$ is applied, and when the wetland is *receding*, r_R is applied. Note that when the area is receding, $A(k+1) - A(k)$ will become negative and the groundwater flux will be added to the surface water compartment. Similar to the previous model, when the wetland is advancing this flux is assumed to act in the vertical direction, and the maximum soil water recharge depth is reduced by the net rainfall. However, when the wetland is receding the flux is assumed to occur in the horizontal direction; groundwater from the surrounding area that was recently flooded can infiltrate back into the wetland surface water compartment. The soil should be fully saturated since it was recently flooded and is assumed independent of precipitation. Therefore the r_R parameter does not vary temporally.

$$S1(k+1) = S1(k) + [P(k) - \alpha_E E(k)]\frac{1}{2}[A(k) + A(k+1)] - r[A(k+1) - A(k)] + Q_{IN}(k) - Q_{12}(k) \quad [59]$$

$$S2(k+1) = S2(k) + Q_{12}(k) - Q_{OUT}(k) \quad [60]$$

where:

$$r = r_A(k) \quad if\ A(k+1) > A(k)$$

$$r = r_R \quad if\ A(k) > A(k+1)$$

$$A(k) = \frac{1}{d}[S1(k-1) - S1_{MIN} + dA_{MIN}] \quad [61]$$

$$Q_{12}(k) = \frac{\alpha_{Q12}}{2}[S1(k) + S1(k+1)] \quad [62]$$

$$Q_{OUT}(k) = Q_{OUT,MIN} + \alpha_{QOUT}\left[\frac{1}{2}\big(S2(k) + S2(k+1)\big) - S2_{MIN}\right] \quad [63]$$

where:

k = Temporal index
S1 = surface water storage (m^3)
S2 = routing compartment storage (m^3)

$S1_{MIN}$ = minimum surface water storage (m^3)
$S2_{MIN}$ = minimum routing compartment storage (m^3)
A = Flooded area of wetland (m^2)
d = average depth of water (m)
r_A = soil water recharge depth when wetland is expanding (m)
r_R = soil water recharge distance when wetland is contracting (m)
α_E = parameter to correct bias in ET rates
E = Evapotranspiration over flooded area (m/month)
P = Precipitation over flooded area (m/month)
Q_{IN} = Sudd inflows (m^3/month)
Q_{12} = flux between surface water storage and routing compartment (m^3)
Q_{OUT} = Sudd outflows (m^3/month)
α_{Q12} = linear routing flux parameter
α_{QOUT} = linear outflow-storage parameter

Equations 61, 62, and 63 can be substituted into Equations 59 and 60, and the terms can be re-arranged to solve for S(k+1) explicitly, yielding Equations 64 and 65.

$$S1(k+1) = \frac{1}{1+\frac{\alpha_{Q12}}{2}}\left[\left[1+\frac{1}{2d}[P(k)-\alpha_E E(k)]-\frac{r}{d}-\frac{\alpha_{Q12}}{2}\right]S1(k) + \left[\frac{1}{2d}[P(k)-\alpha_E E(k)]+\frac{r}{d}\right]S1(k-1) + \frac{1}{2d}[P(k)-\alpha_E E(k)][2dA_{MIN}-2S1_{MIN}]+Q_{IN}(k)\right] \quad [64]$$

$$S2(k+1) = \frac{1}{1+\frac{\alpha_{QOUT}}{2}}\left[\left[1-\frac{\alpha_{QOUT}}{2}\right]S2(k)+Q_{12}(k)+S2_{MIN}-Q_{OUT,MIN}\right] \quad [65]$$

A more convenient way of representing this system of equations is presented in Equations 66 through 73. The Beta and Gamma terms are functions of the model parameters and precipitation and ET fluxes, and they represent the relative contributions of flows and storage in previous time steps in the *S1* and *S2* simulation equations. If the Beta and Gamma terms are very large or have multi-year trends, then the storage would be unstable.

$$S1(k+1) = \beta_0(k)S1(k) + \beta_1(k)S1(k-1) + \beta_2 Q_{IN}(k) + \beta_3(k)(2dA_{MIN} - 2S1_{MIN}) \quad [66]$$

$$S2(k+1) = \gamma_0 S2(k) + \gamma_1 Q_{12}(k) + \gamma_1\left(S2_{MIN} - Q_{OUT,MIN}\right) \quad [67]$$

$$\beta_0(k) = \left[\frac{1 + \frac{1}{2d}[P(k) - \alpha_E E(k)] - \frac{r}{d} - \frac{\alpha_{Q12}}{2}}{1 + \frac{\alpha_{Q12}}{2}}\right] \quad [68]$$

$$\beta_1(k) = \left[\frac{\frac{1}{2d}[P(k) - \alpha_E E(k)] + \frac{r}{d}}{1 + \frac{\alpha_{Q12}}{2}}\right] \quad [69]$$

$$\beta_2 = \frac{1}{1 + \frac{\alpha_{Q12}}{2}} \quad [70]$$

$$\beta_3(k) = \left[\frac{\frac{1}{2d}[P(k) - \alpha_E E(k)]}{1 + \frac{\alpha_{Q12}}{2}}\right] \quad [71]$$

$$\gamma_0 = \frac{1 - \frac{\alpha_{QOUT}}{2}}{1 + \frac{\alpha_{QOUT}}{2}} \quad [72]$$

$$\gamma_1 = \frac{1}{1 + \frac{\alpha_{QOUT}}{2}} \quad [73]$$

This model has 7 parameters ($\alpha_E, r_A, r_R, d, S1_{MIN}, \alpha_{Q12}, \alpha_{QOUT}$) that need to be calibrated. Note that $S2_{MIN}$ is not considered a parameter and was calculated during the model simulation. An initial value of the storage in *S2* was assumed to be equal to one-quarter of $S1_{MIN}$, allowing the *S2* storage to be simulated over the full time span. $S2_{MIN}$ was then calculated from the *S2* storage time series, and the simulation was repeated until $S2_{MIN}$

converged. The convergence of *S2* was defined by when the percent change in each of the outflow values associated with a change in $S2_{MIN}$ was less than 0.005 %. This convergence criterion was typically met with only one iteration unless the parameter set caused the *S2* storage be unstable. The initial value of *S2* could be treated as a parameter instead of assuming that it is one-quarter of $S1_{MIN}$. However, the α_{Q12} and α_{QOUT} terms are the most critical parameters in *S2* mass balance since they stabilize *S2* and can eliminate bias between the routing flux and the observed outflows. $S2_{MIN}$ impacts the magnitude of the storage, but it does not influence the fluctuations that ultimately control the simulated outflows.

The optimal parameters are those that minimize the objective function, presented in Equation 74. The first four terms of the objective function are the same as the previous model and represent the normalized RMSE between the observed and simulated flooded areas and outflows, and the temporal differences between the maximum and minimum simulated and observed flooded areas. The fifth term was added to measure the magnitude of the cumulative bias between the flux into the routing compartment and the observed outflows. This term ensures that the storage in *S2* is stable over time and reduces the bias between the observed and simulated outflows.

$$J = \alpha_{J1}\sqrt{\frac{1}{T}\sum_{k=1}^{T}\left(\frac{A_{OBS}(k) - A_{SIM}(k)}{\max\{A_{OBS}\} - \min\{A_{OBS}\}}\right)^2} + \alpha_{J2}\sqrt{\frac{1}{T}\sum_{k=1}^{T}\left(\frac{Q_{OUT,OBS}(k) - Q_{OUT,SIM}(k)}{\max\{Q_{OUT,OBS}\} - \min\{Q_{OUT,OBS}\}}\right)^2} + \alpha_{J3}\sqrt{\frac{1}{N}\sum_{k=1}^{N}\left(\frac{t_{MAX,OBS}(k) - t_{MAX,SIM}(k)}{2}\right)^2} + \alpha_{J4}\sqrt{\frac{1}{N}\sum_{k=1}^{N}\left(\frac{t_{MIN,OBS}(k) - t_{MIN,SIM}(k)}{4}\right)^2} + \alpha_{J5}\frac{\left|\sum_{k=1}^{T} Q_{12}(k) - \sum_{k=1}^{T} Q_{OUT,SIM}(k)\right|}{0.05\sum_{k=1}^{T}(Q_{IN}(k) - Q_{OUT,OBS}(k))} \quad [74]$$

where:

J = cost
k = temporal index
T = total number of observations/simulations
N = number of years of observations/simulations
A_{OBS} = observed flooded area (derived from MODIS)
A_{SIM} = Simulated flooded area from model
$Q_{OUT,OBS}$ = observed outflows (estimated from flow routing models)
$Q_{OUT,SIM}$ = simulated outflows
Q_{12} = flux between surface water and routing compartment
Q_{IN} = inflows at Mongalla
$t_{MAX,OBS}$ = month when maximum observed flooded area occurs
$t_{MAX,SIM}$ = month when maximum simulated flooded area occurs
$t_{MIN,OBS}$ = month when minimum observed flooded area occurs
$t_{MIN,SIM}$ = month when minimum simulated flooded area occurs
α_{J1}, α_{J2}, α_{J3} α_{J4}, α_{J5}: weights for individual terms

The model presented in Equations 66 to 73 uses the simpler model (Equation 61), where *A(k) = f(S(k-1))*. The more complex model relies on the storage at three time steps, where *A(k) = f(S(k),S(k-1),S(k-2))*, and is presented in Equation 75. Equation 75 can be substituted into the *S1* mass balance equation (Equation 59), and algebraic manipulations

can be applied to obtain a linear system (similar to Equations 62 to 69). The resulting system of equations that can model the storage in the surface water compartment (*S1*) using the multivariate storage-area relationship is presented in Equations 75 through 81. This model has nine parameters ($\alpha_E, r_A, r_R, \alpha_{A1}, \alpha_{A2}, \alpha_{A3}, S1_{MIN}, \alpha_{Q12}, \alpha_{QOUT}$) that need to be calibrated. The mass balance for the routing compartment (*S2*) and the objective function remain the same as the previous model.

$$A(k) = A1_{MIN} + \alpha_{A1}(S(k) - S1_{MIN}) + \alpha_{A2}(S1(k-1) - S1_{MIN}) + \alpha_{A3}(S1(k-1) - S1_{MIN}) \quad [75]$$

$$S1(k+1) = \beta_0(k)S1(k) + \beta_1(k)S1(k-1) + \beta_2(k)S1(k-2) + \beta_3(k)Q_{IN}(k) + \beta_4(k)(A_{MIN} - (\alpha_{A1} + \alpha_{A1} + \alpha_{A3})S1_{MIN}) \quad [76]$$

$$\beta_0(k) = \left[\frac{1 + \frac{\alpha_{A1} + \alpha_{A2}}{2}[P(k) - \alpha_E E(k)] - r(\alpha_{A2} - \alpha_{A1}) - \frac{\alpha_{Q12}}{2}}{1 - \frac{\alpha_{A1}}{2}[P(k) - \alpha_E E(k)] - r\alpha_{A1} + \frac{\alpha_{Q12}}{2}}\right] \quad [77]$$

$$\beta_1(k) = \left[\frac{\frac{\alpha_{A2} + \alpha_{A3}}{2}[P(k) - \alpha_E E(k)] - r(\alpha_{A3} - \alpha_{A2})}{1 - \frac{\alpha_{A1}}{2}[P(k) - \alpha_E E(k)] - r\alpha_{A1} + \frac{\alpha_{Q12}}{2}}\right] \quad [78]$$

$$\beta_2(k) = \left[\frac{\frac{\alpha_{A3}}{2}[P(k) - \alpha_E E(k)] + r\alpha_{A3}}{1 - \frac{\alpha_{A1}}{2}[P(k) - \alpha_E E(k)] - r\alpha_{A1} + \frac{\alpha_{Q12}}{2}}\right] \quad [79]$$

$$\beta_3(k) = \left[\frac{1}{1 - \frac{\alpha_{A1}}{2}[P(k) - \alpha_E E(k)] - r\alpha_{A1} + \frac{\alpha_{Q12}}{2}}\right] \quad [80]$$

$$\beta_4(k) = \left[\frac{[P(k) - \alpha_E E(k)]}{1 - \frac{\alpha_{A1}}{2}[P(k) - \alpha_E E(k)] - r\alpha_{A1} + \frac{\alpha_{Q12}}{2}}\right] \quad [81]$$

6.5.2 Calibration Approach

Because a more complex model of the Sudd is being developed and there are more parameters to calibrate, a systematic and strategic model calibration approach should be employed. To develop this approach, the simpler model (with seven parameters) was first explored through a series of quick calibration experiments. The goal of these experiments was to determine appropriate weights for the objective function, estimate the magnitude of ranges of feasible parameters, and gain a general understanding of how this model can simulate both the flooded areas and outflows. The model was roughly calibrated using different combinations of objective function weights and coarse discretizations of the parameter space, and the resulting simulated storages, areas, and outflows and the objective function values were examined. The following general observations were made from these experiments:

- If the model is calibrated to the outflows only (the first, third and fourth terms were set to zero), then the depth parameter (*d*) increases and the routing flux term (α_{Q12}) decreases. Consequently, the intra-annual fluctuations of *S2* are reduced and a smoother outflow time series is obtained. However, the intra-annual variations of S1 are also reduced and the simulated flooded area time series does not capture the seasonal fluctuations of the Sudd flooded area.
- If the model is calibrated to the flooded area only (the second and fifth term are set to zero), then the ET parameter (α_E) decreases and the routing flux term (α_{Q12}) increases to compensate. A lower RMSE between the simulated and observed flooded areas can be achieved by reducing the influence of the ET

flux and simulating the losses using the routing compartment. However, the system becomes unrealistic and the storage in *S2* is unstable because the model neglects the outflow simulation.

- The magnitude of the cost associated with the outflow bias term was consistently very small because, across the seven parameters, there are many opportunities to make minor adjustments that eliminate the cumulative bias. Therefore, if this term is included along with the flooded area terms, the flooded area performance metrics can be optimized while maintaining a sensible routing flux that will be able to produce unbiased outflows (across the full time series).

To provide balance across the objective function weights in terms of those that represent the flooded areas and those that represent the outflows, standard weights of 1, 1, 0.5, 0.5, and 1 for $\alpha_{J1,}$ α_{J2}, α_{J3} $\alpha_{J4,}$ $\alpha_{J5,}$ respectively were chosen to measure model performance. Considering the abovementioned insights from the rough calibration experiments, the ability of a model to simulate the outflows and flooded areas both individually and jointly was assessed by performing three separate calibrations:

1) Set the second term of the objective function to zero and evaluate the model's ability to simulate the flooded areas.
2) Set the first, third, and fourth terms of the objective function to zero and evaluate the model's ability to simulate the outflows.
3) Use the standard objective function values and evaluate the model's ability to simulate both the flooded areas and outflows jointly.

The first calibration procedure that emphasizes the flooded area simulation can be applied to determine the most appropriate form of the storage-area relationships explored in Section 6.4 and select one of the two models formulated in Section 6.5.1. The selected model can subsequently be calibrated to the outflows only and then to both the outflows and flooded areas to further evaluate its performance.

Prior to performing the model calibration, a sensitivity analysis should be completed to determine suitable discretizations of the feasible parameter space. The same numerical approach that was outlined in Section 6.3 was applied using the revised model formulations, and the resulting sensitivity plots are shown in Figure 104 and Figure 105. These plots were generated using the model that has the simpler storage-area relationship for all parameters except those that correspond with the multivariate storage-area relationship (α_{A1}, α_{A2}, and α_{A3}). Thresholds on the normalized percent change of the flooded areas and outflows are drawn at 2.5%, 1%, and 0.1%.

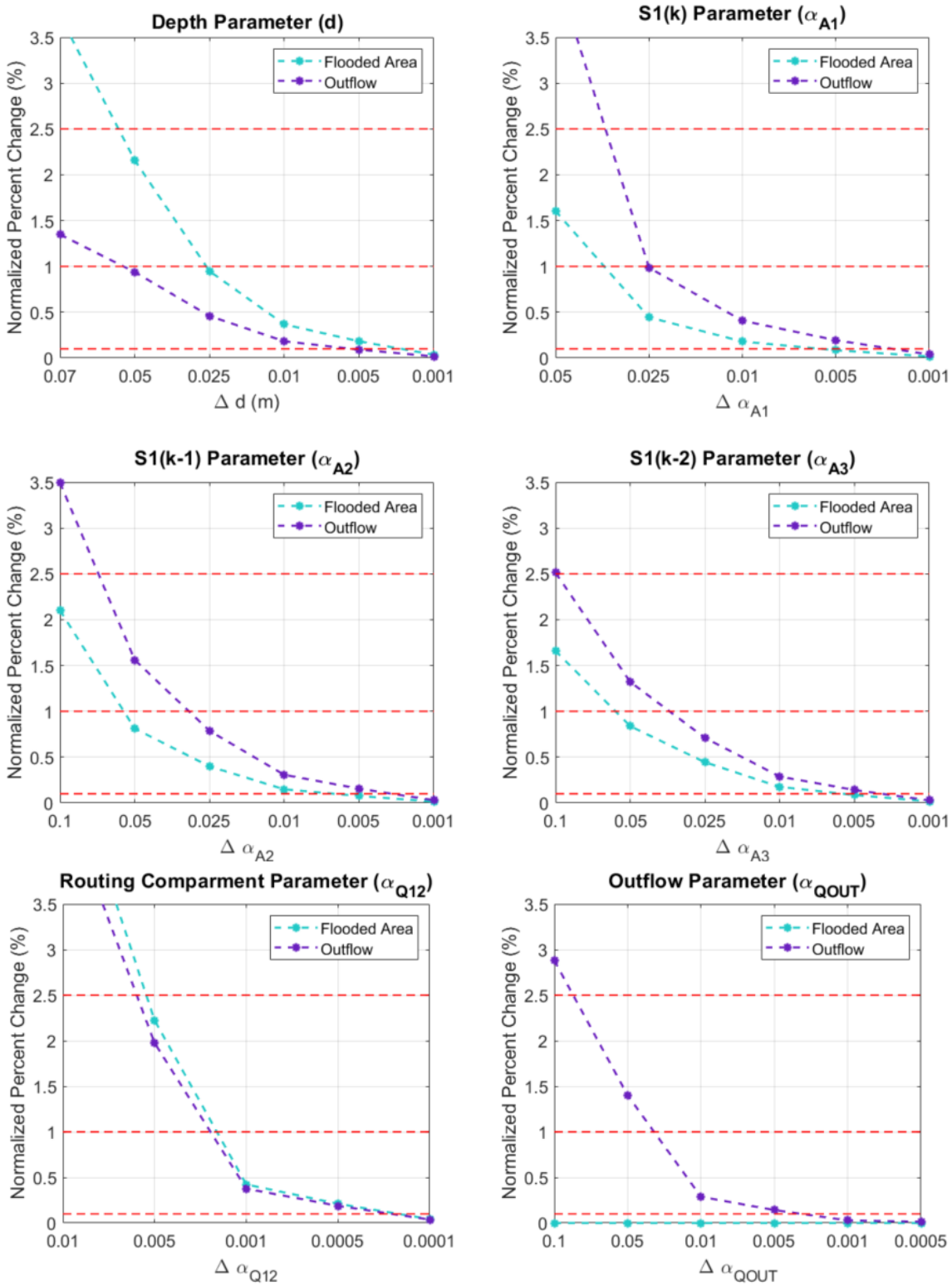

Figure 104: Sensitivity plots for six of ten total model parameters in the revised hydrologic models. The depth parameter corresponds with the simpler storage-area relationship and the S1(k), S1(k-1), and S1(k-2) parameters correspond with the more complex storage-area relationship.

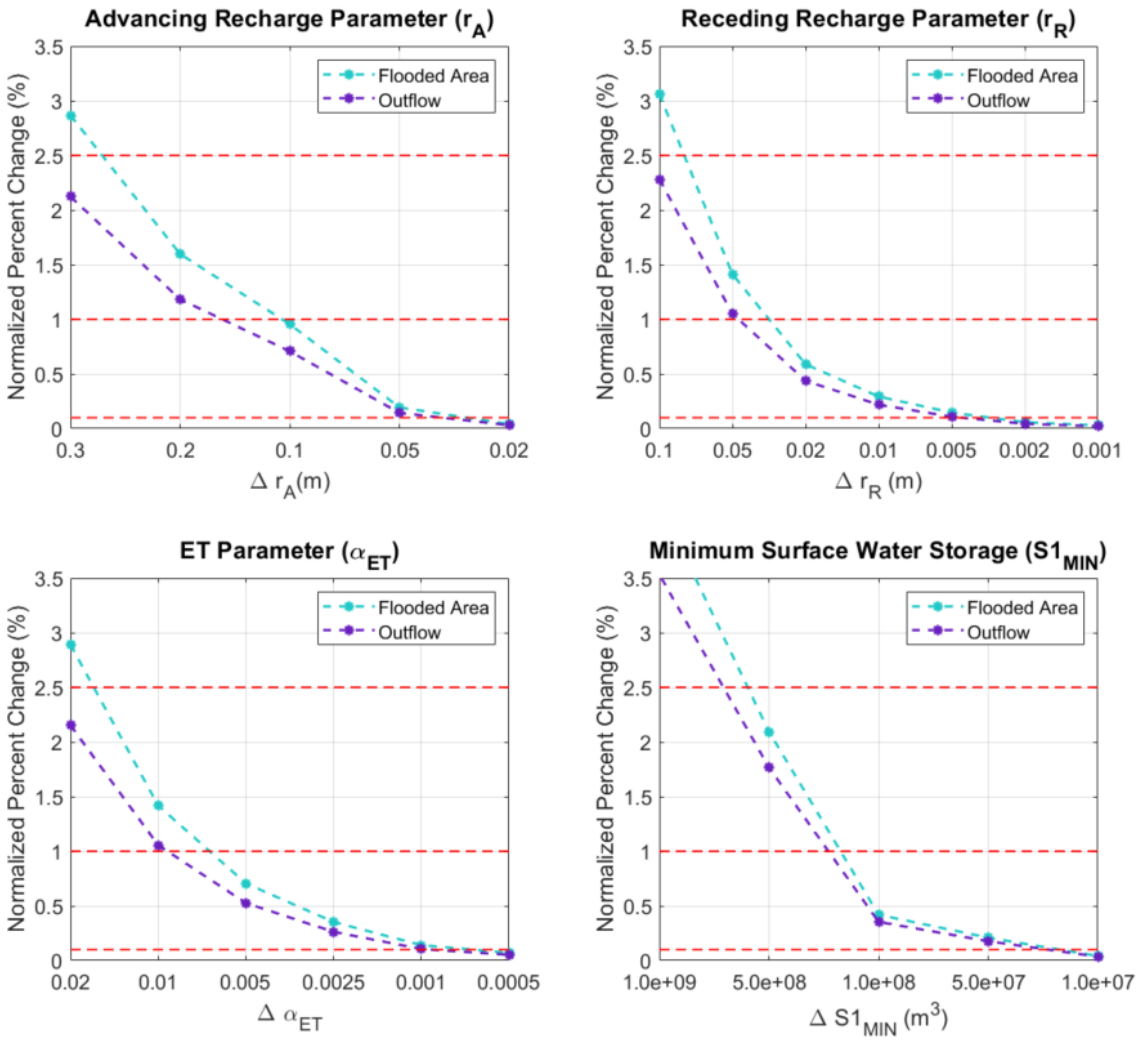

Figure 105: Sensitivity plots for the remaining 4 parameters in the revised hydrologic models.

Considering the larger number of parameters that need to be calibrated, performing model simulations for the full feasible parameter space at fine discretizations is no longer practical. Alternatively, the calibration can be done in stages, starting from a coarse discretization of the parameters and moving to a fine discretization while successively narrowing the outer bounds (or brackets) of the feasible space. Discretizations that represent coarse, medium and fine resolutions were identified from the parameter

sensitivity analysis depicted in Figure 104 and Figure 105 and are listed in Table 22. A flow chart that illustrates this iterative calibration procedure is provided in Figure 106. Computations were performed on the Wake Forest University DEAC Cluster, a centrally managed resource with support provided in part by the University. Performing the calibration on the Cluster allowed multiple calibration exercises to be performed simultaneously.

Table 22: Discretizations of parameter values at coarse, medium, and fine scales associated the 2.5%, 1%, and 0.1% thresholds on the normalized percent change in the flooded areas and outflows.

Parameter	Coarse Discretization (2.5% Change)	Medium Discretization (1% Change)	Fine Discretization (0.1% Change)
Depth, d (m)	0.05	0.025	0.001
S(k) parameter, α_{A1}	0.025	0.01	0.001
S(k-1) parameter, α_{A2}	0.05	0.025	0.001
S(k-2) parameter, α_{A3}	0.1	0.025	0.005
Recharge depth, advancing, $r_{A,}$ (m)	0.2	0.1	0.02
Recharge depth, receding, r_R (m)	0.05	0.02	0.002
ET, α_E	0.02	0.005	0.0005
Min. surface water storage, $S1_{MIN}$ (m^3)	5×10^8	1×10^8	1×10^7
Routing flux, α_{Q12}	0.005	0.001	0.0001
Storage-Outflow, α_{QOUT}	0.1	0.01	0.001

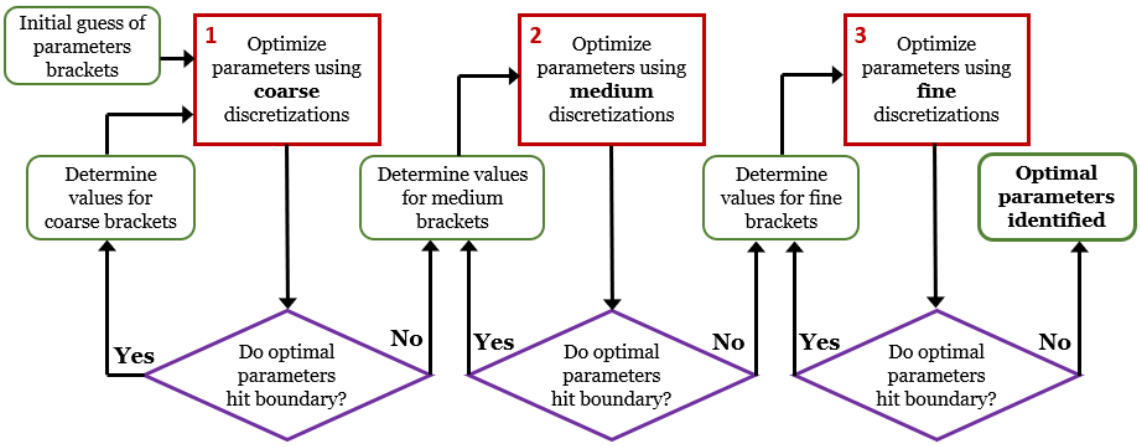

Figure 106: Flow chart illustrating the iterative calibration procedure.

Insights from the exploratory analysis of these models, the optimal parameters obtained from the simpler model presented in Section 6.3, and the examination of the storage-area-outflow relationships described in Section 6.4 were combined to develop initial guesses of the outer parameter brackets. The models were then simulated for coarse discretizations within these outer brackets and the parameters values that minimized the objective function were recorded. If these optimal parameter values were within the pre-defined outer bracket, then the bracket was narrowed around the optimal value and the medium discretization was applied in the next simulation. Alternatively, if the optimal value reached the outer bound of the bracket, then the bracket was shifted accordingly, and the model was re-calibrated using the coarse discretizations. This same process was repeated for the medium and fine discretizations until a final optimal set of parameters was reached.

The outer brackets of each parameter were set independently of other parameters apart from the α_{Q12} term. This term controls the magnitude of the flux between the surface

water and routing compartment. Therefore, the feasible range for α_{Q12} is highly dependent on the magnitude of the storage in *S1*, which is controlled by the storage-area relationship parameters. Therefore, once the storage-area parameters were assumed, the "observed" storages were calculated from the MODIS-observed flooded areas and the fitted storage-area relationship. The center of the α_{Q12} bracket was then calculated as the ratio of the mean of the observed outflows divided by the mean of the "observed" *S1* storage. This ratio represents the slope of the linear relationship between the routing flux and the *S1* storage, if average routing flux is equivalent to the average outflows, which would be the case if there was zero bias between routing flux and the outflows.

The implementation of this calibration procedure required many iterations and modeler interventions. Alternatively, the model could be reformulated as a dynamic optimization problem that employs a more automated algorithm. However, formulating this model in a way that an optimization algorithm would converge on a solution would require further research. Additionally, these algorithms can be computationally intensive if higher order derivatives cannot be computed analytically.

Regardless of whether the bracketing method illustrated Figure 106 is applied or an optimization algorithm is developed, the objective function is multi-modal and the optimal set of parameters may be associated with a local minimum (as opposed to a global minimum). However, the trade-off between identifying a true global minimum value and increased computational costs must be balanced. Additionally, considering the broader goals of the hydrologic model and the errors and uncertainties ingrained in the hydrologic data and structure of the mathematical model, the goal of identifying the true optimal

parameters becomes less significant. The proposed calibration procedure illustrated in Figure 106 using the discretizations listed in Table 22 were carefully designed and are appropriate considering objectives of this research.

6.5.3 Comparison of Two Alternative Model Formulations Using Optimal Parameters

The calibration procedure described in Section 6.5.2 was applied to the two alternative model formulations presented in Section 6.5.1. The second term of the objective function was set to zero to obtain the parameter values that provide the most accurate simulation of the flooded area. The outflow parameter (α_{QOUT}) did not need to be calibrated because it has no influence on the flooded area in these models. The resulting optimal parameters and objective function values are listed in Table 23 and Table 24, respectively. The first model is associated with the single variable storage-area relationship (*A(k)=f(S(k-1))*), and the second model is associated with the multi-variate storage-area relationship (*A(k) = f(S(k),S(k-1),S(k-2))*).

Table 23: Optimal parameters for two hydrologic models with alternative representations of the storage-area (S-A) relationship.

S-A Rel.	*Optimal Parameters*								
	d	α_{A1}	α_{A2}	α_{A3}	r_A	r_R	α_{ET}	$S1_{MIN}$	α_{Q12}
1	0.692	-	-	-	1.16	0.00	0.9820	0	0.4296
2	-	0.510	0.219	0.265	2.00	0.00	0.9380	0	0.2790

Table 24: Optimal objective function values for two hydrologic models with alternative representations of the storage-area (S-A) relationship.

S-A Rel.	*Objective Function Values*					
	J1	*J2*	*J3*	*J4*	*J5*	J_{TOT}
1	0.2024	-	0.4629	0.2273	0.00004	0.8927
2	0.1837	-	0.4432	0.2273	0.000008	0.8543

The optimal parameters were then applied to simulate the flooded areas. The simulated flooded areas and storages for the first model (single-variable storage-area relationship) are presented in Figure 107. A scatter plot comparing the simulated and MODIS-observed flooded areas is shown in Figure 108, along with the fitted linear relationship. This model accurately simulates the flooded areas for particular years and captures the drought from 2009 to 2010. However, the storage in *S1* cannot recover for multiple years following the drought, and consequently the model performs poorly from 2010 to 2013. Additionally, the storage occasionally drops below zero, which is not physically possible, but this behavior will be corrected when the model is calibrated to the outflows. As expected, the *S2* storage lags behind the *S1* storage, which will improve the alignment between the simulated and observed outflows when the outflows are included in the calibration. In general, the errors are much more pronounced during periods of high flows and flooded area extents. A temporal lag between the simulated and observed areas remains for the occurrence the maximum flooded area extent, although the lag has been substantially reduced compared to the model results presented in Section 6.3. The scatter plots in Figure 108 show that there is almost no relationship between the flooded areas and storage during wet periods, and suggest that the calibration of a non-linear relationship would not provide much improvement.

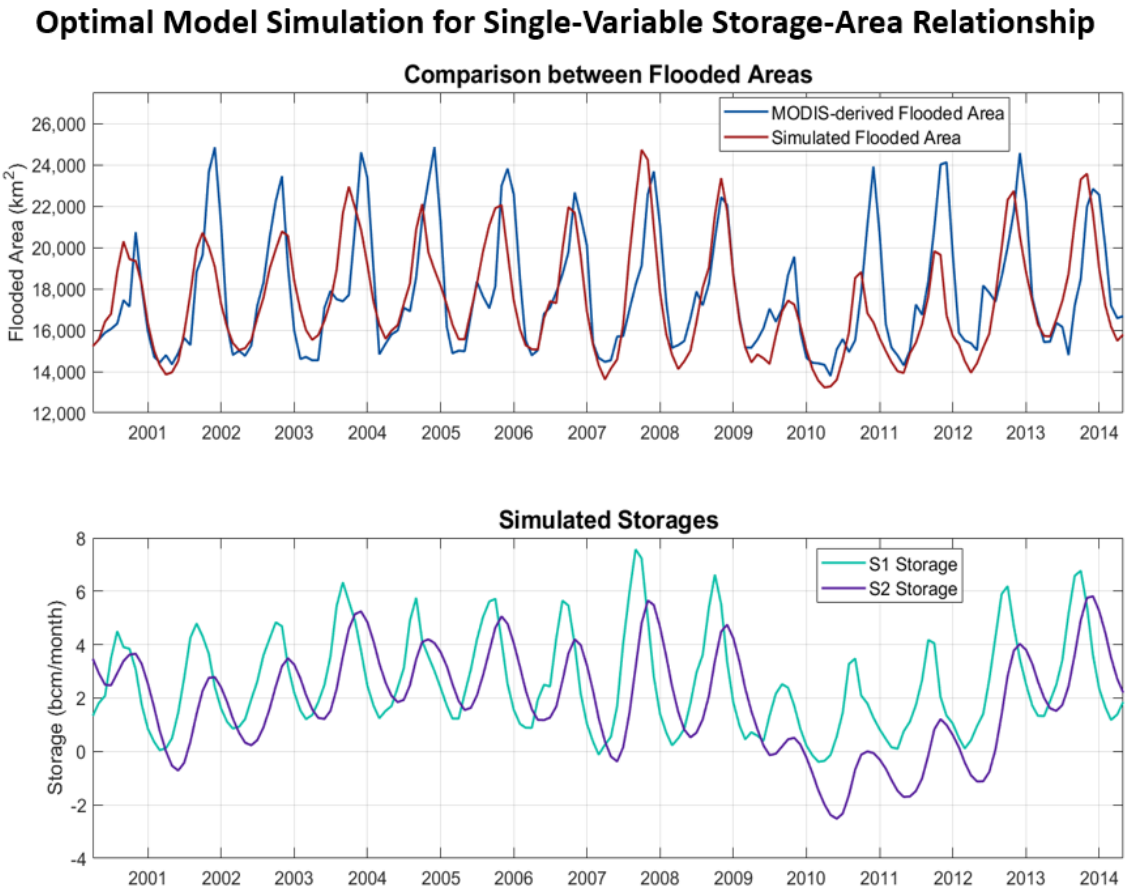

Figure 107: Simulated flooded areas and storages for the revised model that assumes a single-variable storage-area relationship, calibrated to the flooded areas only.

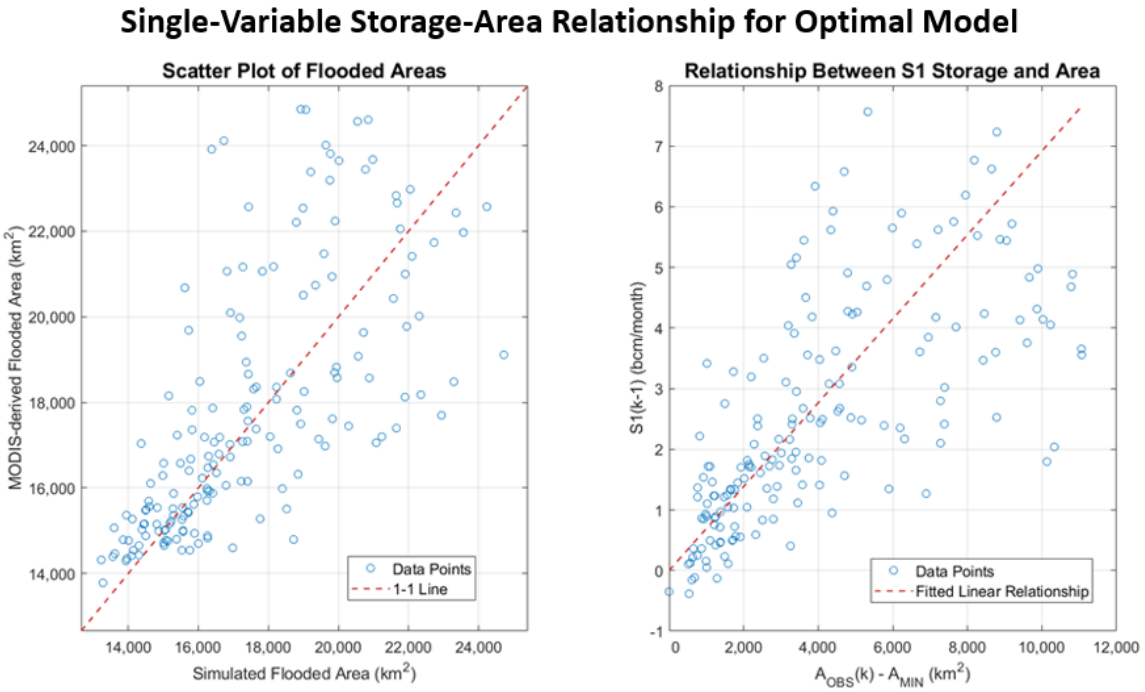

Figure 108: Scatter plots comparing simulated and observed flooded areas (left), and the fitted linear relationship (right) using single-variable storage-area relationship (*A(k)=f(S(k-1))*).

The simulated flooded area and storage for the second model with the multi-variable storage-area relationship are presented in Figure 109, and a scatter plot comparing the fitted and observed flooded areas is provided in Figure 110. The plots and the objective function values show that the lag between the simulated and observed peak flooded areas has been slightly reduced, and there is generally less scatter in the storage-area relationship for wet periods. Additionally, Figure 110 suggests that the storage-area relationship might be improved if a non-linear relationship was calibrated. However, the inclusion of multiple temporal lags in the storage-area relationship has the effect of smoothing the flooded area simulation. While the magnitude of the errors are slightly reduced using the multi-variable storage-area relationship, according to the objective function, the overall behavior of the

simulated flooded area is less similar to the observed flooded areas; the time series is too smooth and has less pronounced peaks. Therefore, the single-variable storage-area relationship is more appropriate considering the general behavior of the time series and the smaller number of parameters that must be calibrated.

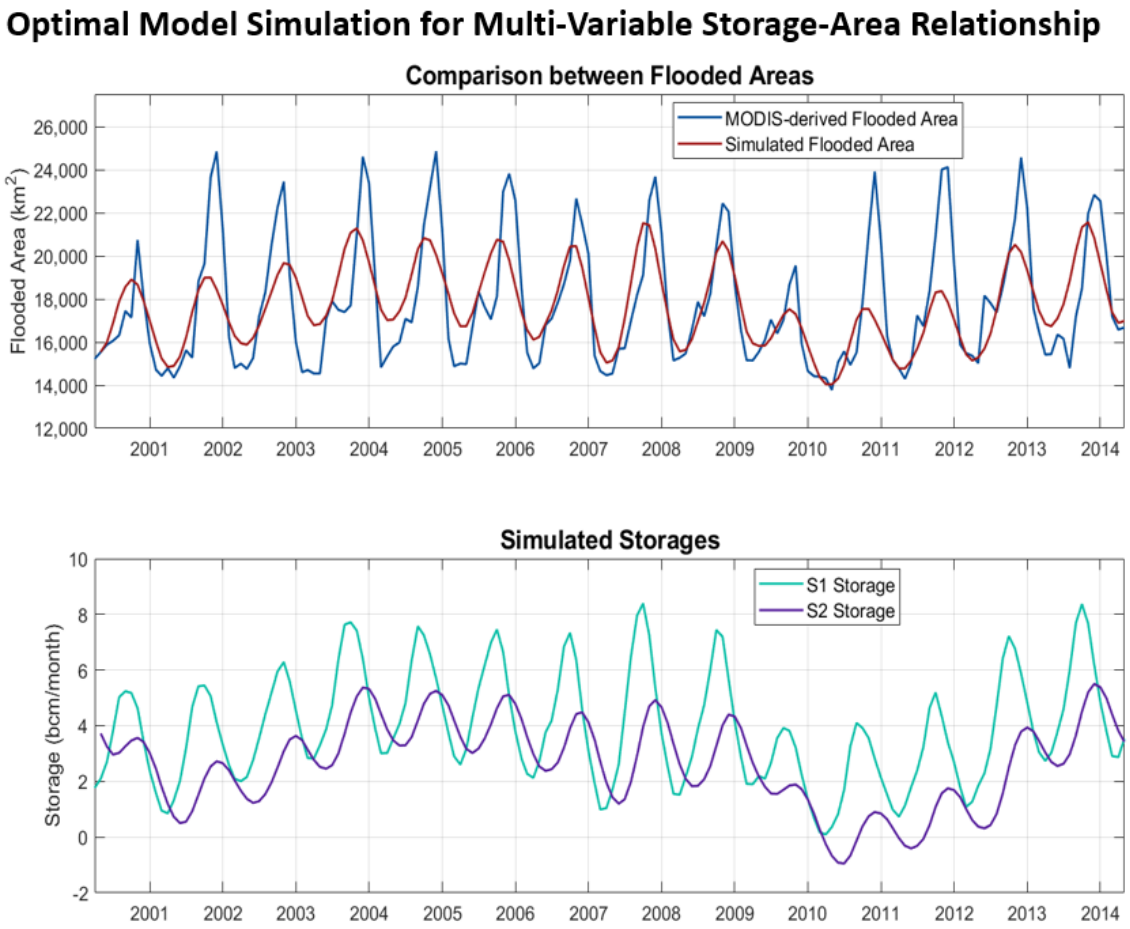

Figure 109: Simulated flooded areas and storages for the revised model that assumes a multi-variable storage-area relationship, calibrated to the flooded areas only.

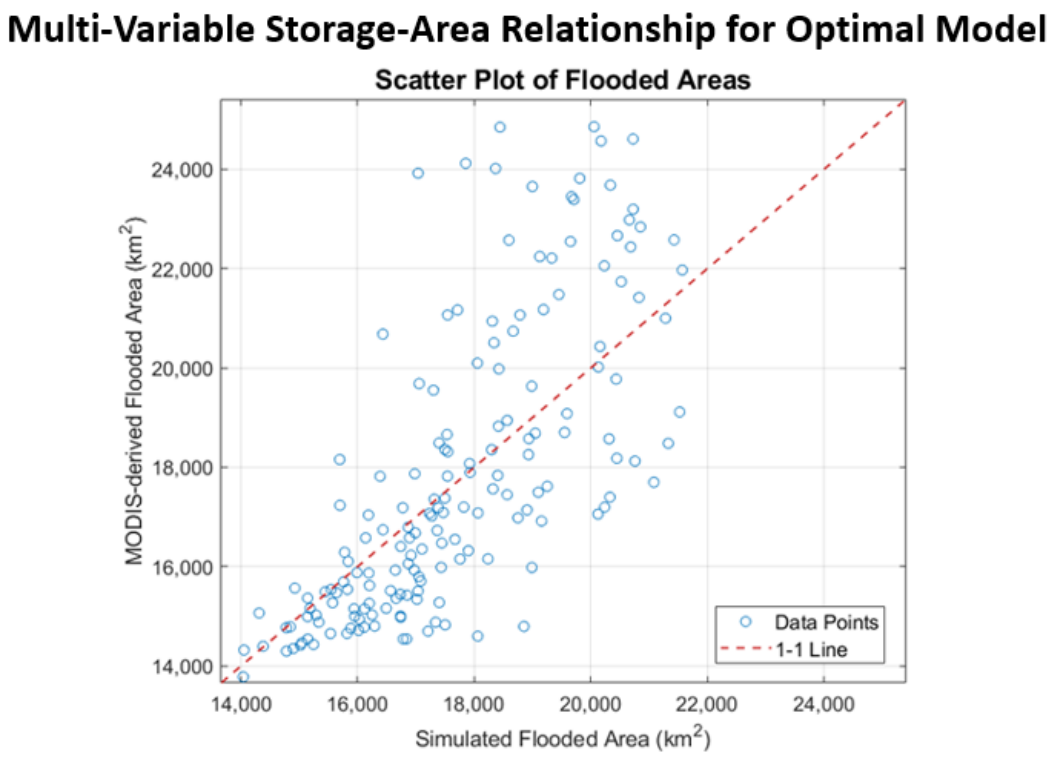

Figure 110: Scatter plots comparing simulated and observed flooded areas, using multi-variable storage-area relationship (*A(k)=f(S(k),S(k-1),S(k-2))*).

6.5.4 Full Model Calibration Results

The hydrologic model with the single-variable storage-area relationship was also calibrated to the outflows only using only the second and fifth objective function terms, and both the flooded areas and outflows using all the objective function terms. The resulting optimal parameter sets and objective function values for all three calibrations are presented in Table 25 and Table 26. Figure 111 and Figure 112 present the simulated flooded areas, outflows, and storage along with the scatter plots between the observed and simulated flooded areas and outflows for the model that was calibrated to the outflow only.

Figure 113 and Figure 114 contain the same information for the model that was calibrated to both the outflows and flooded areas jointly.

Table 25: Summary of optimal parameter values obtained for three model calibration strategies.

Calibration	*Optimal Parameters*						
	d	r_A	r_R	α_{ET}	$S1_{MIN}$ *(bcm)*	α_{Q12}	α_{QOUT}
Full	1.123	1.46	0.00	0.9450	2.50×10^9	0.1584	0.310
Area only	0.692	1.16	0.00	0.9820	0.00×10^9	0.4296	-
Flow only	1.290	2.28	0.00	0.8635	1.89×10^9	0.1636	0.387

Table 26: Summary of optimal objective function values obtained for three model calibration strategies.

Calibration	*Objective Function Values*				
	J1	*J2*	*J3*	*J4*	*J5*
Full	0.1861	0.1176	0.4226	0.2629	0.0001938
Area only	0.2024	-	0.4629	0.2273	0.0000421
Flow only	-	0.1074	-	-	0.0000005

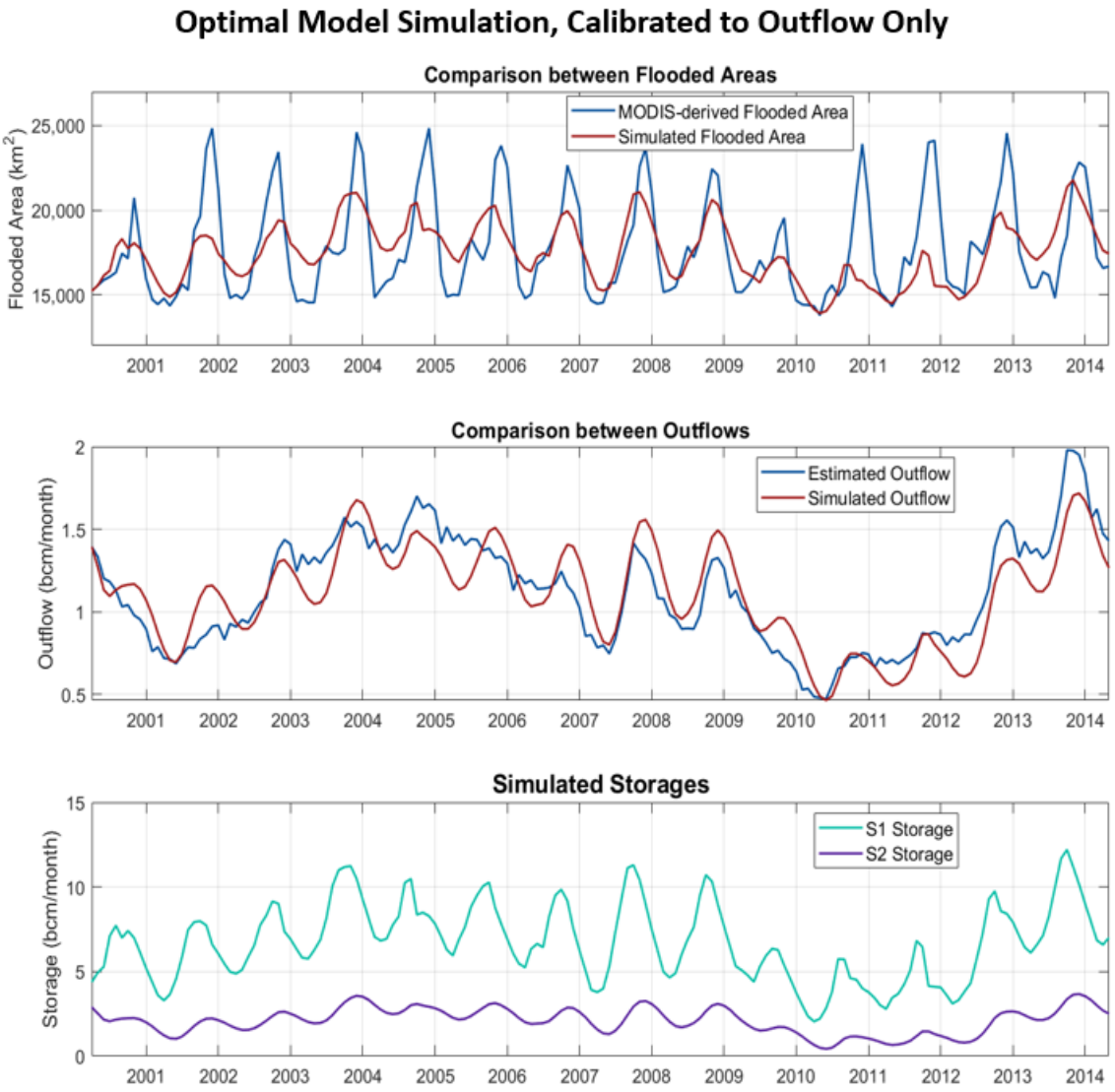

Figure 111: Simulated flooded areas, outflows, and storage for the single-variable storage-area relationship model, calibrated to outflow only.

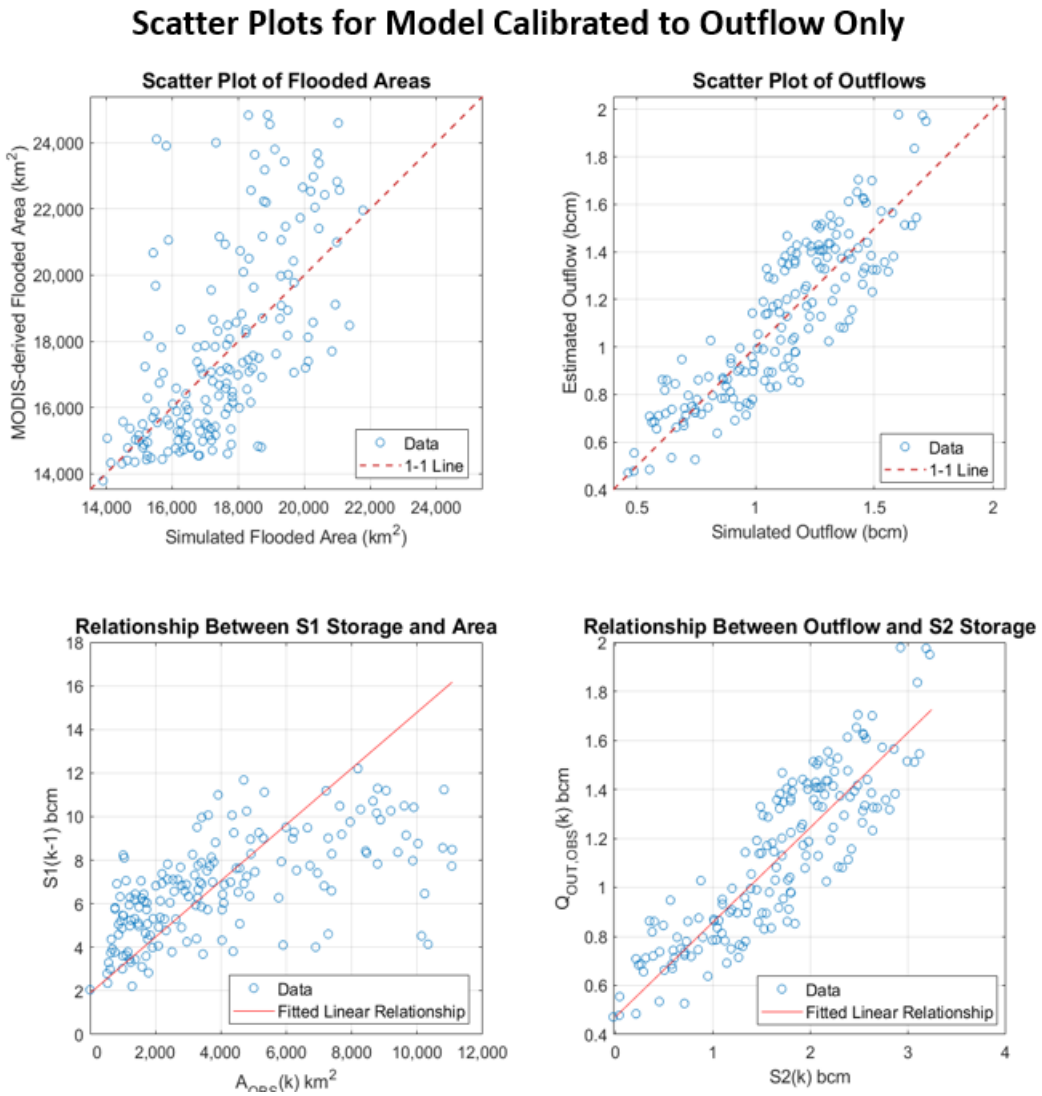

Figure 112: Scatter plots comparing simulated and observed flooded area and outflow, and strength of storage-area and outflow-storage relationships, for optimal model calibrated to outflow only.

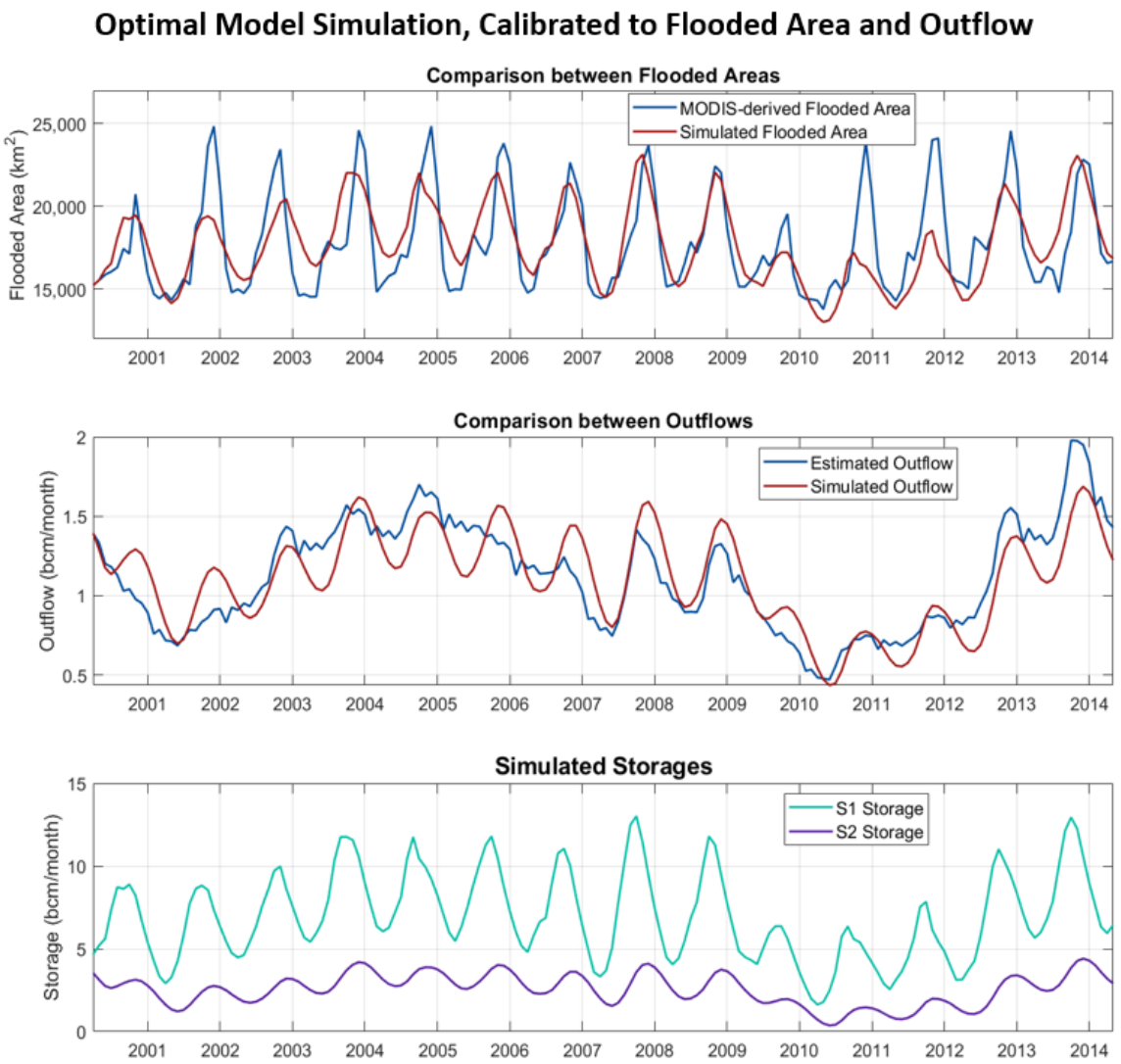

Figure 113: Simulated flooded areas, outflows, and storage for the single-variable storage-area relationship model, calibrated to both area and outflow.

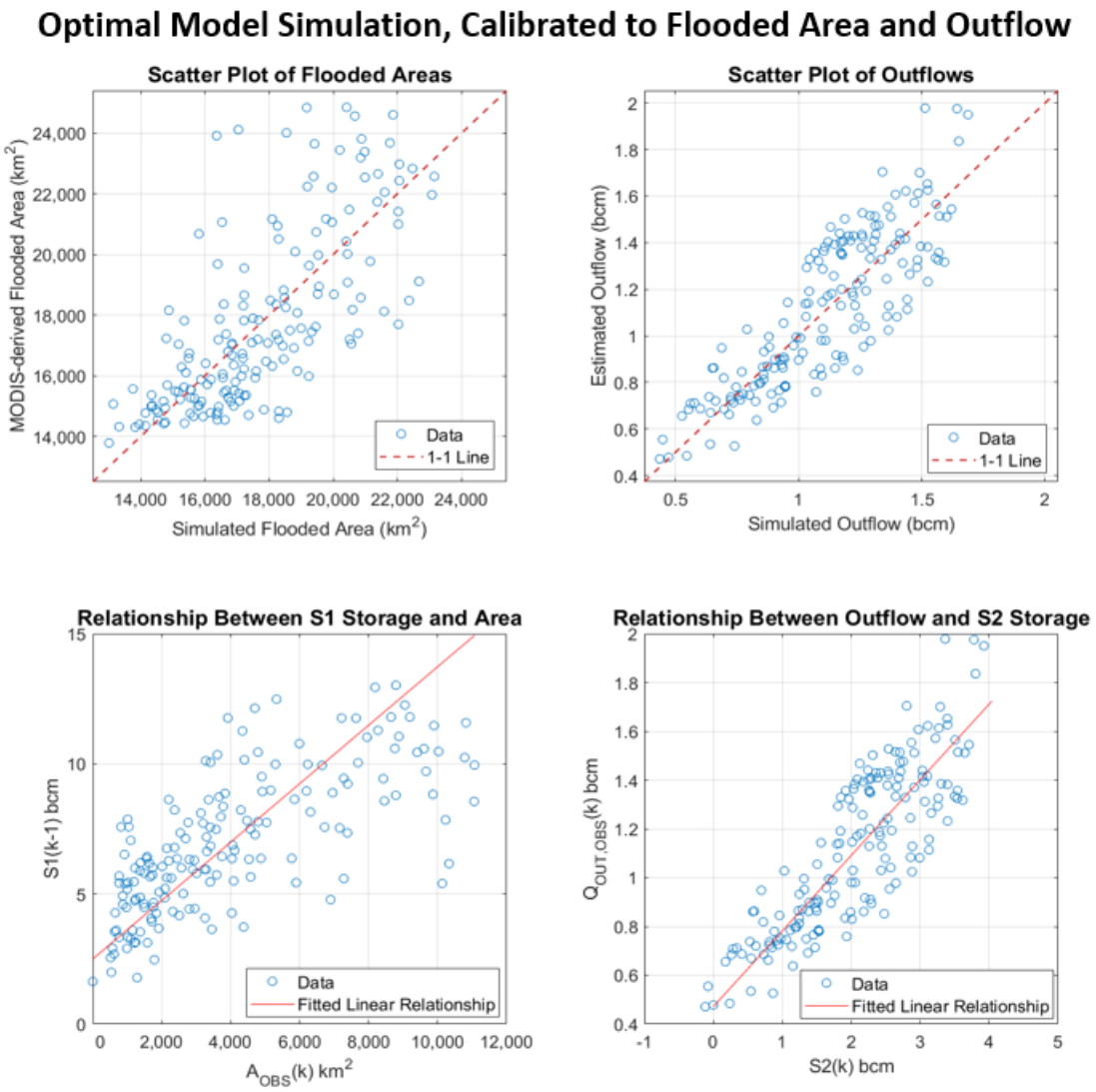

Figure 114: Scatter plots comparing simulated and observed flooded area and outflow, and strength of storage-area and outflow-storage relationships, for optimal model calibrated to both flooded area and outflow.

The optimal simulation that results from calibrating to the flooded areas only contains a larger inter-annual fluctuation of the flooded area because the depth parameter is smaller, allowing relatively small changes in storage to produce significant changes in area. To compensate for these large fluctuations, the ET and routing flux parameters are higher to increase the losses as the wetland contracts. However, this model

parameterization also results in larger fluctuations of the storage in *S2* that controls the outflows. The observed outflows are much smoother than the observed flooded areas. Therefore, when calibrating to the outflows only, the depth and ET parameters decrease and the advancing soil water recharge depth increases, thereby reducing the magnitude of the inter-annual fluctuations in both *S1* and *S2*. When the model is calibrated to both the flooded areas and outflows, the parameters generally lie between these two extremes.

For all model calibrations, the optimal receding recharge parameter is zero. Once the wetland begins to recede, the areas and outflows decrease very rapidly. A groundwater flux directed back into the wetland would attenuate the area and outflow recession and therefore does not improve the alignment between the simulated and observed time series. Similar to the previous model presented in Section 6.3, the advancing soil water recharge depths were very high compared to the depth estimated from in-situ field experiments (0.2 meters to 0.35 meters). This disparity might indicate that losses due to infiltration are more significant and could occur in the horizontal direction in addition to the vertical direction. Alternatively, the model might be using the soil water recharge to reduce the magnitude of the precipitation flux and slow down the progression of the flooded area to achieve a better alignment in the timing of the maximum extent.

Figure 115 shows the values of the β terms in the linear system for the model calibrated to both the outflows and flooded areas. β_1 and β_2 have some extreme oscillations since they fluctuate between the advancing and receding values, but all terms are reasonable, rarely exceed a value of one, and are only slightly negative. The γ terms

associated with the *S2* storage are constant in time and have stable values of 0.73 and 0.87 for γ_1 and γ_2, respectively.

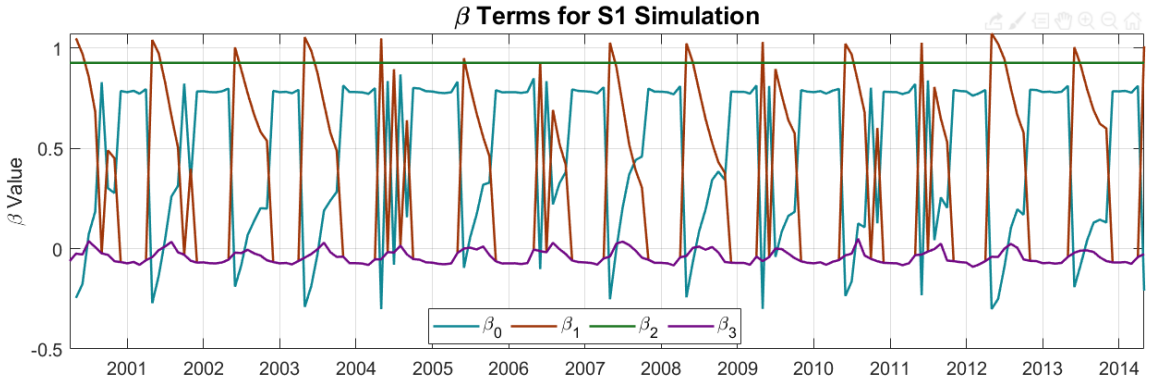

Figure 115: Values for β terms in linear system from optimal model, calibrated to outflow and area, to evaluate the model stability.

Finally, the optimal outflow simulations are compared to the observed outflows with the monthly error standard deviations applied (derived in Chapter 4) in Figure 116. The simulated outflows often surpass the two standard deviation thresholds when the Sudd is very wet or very dry. The hydrologic model produces outflows with seasonal variations that are too extreme, regardless of whether the model is calibrated to the outflows only. Figure 116 shows that the outflow simulation errors associated with limitations of the model structure are more pronounced than the uncertainty of the estimated "observed" outflows. If the error standard deviations were much greater than the errors produced by the model, then efforts should be directed toward obtaining better outflow estimates as opposed to fine-tuning the hydrologic model. However, this comparison suggests that

improving the structure of the hydrologic model is an efficient way to improve the accuracy of the simulated outflows.

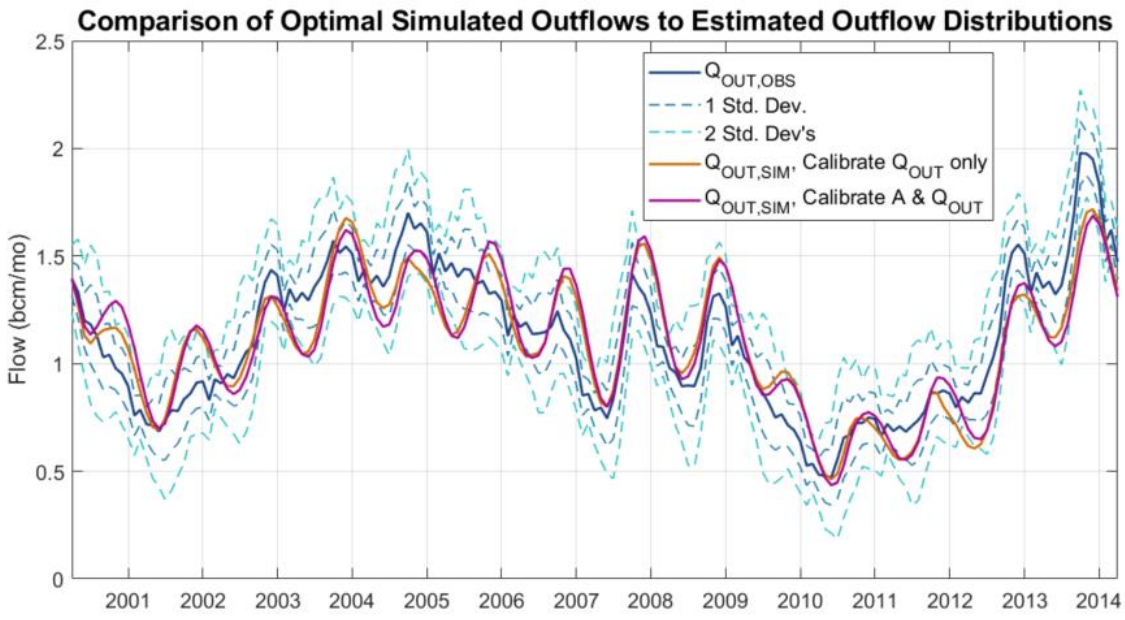

Figure 116: Comparison of optimal simulated outflows to estimated outflows with monthly standard deviations of error applied.

6.5.5 Discussion of Results and Ongoing Model Limitations

The addition of the routing compartment resulted in a significant improvement of outflow simulation. The Nash-Sutcliffe Efficiency (NSE) coefficient is 0.745 for the model calibrated to the outflows only, and 0.703 for the model calibrated to both the outflows and flooded areas. The model presented in Section 6.3 had an NSE coefficient of only 0.52. Figure 111 and Figure 113 show that the inter-annual trends in the simulated and observed outflows align, even when the model is also calibrated to the flooded area. However, there are still some notable discrepancies between the simulated and observed flooded areas. In particular, the simulated flooded areas, a function of the *S1* storage, are much lower than

the observed flooded areas from the years 2010 to 2013. However, both the simulated and observed outflows, related to the *S2* storage, are also low during this period. Because the *S1* and *S2* storage compartments are coupled, a model adjustment that results in an increase in *S1* to more closely match the observed flooded areas would result in an increase in *S2* and consequently reduce the alignment of the simulated and observed outflows.

The misalignment between the simulated and observed areas occurs even when the model is calibrated to the flooded areas only. Considering the simulated flooded areas are consistently low across all model calibrations from 2010 to 2013, combined with the fact that the observed outflows are also low during this period, the MODIS-observed flooded areas should be re-examined. Recall from Chapter 5 that inconsistencies with regards to how the wetland expands during the wet season were evaluated; large areas that are classified as flooded early the wet season are suddenly no longer flooded as the wet season progresses. Because this behavior was observed for the entire 2000 to 2015 period, these inconsistent areas are not believed to be classification errors and instead represent areas where flooding is controlled by rainfall as opposed to river flow. These areas are believed to be connected to the wetland only temporarily, and the water may not travel into the main wetland system and contribute to the outflows.

The fragmentation of the wetland flooded areas might be more pronounced following a very dry period, such as that observed in 2010. Conceptually, when the flooded area recedes, new ridges and geographic boundaries within the Sudd might be exposed. Consequently, the outer extents of the Sudd might flood from local rainfall and runoff from upland areas, but the water would infiltrate and evaporate before it reaches the main

wetland surface water body that is coupled with the river flows. Therefore, the MODIS-derived flood maps are likely showing flooded areas, but the satellites cannot distinguish between areas that are connected or disconnected to the main wetland water body. This limitation of the satellite-derived flood maps is related to the relatively coarse spatial resolution of MODIS (approximately 500 meters) and the dense vegetation within the Sudd that makes the detection of surface water beneath the canopy challenging.

Considering the relatively close alignment of the simulated and observed outflows and the questionable connectivity of the MODIS-derived flood maps, this hydrologic model is believed to be reasonably accurate. However, the model can only simulate the flooded areas that are part of the main wetland water body, coupled to the river flow. To more accurately model the flooded area extents from the satellite's perspective, an additional water balance model that accounts for rainfall and runoff in the areas surrounding the main water body could be developed, calibrated, and tested. This "outer" model would exchange water with the main Sudd water body through surface water and shallow groundwater flows, but it would not be directly coupled to the *S2* storage compartment that controls the Sudd outflows. However, the storage in this outer model would be combined with the *S1* storage for the wetland surface water body in the area-storage relationship that produces the simulated areas. This three-compartment model will be the focus of future research. Similar to the current proposed model, refining this model would be an iterative process that considers the relative importance of various hydrologic fluxes and the relationships between them. Additionally, some of the procedures developed

to obtain the MODIS-derived flood maps would need to be re-evaluated in light of this new perspective on the wetland connectivity.

6.6 Model Sensitivity and Uncertainty Assessment

6.6.1 Parameter Sensitivity

The sensitivity of the flooded area and outflow simulations to perturbations of the parameters was explored to understand the role that each parameter plays in the model. Beginning with the optimal parameter set shown in Table 25 for the full model calibration, each of the parameters were nudged around the optimal value, one-at-time, while keeping the other parameter values constant. The magnitudes of the perturbations were guided by the coarse discretizations listed in Table 22. The simulated flooded areas and outflows from each perturbation are shown in Figure 117 to Figure 123 for each of the seven parameters. These figures facilitate a conceptual understanding of the role that each parameter plays in producing the areas and outflows. A brief discussion of these roles follows each figure.

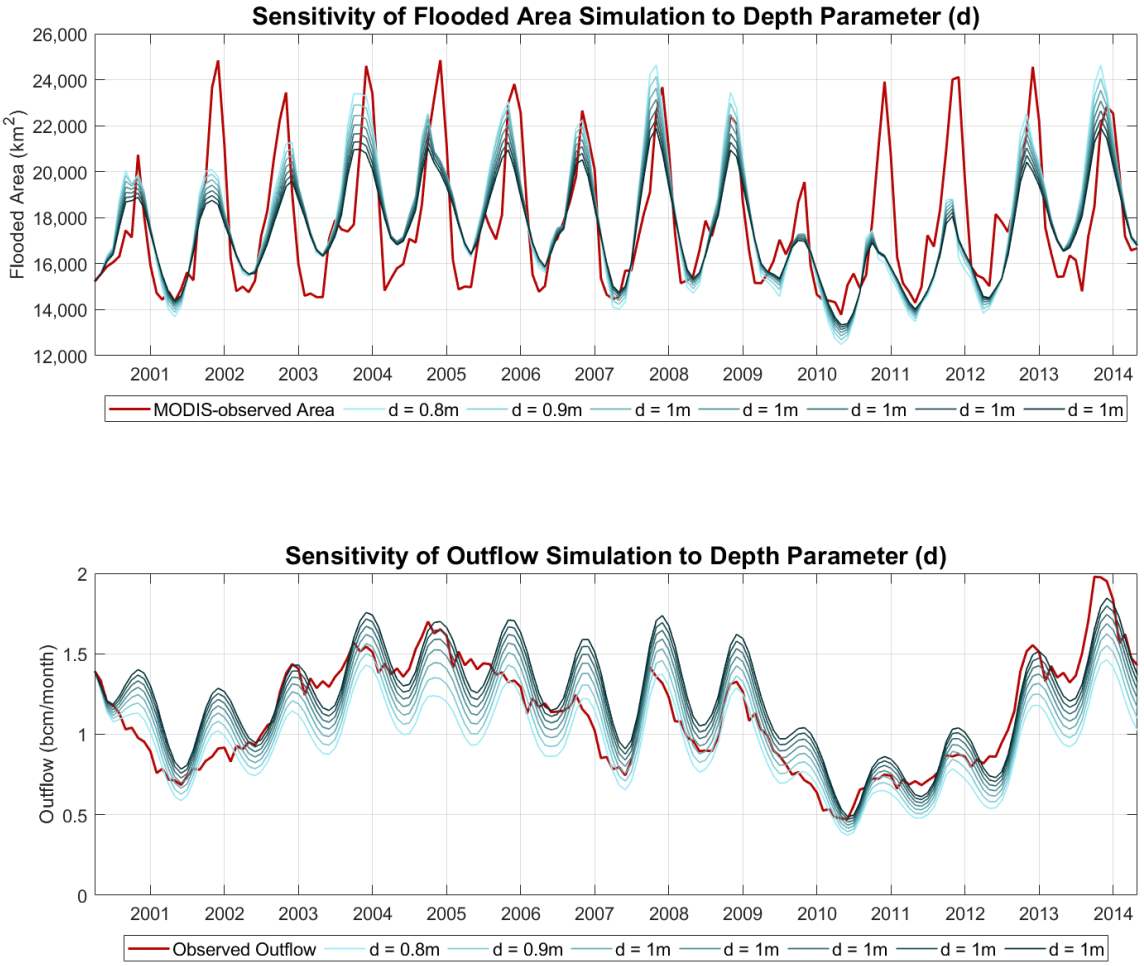

Figure 117: Sensitivity of flooded area and outflow simulations to depth parameter.

When the depth parameter is small, a small increase in storage results in a substantial increase in the flooded area extents. Therefore, the depth parameter plays a significant role when the storage is more variable, during the flood season. A small depth parameter produces large intra-annual variations and significant peaks, and a small depth parameter produces a smoother time series with lower intra-annual fluctuations. The outflows are not directly impacted by the depth; however, a smaller depth results in a larger flooded area and consequently a larger precipitation flux that increases the storage in both

S1 and *S2*, thereby increasing the magnitude and intra-annual fluctuations of outflows. Because the depth parameter influences both the areas and outflows, which have different levels of intra-annual variations, there is a trade-off in terms of how well it can reproduce both time series.

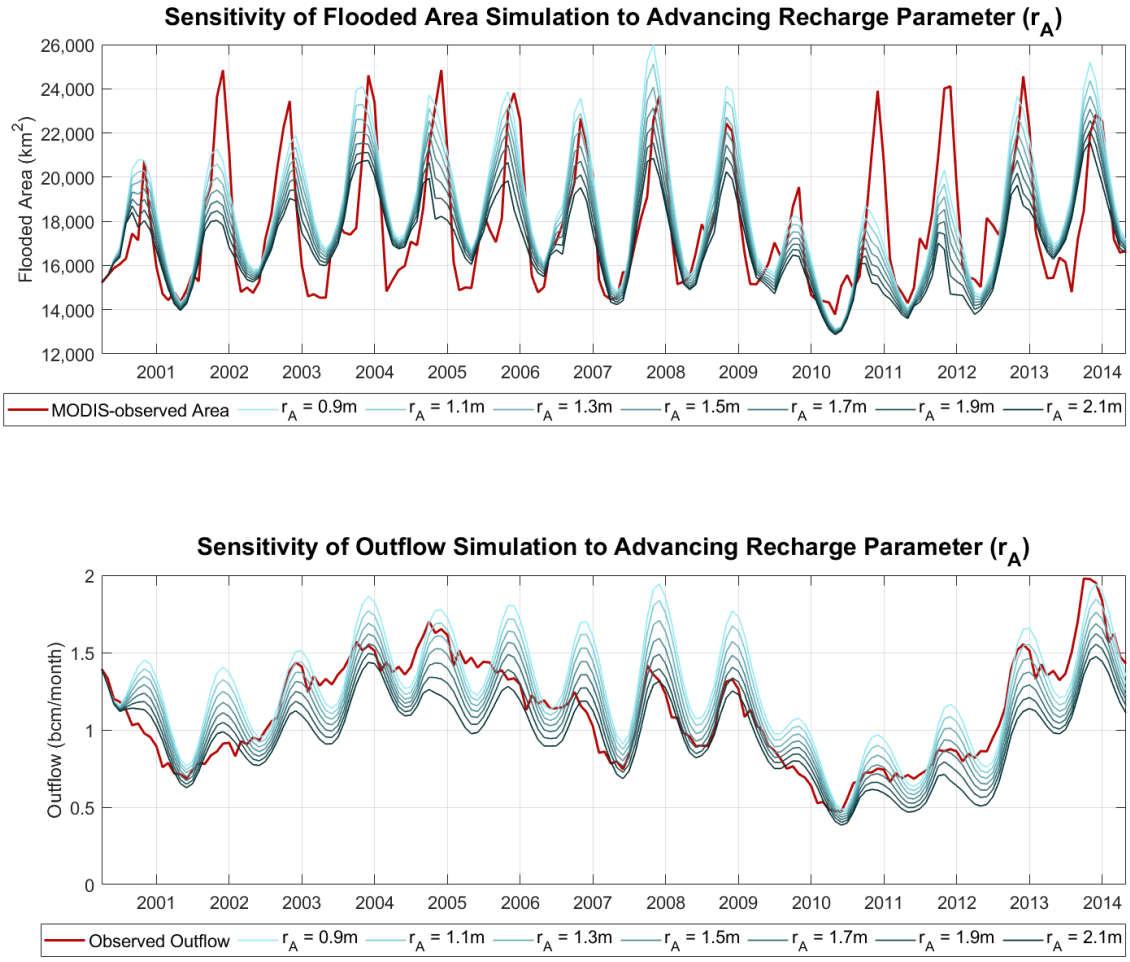

Figure 118: Sensitivity of flooded area and outflow simulations to maximum soil water recharge depth when wetland area is advancing.

Similar to the depth parameter, the advancing recharge parameter plays a larger role in the model when there are large fluctuations in the area, during the wet season. Therefore, the recharge parameter also controls the magnitude of the peaks in both the flooded areas and outflows. While the maximum soil water recharge depth is constant, the actual recharge varies temporally and is reduced by the cumulative rainfall flux. Once the cumulative rainfall reaches a depth equal to that of the maximum soil water depth, infiltration no longer occurs. However, if the maximum depth is very large then this condition is never reached. Consequently, there are more substantial differences in the flooded area simulations toward the end of the wet season during years with relatively low rainfall (2004 to 2005). Again, there is a trade-off in terms of how well the advancing recharge parameter can be fine-tuned to match both the outflows and flooded area extents.

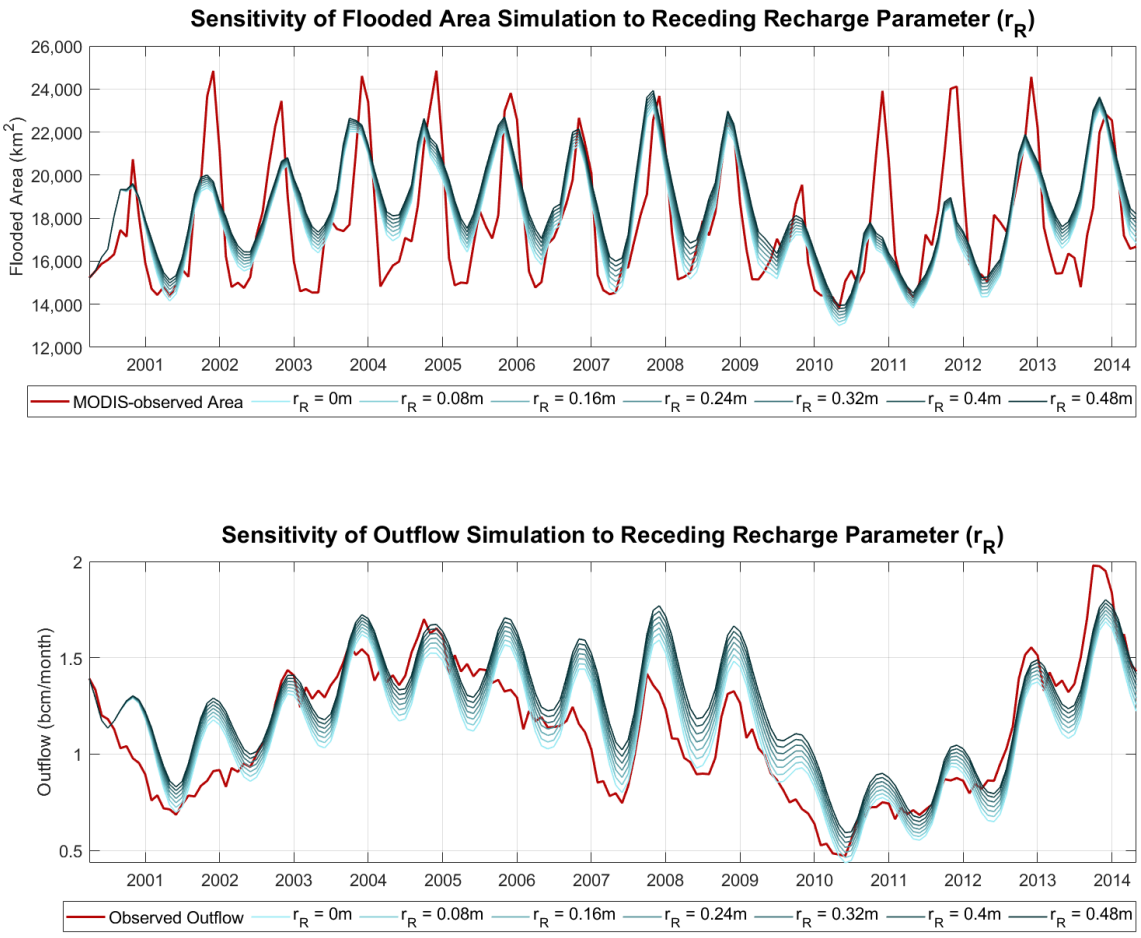

Figure 119: Sensitivity of flooded area and outflow simulations to receding soil water recharge parameter.

The receding recharge parameter affects the flooded area and outflow simulations primarily during the dry season. If this value is zero, and shallow sub-surface water does not re-enter the wetland as it is receding, then the area decreases to a greater extent during the dry season and the magnitude of the intra-annual area fluctuations increases. In terms of the outflows, the receding recharge parameter tends to shift the time series up or down but does not impact the intra-annual variations significantly. Therefore, the receding water

recharge parameter was found to be zero for all model calibrations because it increases the intra-annual area fluctuations without increasing the intra-annual outflow fluctuations.

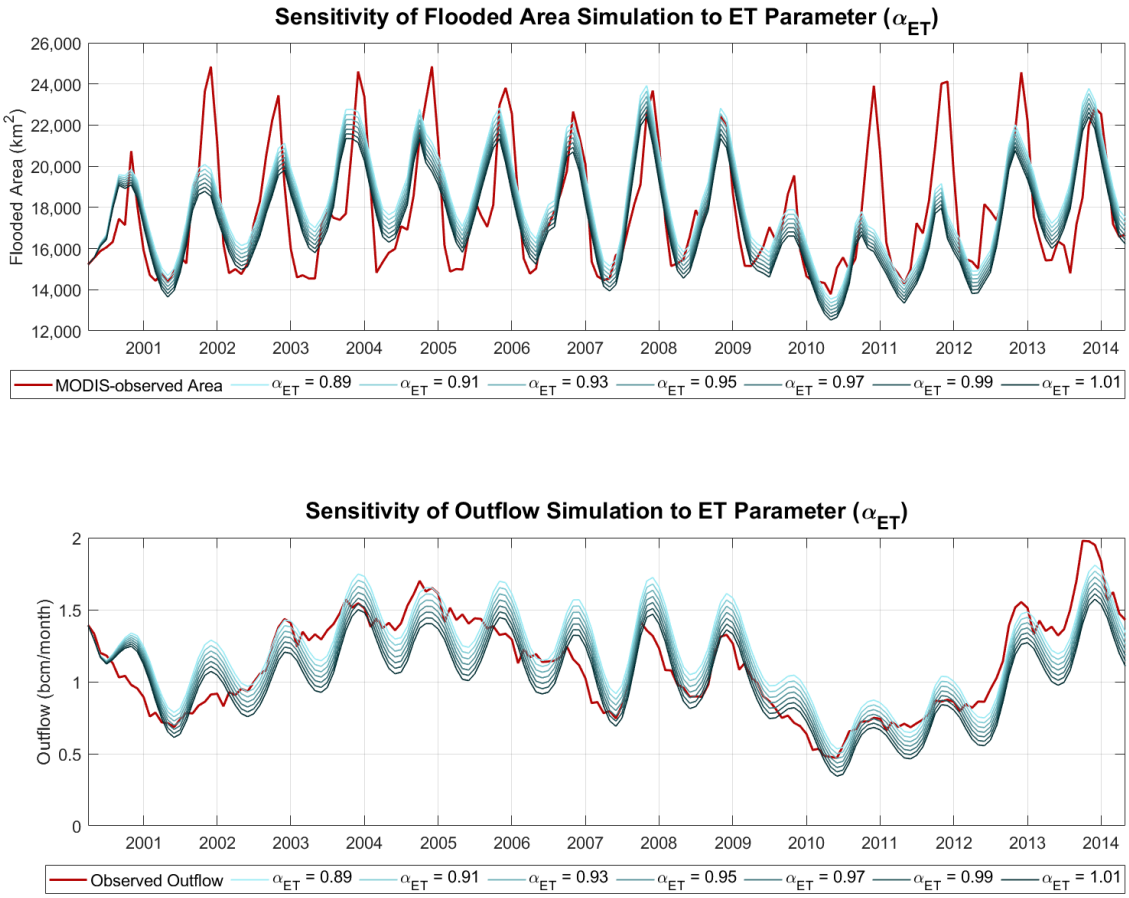

Figure 120: Sensitivity of flooded area and outflow simulations to ET bias correction parameter.

The ET parameter scales the ET flux, which is a very significant flux in the overall mass balance of the Sudd. The ET parameter generally shifts the flooded areas and outflows up or down, but the ET flux varies temporally, so this shift if not consistent from month-to-month or from year-to-year. The value of the ET flux was much lower when the model

was calibrated to the outflows only, and the associated outflow parameter was consequently greater. This combination of the ET and outflow parameters allows the *S2* storage to have greater control over the outflow simulation. However, the combination of parameters that were required to balance the storage in S1 lead to the flooded area simulation being too smooth.

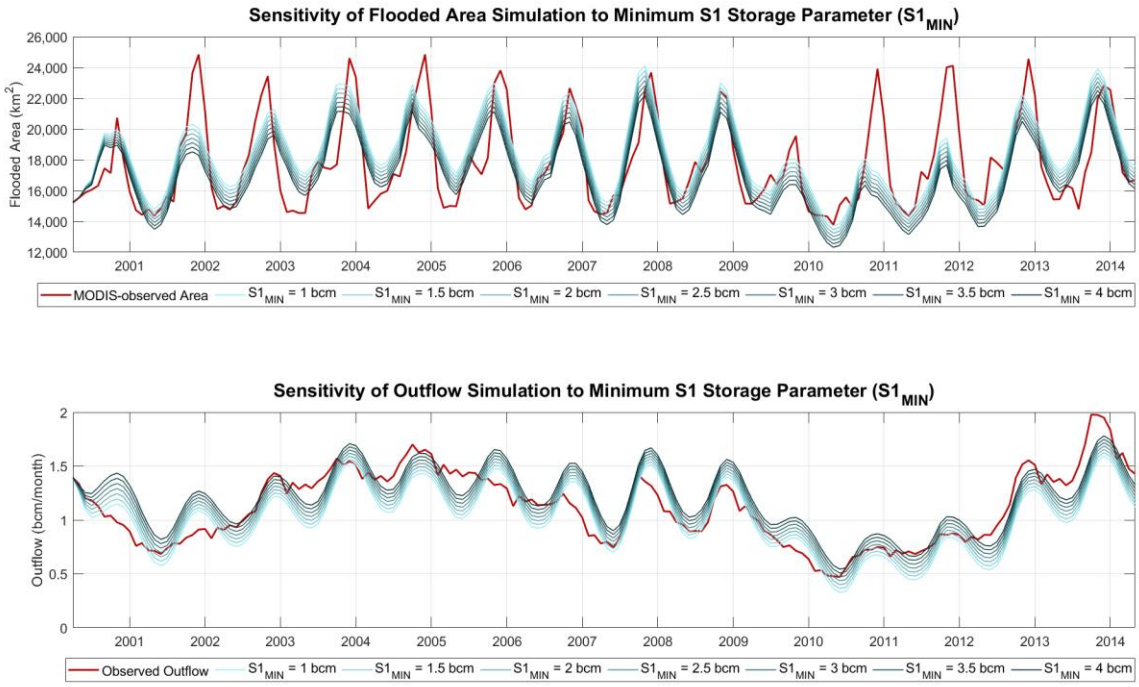

Figure 121: Sensitivity of flooded area and outflow simulations to minimum surface water storage (S1) parameter.

The minimum storage parameter is a constant in the area-storage relationship and informs the initial value of the storage in *S2*. This parameter generally shifts the flood areas and outflows up or down, but the magnitude of this shift is not constant. The variations in this shift for different values of $S1_{MIN}$ is less substantial when there are larger variations in

the magnitude of $S1(k) - S1_{MIN}$, when the wetland is advancing and receding. However, compared to the depth parameter, the minimum storage parameter does not significantly impact the strength of the relationships between the storages, areas, and outflows. The minimum storage in *S1* must be treated as a parameter, as opposed to calculating it from the *S1* storage (similar to the calculation for $S2_{MIN}$), because the storage in *S1* must be initiated from the observed flooded area, and the fitted $S1_{MIN}$ and *d* parameters. Therefore, if $S1_{MIN}$ was calculated from the simulated *S1* storage, the entire *S1* storage sequence would then change, and an iterative calculation procedure for calculating $S1_{MIN}$ from *S1* might not converge.

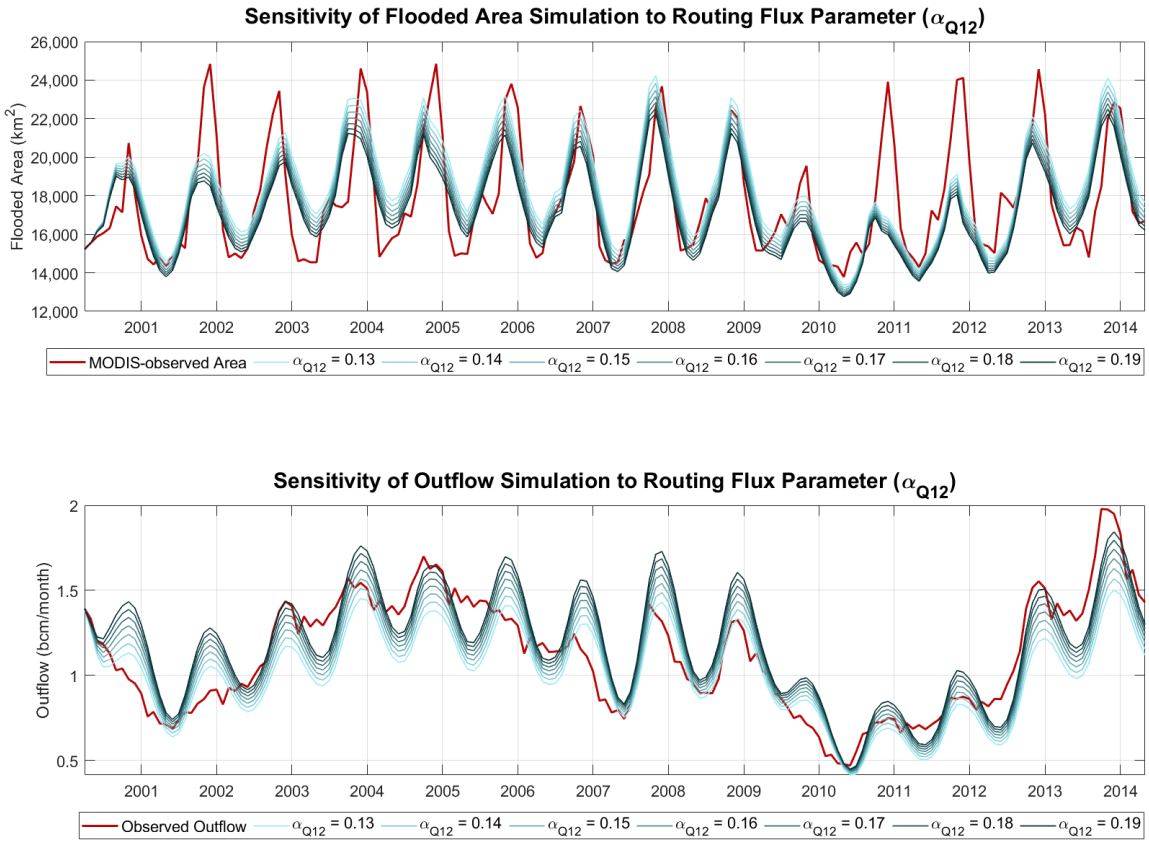

Figure 122: Sensitivity of flooded area and outflow simulations to routing flux parameter.

The routing flux parameter controls the linear relationship between the routing flux and the storage in *S1*. Therefore, higher values result in more of the *S1* storage being sent to *S2*, and by a greater amount when the storage is high. Therefore, in the flooded area simulation, an increase in the routing flux parameter reduces the minimum flood extents by a larger magnitude during the wet years as opposed to the dry years, which makes the minimum flooded area extents more consistent from year-to-year. However, larger values of the routing flux parameter also increase the intra-annual variations of the simulated outflows. Consequently, the optimal value was much larger for the model that was

calibrated to the flooded areas only as opposed to the models that were calibrated to outflows.

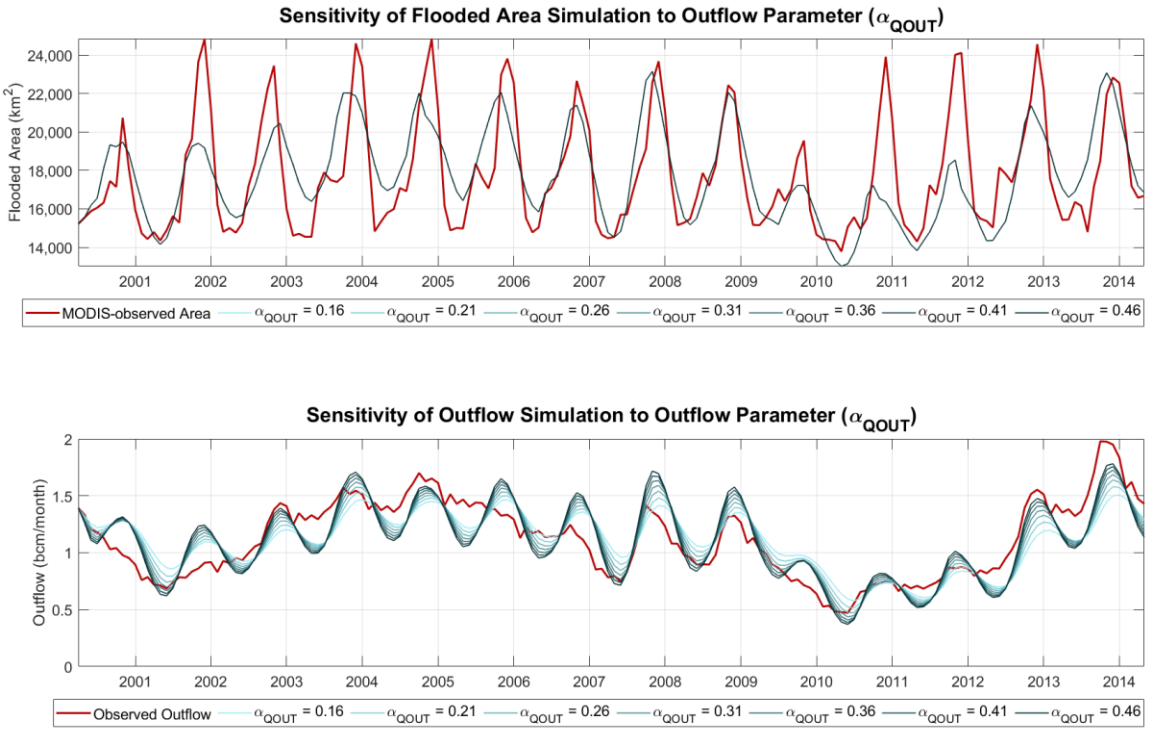

Figure 123: Sensitivity of flooded area and outflow simulations to outflow parameter.

The outflow parameter controls the amount of water from *S2* that is released at the Sudd exit and does not impact the flooded area simulation. A lower value reduces the intra-annual variations of the outflows. However, the optimal outflow parameter must be balanced with the routing flux parameter to ensure the storage in S2 is stable, so the feasible range of the outflow parameter is dependent on the routing parameter.

With the exception of the receding recharge parameter, consistent rules for determining the range of optimal parameter values cannot be clearly identified. Many of

the parameters have similar impacts on the resulting flooded area and outflow time series in terms of the magnitude and intra-annual variations of the fluxes. Additionally, there is always a trade-off between matching the flooded areas and the outflows. The review of wetland models in Chapter 2 discussed how most wetland models are integrated into rainfall-runoff models and calibrated to outflows only. Based on this analysis, the optimal parameters in many of these models may be far from the true parameter values that would represent the areal fluctuations of the wetland.

6.6.2 Model Cross-Validation

Cross-validation can be used to assess how sensitive the optimal model parameters are to sub-sets of training data, the observed areas and outflows in this application. If the model simulations and performance metrics and the optimal parameter set vary drastically for different subsets, then the model is overfitting a data set that does not capture the full system dynamics. Consequently, the model should be considered less reliable for prediction and forecasting. In the context of the Sudd, the model will have low predictive power if the observations from 2000 to 2015 do not capture the full range of flooded areas and outflows that could occur in the Sudd.

Considering there are 14 full years of flooded area and outflow observations available in this study, a seven-fold cross-validation was performed. Two years of continuous data were removed at a time, from April to April to ensure that the truncated time series maintained the same seasonal behaviors. These two-year subsets were removed from the flooded area and outflow observations and the hydrologic fluxes. The optimal

model parameters were then identified using the procedure outlined in Section 6.5.2. The optimal parameter set from the full model calibration (to both the flooded area and outflow) was used to initiate the calibration process using the medium discretizations. The final parameter sets were then determined using the fine discretizations. Computations were again performed on the Wake Forest University DEAC Cluster to implement the seven cross-validation exercises simultaneously. The optimal parameter sets and objective function terms were recorded for each of the seven cross-validations and are presented in Table 27 and Table 28. Values that appear to deviate from the standard values are highlighted.

Table 27: Optimal parameters obtained from 7-fold cross-validation, compared to parameters from full calibration. Values that appear to deviate from the standard values are highlighted.

Years Removed	*Optimal Parameters*						
	d	r_A	r_R	α_{ET}	$S1_{MIN}$ *(bcm)*	α_{Q12}	α_{QOUT}
None	1.123	1.46	0.00	0.9450	2.50×10^9	0.1584	0.310
2000 – 2003	1.050	1.46	0.00	0.9380	2.30×10^9	0.1781	0.278
2003 – 2005	1.170	1.50	0.00	0.9340	2.50×10^9	0.1501	0.337
2005 – 2007	1.345	1.42	0.00	0.9746	2.70×10^9	0.1370	0.380
2007 – 2009	1.030	1.46	0.00	0.9292	2.36×10^9	0.1716	0.300
2009 – 2011	1.160	1.94	0.00	0.8900	3.04×10^9	0.1599	0.376
2011 – 2013	1.028	1.80	0.00	0.8750	3.02×10^9	0.1585	0.431
2013 – 2015	1.055	1.82	0.00	0.8870	2.30×10^9	0.1676	0.260

Table 28: Objective function values from the 7-fold cross-validation, compared to those of the full model calibration. Values that appear to deviate from the standard values are highlighted.

Years Removed	*Objective Function Values*					
	J1	*J2*	*J3*	*J4*	*J5*	J_{TOT}
None	0.1861	0.1176	0.4226	0.2629	0.000194	0.9895
2000 – 2003	0.1899	0.1093	0.4523	0.2611	0.008900	1.0216
2003 – 2005	0.1829	0.1343	0.3989	0.2132	0.000035	0.9293
2005 – 2007	0.1991	0.1312	0.4523	0.2132	0.000010	0.9958
2007 – 2009	0.1979	0.1172	0.4264	0.2132	0.000014	0.9547
2009 – 2011	0.2026	0.1374	0.3693	0.2611	0.000043	0.9705
2011 – 2013	0.1850	0.1526	0.3693	0.2611	0.000177	0.9682
2013 – 2015	0.2063	0.1205	0.3693	0.2611	0.006100	0.9578

The results in Table 27 and Table 28 are not very surprising, and overall the parameters are fairly stable across the seven calibrations. The depth parameter increases when the 2005 to 2007 period is removed, which is a period with relatively large seasonal fluctuations. Therefore, a smaller depth parameter results in a smoother time series. The ET parameter for 2005 to 2007 also increases, which increases the losses and reduces the peak flooded areas. The ET parameters are considerably smaller for the 2009 to 2015 period, which reduces the ET losses. However, the advancing recharge parameter is larger, which increases the infiltration losses and compensates for the lower ET losses. The objective function term that represents the RMSE of the outflows is significantly higher when the 2011 to 2013 period is removed. This is the period following the drought, when the storage and outflows are low, but the MODIS-observed flooded areas are large. This increase in the objective function value suggests that the outflows should be lower than normal following the drought and further supports the hypothesis that the MODIS-derived

flooded area maps from 2011 to 2013 contain areas that are not truly connected to the Sudd water balance.

The model performance using each of the seven optimal parameter sets was evaluated using statistical metrics that measure the differences between the observed and simulated flooded areas and outflows for the two years that were removed from the calibration period. The mean absolute error (MAE) and the mean absolute bias (MAB) for both the flooded area and outflow simulations were recorded and are listed in Table 29. Not surprisingly, the performance metrics show that if the 2011 to 2013 period (following the drought) is removed from the calibration data, then the model does a poor job predicting the flooded areas and outflows. Therefore, if data during a drought period was not available for the model calibration, a model with better performance metrics could be obtained; however, this model would not be appropriate for predicting the Sudd flooded areas and outflows following a drought period.

Table 29: Performance metrics that compare the simulated and observed outflows and areas for the two years that were removed in the 7-fold cross-validation, compared to the full model calibration.

Years Removed	*Flooded Area*		*Outflow*	
	MAE (km^2)	*MAB (km^2)*	*MAE (bcm)*	*MAB (bcm)*
2000 – 2003	1,318	-115	0.173	0.170
2003 – 2005	1,754	-162	0.117	0.032
2005 – 2007	1,856	505	0.185	-0.102
2007 – 2009	1,379	485	0.192	0.052
2009 – 2011	894	-393	0.151	0.152
2011 – 2013	2,382	-2,276	0.055	0.004
2013 – 2015	1,710	205	0.254	-0.254
Average	1,613		0.161	
No years removed	1,602	-62	0.141	-0.028

Each of the optimal parameter sets in Table 27 were applied to simulate the flooded areas and outflows for the full 2000 to 2015 period, and the resulting simulations are plotted together in Figure 128. Relative to the overall differences between the simulated and observed series, the differences between simulations with different optimal parameter sets are small. Therefore, this cross-validation exercise showed that the optimal model parameters are relatively stable and do not overfit the model. However, all of the calibrated models have difficulty simulating the flooded area extents, especially following the 2010 drought.

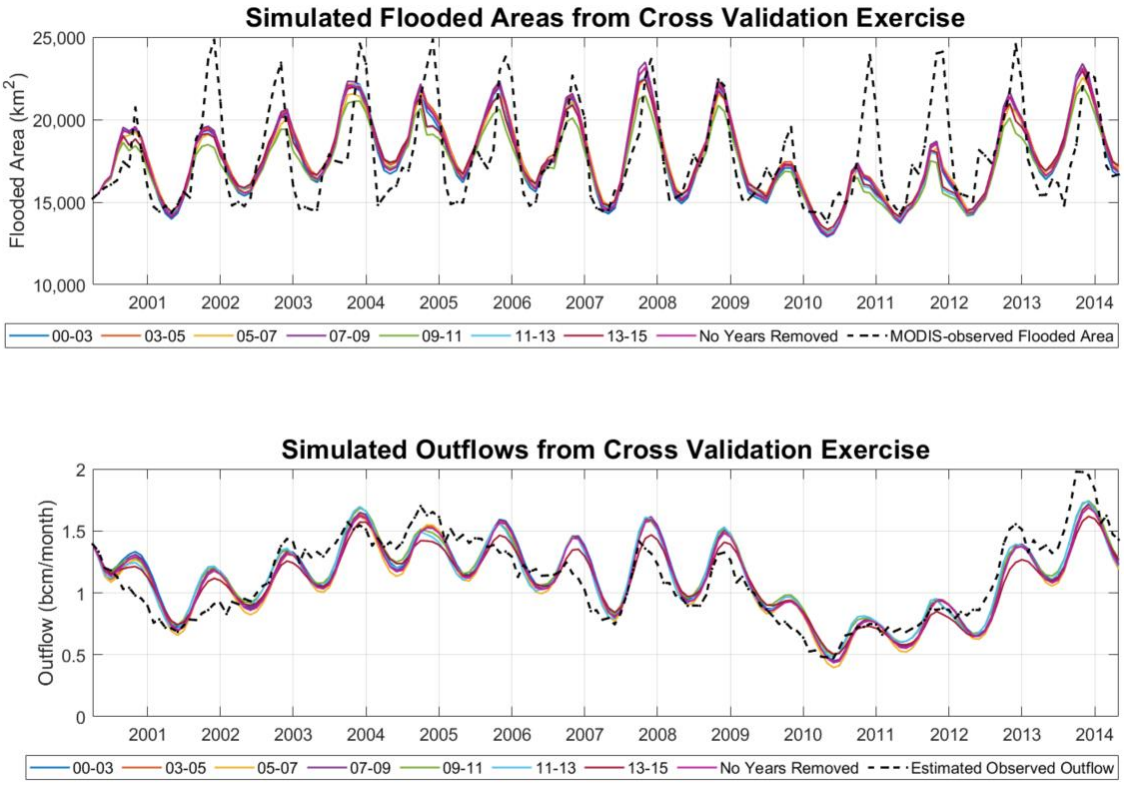

Figure 124: Simulated flooded areas and outflows when using optimal parameter values from 7-fold cross-validation. The years shown in the legend are the years that were removed during the cross-validation.

6.6.3 Hydrologic Data Uncertainty

Sections 6.6.1 and 6.6.2 focused on the model sensitivities and uncertainties related to the model parameters. However, the impact of hydrologic data uncertainties on the model simulations should also be evaluated and compared to identify the most significant sources of uncertainty. Therefore, the optimal model parameters from the full model calibration (Table 25) were used to simulate the flooded areas and outflows for different precipitation and ET data sources, and for inflow estimates that include errors sampled from the monthly error distributions derived in Section 4.5.3. All of the figures in this section were plotted on the same scale to enable a comparison across different types of data.

Model sensitivity to precipitation data sources:

In Chapter 4, four different precipitation data sources were explored, but TRMM consistently had the best performance metrics and was selected to determine the structure of a hydrologic model of the Sudd. Estimating the error of these precipitation estimates is not possible considering the lack of in-situ data in the Sudd that is independent of the satellite-based estimates. Therefore, the model uncertainties due to errors in the precipitation estimates was assessed by simulating the flooded areas and outflows using all four precipitation estimates and comparing the results.

The simulated flooded areas and outflows produced from the four precipitation estimates are shown in Figure 125. The simulation associated with PERSIANN stands out, although this result is not surprising considering the PERSIANN data is believed to

significantly overestimate the Sudd precipitation. The remaining three simulations are relatively similar to one-another. The model parameters could be optimized using these alternative precipitation data sources. However, this exercise is unlikely to result in a significant model improvement considering the larger model deficiencies related to the connectivity of the Sudd flooded areas.

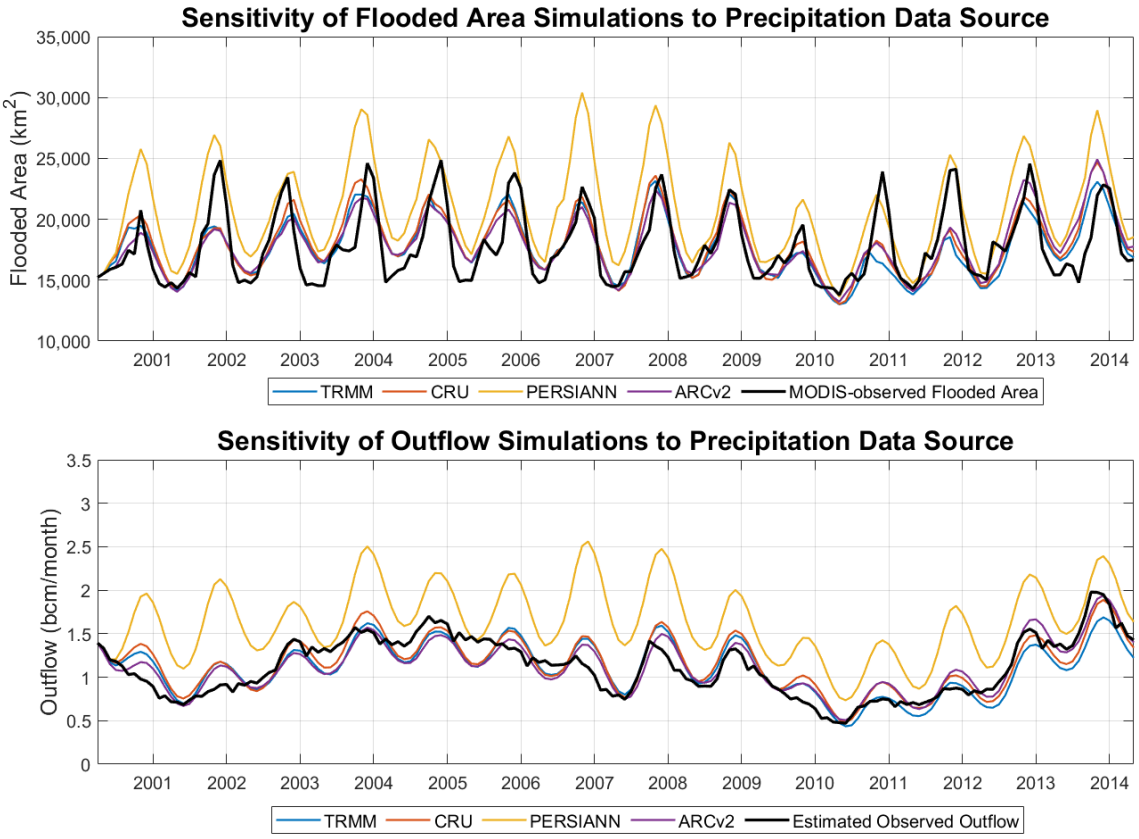

Figure 125: Sensitivity of flooded area and outflow simulations to precipitation data source, using four alternative precipitation estimates obtained in Chapter 4.

Model sensitivity to ET data sources:

Similar to the precipitation uncertainty assessment, the ET uncertainty assessment was performed by simulating the flooded areas and outflows associated with the alternative ET estimates described in Chapter 4. However, to account for the fact that a parameter was introduced to adjust for the bias in the estimated ET and calibrated using the Hargreaves ET, this parameter was adjusted for each of the alternate ET estimates. This adjustment was performed using Equation 82 and ensures there is no bias between the Hargreaves ET and the ET being applied in the model, over the full simulation period.

$$\alpha_{ET,D} = \frac{\alpha_{ET,HAR} \sum_{k=1}^{T} ET_{HAR}(k)}{\sum_{k=1}^{T} ET_{D}(k)} \quad [82]$$

where:

$\alpha_{ET,D}$ *= ET parameter for data source being applied*
$\alpha_{ET,HAR}$ *= optimal ET parameter, model calibrated with Hargreaves ET (0.945)*
k = temporal index
T = total number of time steps used in simulation.
ET_D *= ET flux for data source being applied (m)*
ET_{HAR} *= Hargreaves ET flux (m)*

The resulting simulated flooded areas and outflows are presented in Figure 126. These results are similar to those from the precipitation uncertainty assessment (with the exception of the PERSIANN precipitation). Again, model parameters could be optimized using these alternative ET data sources, but the larger model deficiencies would remain.

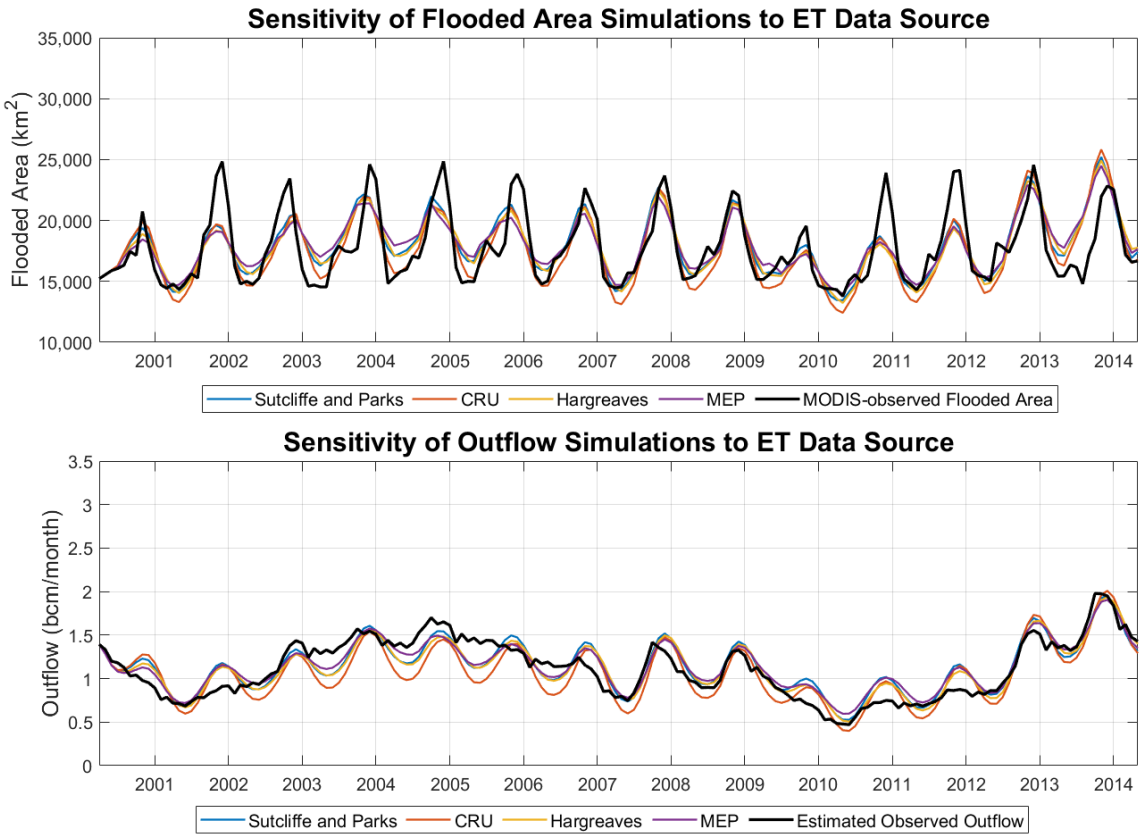

Figure 126: Sensitivity of the simulated flooded areas and outflows to alternate ET data sources that were discussed in Chapter 4.

Model sensitivity to inflow uncertainty:

Recall that in Section 4.5.3 the monthly error distributions describing the uncertainty of the Mongalla flows were derived. The propagation of these errors though the hydrologic model can be evaluated to understand the associated effect on the flooded area and outflow simulations. To perform this analysis, ensemble estimates of the Mongalla flows can be derived by applying the calibrated autoregressive model derived in Section 4.5.3 with estimates of the error terms obtained by randomly sampling from the

monthly error distributions. The autoregressive model was previously presented in Equation 37 and is listed again here for convenience.

$$Q_{MON}(k) = -0.060643 + 0.19474Q_{NIM}(k) - 0.13171Q_{NIM}(k-1) + 0.93112Q_{MON}(k-1) + 0.99677Q_{TOR}(k) - 0.90984Q_{TOR}(k-1) + \varepsilon(k) \quad [37]$$

Equation 37 was simulated at a 10-day resolution in units of mcm/day. The computed flow for time step k replaced the flow at time k-1 in subsequent calculations to provide the most realistic representation of the error propagation. Once the simulations were completed, the flows were aggregated and converted to units of bcm/month. Twelve of these simulations are shown in Figure 127.

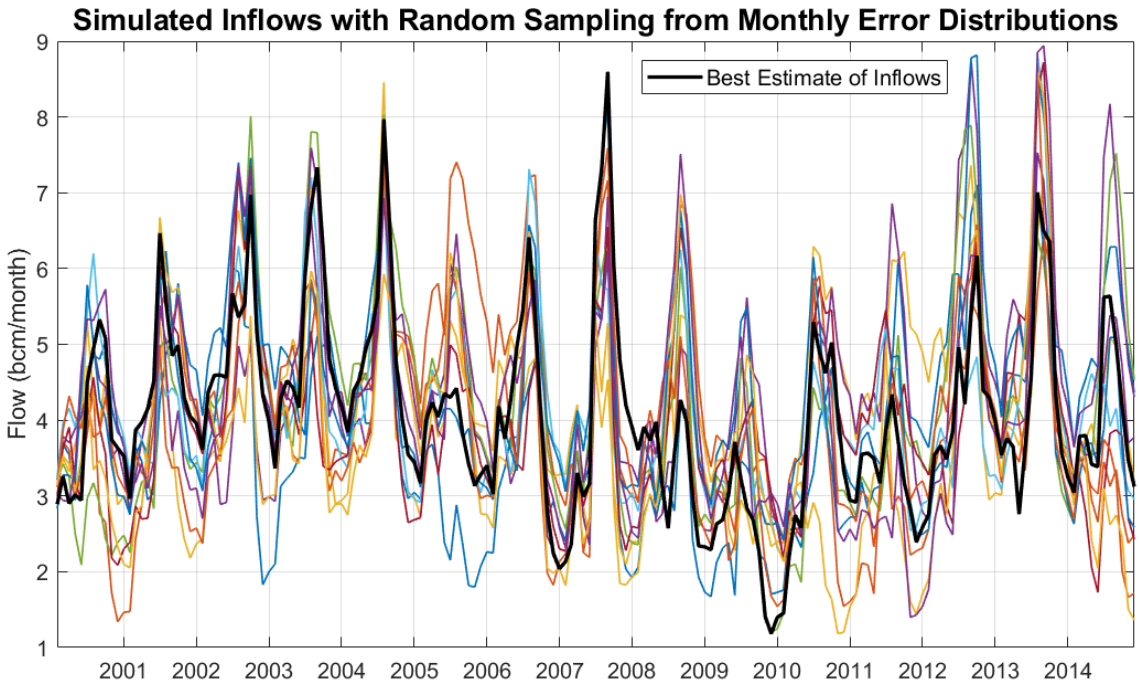

Figure 127: Ensemble inflow series (12 shown) obtained using the fitted autoregressive equation for the Mongalla flows. Errors were estimated by randomly sampling from the monthly distributions derived in Section 4.5.3.

Each of the simulated Mongalla flow estimates were then applied in the hydrologic model, using the optimal parameters obtained from the full calibration (using both outflow and area). The resulting simulated flooded areas and outflows are presented in Figure 128. There is a significant amount of variation between the flooded areas and outflows simulations, indicating that the model's ability to accurately simulate these fluxes is highly dependent on the accuracy of the inflow estimates. The uncertainty from the inflows is much more significant than the uncertainty from the precipitation and ET estimates. Additionally, the model sensitivity to perturbations in parameter values seems relatively minor compared to the simulations presented in Figure 128. The primary source of this uncertainty stems from the Torrents flows, simulated using the calibrated rainfall-runoff

model. Therefore, having access to more accurate flow rates directly at Mongalla, downstream of the Torrents, would substantially reduce the uncertainty of the simulated areas and outflows. However, if the Mongalla flows are measured in the future, the structure and calibration of the hydrologic model should be re-evaluated considering its dependency on the current, uncertain inflow estimates.

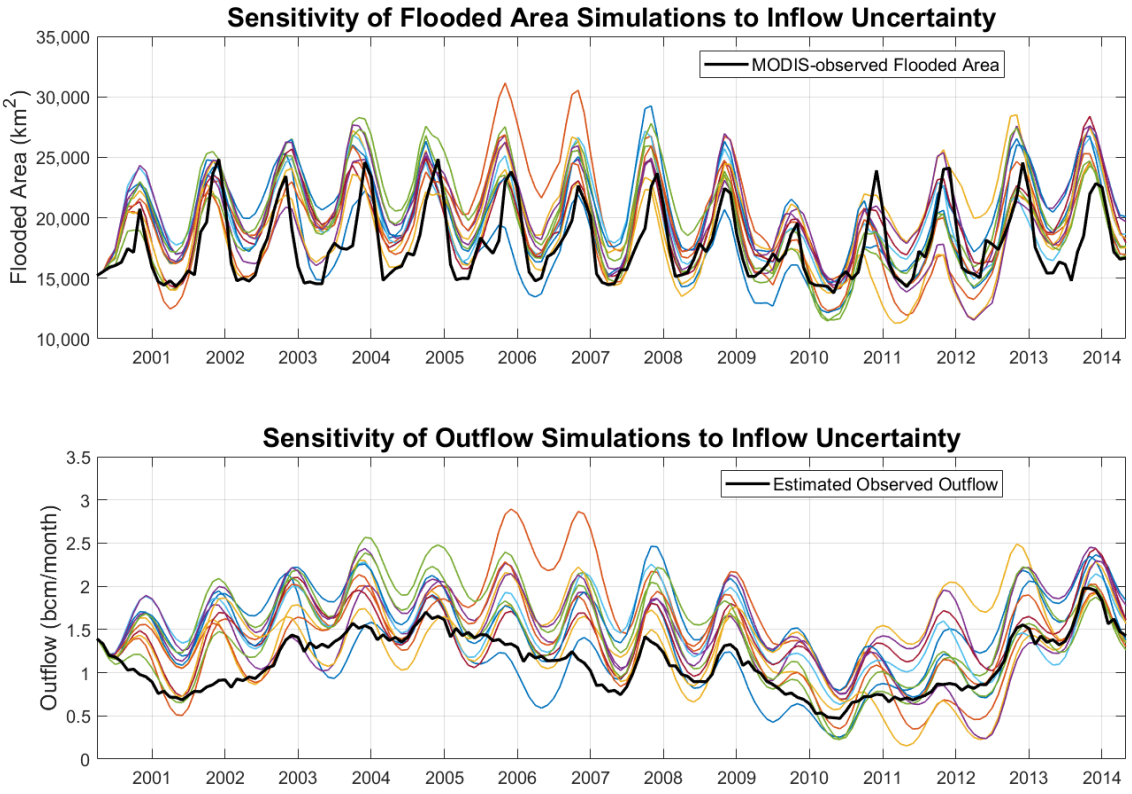

Figure 128: Simulated flooded areas and outflows obtained by applying the ensemble inflow estimates to the calibrated hydrologic model.

6.7 Summary

Consistent with the iterative modeling process outlined in Figure 1, a simple hydrologic model of the Sudd was first evaluated using the MODIS-derived flooded area maps and the estimated Sudd outflows. The model complexity was increased only after carefully evaluating the estimated fluxes and the relationships between them. Model limitations were examined in the context of errors and uncertainties ingrained in all aspects of the model, including the model structure, the optimal parameters, hydrologic fluxes and flows, and the MODIS-derived flooded area maps.

The **key insights** obtained through this modeling exercise that are discussed in detail throughout the Chapter are summarized as follows:

1. The Sudd flooded areas and outflows cannot be simulated from a single storage compartment. The addition of a routing compartment for the outflows significantly improved the model performance and can simulate the storage-attenuation characteristics of the wetland. This improvement also allows the flooded areas and outflows to be modeled from two different storage compartments, allowing for variations in the magnitudes of seasonal variations within the flooded area and outflow simulations.
2. The storage-area relationship (modeled from the surface water storage compartment) requires temporal lags to capture the timing of the maximum and minimum flooded area extents. The magnitude of this temporal lag is believed to vary as the flood season progresses; the lag should increase as the flooded area

increases because the flood water takes longer to reach the outer extents of the wetland. However, conditions for when the transition in lags should occur could not be identified without directly applying the observed flooded areas. Modeling the flooded area as a function of the storage at multiple time steps produces a flooded area simulation that is too smooth. However, applying a one-month lag between the storage and area improves the alignment of the simulated and observed flooded areas while maintaining the magnitude of the seasonal variations of the flooded area extents.

3. The optimal maximum soil-water recharge depth was approximately 1.5 meters and far exceeds the depth estimated from field studies (0.2 to 0.35 meters). However, infiltration could be occurring in both the horizontal and vertical directions.
4. Allowing shallow subsurface groundwater to re-enter the wetland when it is receding did not improve the model performance because once the area begins to recede, it recedes very quickly. However, groundwater could be entering the wetland from the area surrounding the Sudd during the rainy season, before the wetland recedes.
5. The multiple model calibration approaches (using the observed flooded areas and outflows independently and jointly) illustrated that the observed outflows could be simulated from the model with acceptable accuracy (a Nash-Sutcliffe Efficiency coefficient of 0.75 was achieved), but large errors are present when the model simulates the MODIS-derived flooded areas. These errors are likely related to the conclusions in Chapter 4, which question whether the flooded areas depicted in the MODIS-derived maps are truly connected to the surface water storage

compartment. Therefore, the hydrologic model might be accurately simulating the flooded areas that are connected to the surface water storage and contribute to the outflows but is not able model the full extent of the flooded areas estimated from MODIS.

6. The cross-validation and parameter sensitivity analysis showed that the overall behavior of the simulated flooded areas and outflows are not extremely sensitive to the model parameters, using the assumed linear relationships. Adjustments to the model parameters can affect the magnitude and intra-annual variations of the simulated flooded areas and outflows, but there is always a trade-off; both the areas and outflows cannot be improved simultaneously.
7. The hydrologic data uncertainty analysis showed that the model simulations are very sensitive to the estimated errors of the inflows, compared to the uncertainty of the satellite-based estimates of the precipitation and ET rates.

Based on the key insights obtained from this model development process, **future research efforts** that could improve the Sudd hydrologic model have been identified and described throughout this Chapter and are summarized as follows:

1. Develop, calibrate, and evaluate a model, following the same general process implemented here, that adds a third compartment to model the storage in areas surrounding the Sudd. This model would allow both surface water and groundwater to be exchanged between the inner compartment that is connected to the Nile River, and the outer compartment that is controlled by precipitation and ET fluxes.

2. Fine-tune the storage-area-outflow relationships using non-linear relationships or conditional relationships. For example, instead of a constant depth parameter, the depth could vary with the storage in the wetland, and the flooded area might be a non-linear function of the storage. The relationships could also change depending on the state of the system. For example, the temporal lags between the area and storage can shift based on the state of other hydrologic fluxes and storages.
3. Identify the optimal number of model parameters that result in appropriate model performance metrics without overfitting the (uncertain) observed flooded areas and outflows. This analysis could be performed using the Akaike's Information Criterion (AIC) [Akaike, H., 1973]. The AIC measures model performance with the likelihood of the model correctly predicting an observation and includes a penalty term for the number of model parameters. The AIC can be compared across multiple models with an increasing number of parameters, and the model with the lowest AIC is considered the most parsimonious model.
4. Instead of using a single, deterministic set of optimal parameter values, identify distributions of each parameter and perform a Monte-Carlo simulation of the model to obtain an ensemble of flooded area and outflow estimates. The distributions of the parameters could be inferred from the range of optimal parameter values determined through the multi-step calibration approach described in Section 6.5.2, where results were listed in Table 25. The extremes of the ensemble of flooded area and outflow estimates should bracket the observed flooded areas and outflows.
5. The Sudd could be split into multiple sub-basins to more accurately capture the spatial variations of the hydrologic fluxes, model parameters, and storage-area-

outflow relationships. However, the challenge with a semi-distributed model would be obtaining reliable data for calibration. Historical flow records within the interior of the Sudd are available in the Nile Basin Volumes and were digitized to explore the feasibility of splitting the Sudd into multiple sub-basins. Unfortunately, these flow records do not capture the flows across a full transect of the Sudd and therefore could not be used to derive flow estimates during the 2000 to 2015 period that are accurate enough for calibrating a semi-distributed model. However, the development of a semi-distributed model might be beneficial considering the spatial variations in the fluctuations of the flooded areas discussed in Section 5.3, and the multiple temporal lags between the flooded area and storage that were assessed in Section 6.4.2.

CHAPTER 7: CONCLUSIONS AND FUTURE RESEARCH RECOMMENDATIONS

7.1 Conclusions

The guiding research question that was posed in Section 1.1 can now be revisited:

> *How can satellite data be leveraged to develop process-based hydrologic models of wetlands with limited in-situ data, enabling the integration of wetland socio-economic and environmental services into basin-wide water resource assessments and management?*

Recall that this guiding question was broken down into nine sub-questions. Each sub-question is listed below and followed with bullet-point explanations of how the question was explored and/or addressed in this research.

1. *Can multi-temporal satellite imagery be leveraged to improve existing wetland land cover classification procedures?*
    - A novel wetland land cover classification procedure was developed in Chapter 3 that distinguishes between different land cover types and characterizes their flooding regimes. This classification procedure uses all data from a multi-year sequence of optical satellite imagery to develop monthly distributions of remote sensing indices for individual training pixels. These monthly distributions can then be used to classify larger areas based on nonparametric distance measures that measure the similarity between pixel distributions. The methodology also identifies

pixels that have properties of more than one wetland land cover class. The resulting wetland land cover map derived for the Sudd is spatially coherent and provides more information on the wetland land classes and their flood frequency than currently available global or regional land cover maps.

2. *Can wetland inundation maps be derived from satellite imagery with sufficient accuracy and spatial and temporal resolution to inform hydrologic wetland models?*
    - MODIS satellite imagery provides data at a sufficient spatial (500-meter) and temporal (near daily) resolution to derive a time series of inundation maps that could be integrated into a hydrologic model of the Sudd Wetland. Monthly inundation maps from 2000 to 2018 were derived in Chapter 3 using the MODIS-derived wetland land cover map and a geostatistical procedure that can assess whether each pixel is flooded for a monthly temporal resolution. These monthly inundation maps were found to be significantly correlated to the net flux in the Sudd based on the analysis performed in Section 3.5.3, suggesting that they are accurate enough to inform a hydrologic model of the Sudd.
    - However, a comparison of the <u>cumulative</u> net fluxes and MODIS-derived flooded areas in Chapter 5 showed some inconsistencies that led to a more thorough evaluation of the inundation maps. The advancing and receding flood patterns were examined and areas that did not expand chronologically in a manner consistent with the hydrologic fluxes were highlighted. Some of the larger inconsistent areas are believed to be misclassifications caused by the inundation algorithm developed in Chapter 3. However, many of the inconsistent areas are present across multiple

years and are believed to be correctly classified as flooded, but the flooding is caused by local rainfall and the areas might not be truly connected to the main surface water body. An algorithm was developed in Chapter 5 to correct the areas that were believed to be misclassified, but a procedure for identifying areas that are not fully connected to the Sudd water balance could not be produced using currently available data. This hypothesis regarding the wetland connectivity can also explain some of the limitations of the hydrologic model that was developed in Chapter 6. Therefore, in this research satellite imagery was leveraged to map wetland inundated areas, but the pixels that are connected spatially might not be connected hydrologically to the main surface water body that controls the Sudd outflows.

3. *Can reliable estimates of precipitation and evapotranspiration (ET) rates be obtained from satellite-based data products in areas with limited in-situ data?*

    - Four different estimates of precipitation were obtained over the Sudd, and only one (from the CRU) did not use satellite data. With the exception of the PERSIANN product, they were relatively consistent with one-another. Dr. Georg Petersen shared some in-situ precipitation measurements that were collected over a 20-month period, enabling a point-to-pixel comparison with the gridded data products (Section 4.2.2). TRMM estimates generally had the best performance metrics. An additional, indirect assessment of the precipitation accuracy was performed in Section 5.5. The correlation between the MODIS-derived flooded areas and the net water flux was calculated for different combinations of precipitation and ET

sources. The combinations that used TRMM estimates consistently provided the highest correlation coefficients.

- Four different estimates of ET rates over the Sudd were obtained or derived using various physical ET formulations, and were compared to the climatology ET reported in the literature. Two of these estimates were obtained using CRU gridded data products, which do not use satellite information. There was a significant amount bias between the estimates, but a model parameter was introduced that corrects for this bias and allows the magnitude of the ET flux to be adjusted for the Sudd vegetation. With the exception of the GLEAM data product, the ET estimates had similar seasonal trends. The GLEAM product is believed to be inaccurate because the ET was estimated from a surface energy balance algorithm that likely misrepresents the flooded area of the Sudd, and therefore underestimates the soil moisture content. The accuracy of the ET estimates was also evaluated indirectly through the correlation analysis in Section 5.5, which suggested that the Hargreaves ET might be more accurate. The Hargreaves formulation is relatively simple and uses a temperature gradient that was estimated from the CRU data set.
- Based on the accuracy assessments performed in Section 4.2.2 and 5.5, TRMM precipitation and Hargreaves ET estimates were assumed to be the most accurate and were chosen to develop the Sudd hydrologic model. However, these accuracy assessments were not conclusive, and the estimates likely have significant errors. In Section 6.6.3, different precipitation and ET rates were applied to the calibrated Sudd model and did not significantly impact the simulated flooded areas and

outflows (except for the PERSIANN precipitation and GLEAM ET), compared to the impact from the uncertainty of the Sudd inflows.

4. *Can the Sudd inflows and outflows be estimated from a limited amount of in-situ data available upstream and downstream of the Sudd entrance and exit, with sufficient accuracy to calibrate a hydrologic model of the Sudd?*

    - In Section 4.5, the Sudd inflows and outflows during the 2000 to 2015 period were derived primarily from in-situ flow data at Laropi, a location upstream of the Sudd's entrance. The Laropi flows were first gap-filled using satellite altimetry data over Lake Albert, a lake storage-outflow relationship, and a statistical routing equation between the Lake Albert outlet and Laropi that was calibrated using historical Nile River flow data. The Torrents flows that enter the Nile between Laropi and the Sudd's entrance were then estimated by calibrating a simplified rainfall-runoff model. The flows at Mongalla, the Sudd's entrance, were then estimated using an auto-regressing routing model that also depends on the Laropi and Torrents flows and was calibrated using historical Nile flow data. The Sudd outflows were then calculated using an additional auto-regressive routing equation that modeled the losses in the Sudd (Inflows - Outflows).
    - The resulting inflow and outflow time series had similar characteristics to historical flow records and were found to be generally consistent with the precipitation and ET fluxes and the MODIS-derived flooded areas, according to the correlation analysis performed in Section 5.5. However, the uncertainty assessment described in Section 4.5.3 demonstrated that the estimated Torrents flows, produced by the

rainfall-runoff model, introduce large uncertainties in the estimated inflows and outflows for the 2000 to 2015 period.

5. *How does the uncertainty of the estimated hydrologic fluxes and flows propagate through a hydrologic model of the Sudd?*

    - The sensitivity of the calibrated Sudd hydrologic model to uncertainties within the precipitation, ET, and flow estimates was explored in Section 6.6.3. In-situ data was not available to derive statistics that describe the true error of the precipitation and ET data products. Therefore, the uncertainty of the precipitation and ET were evaluated by simply applying the different data products to the hydrologic model and observing the associated variation within the simulated flooded areas and outflows. These variations were relatively insignificant compared to the errors between the simulated and observed flooded areas and flows, indicating that the simulation errors associated with the precipitation and ET uncertainty are relatively minor compared to the uncertainty of the model structure. Monthly error distributions of the Sudd inflows were derived in 4.5.3 and allowed an ensemble of inflows to be simulated using the calibrated auto-regressive equation. The errors were included in the simulations by sampling from the monthly distributions. The inflow ensemble was then applied to the hydrologic model, and the resulting simulated flooded areas and outflows contained a substantial amount of variation. Therefore, the inflow uncertainties significantly impact the performance of the Sudd hydrologic model.

6. *Are the satellite-based estimates of the Sudd flooded area extents, precipitation rates, and ET rates, and estimates of the Sudd inflows and outflows consistent with one-another in terms of the overall Sudd water balance? Can data correction procedures be developed from a holistic comparison of these independently derived estimates?*

    - The consistency between the Sudd fluxes and the MODIS-derived flooded areas was explored in Chapter 5 and leveraged to select amongst multiple data sources and develop data adjustment procedures.
    - A comparison of the annual cumulative water flux in the Sudd and the annual cumulative flooded areas revealed inconsistencies between the data sources (Section 5.2). This observation was followed by a closer examination of the advancing and receding patterns of the MODIS-derived flooded areas. This analysis was summarized in the response to the second question above and refenced a procedure for adjusting the flooded area maps. This procedure is described in Section 5.4 and was developed by leveraged the fact that months with higher flows and precipitation rates should also have larger flooded area extents.
    - In Section 5.5, the net water flux in the Sudd was calculated for multiple combinations of precipitation and ET estimates, and each flux was compared to the MODIS-derived flooded area maps. The correlation coefficients between the net water fluxes and the flooded areas were considered measures of their consistency, and the precipitation and ET estimates with higher correlation coefficients were assumed to be more accurate data sources.

7. *What are the dominant wetland hydrologic processes that must be represented in a model for the Sudd? Are there existing models that can accurately simulate these processes and the wetland response?*

   - The analyses performed in Chapter 5 and the relatively high correlation coefficients that were obtained between the MODIS-derived flooded area extents and Sudd flux using only precipitation, ET, and river flow suggested that an accurate hydrologic model of the Sudd could be develop using these fundamental surface water processes. The existing Sudd model introduced by Sutcliffe and Parks relied on these fundamental processes, along with vertical infiltration over newly flooded areas (estimated as a function of the cumulative rainfall). However, when this model was evaluated using the MODIS-derived flooded area maps in Section 6.2, the simulated flooded areas were over-estimated and the timing of the peaks did not align. In Section 6.3, this model was modified to also simulate the outflows, and the model was not able to simulate both the flooded areas and outflows from a single surface water storage compartment. Therefore, the existing model of the Sudd was limited in its ability to model the wetland response.
   - In Section 6.4, the Sudd water storage was simulated using the existing model and the MODIS-observed areas (as opposed to the simulated areas), to more accurately represent the true water storage in the Sudd that the model should produce. These "observed" storages were then compared to the precipitation, ET, river flow, and observed areas to reformulate the relationships between the storage, flooded area, and outflow. This exploratory exercise led to the development of a revised model (Section 6.5) that contains a second storage compartment (*S2*) that controls the

Sudd outflows and is coupled to the surface water storage compartment (*S1*). The form of the area-storage and outflow-storage relationships were also modified. This revised model did not include any additional hydrologic processes, but allowed the storage-attenuation characteristics of the wetland to be simulated more accurately.

- The revised model was calibrated and assessed in Section 6.5. While there was a significant improvement in the simulation of the Sudd outflows, and a moderate improvement in the simulation of the flooded area extents, discrepancies remained between the simulated and observed flooded areas. As described in response to the second question above, some of the MODIS-derived flooded areas are likely not connected to the main Sudd water body. Therefore, a third compartment should be added to the model that simulates the storage in the area surrounding the Sudd from precipitation and ET fluxes, and is coupled to the *S1* compartment through surface water and groundwater fluxes.

8. *What are the advantages and disadvantages of statistical, physically-based hydrologic (lumped or semi-distributed), and hydrodynamic wetland models, and what model type would be most appropriate for the Sudd, given its dominant processes and data availability?*

    - This question was largely explored in the literature review of wetland hydrologic models in Section 2.3. The successes and limitations of previous modeling efforts indicated that a physically-based, lumped or semi-distributed model of the Sudd is

the most appropriate type of model considering the accuracy and spatial and temporal resolutions of data available in the Sudd region.

- The modeling exercises and uncertainty analysis described in Chapter 6 suggest that a lumped model of the Sudd is more appropriate than a semi-distributed model for the following reasons:
    - The simulated flooded areas and outflows are very sensitive to uncertainties from the estimated Sudd inflows. Therefore, a semi-distributed model with more parameters might be overfitting uncertain data instead of improving the model's representation of the wetland.
    - The potential to derive flow estimates at a location within the Sudd's interior during the 2000 to 2015 period was explored using statistical relationships calibrated to historical data from the Nile Basin Volumes. These flows could have been used to calibrate a semi-distributed model of the Sudd, but the conclusion from this analysis (not included in the dissertation) was that there is too much uncertainty in the predicted flows during the 2000 to 2015 period.

9. *What is a suitable approach for developing a model and assessing its performance in a way that considers the uncertainty from the satellite-derived data, the model structure, and the calibration parameters jointly, to make recommendations on how to incrementally improve the model without overfitting uncertain "observations" of the Sudd flooded areas and outflows?*

- Most of the existing research on physically-based wetland hydrologic modeling that was reviewed in Section 2.3 employed a somewhat linear modeling approach. A single mathematical representation of the wetland was assumed, and the model parameters were calibrated according to an objective function that measures how well the model can simulate outflows at a downstream location. This approach only considers uncertainties from the model parameters and fails to question the underlying model structure and assess the impact of data uncertainties.
- The approach developed in this research was described in Figure 1 and requires an iterative modeling approach that considers all sources of uncertainty (from the data, model structure, and parameters). Some specific examples of how this approach was implemented and deviates from traditional modelling approaches are listed below:
    - Instead of using a single data source for the precipitation and ET estimates, multiple data sources were evaluated according to how consistent they were with the Sudd flooded areas and flows (Section 5.5).
    - Instead of assuming the MODIS-derived areas were exact, they were continuously re-evaluated and adjusted as new insights about the Sudd hydrology were realized (Chapter 5 and Section 6.5.5).
    - Instead of applying a single representation of the relationships between the hydrologic variables, multiple representations were tested, evaluated, and revised after analyzing the model simulations (Section 6.4).
    - Instead of calibrating the model exclusively to river outflows, the model was calibrated to both the flooded areas and outflows both individually and

jointly (Section 6.5.2). This multi-step calibration process provided insights on the largest sources of data uncertainties and model limitations.

- Instead of assuming that increasing the model complexity and adding more parameters is the best way to reduce the value of the objective function, uncertainties related to the model structure and hydrologic data were quantified, and the relative magnitudes of these uncertainties informed how the model should be improved (Section 6.6)

7.2 Future Research Recommendations

Recommendations for future research have been suggested throughout this dissertation and are briefly summarized here within three general categories:

1. Opportunities to improve the Sudd flooded area maps and hydrologic model with **in-situ data and field observations**:
    a. Considering the analysis presented in Section 6.6.3, obtaining in-situ flow records at Mongalla could greatly reduce model uncertainties and would eliminate the need to estimate the Torrents flows.
    b. Field observations of flooding could be used to assess and improve upon the inundation mapping algorithm.
    c. A digital elevation model (DEM) that is more accurate than currently available global products would allow the connectivity of flooded areas

across the wetland to be evaluated. Additionally, a hydrodynamic model of the Sudd could potentially be calibrated.

d. Water depth measurements across transects of the Sudd would provide insight on whether the assumption of a constant depth in the wetland is appropriate.

e. Precipitation gauge data from multiple locations within the Sudd would allow the accuracy of gridded data products to be more thoroughly evaluated, and would provide insights on the rainfall-runoff characteristics of the Sudd.

f. Measurements of ET rates for different types of vegetation in the Sudd using an eddy-flux covariance tower or simple pan evaporation experiments could provide insights on the true ET rates for different areas of the Sudd.

2. Opportunities to improve the **wetland land cover and inundation mapping** algorithm and results:

    a. Evaluate the influence of vegetation phenology on the monthly inundation mapping algorithm and whether it is causing classification errors.

    b. Evaluate the influence of burning practices on the monthly inundation mapping algorithm and whether it is causing classification errors.

    c. Apply the wetland land cover classification and inundation mapping algorithm to another wetland where more in-situ data is available for accuracy assessments.

d. Assess whether recently available synthetic aperture radar (SAR) data from Sentinel-1 can be combined with optical satellite data to improve the wetland land cover and inundation mapping algorithm.

3. Opportunities to improve the **Sudd hydrologic model**:
    a. Develop, calibrate, and evaluate the three-compartment model described in Section 6.5.5.
    b. Improve the storage, area, and outflow relationships in terms of their mathematical structure (including non-linear relationships) and the temporal lags between the model states and fluxes.
    c. Identify a parsimonious model that has an optimal number of parameters according to the AIC metric, identify statistical distributions for each parameter, and apply a Monte-Carlo simulation to obtain ensemble flooded area and outflow estimates that bracket the observed flooded areas and outflows.
    d. Develop a procedure for splitting the Sudd into multiple sub-basins that have unique hydrologic properties, and ensure that the model can be calibrated without overfitting uncertain data.

The implementation of the abovementioned future research areas should be consistent with the iterative modeling framework (Figure 1) that has been emphasized throughout this research. Recall that an important characteristic of this research is that the methods and procedures developed can be applied globally to wetlands in data scarce areas.

In-situ data sources and model structure improvements that have the potential to reduce uncertainties specific to the Sudd have been suggested; however, the main contribution of this research is the demonstration of the general approach to develop a wetland hydrologic model using satellite-based data. In particular, the methodologies, assumptions, and sources that were used to obtain satellite-based estimates of the wetland flooded areas, hydrologic fluxes, and flows were re-evaluated and adjusted based on insights obtained through modeling iterations. This approach was employed to prevent errors and uncertainties related to the satellite observations from dominating the model structure and misrepresenting performance metrics. While the increasing amount of satellite information presents new opportunities to more accurately model wetlands, more complex models that use more data are not necessarily better. The framework presented and demonstrated here serves as a tool for hydrologists and water resources engineers to responsibly incorporate uncertain satellite-derived information into wetland hydrologic models.

REFERENCES

Akaike, H. (1973). Information theory and an extension of the maximum likelihood principle. Second International Symposium on Information Theory, pp. 267-281.

Akratos, C. S., J. N. E. Papaspyros, and V. A. Tsihrintzis (2009), Artificial neural network use in ortho-phosphate and total phosphorus removal prediction in horizontal subsurface flow constructed wetlands, Biosystems Engineering, 102(2), 190-201, doi: https://doi.org/10.1016/j.biosystemseng.2008.10.010.

Ali, A. (2009), Nonlinear multivariate rainfall–stage model for large wetland systems, Journal of Hydrology, 374(3), 338-350, doi: 10.1016/j.jhydrol.2009.06.033.

Alsdorf, D., S. Han, P. Bates, and J. Melack (2010), Seasonal water storage on the Amazon floodplain measured from satellites, Remote Sensing of Environment, 114(11), 2448-2456.

Alsdorf, D., P. Bates, J. Melack, M. Wilson, and T. Dunne (2007), Spatial and temporal complexity of the Amazon flood measured from space, Geophysical research letters, 34(8).

Amado, A. A., M. Politano, K. Schilling, and L. Weber (2016), Investigating Hydrologic Connectivity of a Drained Prairie Pothole Region Wetland Complex using a Fully Integrated, Physically-Based Model, Wetlands, 1-13, doi: 10.1007/s13157-016-0800-5.

Anderson, M. C., J. M. Norman, G. R. Diak, W. P. Kustas, and J. R. Mecikalski (1997), A two-source time-integrated model for estimating surface fluxes using thermal infrared remote sensing, Remote Sensing of Environment, 60(2), 195-216, doi: 10.1016/S0034-4257(96)00215-5.

Arnesen, A. S., T. S. F. Silva, L. L. Hess, E. M. L. M. Novo, C. M. Rudorff, B. D. Chapman, and K. C. McDonald (2013), Monitoring flood extent in the lower Amazon River floodplain using ALOS/PALSAR ScanSAR images, Remote Sensing of Environment, 130, 51-61, doi: http://dx.doi.org/10.1016/j.rse.2012.10.035.

Awange, J., V. Ferreira, E. Forootan, S. Andam-Akorful, N. Agutu, and X. He (2016), Uncertainties in remotely sensed precipitation data over Africa, International Journal of Climatology, 36(1), 303-323.

Bartholomé, E., and A. S. Belward (2005), GLC2000: a new approach to global land cover mapping from Earth observation data, International Journal of Remote Sensing, 26(9), 1959-1977, doi: 10.1080/01431160412331291297.

Bates, P. D. (2012), Integrating remote sensing data with flood inundation models: how far have we got?, Hydrological Processes, 26(16), 2515-2521.

Bates, P. D., and A. De Roo (2000), A simple raster-based model for flood inundation simulation, Journal of hydrology, 236(1-2), 54-77.

Bergé-Nguyen, M., and J.-F. Crétaux (2015), Inundations in the Inner Niger Delta: Monitoring and Analysis Using MODIS and Global Precipitation Datasets, Remote Sensing, 7(2), 2127-2151, doi: 10.3390/rs70202127.

Beven, K. J., and M. J. Kirkby (1979), A physically based, variable contributing area model of basin hydrology/Un modèle à base physique de zone d'appel variable de l'hydrologie du bassin versant, Hydrological Sciences Journal, 24(1), 43-69.

Bourgeau-Chavez, L. L., K. B. Smith, S. M. Brunzell, E. S. Kasischke, E. A. Romanowicz, and C. J. Richardson (2005), REMOTE MONITORING OF REGIONAL INUNDATION PATTERNS AND HYDROPERIOD IN THE GREATER EVERGLADES USING SYNTHETIC APERTURE RADAR, Wetlands, 25(1), 176-191, doi: 10.1672/0277-5212(2005)025[0176:RMORIP]2.0.CO;2.

Brakenridge, R., and E. Anderson (2006), MODIS-BASED FLOOD DETECTION, MAPPING AND MEASUREMENT: THE POTENTIAL FOR OPERATIONAL HYDROLOGICAL APPLICATIONS, in Transboundary Floods: Reducing Risks Through Flood Management, edited by J. Marsalek, G. Stancalie and G. Balint, pp. 1-12, Springer Netherlands, Dordrecht.

Burnash, R., and L. Ferral (1996), Conceptualization of the sacramento soil moisture accounting model, NWSRFS Users Manual, Part II, 3.

Cai, X. (2008), Implementation of holistic water resources-economic optimization models for river basin management – Reflective experiences, Environmental Modelling & Software, 23(1), 2-18, doi: http://dx.doi.org/10.1016/j.envsoft.2007.03.005.

Carroll, M. L., J. R. Townshend, C. M. DiMiceli, P. Noojipady, and R. A. Sohlberg (2009), A new global raster water mask at 250 m resolution, International Journal of Digital Earth, 2(4), 291-308, doi: 10.1080/17538940902951401.

Cattani, E., A. Merino, and V. Levizzani (2016), Evaluation of monthly satellite-derived precipitation products over East Africa, Journal of Hydrometeorology, 17(10), 2555-2573.

Chan, S.-O., and P. S. Eagleson (1980), Water balance studies of the Bahr el Ghazal swamp.

Congalton, R. G., G. Jianyu, K. Yadav, P. Thenkabail, and M. Ozdogan (2014), Global Land Cover Mapping: A Review and Uncertainty Analysis, Remote Sensing, 6(12), 12070-12093, doi: 10.3390/rs61212070.

Cowardin, L. M., V. Carter, F. C. Golet, and E. T. LaRoe (1979), Classification of Wetlands and Deepwater Habitats of the United States*Rep.*, Washington D.C.

Crétaux, J. F., et al. (2011), SOLS: A lake database to monitor in the Near Real Time water level and storage variations from remote sensing data, Advances in Space Research, 47(9), 1497-1507, doi: http://dx.doi.org/10.1016/j.asr.2011.01.004.

Crow, W., and D. Ryu (2009), A new data assimilation approach for improving runoff prediction using remotely-sensed soil moisture retrievals, Hydrology and Earth System Sciences, 13(1), 1-16.

Crow, W. T., F. Chen, R. H. Reichle, and Q. Liu (2017), L band microwave remote sensing and land data assimilation improve the representation of prestorm soil moisture conditions for hydrologic forecasting, Geophysical Research Letters, 44(11), 5495-5503, doi: doi:10.1002/2017GL073642.

Dall'O, Amp, Apos, Michele, W. Kluge, and F. Bartels (2001), FEUWAnet: a multi-box water level and lateral exchange model for riparian wetlands, Journal of Hydrology, 250(1), 40-62, doi: 10.1016/S0022-1694(01)00401-2.

Di Vittorio, C. A., and A. P. Georgakakos (2018), Land cover classification and wetland inundation mapping using MODIS, Remote Sensing of Environment, 204, 1-17, doi: https://doi.org/10.1016/j.rse.2017.11.001.

Dincer, T., S. Child, and B. Khupe (1987), A simple mathematical model of a complex hydrologic system — Okavango Swamp, Botswana, Journal of Hydrology, 93(1), 41-65, doi: 10.1016/0022-1694(87)90193-4.

Draper, C., R. Reichle, G. De Lannoy, and Q. Liu (2012), Assimilation of passive and active microwave soil moisture retrievals, Geophysical Research Letters, 39(4).

Dronova, I., P. Gong, L. Wang, and L. Zhong (2015), Mapping dynamic cover types in a large seasonally flooded wetland using extended principal component analysis and object-based classification, Remote Sensing of Environment, 158, 193-206, doi: http://dx.doi.org/10.1016/j.rse.2014.10.027.

Drusch, M., et al. (2012), Sentinel-2: ESA's Optical High-Resolution Mission for GMES Operational Services, Remote Sensing of Environment, 120, 25-36, doi: https://doi.org/10.1016/j.rse.2011.11.026.

Feng, M., J. O. Sexton, S. Channan, and J. R. Townshend (2016), A global, high-resolution (30-m) inland water body dataset for 2000: first results of a topographic–spectral classification algorithm, International Journal of Digital Earth, 9(2), 113-133, doi: 10.1080/17538947.2015.1026420.

Fernández, A.; Najafi, M. R.; Durand, M.; Mark, B. G., Moritz, M.; Jung, H. C.; Neal, Jeff; Shastry, A.; Laborde, S.; Phang, S. C.; Hamilton, I. M.; Xiao, N. (2016), Testing the skill of numerical hydraulic modeling to simulate spatiotemporal flooding patterns in the Logone floodplain, Cameroon, *Journal of Hydrology*, Volume 539, Pages 265-280, doi:10.1016/j.jhydrol.2016.05.026.

Finlayson, C. M. (2003), The challenge of integrating wetland inventory, assessment and monitoring, Aquatic Conservation: Marine and Freshwater Ecosystems, 13(4), 281-286, doi: 10.1002/aqc.598.

Fluet-Chouinard, E., B. Lehner, L.-M. Rebelo, F. Papa, and S. K. Hamilton (2015), Development of a global inundation map at high spatial resolution from topographic downscaling of coarse-scale remote sensing data, Remote Sensing of Environment, 158, 348-361, doi: http://dx.doi.org/10.1016/j.rse.2014.10.015.

Frei, S., G. Lischeid, and J. H. Fleckenstein (2010), Effects of micro-topography on surface–subsurface exchange and runoff generation in a virtual riparian wetland — A modeling study, Advances in Water Resources, 33(11), 1388-1401, doi: 10.1016/j.advwatres.2010.07.006.

Friedl, M. A., D. Sulla-Menashe, B. Tan, A. Schneider, N. Ramankutty, A. Sibley, and X. Huang (2010), MODIS Collection 5 global land cover: Algorithm refinements and characterization of new datasets, Remote Sensing of Environment, 114(1), 168-182, doi: http://dx.doi.org/10.1016/j.rse.2009.08.016.

Friedl, M. A., et al. (2002), Global land cover mapping from MODIS: algorithms and early results, Remote Sensing of Environment, 83(1–2), 287-302, doi: http://dx.doi.org/10.1016/S0034-4257(02)00078-0.

Gallant, A. L. (2015), The Challenges of Remote Monitoring of Wetlands, Remote Sensing, 7(8), 10938-10950, doi: 10.3390/rs70810938.

Gao, B. (1996), NDWI—A normalized difference water index for remote sensing of vegetation liquid water from space, Remote Sensing of Environment, 58(3), 257-266, doi: http://dx.doi.org/10.1016/S0034-4257(96)00067-3.

Garstin, W. (1904), Basin of the Upper Nile. Report of the Under-Secretary of the Ministry of Public Works*Rep.*, Cairo, Egypt.

Georgakakos, A., A. Tidwell, and L. Visone (2003), Nile Decision Support Tool Watershed Hydrology*Rep.*, The Georgia Water Resources Institute at the Georgia Institute of Technology, Atlanta, GA.

Georgakakos, A. P., and H. Yao (1999), Evaluation of Water Use Scenarios for the Nile Basin. Technical Report developed for the World Bank*Rep.*, 106 pp.

Georgakakos, A. P., and H. Yao (2005), Decision Support System for the Management of the High Aswan Dam (HAD DSS). Technical Completion Report developed for the Ministry of Water Resources and Irrigation, Arab Republic of Egypt*Rep.*, 87 pp, Atlanta, Georgia.

Georgakakos, A. P., and H. Yao (2007), Lake Victoria Decision Support Tool (LV DST). Technical Completion Report developed for the Ugandan Ministry of Energy and Mineral Development *Rep.*, 120 pp.

Georgakakos, A. P., H. Yao, K. Brumbelow, C. DeMarchi, S. Bourne, L. Visone, and A. Tidwell (2003), Nile Decision Support Tool (DST). Multi-Volume Technical Report sponsored by the Food and Agriculture Organization of the United Nations and carried out with the collaboration of all Nile Basin nations*Rep.*, The Georgia Water Resources Institute, Georgia Institute of Technology, Atlanta, GA, Atlanta, GA.

Georgakakos, A. P., H. Yao, M. Kistenmacher, K. P. Georgakakos, N. E. Graham, F. Y. Cheng, C. Spencer, and E. Shamir (2012), Value of adaptive water resources management in Northern California under climatic variability and change: Reservoir management, Journal of Hydrology, 412–413, 34-46, doi: https://doi.org/10.1016/j.jhydrol.2011.04.038.

Georgakakos, A. P., P. Fleming, M. Dettinger, C. Peters-Lidard, T. C. Richmond, K. Reckhow, K. White, and D. Yates (2014), Ch. 3: Water Resources. Climate Change Impacts in the United States: The Third National Climate Assessment edited by J. M. Melillo, T. C. Richmond and G. W. Yohe, pp. 69-112, U.S. Global Change Research Program.

Getirana, A., Rodell, M., Kumar, S., Beaudoing, H.K., Arsenault, K., Zaitchik, B., (2019). GRACE improves groundwater forecast initialization over the U.S. Journal of Hydrometeorology. Accepted for publication.

Glanz, H., L. Carvalho, D. Sulla-Menashe, and M. A. Friedl (2014), A parametric model for classifying land cover and evaluating training data based on multi-temporal remote sensing data, ISPRS Journal of Photogrammetry and Remote Sensing, 97, 219-228, doi: http://dx.doi.org/10.1016/j.isprsjprs.2014.09.004.

Golet, F. C., A. J. K. Calhoun, W. R. DeRagon, D. J. Lowry, and A. J. Gold (1993), Ecology of Red Maple Swamps in the Glaciated Northeast: A Community Profile*Rep.*, 151 pp, Washington D.C.

Groffman, P. M., S. Kareiva, S. Carter, N. B. Grimm, J. Lawler, M. Mack, V. Matzek, and H. Tallis (2014), Ch. 8: Ecosystems, Biodiversity, and Ecosystem Services. Climate Change Impacts in the United States: The Third National Climate Assessment.*Rep.*, 195-219 pp.

Guerschman, J., G. Warren, G. Byrne, L. Lymburner, N. Mueller, and A. Van Dijk (2011), MODIS-based standing water detection for flood and large reservoir mapping: Algorithm development and applications for the Australian continent*Rep.*, Canberra.

Gumma, M. K., P. S. Thenkabail, A. Maunahan, S. Islam, and A. Nelson (2014), Mapping seasonal rice cropland extent and area in the high cropping intensity environment of Bangladesh using MODIS 500 m data for the year 2010, ISPRS Journal of Photogrammetry and Remote Sensing, 91, 98-113, doi: http://dx.doi.org/10.1016/j.isprsjprs.2014.02.007.

Hansen, M. C., R. S. Defries, J. R. G. Townshend, and R. Sohlberg (2000), Global land cover classification at 1 km spatial resolution using a classification tree approach, International Journal of Remote Sensing, 21(6-7), 1331-1364, doi: 10.1080/014311600210209.

Hargreaves, G., and R. Allen (2003), History and Evaluation of Hargreaves Evapotranspiration Equation, Journal of Irrigation and Drainage Engineering, 129(1), 53-63, doi: 10.1061/(ASCE)0733-9437(2003)129:1(53).

Hassanzadeh, E., A. Elshorbagy, H. Wheater, and P. Gober (2014), Managing water in complex systems: An integrated water resources model for Saskatchewan, Canada, Environmental Modelling & Software, 58, 12-26, doi: https://doi.org/10.1016/j.envsoft.2014.03.015.

Hattermann, F. F., V. Krysanova, A. Habeck, and A. Bronstert (2006), Integrating wetlands and riparian zones in river basin modelling, Ecological Modelling, 199(4), 379-392, doi: http://dx.doi.org/10.1016/j.ecolmodel.2005.06.012.

Hess, L. L., J. M. Melack, E. M. L. M. Novo, C. C. F. Barbosa, and M. Gastil (2003), Dual-season mapping of wetland inundation and vegetation for the central Amazon basin, Remote Sensing of Environment, 87(4), 404-428, doi: http://dx.doi.org/10.1016/j.rse.2003.04.001.

House, A., J. Thompson, J. Sorensen, C. Roberts, and M. Acreman (2016), Modelling groundwater/surface water interaction in a managed riparian chalk valley wetland, Hydrological Processes, 30(3), 447-462.

Howell, P., M. Lock, and S. Cobb (1988), The Jonglei Canal impact and opportunity, Cambridge University Press, Cambridge.

Huang, C., Y. Peng, M. Lang, I.-Y. Yeo, and G. McCarty (2014), Wetland inundation mapping and change monitoring using Landsat and airborne LiDAR data, Remote Sensing of Environment, 141, 231-242, doi: http://dx.doi.org/10.1016/j.rse.2013.10.020.

Huang, S.-Y., Y. Deng, and J. Wang (2017), Revisiting the global surface energy budgets with maximum-entropy-production model of surface heat fluxes, Climate Dynamics, 49(5), 1531-1545, doi: 10.1007/s00382-016-3395-x.

Hudak, P. (2014), Inundation patterns and plant growth in constructed wetland characterized by dynamic water budget model, Environmental Earth Sciences, 72(6), 1821-1826, doi: 10.1007/s12665-014-3091-2.

Hurst, H. E., and P. Phillips (1932), Measured discharges of the Nile and its tributaries. The Nile Basin, Vol. II and supplements 1-13., Government Press, Cairo, Egypt.

Jeffreys, H. (1946), An Invariant Form for the Prior Probability in Estimation Problems, Proceedings of the Royal Society of London. Series A, Mathematical and Physical Sciences, 186(1007), 453-461.

Jenny, M. M., G. Thomas, T. McCarthy, P. Frost, W. Konrad, and S. Frank (2003), Flooding Patterns of the Okavango Wetland in Botswana between 1972 and 2000, Ambio, 32(7), 453-457.

Jensen, J. R. (2005), Introductory digital image processing : a remote sensing perspective, 3rd ed.. ed., Upper Saddle River, N.J. : Prentice Hall, Upper Saddle River, N.J.

Ji, L., L. Zhang, and B. Wylie (2009), Analysis of Dynamic Thresholds for the Normalized Difference Water Index, Photogrammetric Engineering & Remote Sensing, 75(11), 1307-1317, doi: 10.14358/PERS.75.11.1307.

Jiménez, C., et al. (2011), Global intercomparison of 12 land surface heat flux estimates, Journal of Geophysical Research: Atmospheres, 116(D2), n/a-n/a, doi: 10.1029/2010JD014545.

Jonglei Investigation Team (1954), The Equatorial Nile Project and its Effects in the Anglo-Egyptian Sudan*Rep.*, Khartoum.

Junk, W. B., P. B.; Sparks, R. E. (1989), The flood pulse concept in river-floodplain systems, paper presented at Proceedings of the International Large River Symposium (LARS), Ontario, Canada.

Jung, Hahn C.; Jasinski, Michael F. 2015. "Sensitivity of a Floodplain Hydrodynamic Model to Satellite-Based DEM Scale and Accuracy: Case Study—The Atchafalaya Basin." *Remote Sens.* 7, no. 6: 7938-7958, doi: 10.3390/rs70607938

Jung, H. C., Jasinski, M., Kim, J.-W., Shum, C. K., Bates, P., Neal, J., Lee, H., and Alsdorf, D. (2012), Calibration of two-dimensional floodplain modeling in the central Atchafalaya Basin Floodway System using SAR interferometry, *Water Resour. Res.*, 48, W07511, doi:10.1029/2012WR011951

Kauth, R. J. T., G. S. (1976), The tasselled cap - A graphic description of the spectral-temporal development of agricultural crops as seen by Landsat, paper presented at Symposium on Machine Processing of Remotely Sensed Data, NASA, West Lafayette, IN.

Kontgis, C., A. Schneider, and M. Ozdogan (2015), Mapping rice paddy extent and intensification in the Vietnamese Mekong River Delta with dense time stacks of Landsat data, Remote Sensing of Environment, 169, 255-269, doi: http://dx.doi.org/10.1016/j.rse.2015.08.004.

Kotir, J. H., C. Smith, G. Brown, N. Marshall, and R. Johnstone (2016), A system dynamics simulation model for sustainable water resources management and agricultural development in the Volta River Basin, Ghana, Science of The Total Environment, 573, 444-457, doi: https://doi.org/10.1016/j.scitotenv.2016.08.081.

Krysanova, V., D.-I. Müller-Wohlfeil, and A. Becker (1998), Development and test of a spatially distributed hydrological/water quality model for mesoscale watersheds, Ecological modelling, 106(2-3), 261-289.

Kuenzer, C., I. Klein, T. Ullmann, E. F. Georgiou, R. Baumhauer, and S. Dech (2015), Remote Sensing of River Delta Inundation: Exploiting the Potential of Coarse Spatial Resolution, Temporally-Dense MODIS Time Series, Remote Sensing, 7(7), 8516-8542, doi: 10.3390/rs70708516.

Kullback, S. (1959), Information theory and statistics, New York, Wiley, New York.

Kullback, S., and R. A. Leibler (1951), On Information and Sufficiency, The Annals of Mathematical Statistics, 22(1), 79-86.

Kumar, S.V., Zaitchik, B.F., Peters-Lidard, C.D., Rodell, M., Reichle, R., Li, B., Jasinski, M., Mocko, D., Getirana, A., De Lannoy, G., Cosh, M., Hain, C.R., Anderson, M., Arsenault, K.R., Xia, Y., Ek., M., (2016). Assimilation of gridded GRACE terrestrial water storage estimates in the North American Land Data Assimilation System. Journal of Hydrometeorology. DOI: 10.1175/JHM-D-15-0157.1

Landmann, T., M. Schramm, R. R. Colditz, A. Dietz, and S. Dech (2010), Wide Area Wetland Mapping in Semi-Arid Africa Using 250-Meter MODIS Metrics and Topographic Variables, Remote Sensing, 2(7), 1751-1766.

Leauthaud, C., G. Belaud, S. Duvail, R. Moussa, O. Grünberger, and J. Albergel (2013), Characterizing floods in the poorly gauged wetlands of the Tana River Delta, Kenya, using a water balance model and satellite data, Hydrology and Earth System Sciences, 17(8), 3059, doi: http://dx.doi.org/10.5194/hess-17-3059-2013.

Leblanc, M., J. Lemoalle, J. C. Bader, S. Tweed, and L. Mofor (2011), Thermal remote sensing of water under flooded vegetation: New observations of inundation patterns for the 'Small' Lake Chad, Journal of Hydrology, 404(1–2), 87-98, doi: http://dx.doi.org/10.1016/j.jhydrol.2011.04.023.

Lehner, B., and P. Döll (2004), Development and validation of a global database of lakes, reservoirs and wetlands, Journal of Hydrology, 296(1–4), 1-22, doi: http://dx.doi.org/10.1016/j.jhydrol.2004.03.028.

Li, B., Rodell, M., Kumar, S., Beaudoing, H.K., Getirana, A., et al., (2019). Global GRACE data assimilation for groundwater and drought monitoring: Advances and challenges. Water Resources Research. DOI: 10.1029/2018WR024618.

Liu, Y., and H. V. Gupta (2007), Uncertainty in hydrologic modeling: Toward an integrated data assimilation framework, Water Resources Research, 43(7), doi: doi:10.1029/2006WR005756.

Liu, Y., W. Yang, and X. Wang (2008), Development of a SWAT extension module to simulate riparian wetland hydrologic processes at a watershed scale, Hydrological Processes, 22(16), 2901-2915, doi: 10.1002/hyp.6874.

Lobser, S. E., and W. B. Cohen (2007), MODIS tasselled cap: land cover characteristics expressed through transformed MODIS data, International Journal of Remote Sensing, 28(22), 5079-5101, doi: 10.1080/01431160701253303.

Lott, R., and R. Hunt (2001), Estimating evapotranspiration in natural and constructed wetlands, Wetlands, 21(4), 614-628, doi: 10.1672/0277-5212(2001)021[0614:EEINAC]2.0.CO;2.

Margono, B. A., J.-R. B. Bwangoy, P. V. Potapov, and M. C. Hansen (2014), Mapping wetlands in Indonesia using Landsat and PALSAR data-sets and derived topographical indices, Geo-spatial Information Science, 17(1), 60-71, doi: 10.1080/10095020.2014.898560.

Martens, B., D. Gonzalez Miralles, H. Lievens, R. van der Schalie, R. A. de Jeu, D. Fernández-Prieto, H. E. Beck, W. Dorigo, and N. Verhoest (2017), GLEAM v3: Satellite-based land evaporation and root-zone soil moisture, Geoscientific Model Development, 10(5), 1903-1925.

Mason, D. C., P. Bates, and J. Dall'Amico (2009), Calibration of uncertain flood inundation models using remotely sensed water levels, Journal of Hydrology, 368(1-4), 224-236.

Millennium Ecosystem Assessment (2005), Ecosystems and Human Well-being: Wetlands and Water Synthesis*Rep.*, World Resources Institute, Washington. D.C.

Min, J.-H., R. Paudel, and J. W. Jawitz (2010), Spatially distributed modeling of surface water flow dynamics in the Everglades ridge and slough landscape, Journal of Hydrology, 390(1), 1-12, doi: 10.1016/j.jhydrol.2010.06.023.

Miralles, D., T. Holmes, R. De Jeu, J. Gash, A. Meesters, and A. Dolman (2011), Global land-surface evaporation estimated from satellite-based observations, Hydrology and Earth System Sciences, 15(2), 453.

Mitsch, W. J., and J. G. Gosselink (2007), Wetlands, 4th ed.. ed., Hoboken, N.J. : Wiley, Hoboken, N.J.

Mohamed, Y. A., W. G. M. Bastiaanssen, and H. H. G. Savenije (2004), Spatial variability of evaporation and moisture storage in the swamps of the upper Nile studied by remote

sensing techniques, Journal of Hydrology, 289(1–4), 145-164, doi: http://dx.doi.org/10.1016/j.jhydrol.2003.11.038.

Mohamed, Y. A., B. J. J. M. van den Hurk, H. H. G. Savenije, and W. G. M. Bastiaanssen (2005), Impact of the Sudd wetland on the Nile hydroclimatology, Water Resources Research, 41(8), n/a-n/a, doi: 10.1029/2004WR003792.

Mueller, B., et al. (2013), Benchmark products for land evapotranspiration: LandFlux-EVAL multi-data set synthesis, Hydrology and Earth System Sciences, 17(10), 3707, doi: 10.5194/hess-17-3707-2013.

Naz, M., S. Uyanik, M. I. Yesilnacar, and E. Sahinkaya (2009), Side-by-side comparison of horizontal subsurface flow and free water surface flow constructed wetlands and artificial neural network (ANN) modelling approach, Ecological Engineering, 35(8), 1255-1263, doi: https://doi.org/10.1016/j.ecoleng.2009.05.010.

Neal, J., G. Schumann, and P. Bates (2012), A subgrid channel model for simulating river hydraulics and floodplain inundation over large and data sparse areas, Water Resources Research, 48(11).

Neitsch, S. L., J. G. Arnold, and J. R. Williams (2011), Soil and Water Assessment Tool Theoretical Documentation Version 2009*Rep.*, Texas A&M College Station, TX.

Nie, W., Zaitchik, B.F., Rodell, M., Kumar, S.V., Arsenault, K.R., Li, B., Getirana, A., (2019). Assimilating GRACE into a Land Surface Model in the presence of an irrigation-induced groundwater trend. Water Resources Research. Accepted for publication.

Nile Basin Initiative (2016), Nile Basin Trans-boundary Wetlands, edited, Entebbe, Uganda.

Nile Basin Initiative (2017), Corporate Report 2017*Rep.*, Entebbe, Uganda.

Nile Basin Initiative NBI (2016), Annual Corporate Report*Rep.*

Novella, N. S., and W. M. Thiaw (2012), African Rainfall Climatology Version 2 for Famine Early Warning Systems, Journal of Applied Meteorology and Climatology, 52(3), 588-606, doi: 10.1175/JAMC-D-11-0238.1.

Ogilvie, A., G. Belaud, C. Delenne, J.-S. Bailly, J.-C. Bader, A. Oleksiak, L. Ferry, and D. Martin (2015), Decadal monitoring of the Niger Inner Delta flood dynamics using MODIS optical data, Journal of Hydrology, 523, 368-383, doi: http://dx.doi.org/10.1016/j.jhydrol.2015.01.036.

Olofsson, P., G. M. Foody, M. Herold, S. V. Stehman, C. E. Woodcock, and M. A. Wulder (2014), Good practices for estimating area and assessing accuracy of land change, Remote Sensing of Environment, 148, 42-57, doi: 10.1016/j.rse.2014.02.015.

Ordoyne, C., and M. A. Friedl (2008), Using MODIS data to characterize seasonal inundation patterns in the Florida Everglades, Remote Sensing of Environment, 112(11), 4107-4119, doi: http://dx.doi.org/10.1016/j.rse.2007.08.027.

Papa, F., C. Prigent, F. Aires, C. Jimenez, W. B. Rossow, and E. Matthews (2010), Interannual variability of surface water extent at the global scale, 1993-2004, Journal of Geophysical Research. Atmospheres, 115(12), doi: http://dx.doi.org/10.1029/2009JD012674.

Petersen, G. (2005), Environmental impacts assessment (EIA) of the Bor-Mabior Dike Rehabilitation Project*Rep.*, United States Agency for International Development, Nairobi, Kenya.

Petersen, G., and N. Fohrer (2010), Flooding and drying mechanisms of the seasonal Sudd flood plains along the Bahr el Jebel in southern Sudan, Hydrological Sciences Journal, 55(1), 4-16, doi: 10.1080/02626660903525278.

Prigent, C., E. Matthews, F. Aires, and W. B. Rossow (2001), Remote sensing of global wetland dynamics with multiple satellite data sets, Geophysical Research Letters, 28(24), 4631-4634, doi: 10.1029/2001GL013263.

Pulvirenti, L., M. Chini, N. Pierdicca, L. Guerriero, and P. Ferrazzoli (2011), Flood monitoring using multi-temporal COSMO-SkyMed data: Image segmentation and signature interpretation, Remote Sensing of Environment, 115(4), 990-1002, doi: http://dx.doi.org/10.1016/j.rse.2010.12.002.

Pyzoha, J. E., T. J. Callahan, G. Sun, C. C. Trettin, and M. Miwa (2008), A conceptual hydrologic model for a forested Carolina bay depressional wetland on the Coastal Plain of South Carolina, USA, Hydrological Processes, 22(14), 2689-2698, doi: 10.1002/hyp.6866.

Rahman, M. M., J. R. Thompson, and R. J. Flower (2016), An enhanced SWAT wetland module to quantify hydraulic interactions between riparian depressional wetlands, rivers and aquifers, Environmental Modelling & Software, 84, 263-289, doi: https://doi.org/10.1016/j.envsoft.2016.07.003.

Ramsar Convention Secretariate (2013), The Ramsar Convention Manual: a guide to the Convention on Wetlands (Ramsar, Iran 1971), 6th ed.*Rep.*, Gland, Switzerland.

Rebelo, L. M., G. B. Senay, and M. P. McCartney (2012), Flood Pulsing in the Sudd Wetland: Analysis of Seasonal Variations in Inundation and Evaporation in South Sudan, Earth Interactions, 16(1), 1.

Reichle, R. H., D. B. McLaughlin, and D. Entekhabi (2002), Hydrologic data assimilation with the ensemble Kalman filter, Monthly Weather Review, 130(1), 103-114.

Remondi, Federica & Georgakakos, Aris & Castelletti, Andrea. (2013). A hydrological model for the Sudd wetland using remotely sensed and ground data. 11486-. 10.13140/RG.2.1.1370.1285.

Rouse, J. W. J. H., R. H.; Schell, J. A.; Deering, D. W. (1974), Monitoring vegetation systems in the Great Plains with ERTS, in *Third Earth Resources Technology Satellite-1 Symposium*, edited, pp. 309-317, NASA.

Said, A., M. Ross, K. Trout, and J. Zhang (2007), Simulation of Surface Water for Un-Gauged Areas with Storage-Attenuation Wetlands 1, JAWRA Journal of the American Water Resources Association, 43(2), 546-556.

Salvucci, G. D., and D. Entekhabi (2011), An alternate and robust approach to calibration for the estimation of land surface model parameters based on remotely sensed observations, Geophysical Research Letters, 38(16).

Schmid, B. H., and J. Koskiaho (2006), Artificial Neural Network Modeling of Dissolved Oxygen in a Wetland Pond: The Case of Hovi, Finland, Journal of Hydrologic Engineering, 11(2), 188-192, doi: doi:10.1061/(ASCE)1084-0699(2006)11:2(188).

Sexton, J. O., D. L. Urban, M. J. Donohue, and C. Song (2013), Long-term land cover dynamics by multi-temporal classification across the Landsat-5 record, Remote Sensing of Environment, 128, 246-258, doi: http://dx.doi.org/10.1016/j.rse.2012.10.010.

Smith, M., R. Allen, and L. Pereira (1998), Revised FAO methodology for crop-water requirements*Rep.*

Sosnowski, A., E. Ghoneim, J. J. Burke, E. Hines, and J. Halls (2016), Remote regions, remote data: A spatial investigation of precipitation, dynamic land covers, and conflict in the Sudd wetland of South Sudan, Applied Geography, 69, 51-64, doi: https://doi.org/10.1016/j.apgeog.2016.02.007.

Soti, V., A. Tran, J.-S. Bailly, C. Puech, D. L. Seen, and A. Bégué (2009), Assessing optical earth observation systems for mapping and monitoring temporary ponds in arid areas,

International Journal of Applied Earth Observation and Geoinformation, 11(5), 344-351, doi: http://dx.doi.org/10.1016/j.jag.2009.05.005.

Su, M., W. J. Stolte, and G. van der Kamp (2000), Modelling Canadian prairie wetland hydrology using a semi-distributed streamflow model, Hydrological Processes, 14(14), 2405-2422, doi: 10.1002/1099-1085(20001015)14:14<2405::AID-HYP92>3.0.CO;2-B.

Sudan Tribune (2014), Floods displace South Sudan swamp communities, in *Sudan Tribune*, edited, Bor.

Sutcliffe, J., and E. Brown (2018), Water losses from the Sudd, Hydrological Sciences Journal, 63(4), 527-541, doi: 10.1080/02626667.2018.1438612.

Sutcliffe, J. V. (2005), Comment on 'Spatial variability of evaporation and moisture storage in the swamps of the upper Nile studied by remote sensing technique' by Y.A. Mohamed et al., 2004. Journal of Hydrology 289, 145–164, Journal of Hydrology, 314(1), 45-47, doi: https://doi.org/10.1016/j.jhydrol.2005.03.036.

Sutcliffe, J. V., and Y. P. Parks (1987), Hydrological modelling of the Sudd and Jonglei Canal, Hydrological Sciences Journal, 32(2), 143-159, doi: 10.1080/02626668709491174.

Sutcliffe, J. V., and Y. P. Parks (1999), The Hydrology of the Nile*Rep.*, Wallingford, UK.

Teng, J., A. J. Jakeman, J. Vaze, B. F. W. Croke, D. Dutta, and S. Kim (2017), Flood inundation modelling: A review of methods, recent advances and uncertainty analysis, Environmental Modelling & Software, 90, 201-216, doi: https://doi.org/10.1016/j.envsoft.2017.01.006.

The Jonglei Investigation Team (1955), The Equatorial Nile Project and its Effects in the Anglo-Egyptian Sudan: Introduction and Summary*Rep.*, Cairo, Egypt.

The MathWorks Inc. (2016), MATLAB and Statistics Toolbox Release 2016a, edited, Natick, Massachusetts.

The Ramsar Convention Secretariate (2006), Sudan's designation of the Sudd marshes on World Environment Day 2006, edited.

Thiemig, V., R. Rojas, M. Zambrano-Bigiarini, V. Levizzani, and A. De Roo (2012), Validation of satellite-based precipitation products over sparsely gauged African river basins, Journal of Hydrometeorology, 13(6), 1760-1783.

Tidwell, V. C., H. D. Passell, S. H. Conrad, and R. P. Thomas (2004), System dynamics modeling for community-based water planning: Application to the Middle Rio Grande, Aquatic Sciences, 66(4), 357-372, doi: 10.1007/s00027-004-0722-9.

Torbick, N., and W. Salas (2015), Mapping agricultural wetlands in the Sacramento Valley, USA with satellite remote sensing, Wetlands Ecology and Management, 23(1), 79-94, doi: 10.1007/s11273-014-9342-x.

Tropical Rainfall Measuring Mission Project (TRMM) (2011), TRMM/TMPA 3B43 TRMM and Other Sources Monthly Rainfall Product V7, edited by G. S. F. C. D. A. A. C. G. DAAC), Greenbelt, MD.

United Nations Environment Programme (2018), South Sudan: First State of Environment and Outlook Report*Rep.*, Nairobi, Kenya.

University of East Anglia Climatic Research Unit (2017), CRU TS4.01: Climatic Research Unit (CRU) Time-Series (TS) version 4.01 of high-resolution gridded data of month-by-month variation in climate (Jan. 1910 - Dec. 2016), edited, Center for Environmental Data Analysis.

Vermote, E. (2015), MOD09A1 MODIS/Terra Surface Reflectance 8-Day L3 Global 500m SINGrid V006, edited by N. E. L. P. DAAC.

Vermote, E., and A. Vermeulen (1999), Atmospheric Correction Algorithm: Spectral Reflectances (MOD09). Algorithm Technical Background Document (ATBD)*Rep.*, University of Maryland, Department of Geography, Silver Spring, MD.

Wang, J., and R. L. Bras (2011), A model of evapotranspiration based on the theory of maximum entropy production, Water Resources Research, 47(3), n/a-n/a, doi: 10.1029/2010WR009392.

Wang, X., W. Yang, and A. M. Melesse (2008), Using Hydrologic Equivalent Wetland Concept Within SWAT to Estimate Streamflow in Watersheds with Numerous Wetlands, 51(1), doi: 10.13031/2013.24227.

Wang, X., W. Yang, and A. M. Melesse (2008), Using hydrologic equivalent wetland concept within SWAT to estimate streamflow in watersheds with numerous wetlands, Transactions of the ASABE, 51(1), 55-72.

Wang, X., S. Shang, Z. Qu, T. Liu, A. M. Melesse, and W. Yang (2010), Simulated wetland conservation-restoration effects on water quantity and quality at watershed scale, Journal of

Waske, B. F., J.; Benediktsson, J.; Chanussot, J. (2009), Machine Learning Techniques in

water lake in response to hydro-climatic drought, International Journal of Remote Sensing, 35(11-12), 4544-4558, doi: 10.1080/01431161.2014.916444.

Xiao, X., S. Boles, J. Liu, D. Zhuang, S. Frolking, C. Li, W. Salas, and B. Moore Iii (2005), Mapping paddy rice agriculture in southern China using multi-temporal MODIS images, Remote Sensing of Environment, 95(4), 480-492, doi: http://dx.doi.org/10.1016/j.rse.2004.12.009.

Xu, H. (2006), Modification of normalised difference water index (NDWI) to enhance open water features in remotely sensed imagery, International Journal of Remote Sensing, 27(14), 3025-3033, doi: 10.1080/01431160600589179.

Xu, X., J. Li, and B. A. Tolson (2014), Progress in integrating remote sensing data and hydrologic modeling, Progress in Physical Geography, 38(4), 464-498.

Yamazaki, D., D. Ikeshima, R. Tawatari, T. Yamaguchi, F. O'Loughlin, J. C. Neal, C. C. Sampson, S. Kanae, and P. D. Bates (2017), A high-accuracy map of global terrain elevations, Geophysical Research Letters, 44(11), 5844-5853, doi: doi:10.1002/2017GL072874.

Zhang, G., X. Xiao, J. Dong, W. Kou, C. Jin, Y. Qin, Y. Zhou, J. Wang, M. A. Menarguez, and C. Biradar (2015), Mapping paddy rice planting areas through time series analysis of MODIS land surface temperature and vegetation index data, ISPRS Journal of Photogrammetry and Remote Sensing, 106, 157-171, doi: http://dx.doi.org/10.1016/j.isprsjprs.2015.05.011.

Zhang, J., M. Ross, K. Trout, and D. Zhou (2009), Calibration of the HSPF model with a new coupled FTABLE generation method, Progress in Natural Science, 19(12), 1747-1755.

Zhang, L., and W. J. Mitsch (2005), Modelling hydrological processes in created freshwater wetlands: an integrated system approach, Environmental Modelling and Software, 20(7), 935-946, doi: 10.1016/j.envsoft.2004.03.020.

Zhang, X., M. A. Friedl, C. B. Schaaf, A. H. Strahler, and Z. Liu (2005), Monitoring the response of vegetation phenology to precipitation in Africa by coupling MODIS and TRMM instruments, Journal of Geophysical Research: Atmospheres, 110(D12), n/a-n/a, doi: 10.1029/2004JD005263.

Zhang, Y., F. H. Chiew, L. Zhang, and H. Li (2009), Use of remotely sensed actual evapotranspiration to improve rainfall–runoff modeling in Southeast Australia, Journal of Hydrometeorology, 10(4), 969-980.

Zhang, Z., N. E. Zimmermann, J. O. Kaplan, and B. Poulter (2016), Modeling spatiotemporal dynamics of global wetlands: comprehensive evaluation of a new sub-grid TOPMODEL parameterization and uncertainties, Biogeosciences, 13(5), 1387-1408.

Zhou, Y., X. Xiao, Y. Qin, J. Dong, G. Zhang, W. Kou, C. Jin, J. Wang, and X. Li (2016), Mapping paddy rice planting area in rice-wetland coexistent areas through analysis of Landsat 8 OLI and MODIS images, International Journal of Applied Earth Observation and Geoinformation, 46, 1-12, doi: http://dx.doi.org/10.1016/j.jag.2015.11.001.

Zhu, X., Q. Zhuang, Z. Qin, M. Glagolev, and L. Song (2013), Estimating wetland methane emissions from the northern high latitudes from 1990 to 2009 using artificial neural networks, Global Biogeochemical Cycles, 27(2), 592-604, doi: doi:10.1002/gbc.20052.